

The University of Nottingham

UNITED KINGDOM · CHINA · MALAYSIA

Synthetic Analogues of the Active site of [NiFe] Hydrogenase

Gemma Skelton, MSci

Thesis submitted to the University of Nottingham for the degree of Doctor of Philosophy

September 2016

Declaration

Except where specific reference is made to other sources, the work presented in this thesis is the original work of the author. It has not been submitted, in whole or on part, for any other degree.

Signed: Gemma Skelton

Date:

Abstract

This thesis describes the synthesis of new [Ni]- and [NiFe]-containing complexes as analogues of the active site of the [NiFe] hydrogenases and which have the potential as catalysis for the electro- or photochemical production of H_2. The research described in the thesis focuses on two key aspects: (i) the modulation of the potential at which proton reduction may occur through the nature of the ligand about the metal centres and (ii) the incorporation of photosensitiser units into [Ni]- and [NiFe]-containing complexes.

Chapter 1 provides an introduction to the [FeFe] and [NiFe] hydrogenases and provides the context for the research carried out in this thesis. Relevant coordination chemistry is surveyed with a focus on mononuclear and heteronuclear coordination compounds containing Ni-centres in S-rich coordination environments. The electro- and photocatalytic properties of some of the centres are discussed.

Chapter 2 describes the attempted synthesis and characterisation of the novel [Ni(p-qdt^{R1,R2})] ($R^1 = R^2 =$ Me ; R^1= H and R = ^{t}Bu) and [Ni(p-q^{6,7}dt^{R1,R2})] ($R^1 = R^2 =$ Me, Et and Ph; R^1 = H and R = ^{t}Bu) complexes. The complexes contain quinoxaline units that (i) may shift the reduction potentials to more positive for each complex and (ii) contain N atoms that may serve as protonation sites that may facilitate the reduction of protons. [Ni(p-q^{6,7}dt^{R1,R2})] ($R^1 = R^2 =$ Me, Et and Ph; R^1 = H and R = ^{t}Bu) undergo an electrochemically reversible reduction process at *ca.* -1.47 V *vs* Fc^+/Fc to generate the EPR-active [Ni(p-q^{6,7}dt^{R1,R2})]$^-$ anions. The spin Hamiltonian parameters derived from simulations of the EPR spectra are consistent with a SOMO that is principally metal-centred. Density functional calculations provide a framework for the interpretation of the spectroscopic properties of [Ni(p-q^{6,7}dt^{R1,R2})] ($R^1 = R^2 =$ Me, Et and Ph; R^1 = H and R = ^{t}Bu) and suggest that the redox-active LUMO is delocalised over the NiS_4 centre. Cyclic voltammetric measurements of [Ni(p-q^{6,7}dt^{R1,R2})] ($R^1 = R^2 =$ Me, Et and Ph; R^1 = H and R = ^{t}Bu) in acidic solutions show that these complexes are potential electrocatalysts for the reduction of H^+ and operate at *ca.* -1.7 V *vs* Fc^+/Fc at a comparable potential to [Ni(L^A)]. Comparisons of the cathodic currents produced by [Ni(p-q^{6,7}dt^{R1,R2})] ($R^1 = R^2 =$ Me, Et and Ph; R^1 = H and R = ^{t}Bu), [Ni(L^A)] and [Ni(L^A)$Fe_2(CO)_6$] suggest that the catalytic activities of [Ni(p-

$q^{6,7}dt^{R1,R2}$)] (R^1 = R^2 = Me, Et and Ph; R^1 = H and R = ^{t}Bu) and [Ni(L^A)] are comparable and higher than that for the benchmark [Ni(L^A)$Fe_2(CO)_6$] compound.

Chapter 3 describes the syntheses and characterisations of [Ni($qdt^{R1,R2}$)(dppe)] (R^1 = R^2 = Me; R^1 =H and R^2 = ^{t}Bu) and [Ni($q^{6,7}dt^{R1,R2}$)(dppe)] (R^1 = R^2 = Me, Et and Ph; R^1 = H and R = ^{t}Bu) complexes [Ni($qdt^{R1,R2}$)(dppe)] (R^1 = R^2 = Me; R^1 = H and R^2 = ^{t}Bu) and [Ni($q^{6,7}dt^{R1,R2}$)(dppe)] (R^1 = R^2 = Me, Et and Ph; R^1 = H and R = ^{t}Bu) undergo an electrochemically reversible reduction process at *ca.* -1.79 and *ca.* -1.86 V *vs* Fc^+/Fc, respectively, to generate the EPR-active [Ni($qdt^{R1,R2}$)(dppe)]$^-$ and [Ni($q^{6,7}dt^{R1,R2}$)(dppe)]$^-$ anions. The EPR spectra are consistent with DFT calculations that reveal SOMOs that involve contributions from Ni $3d_{xy}$ and S/P-σ combinations. Cyclic voltammetric studies show that [Ni($qdt^{R1,R2}$)(dppe)] (R^1 = R^2 = Me; R^1 = H and R^2 = ^{t}Bu) and [Ni($q^{6,7}dt^{R1,R2}$)(dppe)] (R^1 = R^2 = Me, Et and Ph; R^1 = H and R ^{t}Bu) are electrocatalysts that function at *ca.* -1.8 V *vs* Fc^+/Fc, and comparisons of the cathodic currents produced by [Ni($qdt^{R1,R2}$)(dppe)] (R^1 = R^2 = Me; R^1 = H and R^2 = ^{t}Bu), [Ni($q^{6,7}dt^{R1,R2}$)(dppe)] (R^1 = R^2 = Me, Et and Ph; R^1 = H and R = ^{t}Bu), [Ni(p-$q^{6,7}dt^{Et,Et}$)] and [Ni(L^A)$Fe_2(CO)_6$] suggested that the catalytic activities of [Ni($qdt^{R1,R2}$)(dppe)] (R^1 = R^2 = Me; R^1 = H and R^2 = ^{t}Bu) and [Ni($q^{6,7}dt^{R1,R2}$)(dppe)] (R^1 = R^2 = Me, Et and Ph; R^1 = H and R = ^{t}Bu) are comparable to [Ni(L^A)$Fe_2(CO)_6$] and lower than that for [Ni(p-$q^{6,7}dt^{Et,Et}$)].

Chapter 4 discusses the reactions of the Ni^{II} precursor complexes [Ni(p-$qdt^{R1,R2}$)] [Ni(p-$q^{6,7}dt^{R1,R2}$)], [Ni($qdt^{R1,R2}$)(dppe)] and [Ni($q^{6,7}dt^{R1,R2}$)(dppe)] described in Chapters 2 and 3 with [Fe]-containing fragments to isolate [NiFe] compounds as analogues of the active sites of the [NiFe] hydrogenases. The syntheses of [Ni($q^{6,7}dt^{R1,R2}$)$_2Fe_2(CO)_6$] and [Ni($q^{6,7}dt^{R1,R2}$)$_2$FeCp$(CO)_2$](BF_4) were confirmed by FTIR spectroscopy and mass spectrometry and [Ni($q^{6,7}dt^{Me,Me}$)$_2Fe_2(CO)_6$] was characterised by X-ray crystallography. In addition, [Ni($q^{6,7}dt^{Et,Et}$)$_2Fe_2(CO)_6$] and [Ni($q^{6,7}dt^{H,tBu}$)$_2Fe_2(CO)_6$] undergo an electrochemically reversible reduction process at *ca.*-1.22 V *vs* Fc^+/Fc. FTIR spectroscopy confirms the successful synthesis of [Ni($q^{6,7}dt^{R1,R2}$)(dppe)FeCp$(CO)_2$](BF_4) and [Ni($q^{6,7}dt^{Et,Et}$)(dppe)FeCp$(CO)_2$](BF_4) and [Ni($q^{6,7}dt^{H,tBu}$)(dppe)FeCp$(CO)_2$](BF_4) were characterised by X-ray crystallography.

Chapter 5 describes research towards the incorporation of photosensitising units into [Ni]- and [NiFe]-containing complexes. A novel dithiol substituted dppz complex, [Ni(dppz(S)$_2$)(dppe)], was characterised by X-ray crystallography and represents the first example of a Ni^{II} centre bound to S-donors from a dppz ligand. Additional reactions between this unit and [ReCl(CO)$_3$] fragments, and between [ReCl(CO)$_3$(dppz(S)$_2$)] and Ni^{II}-precursors are described, together with attempts to synthesise a NiS_4 complex containing two dppz units.

Chapter 6 draws together the main conclusions of the thesis and suggests areas for future work.

Acknowledgements

I would like to thank my supervisors, Dr Jonathan McMaster and Professor Martin Schröder. Without their help, guidance and patience this work would not have been possible. I wish to thank Dr E. Stephen Davies for his invaluable knowledge and assistance. Many thanks to Dr William Lewis and Professor Alexander Blake for their help with crystallography. I am also very grateful to the technical staff of the School of Chemistry, especially Mark Guyler, Graham Coxhil, Dr Mick Cooper and Clive Dixon.

I would like to say a big thank you to Dr Joe Dawson for training me at the start of my PhD and for always helping through invaluable discussions and playing devil's advocate. Special thanks to George, Jere and Joe, I couldn't have asked for better company (Jere you kept me sane by being the insane one). A thank you to Becky, Saz, Jenny and Zoe for being great friends and never failing to lift my spirits.

I would also like to acknowledge the valuable contributions of my project students Gabby, Divya and Mathew. Thanks also to Ben, Emma, Carlo, Charlene, Fran, Jess, Bahar, Nick, Pete, Jack, Martyn, Will, Maggie, Nevo, Chris and everyone else in the Schröder/McMaster group, past and present, who have made the last 4 years so enjoyable.

I am grateful to Alistair for his support and encouragement during my PhD. I would like to thank my amazing big family, I am especially grateful to the Skelarks for all the tea and cake, it has been lovely to a home away from home, thank you.

Finally, I would like to dedicate this thesis to Mum, Dad and Amy, without their love, understanding and most of all their never faltering faith in me I could not have achieved any of this.

Declaration. i
Abstract. ii
Acknowledgements v
Table of contents vi
Abbreviations.

1.Introduction

1.1 Bioinorganic Chemistry 2
1.2 The Hydrogenases 2
1.2.1 [FeFe] Hydrogenases 3
1.2.2 [NiFe] Hydrogenase 4
1.2.3 [NiFeSe] Hydrogenase 5
1.3 Redox states of the [NiFe] Hydrogenase 6
1.4 The Catalytic Mechanism of [NiFe] Hydrogenase 7
1.5 Synthetic Analogues of the [NiFe] Hydrogenase 8
1.5.1 Nickel thiolate ligated complexes 9
1.5.2 Binuclear [NiFe] thiolate-ligated complexes 13
1.5.3 [NiFe] Complexes incorporating thiolate and phosphine donors 15
1.5.4 [NiFe] Polymetallic complexes 17
1.6 Analogues of [NiFe] Hydrogenase Incorporating Proton Relay sites 19
1.6.1 Nickel Complexes Incorporating Protonation sites 19
1.6.2 [NiFe] Complexes That Incorporate Protonation Sites 21
1.7 Hydrogenase Bio-mimetic Compounds in Artificial Photosynthetic Systems 22
1.7.1 Photocatalytic H_2 production 22
1.7.2 Catalysis incorporating photosensitiser systems 23
1.7.3 Photocatalytic H_2 production using $[Re(CO)_3Cl(bpy)]$ as a photosensitiser and [NiFe] as a catalyst in CH_2Cl_2 23
1.7.4 Studies into a supramolecular system containing a Rhenium Photosensitiser Covalently linked to a [NiFe] Catalyst for Photochemical H_2 production 24
1.8 Aims of This Work 25
1.9 References 26

2. NiS_4 Complexes Containing Two Quinoxaline Units: Synthesis, Characterisation and Catalytic Studies.

2.1 Introduction 33
2.2 Aims 36
2.3 Ligand Synthesis 37
2.3.1 Synthesis of substituted quinoxaline-2,3-dithiols, $qdt^{R1,R2}H_2$ (R^1 = R^2 = Me and R^1 = H, R^2 = ^{t}Bu) 38

2.3.2	Synthesis of quinoxaline-6,7-dithiols $q^{6,7}dt^{R1,R2}H_2$ ($R^1 = R^2 =$ Me, Et, Ph; $R^1 =$ H, $R^2 = {}^t$Bu)	39
2.3.3	The structural characterisation of $q^{6,7}dt^{R1,R2}(SCN)_2$ ($R^1 = R^2 =$ Me, Et, and Ph; $R^1 =$ H, $R^2 = {}^t$Bu)	40
2.3.4	The structural characterisation of $q^{6,7}dt^{R1,R2}(SCN)_2$ ($R^1 = R^2 =$ Me, Et, and Ph; $R^1 =$ H, $R^2 = {}^t$Bu)	42
2.3.5	The structural characterisation of $q^{6,7}dt^{R1,R2}(SCN)_2$ ($R^1 = R^2 =$ Me, Et, and Ph; $R^1 =$ H, $R^2 = {}^t$Bu)	43
2.4	**Syntheses of Ni^{II} complexes**	44
2.4.1	The synthesis of $[Ni(L^A)]$	44
2.4.2	The syntheses of $[Ni(p\text{-}qdt^{R1,R2})]$ ($R^1 = R^2 =$ Me; $R^1 =$ H, $R^2 = {}^t$Bu)	44
2.4.3	The syntheses attempted of $[Ni(p\text{-}q^{6,7}dt^{R1,R2})]$ ($R^1 = R^2 =$ Me, Et, Ph and $R^1 =$ H, $R^2 = {}^t$Bu)	45
2.5	**The single crystal X-ray structures of $[Ni(p\text{-}q^{6,7}dt^{Et,Et})]$ and $[Ni(p\text{-}q^{6,7}dt^{H,tBu})]$ and $[Ni(L^A)]$**	46
2.6	**Cyclic Voltammetric studies**	50
2.6.1	Cyclic Voltametric studies of $[Ni(L^A)]$	50
2.6.2	Cyclic voltammetric studies of $[Ni(p\text{-}q^{6,7}dt^{R1,R2})]$ ($R^1 = R^2 =$ Me, Et, Ph; $R^1 =$ H, $R^2 = {}^t$Bu)	51
2.7	**Spectroelectrochemistry of $[Ni(p\text{-}q^{6,7}dt^{R1,R2})]$ ($R^1 = R^2 =$ Et, $R^1 =$ H, $R^2 = {}^t$Bu)**	52
2.8	**EPR Spectroscopy of $[Ni(p\text{-}q^{6,7}dt^{Et,Et})]^-$ and $[Ni(p\text{-}q^{6,7}dt^{H,tBu})]^-$**	55
2.9	**Cyclic Voltammetric studies in the presence of TFA**	55
2.9.1	Cyclic Voltammetric studies of $[Ni(L^A)]$ in the presence of TFA	56
2.9.2	Cyclic Voltammetric studies of $[Ni(p\text{-}q^{6,7}dt^{Et,Et})]$ and $[Ni(p\text{-}q^{6,7}dt^{H,tBu})]$ in the presence of TFA	58
2.9.3	Comparison of the Cyclic Voltammetric studies of $[Ni(p\text{-}q^{6,7}dt^{Et,Et})]$, $[Ni(p\text{-}q^{6,7}dt^{H,tBu})]$ and $[Ni(L^A)]$ in the presence of TFA	60
2.9.4	Comparison of Cyclic Voltammetric studies of $[Ni(p\text{-}q^{6,7}dt^{Et,Et})]$, $[Ni(L^A)]$ and $[Ni(L^A)Fe_2(CO)_6]$ in the presence of TFA	61
2.10	**UV/vis spectroscopy of $[Ni(p\text{-}q^{6,7}dt^{Et,Et})]$ in the presence of TFA**	62
2.11	**DFT Studies**	65
2.11.1	DFT Studies of protonation of $[Ni(p\text{-}q^{6,7}dt^{Et,Et})]$	68
2.12	**Conclusion**	71
2.13	**Experimental**	73
2.13.1	The synthesis of 6,7-^{R1,R2}quinoxaline-2,3-dione (3) ($R^1 = R^2 =$ Me and $R^1 =$ H, $R^2 = {}^t$Bu)	73
2.13.2	The synthesis of 6,7-^{R1R2}-2,3-dichloroquinoxaline (4) ($R^1 = R^2 =$ Me and $R^1 =$ H, $R^2 = {}^t$Bu)	73
2.13.3	The synthesis crude of $qdt^{R1,R2}H_2$ ($R^1 = R^2 =$ Me and $R^1 =$ H, $R^2 = {}^t$Bu)	74

2.13.4	The synthesis of crude [Ni(p-qdt^{R1,R2})] ($R^1 = R^2$ = Me and R^1 = H, R^2 = ^{t}Bu)	75
2.13.5	The synthesis of 3,3-dimethyl-2-oxobutanal	76
2.13.6	The synthesis of q^{6,7}dt^{R1,R2}(SCN)$_2$ ($R^1 = R^2$ = Me, Et, Ph; R^1 = H, R^2 = ^{t}Bu)	76
2.13.7	The synthesis of crude q^{6,7}dt^{R1,R2}H$_2$ ($R^1 = R^2$ = Me, Et, Ph; R^1 = H, R^2 = ^{t}Bu)	77
2.13.8	Synthesis of [Ni(p-q^{6,7}dt^{R1,R2})] ($R^1 = R^2$ = Me, Et, Ph; R^1 = H, R^2 = ^{t}Bu)	78
2.14	**References**	79

3. NiS$_2$P$_2$ Complexes Containing a Quinoxaline Unit: Synthesis, Characterisation and Catalytic Studies.

3.1	**Introduction**	82
3.2	**Ligand Synthesis**	84
3.3	**The Syntheses of Ni^{II} Complexes**	85
3.3.1	The synthesis of [Ni(qdt^{R1,R2})(dppe)] ($R^1 = R^2$ = Me; R^1 = H, R^2 = ^{t}Bu)	85
3.3.2	The synthesis of [Ni(q^{6,7}dt^{R1,R2})(dppe)] ($R^1 = R^2$ = Me, Et, Ph; R^1 = H, R^2 = ^{t}Bu)	86
3.4	**Single Crystal X-ray structures**	87
3.4.1	The single crystal x-ray structures of [Ni(qdt^{R1,R2})(dppe)] ($R^1 = R^2$ = Me; R^1 = H, R^2 = ^{t}Bu)	87
3.4.2	The single crystal x-ray structures of [Ni(q^{6,7}dt^{R1,R2})(dppe)] ($R^1 = R^2$ = Me, Et, Ph; R^1 = H, R^2 = ^{t}Bu)	89
3.4.3	Summary of the x-ray crystal structures of [Ni(qdt^{R1,R2})(dppe)] ($R^1 = R^2$ = Me; R^1 = H, R^2 = ^{t}Bu) and [Ni(q^{6,7}dt^{R1,R2})(dppe)] ($R^1 = R^2$ = Me, Et, Ph; R^1 = H, R^2 = ^{t}Bu)	91
3.5	**Cyclic Voltammetric Studies of [Ni(qdt^{R1,R2})(dppe)] ($R^1 = R^2$ = Me; R^1 = H, R^2 = ^{t}Bu) and [Ni(q^{6,7}dt^{R1,R2})(dppe)] ($R^1 = R^2$ = Me, Et; R^1 = H, R^2 = ^{t}Bu)**	92
3.5.1	A comparison of the Cyclic Voltammetric Studies of [Ni(qdt^{R1,R2})(dppe)] ($R^1 = R^2$ = Me; R^1 = H, R^2 = ^{t}Bu) and [Ni(q^{6,7}dt^{R1,R2})(dppe)] ($R^1 = R^2$ = Me, Et; R^1 = H, R^2 = ^{t}Bu)	95
3.6	**Spectroelectrohemistry of [Ni(qdt^{R1,R2})(dppe)] ($R^1 = R^2$ = Me; R^1 = H, R^2 = ^{t}Bu)) and [Ni(q^{6,7}dt^{R1,R2})(dppe)] ($R^1 = R^2$ = Me, Et; R^1 = H, R^2 = ^{t}Bu)**	96
3.7	**EPR Studies of [Ni(qdt^{R1,R2})(dppe)]$^-$ ($R^1 = R^2$ = Me; R^1 = H, R^2 = ^{t}Bu) and [Ni(q^{6,7}dt^{R1,R2})(dppe)]$^-$ ($R^1 = R^2$ = Me, Et, Ph; R^1 = H, R^2 = ^{t}Bu)**	102

3.8	**Cyclic Voltammetric Studies of [Ni(qdt^{R1,R2})(dppe)]$^-$ ($R^1 = R^2$ = Me; R^1 = H, R^2 = ^{t}Bu) and [Ni(q^{6,7}dt^{R1,R2})(dppe)]$^-$ ($R^1 = R^2$ = Me, Et, Ph; R^1 = H, R^2 = ^{t}Bu) in the presence of TFA**	106
3.8.1	Comparisons of the Cyclic Voltammetric Studies of [Ni(qdt^{R1,R2})(dppe)]$^-$ ($R^1 = R^2$ = Me; R^1 = H, R^2 = ^{t}Bu) and [Ni(q^{6,7}dt^{R1,R2})(dppe)]$^-$ ($R^1 = R^2$ = Me, Et; R^1 = H, R^2 = ^{t}Bu), [Ni(L^A)Fe$_2$(CO)$_6$], [Ni(p-q^{6,7}dt^{Et,Et})] and [Ni(L^A)] in the presence of TFA	110
3.8.2	Comparisons of The Cyclic Voltammetric Studies of [Ni(qdt^{Me,Me})(dppe)] to [Ni(L^A)Fe$_2$(CO)$_6$] in the presence of TFA	112
3.9	**DFT Studies**	114
3.9.1	DFT Studies of Protonation of [Ni(qdt^{Me,Me})(dppe)] and [Ni(q^{6,7}dt^{Et,Et})(dppe)]	119
3.10	**Conclusions**	123
3.11	**Experimental**	124
3.11.1	The Synthesis of [Ni(qdt^{R1,R2})(dppe)] ($R^1 = R^2$ = Me; R^1 = H, R^2 = ^{t}Bu)	124
3.11.2	The Synthesis of [Ni(q^{6,7}dt^{R1,R2})(dppe)] ($R^1 = R^2$ = Me, Et, Ph; R^1 = H, R^2 = ^{t}Bu)	125
3.12	**References**	126

4. Synthesis Towards [NiFe] Complexes Incorporating Quinoxaline-based Ligands: Synthesis and Characterisation.

4.1	**Introduction**	129
4.2	**Aims**	131
4.3	**Attempted Syntheses of [NiFe] complexes using [Ni(p-qdt^{H,tBu})] as the Ni^{II} precursor**	132
4.3.1	The reaction between [Ni(p-qdt^{H,tBu})] and Fe$_3$(CO)$_{12}$	132
4.3.2	The reaction between [Ni(p-qdt^{H,tBu})] and [Fe(CO)$_4$I$_2$]	132
4.3.3	The reaction between [Ni(p-qdt^{H,tBu})] and [FeCp(CO)$_2$I]	133
4.3.4	The reaction between [Ni(p-qdt^{H,tBu})] and [FeCp(CO)$_2$(THF)](BF$_4$)	133
4.4	**The synthesis of [NiFe] complexes using [Ni(p-q^{6,7}dt^{R1,R2})] ($R^1 = R^2$ = Me, Et and Ph; R^1 = H, R^2 = ^{t}Bu)**	134
4.4.1	The synthesis of [Ni(p-q^{6,7}dt^{R1,R2})Fe$_2$(CO)$_6$] ($R^1 = R^2$ = Me, Et and Ph; R^1 = H, R^2 = ^{t}Bu)	134
4.4.2	The reactions between [Ni(p-q^{6,7}dt^{R1,R2})] and [FeCp(CO)$_2$(THF)](BF$_4$)	136
4.4.3	The deactivation of the thiolate S-donors in [Ni(p-qdt^{R1,R2})]	137
4.4.4	The single crystal X-ray structure of [Ni(q^{6,7}dt^{Me})$_2$Fe$_2$(CO)$_6$]	139
4.5	**Cyclic voltametric studies of [Ni(p-q^{6,7}dt^{R1,R2})Fe$_2$(CO)$_6$] ($R^1 = R^2$ = Et; R^1 = H, R^2 = ^{t}Bu)**	142

4.6 The Synthesis of [NiFe] Compounds from [Ni($q^{6,7}dt^{R1,R2}$)(dppe)] ($R^1 = R^2$ = Me, Et, Ph and R^1 = H R^2 = ^{t}Bu) and [Ni($qdt^{R1,R2}$)(dppe)] ($R^1 = R^2$ = Me, and R^1 = H R^2 = ^{t}Bu) precursors 145

4.6.1 The reaction between [Ni($q^{6,7}dt^{Et,Et}$)dppe] and $Fe_3(CO)_{12}$ 146

4.6.2 The reaction between [Ni(p-$q^{6,7}dt^{Et,Et}$)(dppe)] and [$FeCp(CO)_2I$] 146

4.6.3 The reaction between [Ni($q^{6,7}dt^{Et,Et}$)(dppe)] and [$FeCp(CO)_2(THF)$][BF_4] 147

4.6.4 The syntheses of [Ni($qdt^{R1,R2}$)(dppe)$FeCp(CO)_2$][BF_4] ($R^1 = R^2$ = Me; R^1 = H, R^2 = ^{t}Bu) and [Ni($q^{6,7}dt^{R1,R2}$)(dppe)$FeCp(CO)_2$][BF_4] ($R^1 = R^2$ = Me, Ph; R^1 = H, R^2 = ^{t}Bu) 148

4.6.5 The single crystal X-ray structures of [Ni($q^{6,7}dt^{R1,R2}$)(dppe)$FeCp(CO)_2$][BF_4] ($R^1 = R^2$ = Et; R^1 = H, R^2 = ^{t}Bu) 149

4.7 Conclusion 151

4.8 Experimental 153

4.8.1 The attempted Synthesis of [Ni(p-$qdt^{H,tBu}$)$Fe_2(CO)_6$] 153

4.8.2 The attempted Synthesis of [Ni(p-$qdt^{H,tBu}$)FeCp(CO)]I 153

4.8.3 The synthesis of [$CpFe(CO)_2(THF)$][BF_4] 153

4.8.4 The attempted Synthesis of [Ni(p-$qdt^{H,tBu}$)FeCp(CO)][BF_4] 154

4.8.5 The synthesis of crude [Ni(p-$q^{6,7}dt^{R1,R2}$)$Fe_2(CO)_6$] ($R^1 = R^2$ = Me, Et, Ph; R^1 = H, R^2 = ^{t}Bu) 154

4.8.6 Attempted syntheses of [Ni(p-$q^{6,7}dt^{R1,R2}$)$FeCp(CO)_2$][BF_4] ($R^1 = R^2$ = Me, Et, Ph; R^1 = H, R^2 = ^{t}Bu) 155

4.8.7 The attempted Synthesis of [Ni($q^{6,7}dt^{Et,Et}$)(dppe)$Fe_2(CO)_6$] 155

4.8.8 The reaction between [Ni($q^{6,7}dt^{Et,Et}$)(dppe)$Fe_2(CO)_6$] and [$FeCp(CO)_2I$] 156

4.8.9 The syntheses of crude [Ni($qdt^{R1,R2}$)(dppe)$FeCp(CO)_2$][BF_4] ($R^1 = R^2$ = Me; R^1 = H, R^2 = ^{t}Bu) and [Ni($q^{6,7}dt^{R1,R2}$)(dppe)$FeCp(CO)_2$][BF_4] ($R^1 = R^2$ = Me, Et, Ph R^1 = H, R^2 = ^{t}Bu) 156

4.9 References 157

5. Ni^{II} and [NiFe] Complexes Incorporating a Fused Photoactive Centre for the Light-driven Production of H_2: Synthesis and Characterisation.

5.1 Introduction 160

5.2 Aims 162

5.3 Synthetic design 163

5.4 Synthesis towards a Ni^{II} and [NiFe] compound containing a photosensitiser unit: Approach A 167

5.4.1 The synthesis of [$ReCl(CO)_3$(dppz$(SCN)_2$)],1 168

5.4.2	The synthesis of $[ReCl(CO)_3(dppz(SH)_2)]$, 2	169
5.4.3	The attempted Synthesis of $\{Ni[ReCl(CO)_3dppz(S)_2]_2\}$, 3	171
5.5	**Synthesis towards a Ni^{II} and [NiFe] compound containing a photosensitiser unit: Approach B**	171
5.5.1	The attempted synthesis of $[Ni(p\text{-}dppz(S)_2)_2]$, 5	172
5.5.2	The attempted synthesis of $\{Ni[ReCl(CO)_3(p\text{-}dppz(S)_2)]_2\}$, 3	173
5.5.3	The attempted synthesis of $\{Ni[ReCl(CO)_3(p\text{-}dppz(S)_2)]_2Fe\text{-}_2(CO)_6\}$, 4	174
5.6	**Towards a Ni^{II} and [NiFe] compound containing a single photosensitiser unit**	175
5.6.1	The synthesis of $[Ni(dppz(S)_2)(dppe)]$	176
5.6.2	Single X-ray crystallography of $[Ni(dppz(S)_2)(dppe)]$	177
5.6.3	The attempted synthesis of $\{Ni[ReCl(CO)_3(dppz(S)_2)](dppe)\}$: Route A	181
5.6.4	Attempted synthesis of $[Ni(ReCl(CO)_3dppz(S)_2)dppe]$: Route B	182
5.6.5	Attempted synthesis of $[Ni(dppz(S)_2)(dppe)FeCp(CO)_2]$	183
5.7	**Conclusion**	184
5.8	**Future work**	185
5.9	**Experimental**	187
5.9.1	The attempted synthesis of $[ReCl(CO)_3(dppz(H)_2)]$ using $Na_2S{\cdot}9H_2O$ in water	187
5.9.2	The synthesis of crude $[ReCl(CO)_3(dppz(SH)_2)]$	187
5.9.3	The attempted synthesis of $\{Ni[(ReCl(CO)_3)_2(p\text{-}dppz(S)_2)]\}$	187
5.9.4	The attempted synthesis of $[Ni(p\text{-}dppz(S)_2)]$	188
5.9.5	The synthesis of crude $\{Ni[(ReCl(CO)_3)_2(p\text{-}dppz(S)_2)]\}$	188
5.9.6	The attempted synthesis of $[Ni(dppz(S)_2)_2Fe_2(CO)_6]$	189
5.9.7	The synthesis of crude $[Ni(dppz(S)_2)(dppe)]$	189
5.9.8	The attempted synthesis of $\{Ni[ReCl(CO)_3(dppz(S)_2)](dppe)\}$: Method 1	190
5.9.9	The attempted synthesis of $\{Ni[ReCl(CO)_3(dppz(S)_2)](dppe)\}$: Method 2	190
5.10	**References**	190
6. Conclusions		193
Appendix		197

Abbreviations

2-pedt	1-(pyridine-2'-yl)ethane-1,2-dithiolate	E_p^c, E_p^a	cathodic or anodic peak potential
3-pedt	-(pyridine-3'-yl)ethane-1,2-dithiolate	EPR	electron paramagnetic resonance
4-pedt	1-(pyridine-4'-yl)ethane-1,2-dithiolate	Fc	Ferrocene
A_{ii}	a value (EPR spectroscopy)	FTIR	Fourier transform infrared spectroscopy
Ar	Aromatic	g_{ii}	g value (EPR spectroscopy)
bdt	benzene-1,2-dithiolate	HOMO	highest unoccupied orbital
bipy	2,2'-bipyridine	HYSCORE	hyperfine sublevel
cm^{-1}	wavenumber	I_p^c, I_p^a	cathodic or anodic peak current
Cp	cyclopentadienyle		
CV	cyclic voltammetry	L	general ligand
Cys	cysteine	LUMO	lowest unoccupied orbital
d	doublet	NHE	normal hydrogen electrode
DCM	dichloromethane	NMR	nuclear magnetic resonance
DFT	density functional theory	m	multiplet
DMF	dimethylformamide	Me	methyl
DMSO	Dimethyl sulfoxide	Ph	phenyl
dppe	1,2-bis(diphenylphosphino)ethane	qdt	2,3-Quinoxaline-dithiolate
		$q^{6,7}$dt	6,7-Quinoxaline-dithiolate
dppz	dipyridophenazine	R	general substituent
dt	1,2-dithiolate	s	singlet
E	potential, energy or electrochemical process according to context	Sec	selenocysteine
		SCE	saturated calomel electrode
		sdt	
$E_{1/2}$	half-wave potential	SHE	standard hydrogen electrode
Et	ethyl	t	triplet
ENDOR	electron nuclear double resonance	tBu	*Tert*-butyl
		TFA	trifluoroacetic acid
		Tof	turnover frequency

ToN	turnover number	W_{ii}	Gaussian width (EPR simulation)
UV/Vis	ultraviolet-visible spectroscopy	XAS	X-ray diffraction
v	scan rate or frequency depending on the context	δ	chemical shift
		S	electron spin

CHAPTER ONE
Introduction

With a rising standard of living and a growing population, global energy consumption is set to increase drastically by 2050.[1] Therefore the challenge is to develop clean and sustainable sources of energy.[2,3] While conventional fossil fuels may be sufficient over the short term (50-70 years),[4] other factors such as the economy and their impact on the environment makes the development of sustainable and renewable sources particularly pressing.[1,5] It is clear that the current atmospheric CO_2 levels of 380 ppm are significantly higher than any point in the last 650,000 years[6,7] and the response of the climate to continued runaway CO_2 emissions remains unclear.

H_2 is a green fuel as it produces only water and energy on combustion. Therefore, H_2 is a viable option as a sustainable fuel provided a sustainable method for its production can be developed. Currently, the most commonly used route for the production of H_2 is *via* steam reformation from methane gas. However, this process requires high pressure and temperature (13–20 bar and 800–1000 °C, respectively)[8] and consequently the current method of H_2 production is not sustainable.[9] The research described in this thesis focuses on the development of catalysts for H_2 production that are inspired by the structure of the active site of the [NiFe] hydrogenases in an attempt to address this issue. The hydrogenases catalyse the cleavage of H_2 into protons or catalyse the generation of H_2 from the reduction of protons (Equation 1.1). The generation of H_2 by the [NiFe] hydrogenases typically occurs with a turnover rate of *ca.* 1500-9000 ToN s^{-1} at 30 ^{0}C and at redox potentials close to -400 mV *vs* SHE.[10–12] Hydrogenase enzymes are air, temperature and pH sensitive, and consequently are not currently a viable option for H_2 production on a large scale.[13]

$$H_2 \rightleftharpoons 2H^+ + 2e^-$$

Equation 1.1: The reversible two-electron oxidation of dihydrogen.[14]

Thus, in order for significant progress to be made for the production of H_2 and its implementation as a fuel on a global scale, new systems and design strategies must be pursued that allow H_2 to be generated, or photogenerated, at low electrochemical overpotentials.[1,15]

1.1 Bioinorganic Chemistry[16]

Enzymes are large folded proteins with typical molecular weights in the range 20000-100000 Da[17] and which catalyse reactions under mild conditions (30-40 ^{0}C, pH 7). [17] Enzymes also usually operate with high regio-, stereo- and enantio-selectivity[18] with relatively high turnover frequencies.[19] For many enzymes spectroscopic and X-ray crystallographic studies have revealed the presence of trace elements such as Cu, Zn, Ni, Co, Fe, Mo and Mn at the active site,[20,21] which usually play critical roles in modulating the chemistry of the enzyme and take advantage of the variable coordination spheres and oxidation states exhibited by transition metal centres.[22]

The large size of metalloenzymes means it can be difficult to obtain high-resolution structural information about the metal-containing active site, which can limit the conclusions that may be drawn with respect to the structure-function relationships associated with the enzyme. The development of small molecular analogues, based on the available structural information for the active site of the enzyme, can generate new compounds that reproduce the physical and/or chemical properties of the enzyme. Thus, these analogues may provide insight into the structural and mechanistic properties of the active sites of enzymes and may have the potential to be developed into *in vitro* catalysts for the same chemical reactions catalysed by the biological systems.

1.2 The Hydrogenases

The atmosphere of the early Earth was H_2-rich and it has been presumed that the hydrogenase enzymes evolved during this period with some of the earliest bacterial life utilising H_2 as an energy source.[23] The name hydrogenase was first adopted by Stephenson and Stickland in 1931 after the observation of dihydrogen production and its use in substrate reduction by colon bacteria.[24] Phylogenetic analyses have led to the identification of three distinct classes of hydrogenases:[25] the [NiFe]-hydrogenases, [FeFe]-hydrogenases, and iron-sulfur-free hydrogenases (known as the [Fe] hydrogenases).[26,27]

1.2.1 [FeFe] Hydrogenases

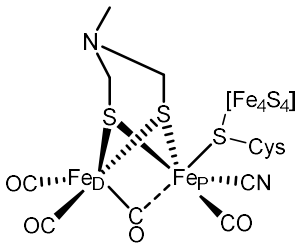


Figure 1.1: The structure of the active site of [FeFe]-hydrogenase. The distal Fe centre (Fe_D) centre is ligated by two terminal CO ligands and by a bridging CO ligand to proximal Fe centre (Fe_P), which is bound to a further terminal CO and CN^- ligand and to S group bound to a cysteine group and a $[Fe_4S_4]$ cluster.[14]

The X-ray crystal structure of [FeFe]-hydrogenase from *Clostridium pasteurianum* and *Desulfovibrio desulfuricans* was first solved in 1998 by two independent groups: Peters *et al.*[28] and Nicolet *et al.*[29], respectively. The [FeFe] hydrogenases are usually isolated as monomeric enzymes which contain up to four Fe-S centres and a H-cluster (proximal cluster). The H-cluster is a binuclear Fe-Fe centre (Figure 1.1) where the distal Fe centre (Fe_D) centre is ligated by two terminal CO ligands and by a bridging CO ligand to proximal Fe centre (Fe_P) which is bound to a further terminal CO and CN^- ligand, and to a $[Fe_4S_4]$ cluster. The two Fe centres in the H-cluster are also bridged by a di(thiomethyl)amine unit.[28–31] Dimeric, trimeric, and tetrameric [FeFe] hydrogenases are also known, and all contain a similar H-cluster.[28,32–36]

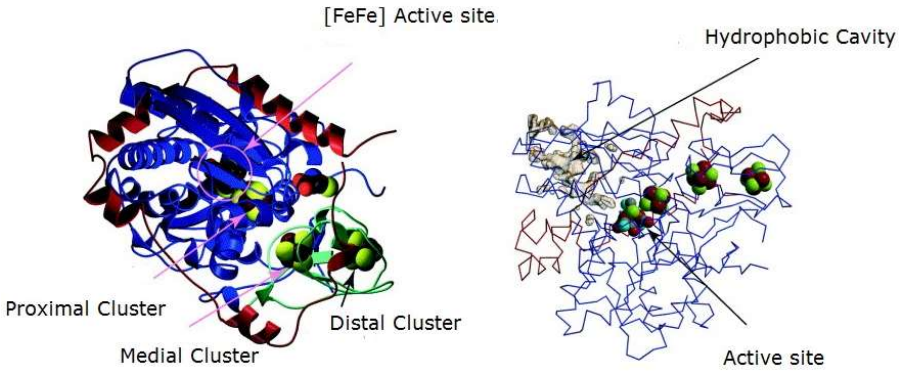


Figure 1.2: Left: Schematic representation of the structure of the [FeFe] hydrogenase from *Desulfovibrio desulfuricans* and Right: Hydrophobic channels, active sites and the proximal, medial and distal [4Fe4S] clusters.[32]

X-ray crystallography has identified a hydrophobic channel that runs from the surface of the enzyme to the active site and points at the [FeFe] centre. This

hydrophobic channel may facilitate the diffusion of H_2 gas to and from the active site.[28,37,38] A proposed route for the proton-transfer pathway within [FeFe] hydrogenase, derived from the X-ray crystallographic data, involves the N atom at the bridgehead [di(thiomethyl)amine] as a proton relay site, from which the proton can be transferred to the surface.[36–38]

1.2.2 [NiFe] Hydrogenase

The first reported crystal structure of [NiFe] hydrogenase *Desulfovibrio gigas* was published in 1995 by Volbeda *et al.*[39] The crystal structure shows that [NiFe] hydrogenase consists of two subunits: a large α-subunit of *ca.* 60 kDa hosting the bimetallic active site and the small β-subunit with molecular weight of about 28 kDa, hosting the three [Fe_4S_4] clusters.[40,41] Studies have shown that the two subunits interact extensively through a large contact surface and form a globular heterodimer.[41–44]

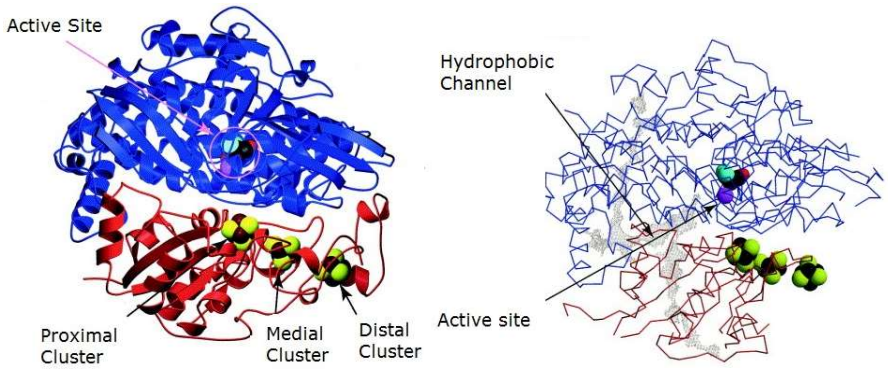


Figure 1.3: Left: Schematic representation of the structure of the [NiFe] hydrogenase and right: Hydrophobic channels, active sites and the proximal, medial and distal [Fe_4S_4] clusters of *Desulfovibrio gigas.*[32]

At the bimetallic active site (Figure 1.3), the Ni and Fe centres are separated by a distance of *ca.* 2.5-2.9 Å[45] and are bridged by the sulfur atoms derived from two cysteine residues (Cys68 and Cys533).[39] The Ni centre is coordinated by two additional cysteine residues (Cys65 and Cys530) bound in a terminal position.[40] The Fe centre is also coordinated by three inorganic diatomic ligands that have been identified by infrared spectroscopy as two CN^- ligands and one CO group.[46–48] Hydrophobic channels linking the active site to the surface of the molecule may facilitate H_2 transfer to the active site.

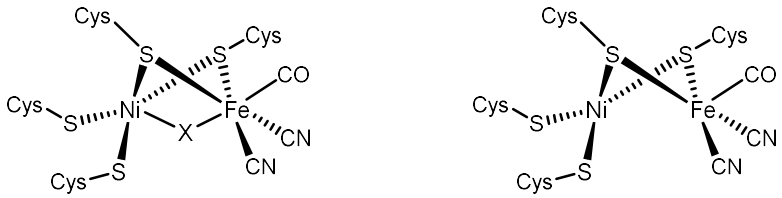


Figure 1.4: Schematic representation of the *D. vulgaris Myazaki F* in the oxidised (left) and reduced forms (right).[44,49] The oxidised form contains species X which is proposed to be a hydro-peroxide (OOH^-) or a hydroxide (OH^-) ligand. [50,51]

The active sites of the as-isolated oxidised forms of [NiFe] hydrogenase *D. vulgaris Myazaki F* also contain an exogenous species that bridge the Ni and Fe centres (Figure 1.4; denoted as X).[50,51] Crystallographic studies suggest that in the as-isolated oxidised forms X may be a peroxide or hydroxide bridging group.[50,51] Lubitz *et al*. have also shown recently that a hydride is present at the bridging site in the active reduced Ni-R form of the [NiFe] hydrogenase.[52]

1.2.3 [NiFeSe] Hydrogenase

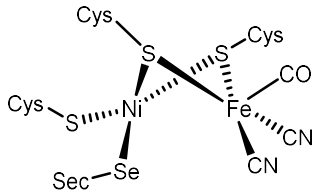


Figure 1.5: Schematic representation of the active site of [NiFeSe]-hydrogenase fromDesulfovibrio vulgaris.[53]

Another member of the hydrogenase family is [NiFeSe]-hydrogenase. [NiFeSe]-hydrogenase is a selenium-containing subclass of the [NiFe]-hydrogenase. Selenium is present in proteins in the amino acid selenocysteine (Sec).[54] The [NiFeSe]-hydrogenase is an example of nature's use of selenium, the active site is identical to that of the [NiFe]-hydrogenases except for the replacement of a terminally coordinated cysteine residue by selenocysteine (Figure 1.5).[55,53] The Sec amino acid is structurally identical to Cys, with a selenium atom replacing the sulfur atom.[53] [NiFeSe]-hydrogenase will not be discussed further within this thesis.

1.3 Redox states of the [NiFe] Hydrogenase

Several different redox states of [NiFe] hydrogenase (Figure 1.6) have been identified by IR,[56] EPR, [57] XAS,[58,59] Mössbauer[60] spectroscopic, and redox titrimetric studies.[37]

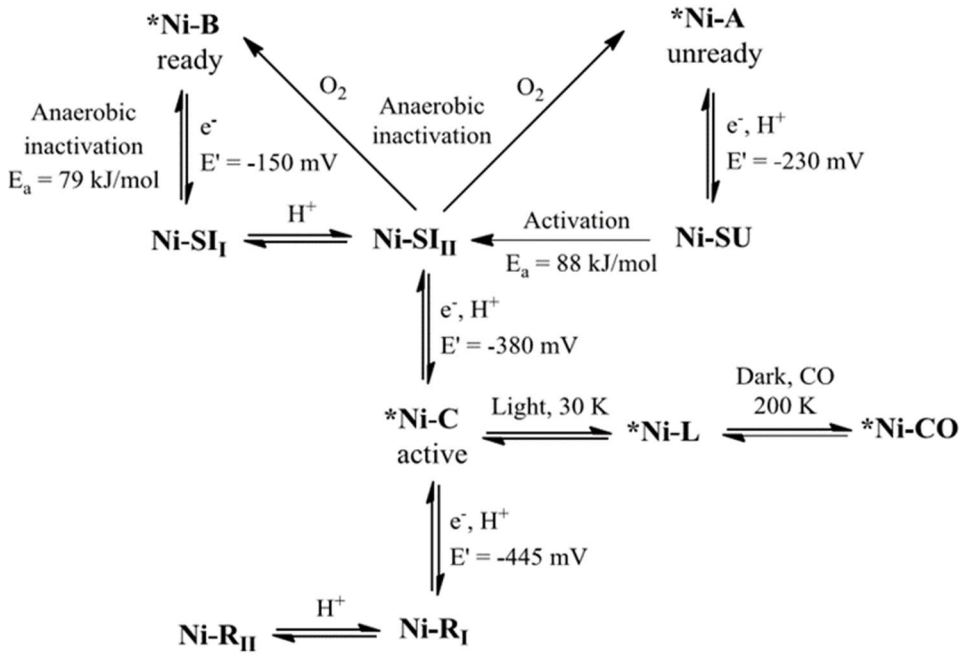


Figure 1.6: Scheme of the different redox states of the active site of [NiFe] hydrogenases.[14] Paramagnetic EPR-active states are marked with an asterisk. The formal redox potentials (at pH 8.0), energy barriers, and pK_a correspond to those measured by FTIR-spectroelectrochemistry of *D. gigas* hydrogenase Ni-A, Ni-B, Ni-S_U, Ni-S_I, Ni-S_{II}, Ni-CO, and Ni-R are named in some references as Ni_u, Ni_r, Ni_u-S, Ni_r-S, Ni_a-S, Ni-S'CO, and Ni-SR, respectively.

Two forms of the active site may be identified, Ni-A and Ni-B, when [NiFe] hydrogenases are isolated under aerobic conditions.[61] These are catalytically inactive and give rise to distinct EPR signals. It has been suggested that the bridging group present in Ni-A is a peroxide[50] and in Ni-B it is a hydroxide group.[14] Redox titrations have shown that the one electron reduction of the EPR-active Ni-A and Ni-B states generate the EPR silent species Ni-SU and Ni-SI_I, respectively.[47] The rates of conversion between the respective inactive and active states are different for each Ni-A and Ni-B form; the Ni-B (ready) form is activated within minutes under an H_2 atmosphere, whereas the Ni-A (unready) form requires several hours of exposure to H_2. The Ni-SU and Ni-SI_I states can be converted to the catalytically active Ni-C state *via* the Ni-SI_{II} state.[62]

EPR spectroscopic studies have shown that the paramagnetic state Ni-C possesses a hydride bridge between the Ni and Fe centres.[63–65] Illumination at 77 K results in the loss of the bridge and the associated proton moves to a nearby base to generate the Ni-L state.[63,66] The one-electron reduction of Ni-C results in the formation of Ni-R state, which exists in three isoelectronic subforms (Ni-R_1, Ni-R_2 and Ni-R_3) distinguishable from one another by infra-red spectroscopy.[26] Recent studies by Ogata *et al*. have demonstrated that Ni-R state of *Desulfovibrio vulgaris* consists of a hydride bridge and a protonated cysteine residue.[52]

EPR and ENDOR spectroscopic experiments show the Fe centre remains as low-spin Fe^{II} in all of the states shown in Figure 1.6,[26] however, the CO and CN^- IR stretching frequencies vary according to the formal oxidation state of the Ni-centre of the active site. Thus, while formal spin changes occur mostly about the Ni centre, formal changes in charge are communicated over the whole bimetallic centre and are sensed by the CO and CN^- ligands bound to the Fe centre.[67]

1.4 The Catalytic Mechanism of [NiFe] Hydrogenase

The catalytic activity of [NiFe] hydrogenase from *Chromatium vinosum* has been investigated electrochemically.[11] These studies show that [NiFe] hydrogenases can catalyse the rapid interconversion of H^+ and H_2 without the requirement of substantial over potentials ($E_{1/2}$ = -390 mV vs SCE at pH 7.0, 30 °C and 0.1 bar H_2).[11] Protein film voltammetric experiments under a H_2-containing atmosphere demonstrate a high catalytic activity towards H_2 oxidation by [NiFe] hydrogenase from *Desulfovibrio vulgaris* Miyazaki F with a turnover number between 1500-9000 s^{-1} at 30 °C at pH 5-8[11] at rates that are comparable to Pt.[68]

Whilst several potentially catalytically relevant states for the [NiFe] hydrogenases have been identified (Section 1.4), their roles in the catalytic mechanism are still widely debated. Several H_2 uptake mechanisms have been proposed but no consensus has yet been reached.[26,40,69–73] Structural determinations have been achieved for three states of the enzyme, namely the oxidized inactive forms, Ni-A and Ni-B, the reduced active form, Ni-C, and the most reduced form, Ni-R and potential mechanisms for the catalytic pathway of the hydrogenases have also been

investigated using Density Functional Theory (DFT) and other computational studies. [52,74]

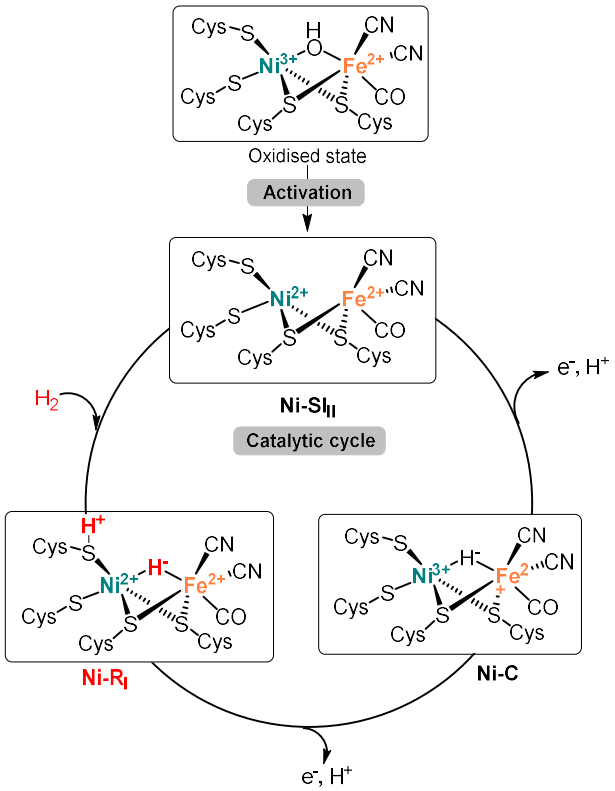


Figure 1.7: Proposed catalytic reaction mechanism of [NiFe] hydrogenase; the different states are named according to the active metal site (Ni–X).[52,74]

One proposed catalytic cycle is shown in Figure 1.7 and involves the active site moving between the Ni-SI$_{II}$, Ni-C and Ni-R$_I$ states.[74] The resting Ni-SI$_I$ state binds H_2, which is cleaved heterolytically to generate the Ni-R state. In this state a hydride ion bridges between the Ni^{II} and Fe^{II} centres and a proton resides at an amino acid base close to the active site, potentially one of the terminal cysteine S-donors.[52,74] The release of a proton on oxidation leads to the paramagnetic Ni-C state that has been probed extensively by ENDOR and HYSCORE spectroscopy. These studies suggest that this state also possesses a hydride bridge between the Ni and Fe centres.[63,75,76] One electron oxidation and proton release regenerates the Ni-SI$_I$ state and completes the cycle.

1.5 Synthetic Analogues of the [NiFe] Hydrogenase

A range of small molecule analogues have been synthesised and characterised to provide insights into the electronic structures of the intermediates in the catalytic

cycles proposed for the [NiFe] hydrogenases. The review of the recent literature that follows focuses on relevant Ni-complexes coordinated by S- and/or P-rich coordination spheres.

1.5.1 Nickel Thiolate Ligated Complexes

Prior to the publication of the X-ray crystallographic structure of the [NiFe] hydrogenase from *Desulfovibrio gigas*, a mononuclear Ni centre had been proposed for the active site of the [NiFe] hydrogenases and the Fe content was believed to be associated exclusively with the $[Fe_4S_4]$-clusters involved in the electron-transfer to and from the active sitre.[14] EXAFS spectroscopic studies showed that the Ni centre possesses a $[Ni(SR)_4]^{2-}$ coordination environment[77–79] and consequently early synthetic work focused on the syntheses of mononuclear Ni-thiolate complexes. These mononuclear Ni-thiolate complexes remain relevant and interesting since they have potential as precursors to bimetallic [NiFe] complexes.

One of the first series of NiS_4 complexes were reported by Rosenfield *et al*. and are of the type $(NR_4)_2[Ni(SAr)_4]$ (Ar = C_6H_5, *p*-C_6H_4Cl, *p*-$C_6H_4CH_3$ and *m*-C_6H_4Cl).[80] These complexes possess a distorted tetrahedral arrangement of S atoms around the Ni centre (Figure 1.8), a result of the unfavourable steric contacts between the *ortho*-H atoms and Ni or S atoms in the complex. The X-ray structures of $(NR_4)_2[Ni(SAr)_4]$ have shown that the distortion from tetrahedral geometry is such that two S-Ni-S angles are close to 90° and the other angles are close to 120° with the average Ni-S distance being 2.281(1) Å.[81] Subsequent X-ray structures of [NiFe] hydrogenases from *Desulfovibrio gigas* show that that the geometry of the Ni centres in $(NR_4)_2[Ni(SAr)_4]$ resembles that of the geometry of the Ni site in the [NiFe] hydrogenases.[81]

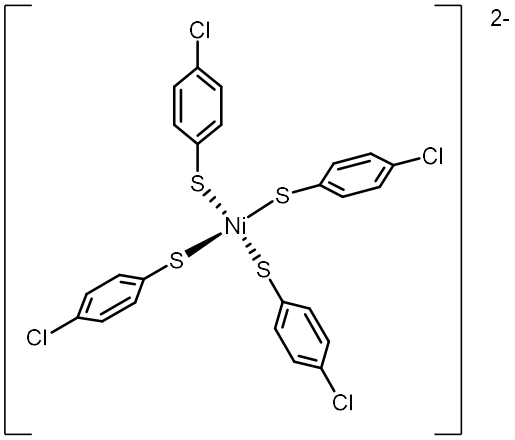


Figure 1.8: The structure of $[Ni(S\text{-}p\text{-}C_6H_4Cl)_4]^{2-}$.[80]

Mononuclear Ni-containing complexes have been synthesised using chelating bidentate thiolate ligands such as ethane-1,2-dithiol (H_2L^1),[79,82–84] butane-2,3-dithiol (H_2L^2),[83] benzene-1,2-dithiol (H_2L^3)[85,86] and norbornane-dithiol (H_2L_4) (Figure 1.9).[77]

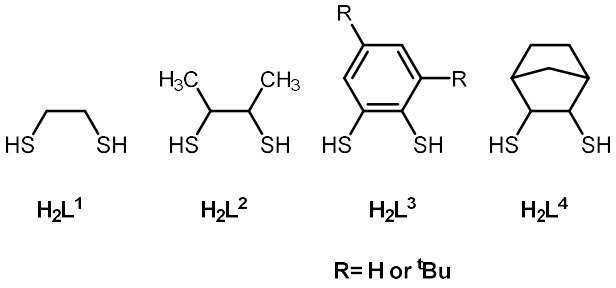


Figure 1.9: Chelating dithiol ligands used for the syntheses of mononuclear Ni complexes.

The dithiol ligands (H_2L^1 and H_2L^2) were reacted in excess with Ni salts to afford the Ni^{II} complexes, $(Ph_4P)_2[Ni(L^1)_2]\cdot 4H_2O$ and $K_2[Ni(L^2)_2]\cdot C_2H_5OH$, respectively.[83] These complexes adopt an essentially square planar geometry about the metal centre, unlike those adopted by complexes containing monodentate thiolate ligands. In protic solvents these complexes generate the dimeric species $[Ni_2(L^1)_3]^{2-}$ and $[Ni_2(L^2)_3]^{2-}$ (Figure 1.10), respectively.[83] $[Ni_2(L^1)_3]^{2-}$ and $[Ni_2(L^2)_3]^{2-}$ possess different electrochemical properties; $[Ni_2(L^1)_3]^{2-}$ possesses an irreversible oxidation process with degradation and/or subsequent chemical reaction of the oxidised species occurring near the electrode surface. In contrast, $[Ni_2(L^2)_3]^{2-}$ possesses an electrochemically reversible $Ni^{III/II}$ oxidation process, with $E_{1/2}$ = -0.51 V vs SHE.[83]

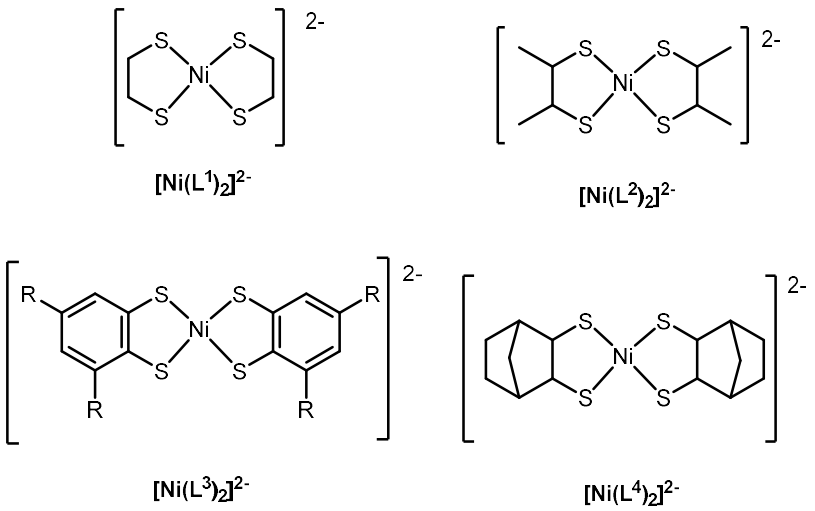


Figure 1.10: $[Ni(L^n)_2]^{2-}$ (n = 1-4) mononuclear complexes containing chelating dithiol ligands. (R = H and ^{t}Bu).[81]

Ligand $[L^3]^{2-}$ (R = H) reacts with $NiCl_2(PPh_3)_2$ in air to give $[Ni^{III}(L^3)_2]^-$;[86] the intermediate $[Ni(L^3)_2]^{2-}$ oxidises spontaneously ($E_{1/2}$ = -0.23 V *vs* SHE) to the corresponding $[Ni(L^3)_2]^-$ anion.[85] Sellmann and co-workers confirmed the formation of the complex anion $[Ni(L^3)_2]^{2-}$(R = ^{t}Bu), which can be oxidised first to $[Ni(L^3)_2]^-$ and then to $[Ni(L^3)_2]^0$ (R = ^{t}Bu).[87] XPS investigations and X-ray crystallographic studies suggest that these oxidation processes are delocalized across the $[NiS_4]$ centre[85,87] such that the L^3 (R = ^{t}Bu) ligands may be viewed as being redox non-innocent.

$[Ni(L^4)_2]^{2-}$ possesses a rigid conformation of the norbornane backbone that enforces a more rigid S-C-C-S chelating unit. [77] This stabilizes the mononuclear complex with respect to the formation of oligomers. Thiolate groups have a strong tendency to form bridges between two or three metals, therefore reactions of simple alkyl thiols or chelating didentate ligands with a Ni^{II} salt often result in the formation of oligonuclear or polynuclear complexes.[81] The tendency of aromatic thiolates to form bridges is markedly less than for alkyl thiolates.[88] Thus, the formation of oligomers may also be limited through the use of aromatic thiolate S-donors rather than alkyl thiolate S-donors.[81]

Sellmann *et al.* synthesised a range of mononuclear or binuclear Ni^{II} complexes from thiolate and thioether donor ligands H_2L^{5-9} (Figure 1.11).[89] The coordination about the Ni^{II} centre is modulated by the ligand through the preferred conformation of the

free ligands, the presence of hard or soft donors in the bridge, and kinetically or sterically favoured chelate ring closures.[89]

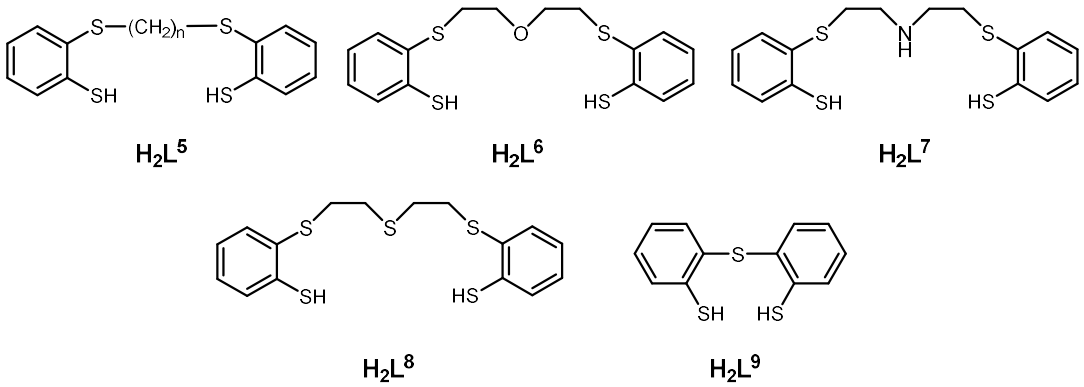


Figure 1.11: A selection of the ligands reported by Sellmann *et al.*[89]

$[L^5]^{2-}$ and $[L^6]^{2-}$ (Figure 1.11) yield binuclear complexes where each ligand bridges between two metal centres; two S-donors of one phenyl ring coordinate to one Ni centre and the other two S-donors to the second Ni centre. The O atom does not coordinate to the Ni centres in $[Ni_2(L^6)_2]$.[89] In contrast, $[L^7]^{2-}$ and $[L^8]^{2-}$ form mononuclear penta-coordinate complexes with Ni^{II} in which the central NH or S group in $[Ni(L^7)]$ and $[Ni(L^8)]$, respectively, coordinates to the Ni centre. Crystallographic studies for $[Ni(L^8)]$ show that the geometry about the Ni centre is square-based pyramidal, which represents the first example of a mononuclear pentacoordinated Ni^{II} complex containing S-ligation.[81] The compounds $[Ni(L^7)]$ and $[Ni(L^8)]$ are mononuclear five-coordinate complexes, in which the NH-group and the central S atom are also involved in coordination to the metal. The binding of the NH-group and the central S atom to the Ni^{II} centre were confirmed by the paramagnetism of the complexes and by H/D exchange studies.[81] Magnetic susceptibility data indicate that $[Ni(L^8)]$ is diamagnetic, both in the solid state and in DMF, THF, and CH_2Cl_2 solutions, but paramagnetic (μ_{eff} = 0.96 μ_B) in pyridine solution.[81] Thus, $[Ni(L^8)]$ appears to remain 5-coordinate, in DMF and THF and in CH_2Cl_2, and partially converts to a 6-coordinate structure in pyridine.[90] No H/D exchange occurs at the NH position since the deuteron and the hydrogen have to bind simultaneously to the N atom and this does not appear to occur while the N donor is coordinated to the Ni centre.[90]

$[L^9]^{2-}$ generates the dinuclear and trinuclear Ni^{II} complexes, $[Ni_2(L^9)_2]$ and $[Ni_3(L^9)_3]$, respectively, which contain bridging thiolate S-donors.[87,91–93] $[Ni_3(L^9)_3]$ reacts with nucleophiles, X = SR^- (R= ^{t}Bu, Cy, Me, Ph), PR_3 (R= Cy, Ph), Cl^- or CN) to give the mononuclear complexes $[Ni(L^9)(X)]$ that possess distorted square planar geometries.[94]

1.5.2 Binuclear [NiFe] Thiolate-Ligated Complexes

The identification of a binuclear Ni-Fe centre of the active site of [NiFe] hydrogenase,[39] prompted the syntheses of thiolate bridged [NiFe] complexes incorporating CO and other π-acceptor ligands bound to the Fe centre. This is a challenging area of research that has yielded few, well-characterized complexes when compared to those synthesized as analogues of the active sites of the [FeFe] hydrogenases.[14]

The first low spin Ni^{II} complex bound in a S only environment was reported by Sellmann *et al.* $[Ni(L^{10})(bdt)]^{2-}$ [H_2L^{10} = bis(2-mercaptophenyl)sulfide] binds by two thiolate bridges to a $[Fe^{II}(CO)(PMe_3)_2]^{2+}$ fragment to give $[(bdt)Ni(L^{10})Fe(CO)(PMe_3)_2]$ (Figure 1.12).[95]

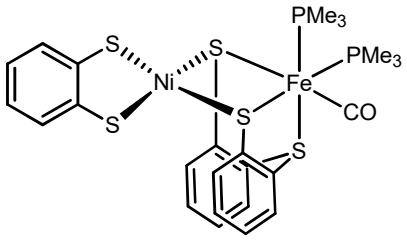


Figure 1.12: $[(bdt)Ni(L^{10})Fe(CO)(PMe_3)_2]$ reported by left: Sellmann *et al.*[95]

Tatsumi *et al.* have reported two structural analogues of the active site of [NiFe] hydrogenase that contain essentially square planar dithiocarbamate Ni^{II} centres bridged by a dithiolate ligand to a $Fe(CN)_2(CO)_2$ fragment [Figure 1.13 (a) and (b)].[96] These species contain the rarely observed simultaneous CO and CN^- ligation at the Fe centre, with Ni-Fe and M-S bond distances (Fe-S(bridge) = 2.337 Å, Ni-S(bridge) = 2.213 Å, Ni-S(terminal) = 2.206 Å) that are similar to those at the active site of the oxidised form of the [NiFe] hydrogenase from *D. gigas* (Fe-S(bridge) = 2.2 Å, Ni-S(bridge) = 2.6 Å and Ni-S(terminal) = 2.2 Å) and *D. fructosovorans* (Fe-S(bridge) = 2.4 Å, Ni-S(bridge) = 2.4 Å and Ni-S(terminal) = 2.3 Å)[39,96,97] Recently,

Tatsumi *et al*. reported the dithiolate-bridged binuclear complex $[(Et_2NCS_2)Ni(\mu\text{-}tpdt)Fe(CO)(CN)_2]^-$ ($tpdt^{2-}$ = 3-thiapentanedithiolate) [Figure 1.13 (c)].[98] This complex possesses a *fac*-$Fe(CN)_2(CO)$ geometry at the Fe centre. The CN^- stretching frequencies (ν_{CN} = 2094 and 2083 cm^{-1}, ν_{CO} = 1944 cm^{-1}) are similar to those associated with the Ni-A (ν_{CN} = 2093 and 2083 cm^{-1}, ν_{CO} = 1945 cm^{-11}), Ni-B (ν_{CN} = 2090 and 2079 cm^{-1}, ν_{CO} = 1944 cm^{-1}) and Ni-SU (ν_{CN} = 2099 and 2089 cm^{-1} ν_{CO} = 1950 cm^{-1}) states of the enzyme.[98]

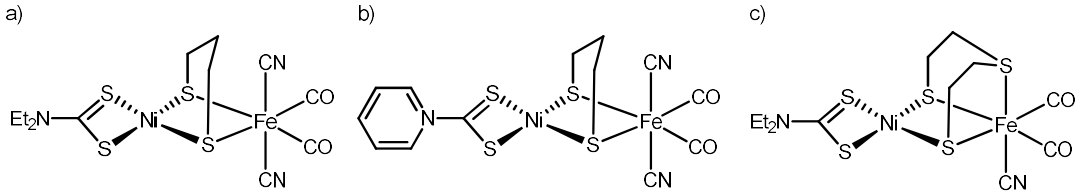


Figure 1.13: View of [NiFe] models reported by Tatsumi *et al.* with CO and CN^- ligation.[99,100]

Schröder *et al*. have reported a heterobinuclear [NiFe] analogue which contains a NiS_4 centre bound to a $[CpFe(CO)]^+$ fragment [Figure 1.14(a)].[101] The Cp^- binding in this system may confer lower over-potentials to the catalyst during H_2 evolution and improve stability while cycling through the catalytic process.[102] A similar [NiFe] complex was reported by Artero *et al*. that incorporates a Ni(xbsms) [H_2xbsms = α,α'-bis(4-mercapto-3,3-dimethyl-2-thiabutyl)-oxylene] precursor [Figure 1.14(b)]. This complex is an electrocatalyst for sustained H_2 evolution from trifluoroacetic acid (TFA) in DMF. It is suggested that the catalytic cycle for [(xbsms)Ni(μ-H)FeCp] may possess intermediates similar to those that may be involved in the catalytic mechanism of [NiFe] hydrogenase.[102]

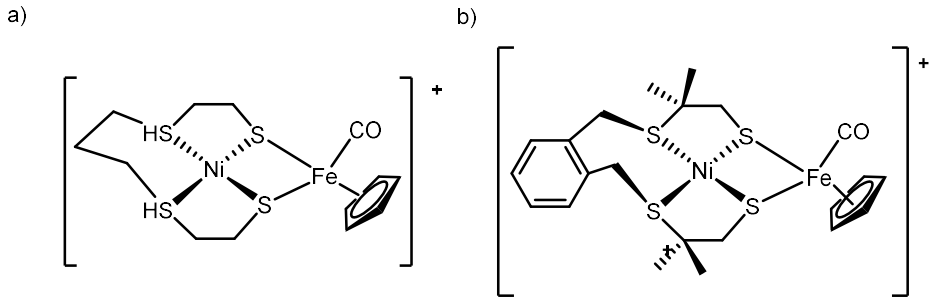


Figure 1.14: Heterobinuclear [NiFe] complexes reported by left: Schröder *et al.*[101] and right: Artero *et al.*[102]

1.5.3 [NiFe] Complexes Incorporating Thiolate and Phosphine Donors

Analogues of the active site of [NiFe] hydrogenase that incorporate a Ni^{II} centre bound to mixed P- and S- donors have been reported. {[Fe(NS_3)$(CO)_2$-S,S']NiCl(dppe)} [NS_3 = $[N(CH_2CH_2S)_3]^{3-}$; dppe = 1,2-bis(diphenylphosphino)ethane] (Figure 1.15 (a))[103,104] contains structural and spectroscopic features similar to those of the [NiFe] hydrogenases.[103,104] The IR spectrum of {[Fe(NS_3)$(CO)_2$-S,S']NiCl(dppe)} possesses a stretching frequency at 1944 cm^{-1}, similar to that for the inactive form the [NiFe] hydrogenase from *D. gigas* (ν_{CO} = 1947 cm^{-1}).[43] The Ni-Fe distance for {[Fe(NS_3)$(CO)_2$-S,S']NiCl(dppe)} is 3.0216(5) Å, similar to that for inactive form [NiFe] hydrogenase from *D. gigas* (Ni-Fe = 2.9 Å).

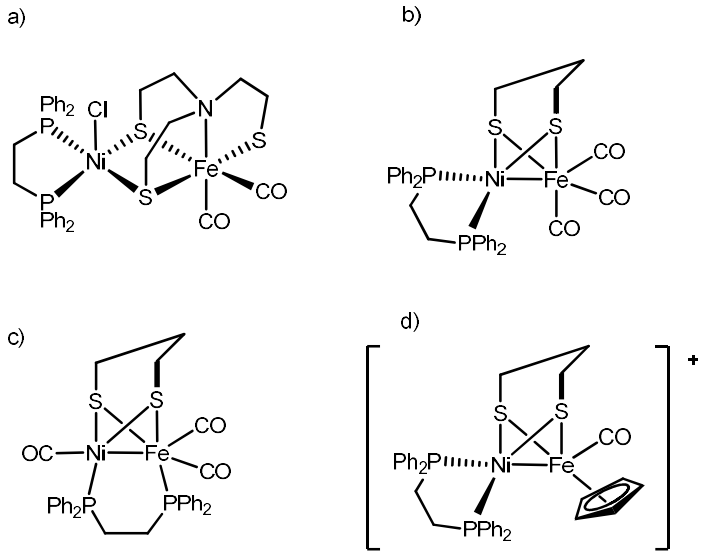


Figure 1.15: Views of the complexes a): {[Fe(NS_3)$(CO)_2$-S,S']NiCl(dppe)} (NS_3 = $[N(CH_2CH_2S)_3]_3-$; dppe = 1,2-diphenylphosphinoethane) reported by Evans *et al.*[103,104] b): [(dppe)Ni(μpdt)Fe$(CO)_3$] c): [(OC)Ni(μ-dppe)(μ-pdt)Fe$(CO)_2$], d): [(dppe)Ni(pdt)Fe(CO)(Cp)]PF_6 reported by Schröder *et al.*[101]

Schröder *et al.* reported the reactions of [Ni(dppe)(pdt)] (pdt = 1,3-propanedithiolate) with [Fe$(CO)_3$(bda)] (bda = benzylidene acetone) or [$Fe_3(CO)_{12}$] to give [(dppe)Ni(μ-pdt)Fe$(CO)_3$] [Figure 1.15(b)].[101] The Ni^{II} unit possesses a distorted tetrahedral P_2S_2 centre that bridges to a square based pyramidal Fe^0 centre.[101] [(dppe)Ni(μ-pdt)Fe$(CO)_3$] converts to [(OC)Ni(μ-dppe)(μ-pdt)Fe$(CO)_2$] in solution, both [(dppe)Ni(μ-pdt)Fe$(CO)_3$] and [(OC)Ni(μ-dppe)(μ-pdt)Fe$(CO)_2$] contain a Ni-Fe distance of 2.4666(6) Å consistent with the presence of a formal Ni-Fe bond. DFT calculations suggest that a similar Ni-Fe bond may be important in the reduced, active form of the [NiFe] hydrogenases.[105] The dihedral angle between the Ni-S-S and Fe-S-S planes is 80.3° which compares to that at the active site of [NiFe] hydrogenase in its reduced form (88.95°).[42]

The reaction of [Ni(dppe)(pdt)] with [Fe(Cp)$(CO)_2$I] followed by precipitation with NH_4PF_6 affords [(dppe)Ni(pdt)Fe(Cp)(CO)]PF_6 [Figure 1.5 (d)]. The approximately square planar Ni^{II} centre binds to a $[Fe(Cp)(CO)]^+$ unit *via* two bridging μ_2-thiolate S-donors.[101] [(dppe)Ni(pdt)Fe(Cp)(CO)]PF_6 exhibits a Ni-Fe distance of 2.7795(9) Å, which is longer than that found in [(dppe)Ni(μ-pdt)Fe$(CO)_3$] [2.4666(6) Å].[95]

[(dppe)Ni(μ-pdt)Fe$(CO)_3$] is readily protonated following treatment with $HBF_4.Et_2O$ in CH_2Cl_2 to give [(dppe)Ni(μ-pdt)(μ-H)Fe$(CO)_3$]BF_4, which represents the first

example of a synthetic [NiFe] complex containing a bridging hydride ligand.[106] Furthermore, Rauchfuss *et al*. demonstrated that [(dppe)Ni(μ-pdt)(μ-H)Fe(CO)$_3$]BF$_4$ is an active catalyst for the reduction of protons to H_2 at potentials near -1.37 V *vs* Fc^+/Fc.[106]

1.5.4 [NiFe] Polymetallic Complexes

Two polymetallic systems containing Ni and Fe have been reported to show electrocatalytic activity involving the reduction of protons to H_2.[14] The trinuclear complex [('S$_2$')(Ni(PMe$_3$))$_2$Fe(CO)('S$_2$')$_2$] ('S$_2$'= 1,2-benzenedithiolate)[107] (Figure 1.16) exhibits a reversible reduction process at -0.095 V vs SHE in CH_2Cl_2 and bulk electrolysis experiments show that [('S$_2$')(Ni(PMe$_3$))$_2$Fe(CO)('S$_2$')$_2$] possesses a low activity 0.1 h^{-1} turnover frequency (ToF) for H_2 production.[108]

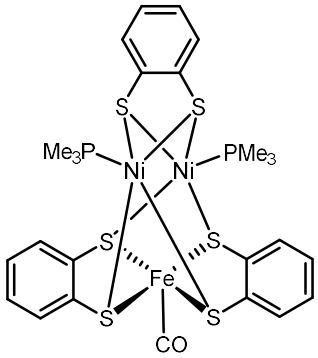


Figure 1.16: View of the complex {('S$_2$')[Ni(PMe$_3$)]$_2$Fe(CO)('S$_2$')$_2$} reported by Sellmann *et al*.[107,108]

[Ni(L^A)Fe$_2$(CO)$_6$] and [Ni(L$^{A'}$)Fe$_2$(CO)$_6$] (L^A = (CH$_3$C$_6$H$_3$S$_2$)$_2$(CH$_2$)$_3$), L$^{A'}$ = (C$_6$H$_4$S$_2$)$_2$(CH$_2$)$_3$) have been reported by Schröder *et al*.[109] These heterotrinuclear clusters are synthesised from [Ni(L^A)] and [Ni(L$^{A'}$)], respectively, by their reaction with Fe$_3$(CO)$_{12}$. The geometries of the [Ni(L^A)] and [Ni(L$^{A'}$)] consist of Ni^{II} centres in a distorted square planar geometry.[110] In each complex, the Ni^{II} centres are bound to two thioether S and two thiolate S donors with the thiolate S donors bridging the Ni and Fe centres. The coordination sphere about the Ni^{II} is completed by formal Ni-Fe bonds to each Fe centre to give an overall distorted octahedral geometry. Each Fe centre also possesses a distorted octahedral coordination geometry involving one Ni and one Fe atom, one thiolate donor and three terminally bound CO ligands. The Ni-Fe bond lengths are in the range 2.4789(9) - 2.4936(8) Å and are similar to those

found in the active site of the [NiFe] hydrogenase from *D. baculatum* (2.5 Å in the reduced form) and *D. vulgaris Myazaki F* (2.55 and 2.59 Å for the oxidised and reduced forms, respectively).[39,44,111]

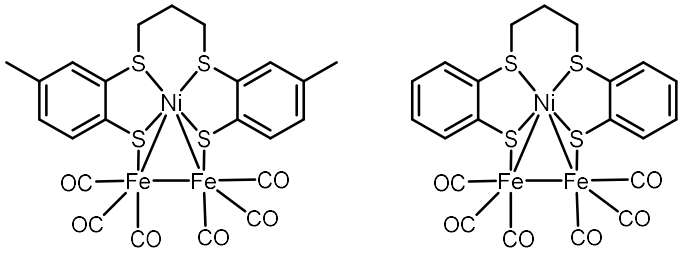
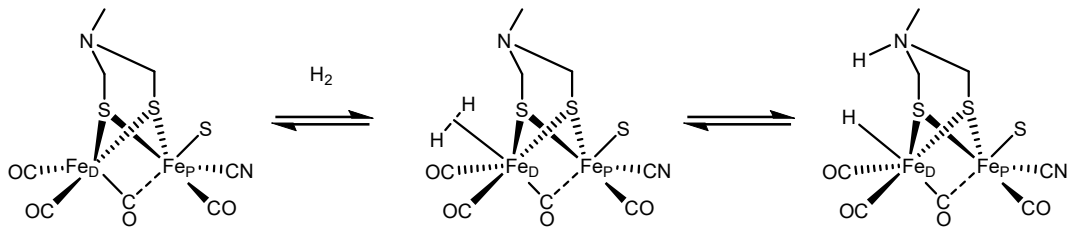


Figure 1.17: (a) $[Ni(L^A)Fe_2(CO)_6]$ and (b) $[Ni(L^{A'})Fe_2(CO)_6]$ reported by Schröder et al.[109]

$[Ni(L^A)Fe_2(CO)_6]$ undergoes an electrochemically reversible one-electron reduction process at $E_{1/2}$ = -1.31 V vs Fc^+/Fc to form the paramagnetic species $[Ni(L^A)Fe_2(CO)_6]^-$. The addition of TFA to $[Ni(L^A)Fe_2(CO)_6]$ in CH_2Cl_2 generates a catalytic cathodic current response in the cyclic voltammogram that is directly proportional to the concentration of TFA. Gas chromatography was employed to confirm the production of H_2 in this experiment.[112] $[Ni(L^A)Fe_2(CO)_6]$ demonstrates a ToN of 6 h^{-1} in the presence of TFA (50 mM) at an applied potential of -1.64 V vs Fc^+/Fc.[112] An in-plane delocalised SOMO that is antibonding with respect to the metal-metal bonds was confirmed by detailed EPR, IR spectroscopic and DFT studies of $[Ni(L^A)Fe_2(CO)_6]^-$.[112] DFT calculations showed the SOMO in $[Ni(L^A)Fe_2(CO)_6]^-$ possesses 24 % Ni and 16-17 % Fe character, with smaller contributions from the thioether (2.8 %) and thiolate (1.4-1.7 %) donors. The composition of the SOMO suggests that the potential protonation site is likely to be metal- and not S-based. $[Ni(L^A)Fe_2(CO)_6]$ represents the first heterobinuclear Ni–Fe cluster, containing biologically relevant ligands, that supports the catalytic production of H_2 at comparable rates of turnover to the synthetic analogues of the [FeFe] hydrogenases at potentials that are considerably more anodic (*ca.* +900 mV).[112]

1.6 Analogues of [NiFe] Hydrogenase Incorporating Proton Relay sites

A proton relay is a pendant base within a catalyst that may facilitate the transfer of protons between the solution and the catalytic site.[113] When compared to an organic basic site, a metal centre can be slow to protonate.[114] A basic site in close proximity to the catalytic centre may be ideally positioned to relay protons and promote the formation of a metal hydride intermediate that may be required for the reversible oxidation of H_2. The nature of active site of the [FeFe] hydrogenases has been used as inspiration for the incorporation of a pendant base as a proton relay in models of the active sites of the hydrogenases.[37,71] Thus, it has been proposed that the activation of H_2 by [FeFe] hydrogenases is assisted by the amine N atom present in the bridge of the dithiolate ligand. The activation of H_2 occurs *via* the binding of H_2 to the distal Fe atom (Fe_D) to form a dihydrogen complex. This is followed by heterolytic cleavage to produce a Fe hydride and a protonated amine (Scheme 1.1).



Scheme 1.1: A proposed mechanism of [FeFe] hydrogenase in reaction with H_2.[37,71]

1.6.1 Nickel Complexes Incorporating Prontonation sites

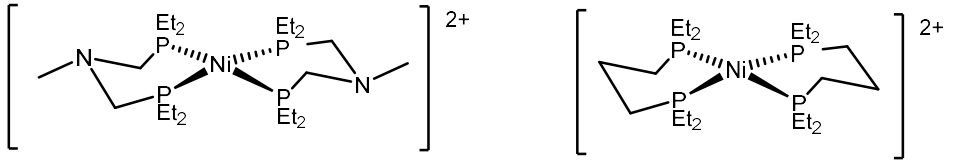


Figure 1.18: View of left: $[Ni(PNP)_2]^{2+}$ containing two NMe basic groups and right: the analogous complex $[Ni(depp)_2]^{2+}$ incorporating no amine sites.[113]

$[Ni(PNP)_2]^{2+}$ (PNP = $Et_2PCH_2NMeCH_2PEt_2$) (Figure 1.18) reported by Curtis *et al.*[113] incorporates two basic amine groups within the ligand system. The amine groups are incorporated within a strained six-membered ring and do not coordinate to the Ni^{II} centre. $[Ni(PNP)_2]^{2+}$ is an electrocatalyst for the oxidation of H_2 to protons, and stoichiometric reaction with H_2 forms $[HNi(PNP)(PNHP)]^+$, in which a H^- ligand is bound to Ni and a proton is bound to a pendant N atom of one PNP

ligand.[113] Cyclic voltammetric studies of $[HNi(depp)_2](PF_6)$ (depp = $Et_2PCH_2CH_2CH_2PEt_2$) were undertaken as a control experiment highlighting the important role of the bridging N atom of the PNP ligand in proton exchange reactions.[113] The cathodic shift of 0.6 V in the oxidation of $[HNi(PNP)_2]^+$ was observed compared to $[HNi(depp)_2]^+$, suggesting a fast (or coupled) intramolecular proton-transfer from the Ni centre to the amine of the PNP ligand upon oxidation of the metal from Ni^{II}-H to Ni^{III}-H. The pendant base appears to promote the intermolecular exchange between the H^- ligand and the protons in solution as well as facilitating the intramolecular heterolytic cleavage of H_2.[115]

Dubois *et al.* have reported the novel Ni^{II} phosphine complex, $[Ni(P^R_2N^{R'}_2)_2]^{2+}$ (R= cyclohexyl; R' = benzyl, Figure 1.19) which incorporates basic amine groups orientated in a boat conformation, such that the basic groups are above the Ni^{II} centre. This arrangement templates the binding of an incoming H_2 molecule (Figure 1.18).[116–118] $[Ni(P^R_2N^{R'}_2)_2]^{2+}$ demonstrate relative high rates of electrocatalysis that can be tuned for either H_2 oxidation or production by changing the substituents of the diphosphine ligands.[115] Bulky groups substituents on the P-donors result in a larger tetrahedral distortion and a greater affinity for hydride at the Ni^{II} centre, resulting in an increased in observed rates of catalysis.[116–118]

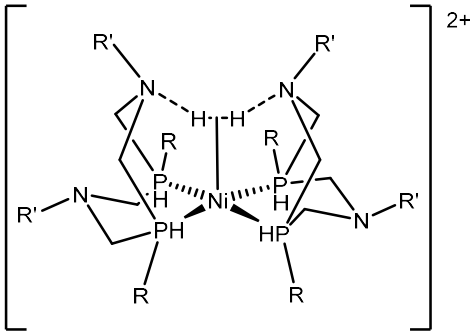


Figure 1.19: View of the complex $[Ni(P^R_2N^{R'}_2)_2]^{2+}$ (R = cyclohexyl; R' = benzyl) showing a potential interaction with H_2.[117,118]

The analogous system $[Ni(dppp)(NP^{Ph}_2N^{Bz}_2)]^{2+}$ [$P^{Ph}_2N^{Bz}_2$ = 1,5-dibenzyl-3,7-diphenyl-1,5-diaza-3,7-diphosphacyclooctane; dppp = 1,3-bis(diphenylphosphino)propane] (Figure 1.20) is also an electrocatalyst for H_2 oxidation. However, $[Ni(dppp)(NP^{Ph}_2N^{Bz}_2)]^{2+}$ shows catalytic activity *ca.* 20 times lower than $[Ni(P^R_2N^{R'}_2)_2]^{2+}$, presumably because of the co-operative participation

and positions of the two pendant bases the relative positions of the two pendant bases in $[Ni(P^{R}_2N^{R'}_2)_2]^{2+}$ as compared to $[Ni(dppp)(NP^{Ph}_2N^{Bz}_2)]^{2+}$.[119] This suggests that the number and position of the pendant bases are important in the design of novel molecular catalysts for H_2 cleavage or production.

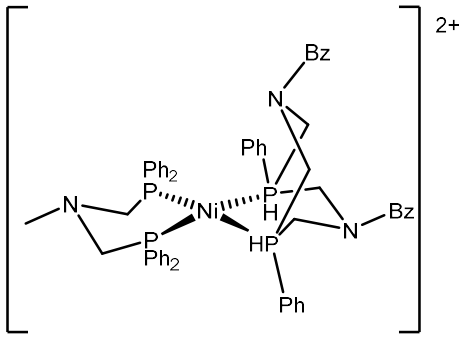


Figure 1.20: Complex $[Ni(dppp)(NP^{Ph}_2N^{Bz}_2)]^{2+}$ reported by Yang *et al.*[119]

Dubois *et al.* reported the synthesis of $[Ni(P^{Ph}_2N^{Ph})_2]^{2+}$ ($P^{Ph}_2N^{Ph}$ = 1,3,6-triphenyl-1-aza-3,6-diphosphacycloheptane) (Figure 1.21).[120] $[Ni(P^{Ph}_2N^{Ph})_2]^{2+}$ is an electrocatalyst for H_2 production with a ToF above 100,000 s^{-1} and higher than that reported for [FeFe] hydrogenases (9000 s^{-1}). The Ni^{II} complex also demonstrates improved catalytic performance when H_2O is added in the electochemical cell.[120]

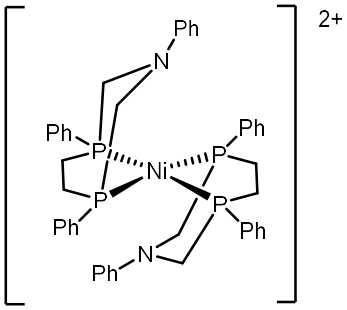


Figure 1.21: View of the complex $[Ni(P^{Ph}_2N^{Ph})_2]^{2+}$, the first catalyst to show rates for H_2 production greater than those of the [NiFe] hydrogenase enzyme.[120]

1.6.2 [NiFe] Complexes That Incorporate Protonation Sites

There has been much less focus on the functionalisation of [NiFe] complexes containing protonation sites. Sun *et al.* have reported the trinuclear $[NiFe_2]$ complexes $[Fe_2(CO)_6(\mu_3\text{-}S)_2Ni(Ph_2PCH_2)_2NR]$ (R = ^{n}Bu, Ph) (Figure 1.22).[121]

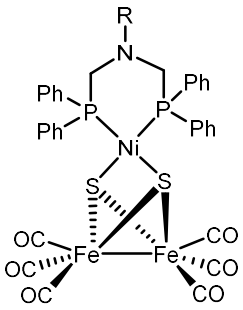


Figure 1.22: The structure of the $[Fe_2(CO)_6(\mu_3\text{-}S)_2Ni(Ph_2PCH_2)_2NR]$ (R = ^{n}Bu, Ph).[121]

Treatment of $[Fe_2(CO)_6(\mu_3\text{-}S)_2Ni(Ph_2PCH_2)_2N(^n Bu)]$ with TFA produces a stable protonated form of the complex, in which the [2Fe-2S] units adopt butterfly configurations with the Fe centres in square-pyramidal geometries, and the six membered rings involving Ni^{II} centres and the diphosphine ligands adopting chair conformations. A comparison of $[Fe_2(CO)_6(\mu_3\text{-}S)_2Ni(Ph_2PCH_2)_2N(^n Bu)]$ and its protonated form confirms that protonation of the basic site has almost no influence on the metal framework of the complex. The basic site in this heterotrinuclear complex can be readily protonated, however it is not reported how the protonation sites influence the catalytic activity of these complexes.[121]

1.7 Hydrogenase Bio-mimetic Compounds in Artificial Photosynthetic Systems

Sunlight is naturally converted into chemical energy *via* photosynthesis, the process that splits water to produce O_2 and energy rich molecules including carbohydrates and H_2.[122] A system inspired by photosynthesis, that could split water into H_2 and O_2 may provide a route to the sustainable production of H_2. This area of research is commonly referred to as artificial photosynthesis.

1.7.1 Photocatalytic H_2 Production

The conversion of H_2O to H_2 using solar energy can be a complex, multistep, and multi-electron process involving charge separation and bond breaking and formation.[122] Systems containing light-absorbing units, electron relays, and redox catalysts have been targeted to overcome these chemical challenges and has led to the development of a three-component system.[1] These systems consist of a photosensiter, an electron mediator and a metal complex that catalyses the reduction of protons to H_2.[123] The development of a range of homogeneous catalysts

containing Co, Pt, Pd, Rh, Fe, and Ni centres has facilitated investigations into the mechanism of proton reduction in homogeneous media.[124–126]

1.7.2 Catalysis Incorporating Photosensitiser Systems

Most investigations within this area have concentrated on systems inspired by the active sites of the [FeFe] hydrogenases. Li *et al* have reported a Zn^{II} tetraphenylporphyrin (ZnTPP) and pyridyl-functionalized $[Fe_2S_2]$ complex (Figure 1.23).[127] When radiated with visible light in the presence of a electron donor and a proton source the complex produces H_2.[127,128]

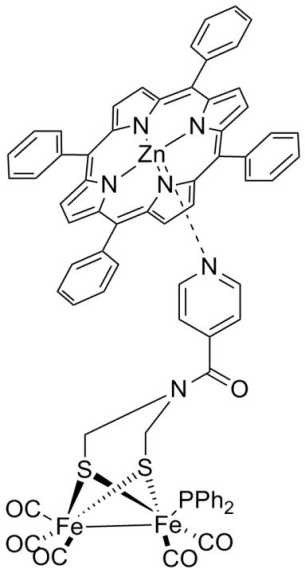


Figure 1.23: Zn^{II} tetraphenylporphyrin (ZnTPP) and pyridyl-functionalized $[Fe_2S_2]$ complex.[127]

1.7.3 Photocatalytic H_2 Production using $[Re(CO)_3Cl(bpy)]$ as a photosensitiser and [NiFe] as a catalyst in CH_2Cl_2

Summers *et al.* have reported the photoproduction of H_2 by $[Ni(L^A)Fe_2(CO)_6]$ (Section 1.6.4), reduced by the photosensitiser (PS), $[Re(CO)_3Cl(bpy)]$.[123] $[ReCl(CO)_3(bpy)]$ was chosen as the photosensitiser unit because of its favourable photophysical, electron transfer and redox properties and because the ν(CO) bands of $[ReCl(CO)_3(bpy)]$ unit can provide a valuable probe by which the electron transfer can be monitored.

$[Ni(L^A)Fe_2(CO)_6]$ can be reduced photochemically to the catalytically active anion $[Ni(L^A)Fe_2(CO)_6]^-$ by $[ReCl(CO)_3(bpy)]$ (PS) in the presence of a sacrificial electron

donor, NEt_3 or TEOA. $[Ni(L^A)Fe_2(CO)_6]$ within a system containing $[ReCl(CO)_3(bpy)]$ and TEOA has a maximum turnover frequency of 52 h^{-1} over *ca.* 0.4 h of photolysis. This system provides the first example of light-driven H2 production involving a low molecular weight analogue of the active site of the [NiFe] hydrogenase (Figure 1.24).[123]

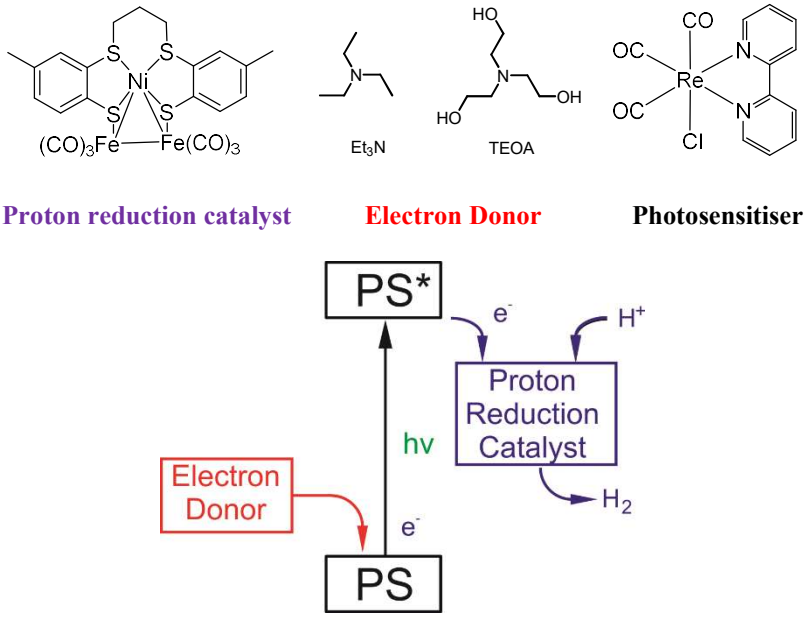


Figure 1.24: The proposed cycle for the photo-production of H_2 using $[Re(CO)_3Cl(bpy)]$ as a photosensitiser and [NiFe] as a catalyst.

1.7.4 Studies into a Supramolecular system containing a Rhenium Photosensitiser Covalently linked to a [NiFe] Catalyst for Photochemical H_2 production

Further investigations into the photo-production of H_2 led to the development of a linked dyad ([Re]-[NiFe], Figure 1.25) containing an analogue of the active site of [NiFe] hydrogenase ($[Ni(L^A)Fe_2(CO)_6]$), covalently bound to a Re-diimine photosensitiser ([Re]).[129] Excitation of the [Re] centre results in the population of the ^{3}MLCT excited state, $[Re]^*$-$[NiFe_2]$. Reductive quenching of $[Re]^*$-$[NiFe_2]$ by NEt_3 forms $[Re]^-$-$[NiFe_2]$, which subsequently undergoes electron transfer to the $[NiFe_2]$ centre to form $[Re]$-$[NiFe_2]^-$. The key driver for binding the photosensitiser and catalyst together is the potential to increase the rate of electron transfer between the units. However, the $[Re]$-$[NiFe_2]$ dyad has a slower electron transfer then in the $[Re]/[NiFe_2]$ mixture previously described by Summers *et al.*[129,123] Decomposition

of the photosensitiser unit in the [Re]-[$NiFe_2$] dyad system is observed. Thus, the ester-linked dyad linking the catalytic and photosensitising moieties appears to be detrimental to the electron transfer rate and the chemical stability of the system under continuous photolysis.[129] Future investigations would need to take these drawbacks into consideration to develop systems to overcome these problems so that the benefits of linked dyads can be exploited.

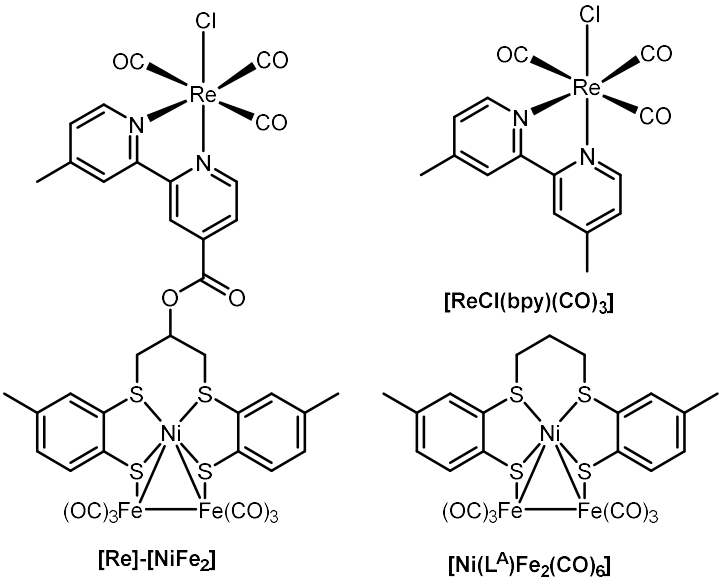


Figure 1.25: Structures of [$Ni(L^A)Fe_2(CO)_3$], [$ReCl(bpy)(CO)_3$] and [Re]-[$NiFe_2$] reported by Summers et al.[129]

1.8 Aims of This Work

The review of the literature presented above suggests that incorporation of protonation sites around the ligand frameworks in monomeric [Ni]- and heteronuclear [NiFe]-containing complexes could provide routes for the preparation of new low molecular weight analogues of the active site of the [NiFe] hydrogenases as catalysts for H_2 production. With this in mind we aim to:

(i) incorporate quinoxaline-units into NiS_4 and NiS_2P_2 complexes and investigate their electrochemical and spectroscopic properties, and their potential as catalysts for H_2 production;

(ii) use the NiS_4 and NiS_2P_2 as precursors to [NiFe] containing complexes as analogues of the active sites of the [NiFe]-containing hydrogenases;

(iii) investigate new approaches for the incorporation of photosensitizing units into Ni^{II} and [NiFe] complexes that may have the potential to catalysis the photochemical production of H_2.

1.9 References

1 A. J. Esswein and D. G. Nocera, *Chem. Rev.*, 2007, **107**, 4022–4047.

2 R. Eisenberg and D. G. Nocera, *Inorg. Chem.*, 2005, **44**, 6799–6801.

3 T. M. L. W. Martin I Hoffert, Ken Caldeira, Atul K Jain, Erik F Haites, L D Danny Harvey, Seth D Potter, Michael E Schlesinger, Stephen H Schneider, Robert G Watts, *Nature*, 1998, **395**, 881–884.

4 CIA, *CIA World Factb.*, 2004.

5 R. R. Richard Cammack, Michel Frey, *Hydrogen as a Fuel: Learning from Nature*, CRC Press, London, 2002.

6 U. Siegenthaler, T. F. Stocker, E. Monnin, D. Lüthi, J. Schwander, B. Stauffer, D. Raynaud, J.-M. Barnola, H. Fischer, V. Masson-Delmotte and J. Jouzel, *Science*, 2005, **310**, 1313–7.

7 J. R. Petit, J. Jouzel, D. Raynaud, N. I. Barkov, J.-M. Barnola, I. Basile, M. Bender, J. Chappellaz, M. Davis, G. Delaygue, M. Delmotte, V. M. Kotlyakov, M. Legrand, V. Y. Lipenkov, C. Lorius, L. PÉpin, C. Ritz, E. Saltzman and M. Stievenard, *Nature*, 1999, **399**, 429–413.

8 J. R. Hufton, S. Mayorga and S. Sircar, *AIChE J.*, 1999, **45**, 248–256.

9 J. A. Turner, *Science*, 2004, **305**, 972–974.

10 C. Léger, A. K. Jones, W. Roseboom, S. P. J. Albracht and F. A. Armstrong, *Biochemistry*, 2002, **41**, 15736–15746.

11 H. R. Pershad, J. L. Duff, H. A. Heering, E. C. Duin, S. P. Albracht and F. A. Armstrong, *Biochemistry*, 1999, **38**, 8992–8999.

12 D. J. Evans and C. J. Pickett, *Chem. Soc. Rev.*, 2003, **32**, 268.

13 F. A. Armstrong, N. A. Belsey, J. A. Cracknell, G. Goldet, A. Parkin, E. Reisner, K. A. Vincent and A. F. Wait, *Chem. Soc. Rev.*, 2009, **38**, 36–51.

14 C. Tard and C. J. Pickett, *Chem. Rev.*, 2009, **109**, 2245–2274.

15 S. Kaur-Ghumaan and M. Stein, *Dalt. Trans.*, 2014, **43**, 9392.

16 F. Vella, *Biochem. Educ.*, 1995, **23**, 115.

17 T. D. H. Bugg, *Introduction to Enzyme and Coenzyme Chemistry*, John Wiley & Sons, second., 2005.

18 W. Kaim and B. Schwederski, *Bioinorganic chemistry*, Wiley, 1994.

19 M. Boudart, *Chem. Rev.*, 1995, **95**, 661–666.

20 W. P. C and W. R. G, *Inorganic Chemistry in Biology*, Oxford University Press, Oxford, 1997.

21 D.E.Fenton, *Biocoordination Chemistry*, Oxford University Press, Oxford, 1995.

22 R. J. P. Williams, J. J. R. Frausto da Silva, *The Biological Chemistry of the Elements: The*

Inorganic Chemistry of Life, 2001.

23 F. Tian, O. B. Toon, A. A. Pavlov and H. De Sterck, *Science*, 2005, **308**, 1014–1017.

24 M. S. and L. H. Stickland, M. Stephenson and L. Stickland, *Biochem. J.*, 1931, **25**, 205–214.

25 L. Wu, *FEMS Microbiol. Lett.*, 1993, **104**, 243–269.

26 A. L. De Lacey, V. M. Fernandez, M. Rousset and R. Cammack, *Chem. Rev.*, 2007, **107**, 4304–4330.

27 S. Shima and R. K. Thauer, *Chem. Rec.*, 2007, **7**, 37–46.

28 J. W. Peters, *Science (80-.).*, 1998, **282**, 1853–1858.

29 Y. Nicolet, C. Piras, P. Legrand, C. E. Hatchikian and J. C. Fontecilla-Camps, *Structure*, 1999, **7**, 13–23.

30 Y. Nicolet, *Trends Biochem. Sci.*, 2000, **25**, 138–143.

31 T. M. Spek, A. F. Arendsen, R. P. Happe, S. Yun, K. A. Bagley, D. J. Stufkens, W. R. Hagen, S. P. J. Albracht and W. R. Hagen, *Fed. Eur. Biochem. Soc. J.*, 1996, **237**, 629–634.

32 Y. Nicolet, C. Cavazza and J. C. Fontecilla-Camps, *J. Inorg. Biochem.*, 2002, **91**, 1–8.

33 P. M. Vignais, B. Billoud and J. Meyer, *FEMS Microbiol. Rev.*, 2001, **25**, 455–501.

34 M. Kaji, Y. Taniguchi, O. Matsushita, S. Katayama, S. Miyata, S. Morita and A. Okabe, *FEMS Microbiol. Lett.*, 1999, **181**, 329–336.

35 J. Meyer and J. Gagnon, *Biochemistry*, 1991, **30**, 9697–9704.

36 J. W. Peters, *Curr. Opin. Struct. Biol.*, 1999, **9**, 670–676.

37 Y. Nicolet, A. L. de Lacey, X. Vernède, V. M. Fernandez, E. C. Hatchikian and J. C. Fontecilla-Camps, *J. Am. Chem. Soc.*, 2001, **123**, 1596–1601.

38 Y. Nicolet, C. Piras, P. Legrand, C. E. Hatchikian and J. C. Fontecilla-Camps, *Structure*, 1999, **7**, 13–23.

39 A. Volbeda, M. H. Charon, C. Piras, E. C. Hatchikian, M. Frey and J. C. Fontecilla-Camps, *Nature*, 1995, **373**, 580–7.

40 W. Lubitz, E. Reijerse and M. van Gastel, *Chem. Rev.*, 2007, **107**, 4331–4365.

41 P. M. Vignais and B. Billoud, *Chem. Rev.*, 2007, **107**, 4206–4272.

42 E. Garcin, X. Vernede, E. Hatchikian, A. Volbeda, M. Frey and J. Fontecilla-Camps, *Structure*, 1999, **7**, 557–566.

43 A. Volbeda, E. Garcin, C. Piras, A. L. de Lacey, V. M. Fernandez, E. C. Hatchikian, M. Frey and J. C. Fontecilla-Camps, *J. Am. Chem. Soc.*, 1996, **118**, 12989–12996.

44 Y. Higuchi, T. Yagi and N. Yasuoka, *Structure*, 1997, **5**, 1671–1680.

45 A. Messerschmidt, W. Bode and M. Cygler, *Handbook of Metalloproteins*, John Wiley & Sons, Incorporated, 2003.

46 A. L. De Lacey, C. Stadler, V. M. Fernandez, E. C. Hatchikian, H.-J. Fan, S. Li and M. B. Hall, *J. Biol. Inorg. Chem.*, 2002, **7**, 318–326.

47 B. Bleijlevens, F. A. van Broekhuizen, A. L. De Lacey, W. Roseboom, V. M. Fernandez and S. P. J. Albracht, *J. Biol. Inorg. Chem.*, 2004, **9**, 743–752.

48 R. P. Happe, W. Roseboom, A. J. Pierik, S. P. Albracht and K. A. Bagley, *Nature*, 1997, **385**, 126.

49 H. Ogata, Y. Mizoguchi, N. Mizuno, K. Miki, S. Adachi, N. Yasuoka, T. Yagi, O. Yamauchi, S. Hirota and Y. Higuchi, *J. Am. Chem. Soc.*, 2002, **124**, 11628–11635.

50 H. Ogata, S. Hirota, A. Nakahara, H. Komori, N. Shibata, T. Kato, K. Kano and Y. Higuchi, *Structure*, 2005, **13**, 1635–1642.

51 A. Volbeda, L. Martin, C. Cavazza, M. Matho, B. W. Faber, W. Roseboom, S. P. J. Albracht, E. Garcin, M. Rousset and J. C. Fontecilla-Camps, *J. Biol. Inorg. Chem.*, 2005, **10**, 239–249.

52 H. Ogata, K. Nishikawa and W. Lubitz, *Nature*, 2015, **520**, 571–574.

53 C. S. A. Baltazar, M. C. Marques, C. M. Soares, A. M. DeLacey, I. A. C. Pereira and P. M. Matias, *Eur. J. Inorg. Chem.*, 2011, **2011**, 948–962.

54 E. S. J. Arnér, *Exp. Cell Res.*, 2010, **316**, 1296–1303.

55 C. Wombwell, C. A. Caputo and E. Reisner, *Acc. Chem. Res.*, 2015, **48**, 2858–2865.

56 A. L. de Lacey, E. C. Hatchikian, A. Volbeda, M. Frey, J. C. Fontecilla-Camps and V. M. Fernandez, *J. Am. Chem. Soc.*, 1997, **119**, 7181–7189.

57 M. Teixeira, I. Moura, A. V Xavier, B. H. Huynh, D. V DerVartanian, H. D. H. Peck and J. LeGall, *J. Biol. Chem.*, 1985, **260**, 8942–8950.

58 H. Wang, C. Y. Ralston, D. S. Patil, R. M. Jones, W. Gu, M. Verhagen, M. Adams, P. Ge, C. Riordan, C. A. Marganian, P. Mascharak, J. Kovacs, C. G. Miller, T. J. Collins, S. Brooker, P. D. Croucher, K. Wang, E. I. Stiefel and S. P. Cramer, *J. Am. Chem. Soc.*, 2000, **122**, 10544–10552.

59 J. P. Whitehead, G. J. Colpas, C. Bagyinka and M. J. Maroney, *J. Am. Chem. Soc.*, 1991, **113**, 6288–6289.

60 K. K. Surerus, M. Chen, J. W. van der Zwaan, F. M. Rusnak, M. Kolk, E. C. Duin, S. P. J. Albracht and E. Muenck, *Biochemistry*, 1994, **33**, 4980–4993.

61 S. P. J. Albracht, E.-G. Graf and R. K. Thauer, *FEBS Lett.*, 1982, **140**, 311–313.

62 V. M. Fernandez, E. C. Hatchikian, D. S. Patil and R. Cammack, *Biochim. Biophys. Acta - Gen. Subj.*, 1986, **883**, 145–154.

63 M. Brecht, M. van Gastel, T. Buhrke, B. Friedrich and W. Lubitz, *J. Am. Chem. Soc.*, 2003, **125**, 13075–13083.

64 J. P. Whitehead, R. J. Gurbiel, C. Bagyinka, B. M. Hoffman and M. J. Maroney, *J. Am. Chem. Soc.*, 1993, **115**, 5629–5635.

65 C. Fan, M. Teixeira, J. Moura, I. Moura, J. Le Gall, H. D. Peck and B. M. Hoffman, *J. Am. Chem. Soc.*, 1991, **113**, 20–24.

66 M. Stein and W. Lubitz, *Phys. Chem. Chem. Phys.*, 2001, **3**, 5115–5120.

67 C.-H. Lai, W.-Z. Lee, M. L. Miller, J. H. Reibenspies, D. J. Darensbourg and M. Y. Darensbourg, *J. Am. Chem. Soc.*, 1998, **120**, 10103–10114.

68 A. K. Jones, E. Sillery, S. P. J. Albracht and F. A. Armstrong, *Chem. Commun.*, 2002, **25**,

866–867.

69 S. Canaguier, V. Artero and M. Fontecave, *Dalt. Trans.*, 2008, **25**, 315–325.

70 M. Bruschi, L. De Gioia, G. Zampella, M. Reiher, P. Fantucci and M. Stein, *J. Biol. Inorg. Chem.*, 2004, **9**, 873–884.

71 C. Greco, M. Bruschi, J. Heimdal, P. Fantucci, L. De Gioia and U. Ryde, *Inorg. Chem.*, 2007, **46**, 7256–7258.

72 P. E. M. Siegbahn, J. W. Tye and M. B. Hall, *Chem. Rev.*, 2007, **107**, 4414–4435.

73 M. Pavlov, P. E. M. Siegbahn, M. R. A. Blomberg and R. H. Crabtree, *J. Am. Chem. Soc.*, 1998, **120**, 548–555.

74 W. Lubitz, H. Ogata, O. Rüdiger and E. Reijerse, *Chem. Rev.*, 2014, **114**, 4081–4148.

75 S. Foerster, M. Stein, M. Brecht, H. Ogata, Y. Higuchi and W. Lubitz, *J. Am. Chem. Soc.*, 2003, **125**, 83–93.

76 M. E. Pandelia, P. Infossi, M. Stein, M.-T. Giudici-Orticoni and W. Lubitz, *Chem. Commun.*, 2012, **48**, 823–825.

77 S. Fox, Y. Wang, A. Silver and M. Millar, *J. Am. Chem. Soc.*, 1990, **112**, 3218–3220.

78 T. Yamamura, *Chem. Lett.*, 1986, **15**, 801–804.

79 B. Snyder, C. Rao and R. Holm, *Aust. J. Chem.*, 1986, **39**, 963–974.

80 S. G. Rosenfield, W. H. Armstrong and P. K. Mascharak, *Inorg. Chem.*, 1986, **25**, 3014–3018.

81 E. Bouwman and J. Reedijk, *Coord. Chem. Rev.*, 2005, **249**, 1555–1581.

82 J. R. Nicholson, G. Christou, J. C. Huffman and K. Folting, *Polyhedron*, 1987, **6**, 863–870.

83 N. Baidya, P. K. Mascharak, D. W. Stephan and C. F. Campagna, *Inorganica Chim. Acta*, 1990, **177**, 233–238.

84 T. Yamamura, H. Arai, H. Kurihara and R. Kuroda, *Chem. Lett.*, 1990, **19**, 1975–1978.

85 M. Cha, S. C. Shoner and J. A. Kovacs, *Inorg. Chem.*, 1993, **32**, 1860–1863.

86 M. Cha, J. Sletten, S. Critchlow and J. A. Kovacs, *Inorg. Chim. Acta Chim. Acta*, 1997, **263**, 153–159.

87 D. Sellmann, H. Binder, D. Häußinger, F. W. Heinemann and J. Sutter, *Inorganica Chim. Acta*, 2000, **300**–**302**, 829–836.

88 A. Silver and M. Millar, *J. Chem. Soc., Chem. Commun.*, 1992, **51**, 948–949.

89 D. Sellmann, S. Funfgelder, G. Pohlmann, F. Knoch and M. Moll, *Inorg. Chem.*, 1990, **29**, 4772–4778.

90 M. Cha, C. L. Gatlin, S. C. Critchlow and J. A. Kovacs, *Inorg. Chem.*, 1993, **32**, 5868–5877.

91 D. Sellmann, D. Haussinger and F. Heinemann, *Eur. J. Inorg. Chem.*, 1999, 1715–1725.

92 D. Sellmann, R. Prakash and F. Heinemann, *Eur. J. Inorg. Chem.*, 2004, 4291–4299.

93 D. Sellmann, R. Prakash, F. Geipel and F. Heinemann, *Eur. J. Inorg. Chem.*, 2002, 2138–2146.

94 D. Sellmann, F. Geipel and F. Heinemann, *Eur. J. Inorg. Chem.*, 2000, 271–279.

95 D. Sellmann, F. Geipel, F. Lauderbach and F. W. F. Heinemann, *Angew. Chem. Int. Ed. Engl.*, 2002, **41**, 632–634.

96 Z. Li, Y. Ohki and K. Tatsumi, *J. Am. Chem. Soc.*, 2005, **127**, 8950–8951.

97 C. V. Romão, I. A. C. Pereira, A. V. Xavier, J. Legall and M. Teixeira, *Biochem. Biophys. Res. Commun.*, 1997, **240**, 75–79.

98 S. Tanino, Z. Li, Y. Ohki and K. Tatsumi, *Inorg. Chem.*, 2009, **48**, 2358–2360.

99 M. Ito, M. Kotera, Y. Song, T. Matsumoto and K. Tatsumi, *Inorg. Chem.*, 2009, **48**, 1250–1256.

100 Z. Li, Y. Ohki and K. Tatsumi, *J. Am. Chem. Soc.*, 2005, **127**, 8950–8951.

101 W. Zhu, A. C. Marr, Q. Wang, F. Neese, D. J. E. Spencer, A. J. Blake, P. A. Cooke, C. Wilson and M. Schröder, *Proc. Natl. Acad. Sci. U. S. A.*, 2005, **102**, 18280–18285.

102 S. Canaguier, M. Field, Y. Oudart, J. Pécaut, M. Fontecave and V. Artero, *Chem. Commun.*, 2010, **46**, 5876.

103 S. C. Davies, D. J. Evans, D. L. Hughes, S. Longhurst and J. Roger Sanders, *Chem. Commun.*, 1999, **373**, 1935–1936.

104 M. C. Smith, J. E. Barclay, S. P. Cramer, S. C. Davies, W.-W. Gu, D. L. Hughes, S. Longhurst and D. J. Evans, *J. Chem. Soc. Dalt. Trans.*, 2002, **2**, 2641–2647.

105 M. Kampa, M.-E. Pandelia, W. Lubitz, M. van Gastel and F. Neese, *J. Am. Chem. Soc.*, 2013, **135**, 3915–3925.

106 B. E. Barton, C. M. Whaley, T. B. Rauchfuss and D. L. Gray, *J. Am. Chem. Soc.*, 2009, **131**, 6942–6943.

107 D. Sellmann, F. Lauderbach, F. Geipel, F. W. Heinemann and M. Moll, *Angew. Chem. Int. Ed. Engl.*, 2004, **43**, 3141–3144.

108 F. Lauderbach, R. Prakash, A. W. Götz, M. Munoz, F. W. Heinemann, U. Nickel, B. A. Hess and D. Sellmann, *Eur. J. Inorg. Chem.*, 2007, **2007**, 3385–3393.

109 Q. Wang, J. E. Barclay, A. J. Blake, E. S. Davies, D. J. Evans, A. C. Marr, E. J. L. McInnes, J. McMaster, C. Wilson and M. Schröder, *Chem. Eur. J.*, 2004, **10**, 3384–3396.

110 A.Perra, University of Nottingham, 2007.

111 Y. Higuchi, H. Ogata, K. Miki, N. Yasuoka and T. Yagi, *Structure*, 1999, **7**, 549–556.

112 A. Perra, E. S. Davies, J. R. Hyde, Q. Wang, J. McMaster and M. Schröder, *Chem. Commun.*, 2006, **10**, 1103–1105.

113 C. J. Curtis, A. Miedaner, R. Ciancanelli, W. W. Ellis, B. C. Noll, M. Rakowski DuBois and D. L. DuBois, *Inorg. Chem.*, 2003, **42**, 216–227.

114 J. R. Norton and K. W. Kramarz, *Progress in Inorganic Chemistry, Volume 42*, 1994.

115 M. Rakowski DuBois and D. L. DuBois, *Chem. Soc. Rev.*, 2009, **38**, 62–72.

116 K. Fraze, A. D. Wilson, A. M. Appel, M. Rakowski DuBois and D. L. DuBois, *Organometallics*, 2007, **26**, 3918–3924.

117 A. D. Wilson, R. K. Shoemaker, A. Miedaner, J. T. Muckerman, D. L. DuBois and M. R. DuBois, *Proc. Natl. Acad. Sci. U. S. A.*, 2007, **104**, 6951–6956.

118 A. D. Wilson, R. H. Newell, M. J. McNevin, J. T. Muckerman, M. Rakowski DuBois and D. L. DuBois, *J. Am. Chem. Soc.*, 2006, **128**, 358–366.

119 J. Y. Yang, R. M. Bullock, W. G. Dougherty, W. S. Kassel, B. Twamley, D. L. DuBois and M. Rakowski DuBois, *Dalton Trans.*, 2010, **39**, 3001–3010.

120 M. L. Helm, M. P. Stewart, R. M. Bullock, M. R. DuBois and D. L. DuBois, *Science*, 2011, **333**, 863–6.

121 L. Duan, M. Wang, P. Li, N. Wang, F. Wang and L. Sun, *Inorg. Chim. Acta*, 2009, **362**, 372–376.

122 A. J. Bard and M. A. Fox, *Acc. Chem. Res.*, 1995, **28**, 141–145.

123 P. A. Summers, J. Dawson, F. Ghiotto, M. W. D. Hanson-Heine, K. Q. Vuong, E. S. Davies, X.-Z. Sun, N. A. Besley, J. McMaster, M. W. George and M. Schröder, *Inorg. Chem.*, 2014, **53**, 4430–4439.

124 W. T. Eckenhoff and R. Eisenberg, *Dalt. Trans.*, 2012, **41**, 13004.

125 A. Melis and M. Melnicki, *Int. J. Hydrogen Energy*, 2006, **31**, 1563–1573.

126 J. A. Cracknell, K. A. Vincent and F. A. Armstrong, *Chem. Rev.*, 2008, **108**, 2439–2461.

127 X. Li, M. Wang, S. Zhang, J. Pan, Y. Na, J. Liu, B. Akermark and L. Sun, *J. Phys. Chem. B*, 2008, **112**, 8198–8202.

128 A. M. Kluwer, R. Kapre, F. Hartl, M. Lutz, A. L. Spek, A. M. Brouwer, P. W. N. M. van Leeuwen and J. N. H. Reek, *Proc. Natl. Acad. Sci. U. S. A.*, 2009, **106**, 10460–10465.

129 P. A. Summers, J. A. Calladine, F. Ghiotto, J. Dawson, X.-Z. Sun, M. L. Hamilton, M. Towrie, E. S. Davies, J. McMaster, M. W. George and M. Schröder, *Inorg. Chem.*, 2016, **55**, 527–536.

CHAPTER TWO

NiS_4 Complexes Containing Two Quinoxaline Units: Synthesis, Characterisation and Catalytic Studies.

2.1 Introduction

Research into the design and synthesis of low molecular weight analogues of the active site of [NiFe] hydrogenase could yield effective, low-cost catalysts for proton reduction. A common synthetic strategy for the synthesis of [NiFe] complexes is to react a [Fe]-containing species, which contains labile ligands, with an appropriate Ni^{II}-containing subunit.[1,2] In this Chapter we discuss the synthesis and characterisation of a range of Ni^{II}-containing subunits that possess the potential to coordinate to [Fe]-containing fragments, and investigate the electrochemical properties of these complexes to assess their potential catalytic activity towards proton reduction.

There are two important factors that determine the effectiveness of an electrocatalyst: (i) the turnover frequency and (ii) the potential at which catalysis occurs. $[Ni(L^A)Fe_2(CO)_6]$ (Section 1.6.4) undergoes reduction in a 0.4 M $[N^nBu_4][BF_4]$ solution in CH_2Cl_2 at -1.33 V *vs* Fc^+/Fc . Less negative potentials are more favourable for an efficient catalyst for H_2 production because less energy is required for the catalytic process. One approach at Nottingham that has attempted to generate systems with more positive reduction potentials has been the incorporation of N groups within the ligand frameworks based on $[Ni(L^A)Fe_2(CO)_6]$ (Figure 2.1).

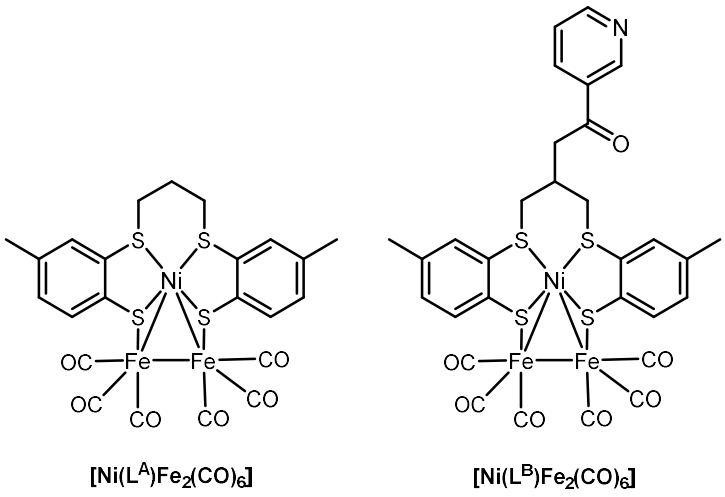
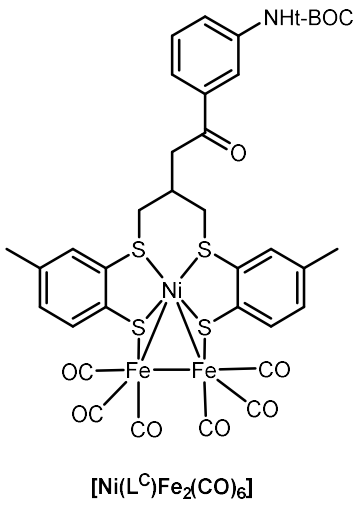


Figure 2.1: The structure of $[Ni(L^A)Fe_2(CO)_6]$ and an example of a [NiFe] complex, $[Ni(L^B)Fe_2(CO)_6]$, incorporating protonation sites investigated at Nottingham.[3]

Thus, pyridine groups have been incorporated on the propane unit within $[Ni(L^A)Fe_2(CO)_6]$ that may serve as proton relay sites for the delivery of protons to the catalytic centre (Section 1.7.2).[3-5] The incorporation of pyridine units into the ligand framework of $[Ni(L^A)Fe_2(CO)_6]$ gives $[Ni(L^B)Fe_2(CO)_6]$ (Figure 2.1). The addition of the pyridine group within $[Ni(L^B)Fe_2(CO)_6]$ complex appears to protonate on the addition of TFA to form a $[Ni(L^B)Fe_2(CO)_6H]^+$ cation. The $[Ni(L^B)Fe_2(CO)_6]^+$ cation generates a reduction potential at -1.09 V *vs* Fc^+/Fc suggesting $[Ni(L^B)Fe_2(CO)_6H]^+$ may provide a pathway to perform catalysis at a more positive potential. In contrast, the incorporation of protected amine groups at the 2 position of the propane bridge to give $[Ni(L^C)Fe_2(CO)_6]$ (Figure 2.2) does not affect the reduction potential of $[Ni(L^C)Fe_2(CO)_6]$. However the addition of TFA produces a greater catalytic current than $[Ni(L^A)Fe_2(CO)_6]$, suggesting that the addition of the amide of a carbamate function acts as a proton relay.



$[Ni(L^C)Fe_2(CO)_6]$

Figure 2.2: The structure of $[Ni(L^C)Fe_2(CO)_6]$ incorporating a proton relay site investigated at Nottingham.[3]

DFT studies of $[Ni(L^A)Fe_2(CO)_6]$ have suggested that the S-donors have a role in modulating the electronic structure and hence the redox properties of the complexes.[4] Thus, the incorporation of basic sites adjacent to the S-donors, instead of at the propane bridge in $[Ni(L^A)Fe_2(CO)_6]$, may have a greater impact on the reduction potential of the centre and generate complexes exhibiting more positive reduction potentials relative to that of $[Ni(L^A)Fe_2(CO)_6]$.

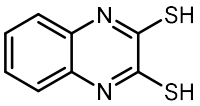


Figure 2.3: The structure of quinoxaline-2,3-dithiol (qdt).

Quinoxaline-2,3-dithiolate (qdt^{2-}) (Figure 2.3) can form complexes with a wide range of transition metal centres including Fe^{I} in $[Fe_2(\mu\text{-qdt})(CO)_6]$,[5] Ni^{II} in [Ni(dcbpy)(qdt)] (dcbpy = 4,4′-dicarboxy-2,2′-bipyridine)[6] and Cu^{II} in $[NBu_4][Cu(qdt)_2]$.[7] The pyrazine N atoms within the qdt^{2-} ligand backbone could serve as protonation sites, which has been shown to couple to a proton reduction process.[8] In addition, electrochemical studies of [Ni(dcbpy)(qdt)] have suggested that this complex can undergo redox processes that are formally metal- and/or ligand-based. Thus, in these respects qdt^{2-} is a redox non-innocent ligand that offers some potential in the development of catalysts for electrochemical proton reduction.[9]

The syntheses and electrochemical analyses of $[NBu_4]_2[Ni(6,7\text{-qdt})_2]$ (Figure 2.4) have been reported.[10] $[Bu_4N]_2[Ni(6,7\text{-qdt})_2]$ possesses an oxidation process at $E_{1/2}$ = +0.12 V *vs* Ag/AgCl that has been assigned to the $[Ni(6,7\text{-qdt})_2]^{-/2-}$ redox couple. The potential of this couple is lower by *ca.* 0.29 V than the corresponding $[Ni(qdt)_2]^{-/2-}$ couple in $[NBu_4]_2[Ni(qdt)_2]$ ($E_{1/2}$ = +0.41 V *vs* Ag/AgCl).[10] This difference in reduction potential may result from the relative positions of the N atoms in the qdt^{2-} and 6,7-qdt^{2-} ligands suggesting that the 6,7-qdt^{2-} ligand is more electron releasing towards the metal centre than the qdt^{2-} ligand. Thus, the location of the pyrazine ring N atoms in quinoxaline-based ligand systems may tune the redox potentials of complexes containing quinoxaline dithiolate ligands.

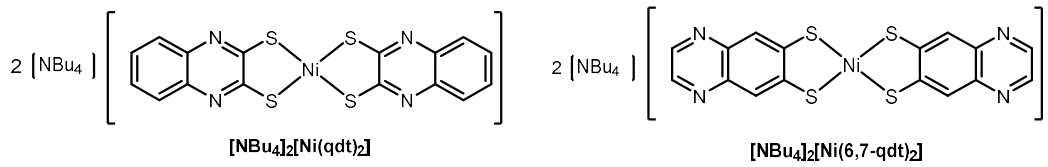


Figure 2.4: Left: The structure of $[Bu_4N]_2[Ni(qdt)_2]$. Right: The structure of $[Bu_4N]_2[Ni(6,7\text{-qdt})_2]$.[10]

Previous research within the group has shown that $[Ni(qdt)_2]^{2-}$ and $[Ni(6,7\text{-qdt})_2]^{2-}$ react with 1,3-diiodopropane under anaerobic conditions in methanol at RT to give [Ni(p-qdt)] and [Ni(p-$q^{6,7}$dt)] (Figure 2.5). The [Ni(p-qdt)] and [Ni(p-$q^{6,7}$dt)]

complexes are similar to the [Ni(L^A)] precursor employed in the synthesis of [Ni(L^A)$Fe_2(CO)_6$].[11] Attempts have been made to react [Ni(p-qdt)] and [Ni(p-$q^{6,7}$dt)] with Fe-containing fragments to produce and isolate products that are analogous to [Ni(L^A)$Fe_2(CO)_6$]. However, these reactions were unsuccessful and only decomposition products were identified.[11]

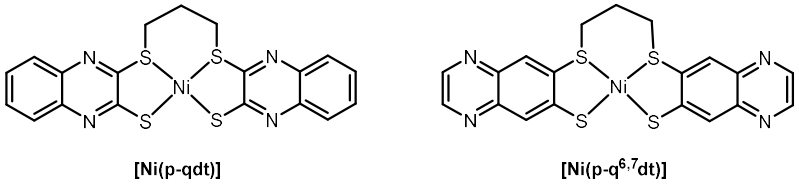


Figure 2.5: The structures of [Ni(p-qdt)] and [Ni(p-$q^{6,7}$dt)] investigated by Dawson et al.[11]

Possible reasons for the failure of the [Ni(p-qdt)] and [Ni(p-$q^{6,7}$dt)] to coordinate to a {$Fe_2(CO)_6$} fragment include:

(i) The flexibility in the geometry about the Ni^{II} centre. The NiS_4 geometry may need to distort away from square planar to accommodate the two formal Ni-Fe bonds involving the Fe centres in the {$Fe_2(CO)_6$} fragment.

(ii) The p-qdt^{2-} and p-$q^{6,7}dt^{2-}$ ligands contain electron withdrawing quinoxaline rings that may deactivate the S atoms that could inhibit the formation of Ni-S(R)-Fe bridges.

(iii) Dawson *et al.*[11] demonstrated that [Ni(p-qdt)] and [Ni(p-$q^{6,7}$dt)] have low solubility in most common solvents (e.g. CH_2Cl_2 and $CHCl_3$). This insolubility may result from π-π interactions involving the quinoxaline rings within each complex.

2.2 Aims

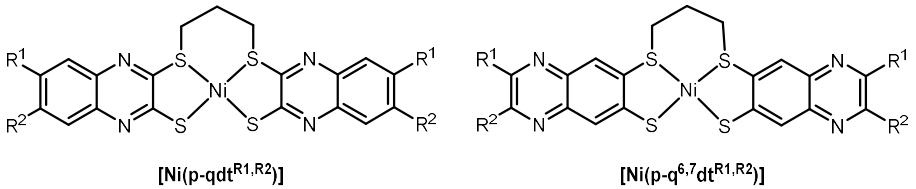


Figure 2.6: The target structures discussed within this chapter, where $R^1 = R^2$ = Me, Et and Ph and R^1= H and R^2 = ^{t}Bu.

Our primary aim was to synthesise [Ni(p-$qdt^{R1,R2}$)] and [Ni(p-$q^{6,7}dt^{R1,R2}$)] ($R^1 = R^2$ = Me, Et, Ph; R^1 = H, R^2 = ^{t}Bu) (Figure 2.6) where the incorporation of the R substituents may improve the solubility of the resulting Ni^{II} complexes in common

solvents by potentially disrupting π-π interactions between the quinoxaline components. We focused on *tert*-butyl groups since these substituents have been used previously to successfully interrupt π-π interactions in tri-*tert*-butyl[5]phenacene (Figure 2.7)[12] and we included the related complexes [Ni(p-qdt^{R1,R2})] and [Ni(p-q^{6,7}dt^{R1,R2})] R_1 = R_2 = Me or Et for comparison. Studies of triphenyl[5]phenacene, (Figure 2.7) were also reported by Pascal *et al.* and Mallory *et al.* alongside the tri-*tert*-butyl[5]phenacene compound. The phenyl rings were believed to improve solubility of the compounds.[12,13] Thus we also included [Ni(p-qdt^{R1,R2})] and [Ni(p-q^{6,7}dt^{R1,R2})] (R^1 = R^2 = Ph) as target compounds in addition to those containing alkyl substituents.

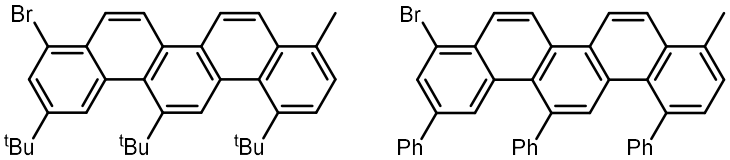


Figure 2.7: The structure of left: tri-*tert*-butyl[5]phenacene and right: tri-phenyl[5]phenacene .[12]

Following the successful synthesis and characterisation of qdt^{R1,R2}H_2 (R^1 = R^2 = Me and R^1 = H, R^2 = ^{t}Bu) and q^{6,7}dt^{R1,R2}H_2 (R^1 = R^2 = Me, Et, Ph; R^1 = H, R^2 = ^{t}Bu) ligands we synthesised and characterised [Ni(p-qdt^{R1,R2})] (R^1 = H, R^2 = ^{t}Bu) and [Ni(q^{6,7}dt^{R1,R2})] (R^1 = R^2 = Me, Et, Ph; R^1 = H, R^2 = ^{t}Bu).

2.3 Ligand Synthesis

The quinoxaline-2,3-dithiols, qdt^{R1,R2}H_2 (R^1 = R^2 = Me and R^1 = H, R^2 = ^{t}Bu) and the quinoxaline-6,7-dithiols, q^{6,7}dt^{R1,R2}H_2 (R^1 = R^2 = Me, Et, Ph; R^1 = H, R^2 = ^{t}Bu) (Figure 2.8) were synthesised as precursors to the mononuclear [Ni^{II}(p-qdt^{R1,R2})] and [Ni^{II}(p-q^{6,7}dt^{R1,R2})] complexes.

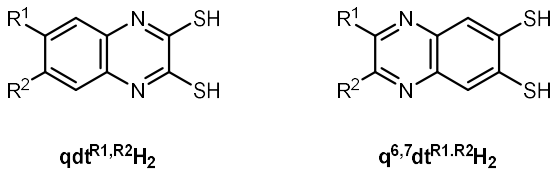
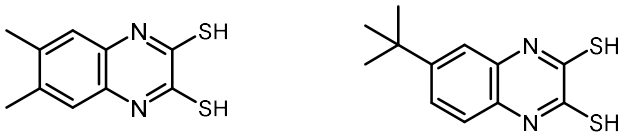


Figure 2.8: The ligand precursors synthesised in this chapter, left: qdt^{R1,R2}H_2 (R^1 = R^2 = Me and R^1 = H, R^2 = ^{t}Bu) and right: q^{6,7}dt^{R1,R2}H_2 (R^1 = R^2 = Me, Et, Ph; R^1 = H, R^2 = ^{t}Bu).

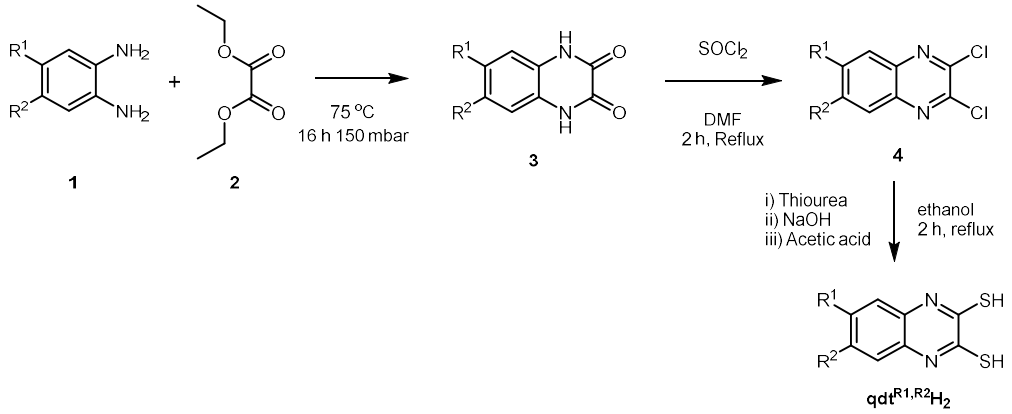
2.3.1 Synthesis of substituted quinoxaline-2,3-dithiols, $qdt^{R1,R2}H_2$ ($R^1 = R^2 = Me$ and $R^1 = H$, $R^2 = {}^tBu$)



$qdt^{Me,Me}H_2$ $qdt^{H,tBu}H_2$

Figure 2.9: The quinoxaline-2,3-dithiol ligand synthesised in this chapter.

The syntheses of $qdt^{Me,Me}H_2$ and $qdt^{H,tBu}H_2$ (Figure 2.9) are shown in Scheme 2.1. Each substituted quinoxaline-2,3-dithiol was synthesised by the same synthetic method, which involves the formation of a substituted dihydroquinoxaline-2,3-dione from a 4,5-subsituted 1,2-phenyldiamine and diethyl oxalate. Dihydroquinoxaline-2,3-dione is reacted with thionyl chloride under reflux to produce the dichloro-quinoxaline precursor. The dichloro-quinoxaline precursor is reacted with thiourea to give $qdtH_2$. The reactions proceeded smoothly and yielded the substituted quinoxaline-2,3-dithiols in overall *ca*. 75 % yields.



Scheme 2.1: The synthetic route to give $qdt^{R1,R2}H_2$ ($R^1 = R^2 = Me$; $R^1 = H$, $R^2 = {}^tBu$)

2.3.2 Synthesis of quinoxaline-6,7-dithiols $q^{6,7}dt^{R1,R2}H_2$ ($R^1 = R^2$ = Me, Et, Ph; R^1 = H, R^2 = ^{t}Bu)

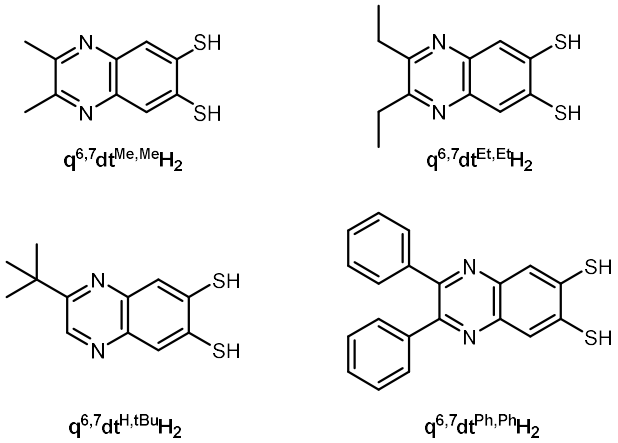
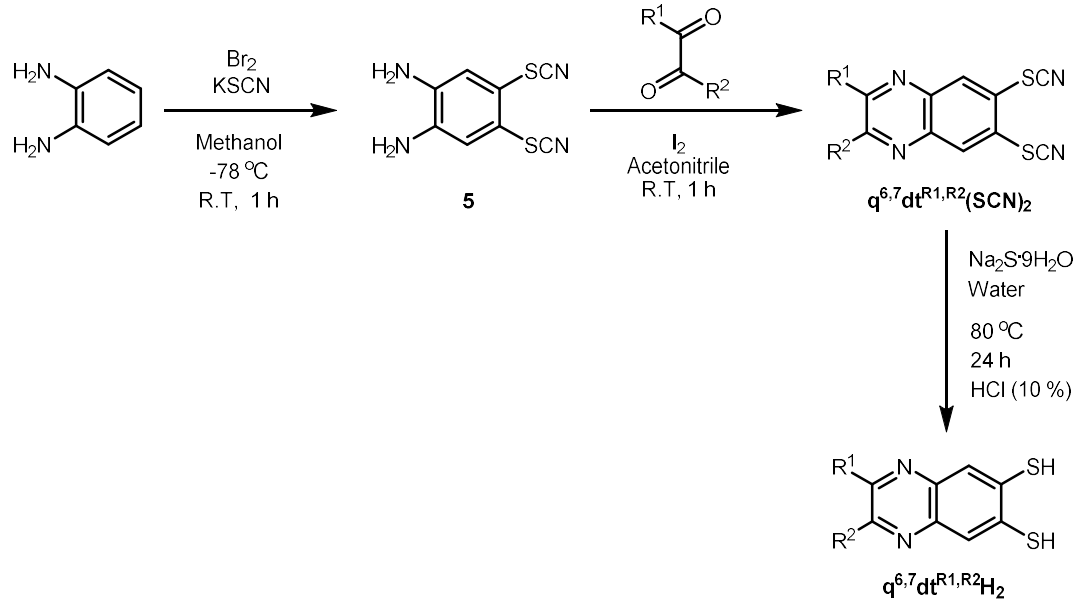


Figure 2.10: The 2,3-quinoxaline-6,7-dithiols synthesised in this chapter.

The synthetic route to $q^{6,7}dt^{Me,Me}H_2$, $q^{6,7}dt^{Et,Et}H_2$, $q^{6,7}dt^{tBu,H}H_2$ and $q^{6,7}dt^{Ph,Ph}H_2$ (Figure 2.10) is shown in Scheme 2.2. The synthesis of each $q^{6,7}dt^{R1,R2}H_2$ was achieved through the condensation of 4,5-dithiocyano-1,2-diaminobenzene with a substituted glyoxal in acetonitrile at room temperature for 1 h with iodine as a catalyst. Each substituted quinoxaline-6,7-dithiocyanate was collected *via* filtration and washed with pentane to give crystalline products. The substituted quinoxaline-6,7-dithiocyanate compounds were then reduced by sodium sulfide in water at 80 °C for 1 h to give brightly coloured solutions. The substituted quinoxaline-6,7-dithiols precipitated from solution following the addition of excess 10% hydrochloric acid. Each precipitate was collect *via* filtration to give crude $q^{6,7}dt^{R1,R2}H_2$ ($R^1 = R^2$ = Me, Et, and Ph; R^1 = H, R^2 = ^{t}Bu).[14] The quinoxaline-6,7-dithiols are sensitive to oxidation and were therefore coordinated immediately in their dithiolate forms to a Ni^{II} centre without further purification.



Scheme 2.2: The synthetic route to give $q^{6,7}dt^{R1,R2}H_2$ ($R^1 = R^2$ = Me, Et, and Ph; R^1 = H, R^2 = ^{t}Bu).

Each quinoxaline-6,7-dithiocyanate precursor, $q^{6,7}dt^{R1,R2}(SCN)_2$ ($R^1 = R^2$ = Me, Et, and Ph; R^1 = H, R^2 = ^{t}Bu), was characterised by IR, ^{1}H-NMR and ^{13}C-NMR spectroscopies and mass spectrometry, and the purity of each compound confirmed by elemental analysis. The $q^{6,7}dt^{R1,R2}(SCN)_2$ ($R^1 = R^2$ = Me, Et, and Ph; R^1 = H, R^2 = ^{t}Bu) compounds were also investigated by electrochemistry to provide insights into any potential ligand-based redox processes (Section 2.3.4).

2.3.3 The structural characterisation of $q^{6,7}dt^{R1,R2}(SCN)_2$ ($R^1 = R^2$ = Me, Et, and Ph; R^1 = H, R^2 = ^{t}Bu)

Crystals of $q^{6,7}dt^{R1,R2}(SCN)_2$ ($R^1 = R^2$ = Me, Et, and Ph; R^1 = H, R^2 = ^{t}Bu) suitable for X-ray diffraction were obtained by washing the precipitated crystals from the reaction mixture with pentane. The solid state structures for $q^{6,7}dt^{R1,R2}(SCN)_2$ ($R^1 = R^2$ = Me, Et, and Ph; R^1 = H, R^2 = ^{t}Bu) are shown in Figure 2.11 and selected bond lengths and angles are presented in Table 2.1.

Table 2.1: Comparison of selected bond lengths and bond angles for $q^{6,7}dt^{R1,R2}(SCN)_2$ ($R^1 = R^2 =$ Me, Et, and Ph; $R^1 =$ H, $R^2 =$ ^{t}Bu).

Bond Length (Å) or Bond Angle (°)	$q^{6,7}dt^{Me,Me}(SCN)_2$	$q^{6,7}dt^{Et,Et}(SCN)_2$	$q^{6,7}dt^{H,tBu}(SCN)_2$	$q^{6,7}dt^{Ph,Ph}(SCN)_2$
S(1)-C(1)	1.697(5)	1.695(4)	1.6867(17)	1.704(4)
S(2)-C(2)	1.695(5)	1.697(4)	1.6996(15)	1.696(4)
S(1)–C(3)	1.782(4)	1.795(3)	1.7822(13)	1.787(4)
S(2)-C(4)	1.788(4)	1.796(3)	1.7901(14)	1.704(4)
N(1)-C(1)	1.149(7)	1.142(5)	1.146(2)	1.153(5)
N(2)-C(2)	1.140(6)	1.148(5)	1.148(2)	1.144(6)
C(3)-S(1)-C(1)	99.3(2)	98.01(16)	99.67(6)	95.64(18)
C(4)-S(2)-C(2)	98.9(2)	98.21(16)	99.21(6)	99.11(19)

The structures of each $q^{6,7}dt^{R1,R2}(SCN)_2$ ($R^1 = R^2 =$ Me, Et, and Ph; $R^1 =$ H, $R^2 =$ ^{t}Bu) are similar and consist of a planar quinoxaline unit substituted by two thiocyanate groups, one of which lies essentially in the plane of the quinoxaline ring and the other, defined by atoms S(1), C(1) and N(1), is essentially perpendicular to the plane. The metric parameters describing each thiocyanate group are similar for $q^{6,7}dt^{R1,R2}(SCN)_2$ ($R^1 = R^2 =$ Me, Et, and Ph; $R^1 =$ H, $R^2 =$ ^{t}Bu) (Table 2.1)

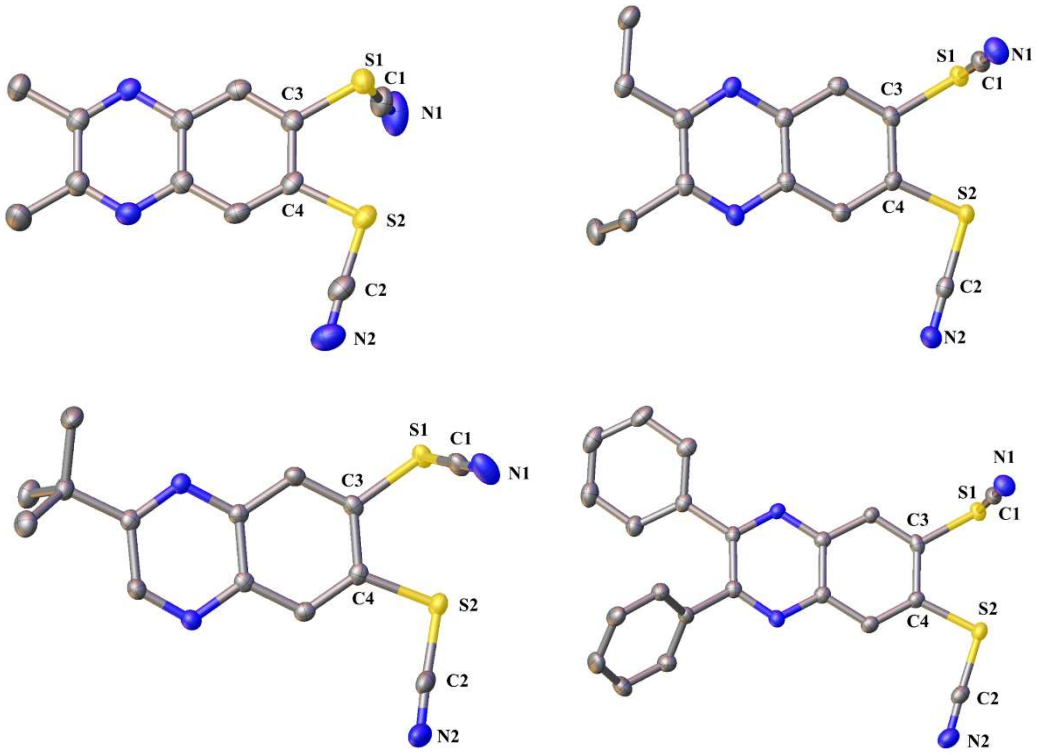


Figure 2.11: The molecular structures of $q^{6,7}dt^{R1,R1}(SCN)_2$ ($R^1 = R^2 =$ Me, Et, Ph; $R^1 =$ H, $R^2 =$ ^{t}Bu) with H atoms omitted for clarity.

Similarly the reported structure for dppz$(SCN)_2$ consists of a planar the dppz skeleton and one thiocyanate group lies in this plane while the other is perpendicular to the plane with C(3)-S(1)-C(1) and C(4)-S(2)-C(2) angles of 100.44(6)° and 100.48(6)°, respectively.[15]

2.3.4 Cyclic Voltammetric studies of $q^{6,7}dt^{R1,R2}(SCN)_2$ ($R^1 = R^2$ = Me, Et, and Ph; R^1 = H, $R^2 = {}^t$Bu)

Each $q^{6,7}dt^{R1,R2}(SCN)_2$ ($R^1 = R^2$ = Me, Et, and Ph; R^1 = H, $R^2 = {}^t$Bu) was studied by cyclic voltammetry (Figure 2.11 with $R^1 = R^2$ = Et as an example) to explore potential ligand-based redox processes and to facilitate comparisons with the electrochemical properties of [Ni(p-$q^{6,7}dt^{R1,R2}$)] (Section 2.6.2). The cyclic voltammograms of 1 mM solutions $q^{6,7}dt^{R1,R2}(SCN)_2$ were recorded at 293 K under Ar in CH_2Cl_2 containing 0.1 M [N^nBu_4][BF_4]. A three-electrode system consisting of a glassy carbon working electrode, a platinum wire secondary electrode and a saturated silver chloride reference electrode was used in these experiments. The potential was referenced to the ferrocenium/ferrocene (Fc^+/Fc) couple by internal calibration. A full description of the cyclic voltammetric experiment is given in the Appendix.

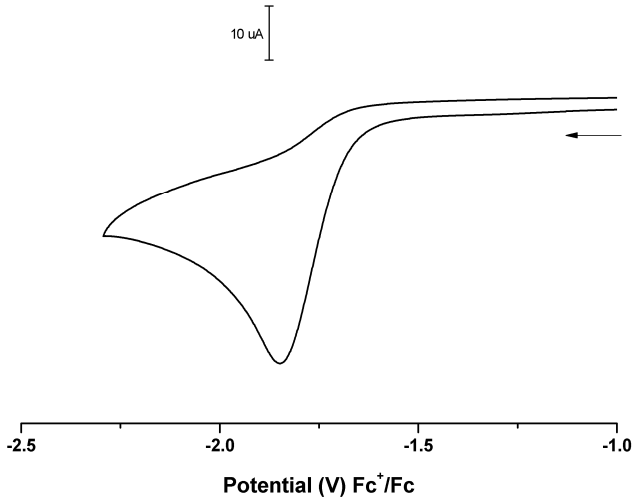


Figure 2.12: The cyclic voltammogram of a 1 mM solution of $q^{6,7}dt^{Et,Et}(SCN)_2$ in CH_2Cl_2 at 293 K containing [N^nBu_4][BF_4] (0.4 M) as supporting electrolyte.

Each cyclic voltammogram of $q^{6,7}dt^{R1,R2}(SCN)_2$ ($R^1 = R^2$ = Me, Et, and Ph; R^1 = H, $R^2 = {}^t$Bu) exhibits an electrochemically irreversible reduction process between E_p^c = -1.57 to -1.85 *vs.* Fc^+/Fc (Table 2.2). The shift in reduction potential generally

mirrors the electron donating/withdrawing nature of substituents on the $q^{6,7}dt^{R1,R2}(SCN)_2$ backbone. Thus, the reduction of $q^{6,7}dt^{Ph,Ph}(SCN)_2$ occurs at more positive potentials than those of $q^{6,7}dt^{R1,R2}(SCN)_2$ ($R^1 = R^2$ = Me, Et; R^1 = H, R^2 = ^{t}Bu) because of the more electron withdrawing nature of the Ph group relative to the $R^1 = R^2$ = Me, Et and R^1 = H, R^2 = ^{t}Bu substituents.

Table 2.2: Electrochemical data for $q^{6,7}dt^{R1,R2}(SCN)_2$ ($R^1 = R^2$ = Me, Et, and Ph; R^1 = H, R^2 = ^{t}Bu), measured at a scan rate of 100 mVs^{-1}.

$q^{6,7}dt^{R1,R2}(SCN)_2$	E_p^c (V *vs.* Fc^+/Fc)
$q^{6,7}dt^{Me,Me}(SCN)_2$	-1.75
$q^{6,7}dt^{Et,Et}(SCN)_2$	-1.85
$q^{6,7}dt^{H,tBu}(SCN)_2$	-1.69
$q^{6,7}dt^{Ph,Ph}(SCN)_2$	-1.66

2.3.5 Cyclic Voltammetric studies of $q^{6,7}dt^{Et,Et}(SCN)_2$ in the presence of trifluoroacetic acid (TFA)

Cyclovoltammetric experiments were undertaken for $q^{6,7}dt^{Et,Et}(SCN)_2$ to assess the effect of protonation on the electrochemical properties of $q^{6,7}dt^{Et,Et}(SCN)_2$.

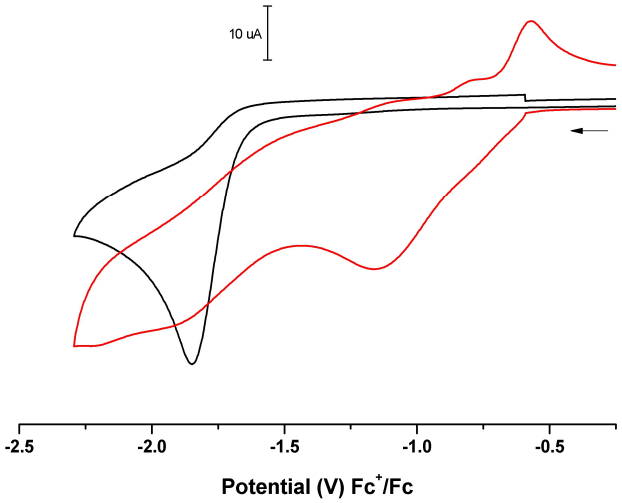


Figure 2.13: The cyclic voltammogram of a 1 mM solution of $q^{6,7}dt^{Et,Et}(SCN)_2$ (black) in CH_2Cl_2 at 293 K containing $[N^nBu_4][BF_4]$ (0.4 M) as supporting electrolyte and $q^{6,7}dt^{Et,Et}(SCN)_2$ after the addition of TFA (50 mM) (red).

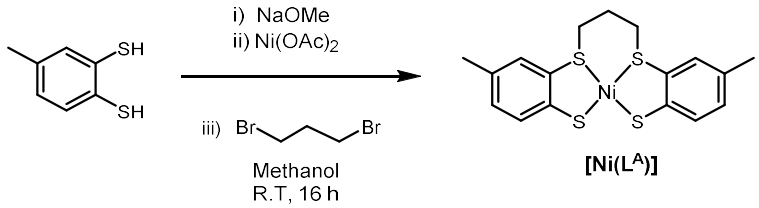
The cyclic voltammogram recorded for a 1 mM solution of $q^{6,7}dt^{Et,Er}(SCN)_2$ in CH_2Cl_2 at 298 K containing 0.4 M $[N^nBu_4][BF_4]$ as the supporting electrolyte under Ar in the presence of TFA (50mM) is shown in Figure 2.13. A full description of the cyclic voltammetric studies in the presence of TFA is given in the Appendix. Upon the addition of TFA no catalytic process was observed within the potential window.

However, the E_p^c associated with the reduction process (E_p^c = -1.15 V *vs* Fc^+/Fc) is more positive than that for $q^{6,7}dt^{Et,Er}(SCN)_2$ in the absence of TFA (E_p^c = -1.85 V *vs* Fc^+/Fc), which is consistent with protonation of $q^{6,7}dt^{Et,Er}(SCN)_2$ by TFA under the conditions of the experiment.

2.4 Syntheses of Ni^{II} complexes

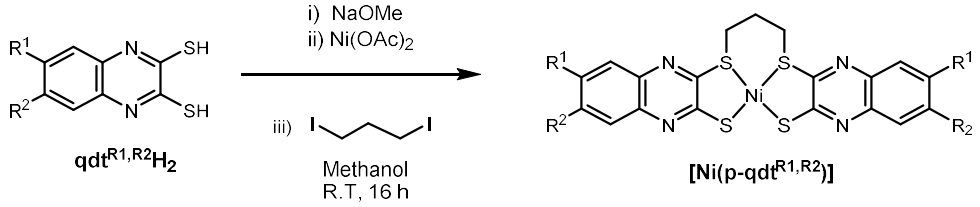
2.4.1 The synthesis of [Ni(L^A)]

[Ni(L^A)] was prepared by a template reaction involving toluene dithiol, 1,3-dibromopropane and $Ni(OAc)_2{\cdot}4H_2O$ (Scheme 2.3). [Ni(L^A)] was synthesised to provide a bench mark for the structural, spectroscopic and electrochemical studies of [Ni(p-$qdt^{R1,R2}$)] and [Ni(p-$q^{6,7}dt^{R1,R2}$)] (Section 2.6.2) as potential catalysts for proton reduction.



Scheme 2.3: The synthesis of [Ni(L^A)].[4]

2.4.2 The attempted syntheses of [Ni(p-$qdt^{R1,R2}$)] ($R^1 = R^2$ =Me; R^1 = H, R^2 = ^{t}Bu)



Scheme 2.4: The synthesis of [Ni(p-$q^{6,7}dt^{R1,R2}$)] ($R^1 = R^2$ = Me and R^1 = H, R^2 = ^{t}Bu).

The syntheses of [Ni(p-$qdt^{R1,R2}$)] ($R^1 = R^2$ =Me; R^1 = H, R^2 = ^{t}Bu) (Scheme 2.4) were attempted by an adaptation of the synthetic method used to prepare [Ni(L^A)].[4] The method involves the deprotonation of the corresponding $qdt^{R1,R2}H_2$ with sodium methoxide in methanol, to give $[qdt^{R1,R2}]^{2-}$. The addition of $Ni(OAc)_2$ in methanol followed by the addition of 1,3-diiodopropane in the absence of light yields the desired complexes. We substituted 1,3-dibromopropane for 1,3-diidopropane, as 1,3-diiodopropane is more reactive due to iodide being a better leaving group than

bromide.[16] In addition, the light sensitivity of 1,3-diiodopropane meant that we carried out the reactions in the absence of light.[17]

The characterisations of [Ni(p-qdt^{R1,R2})] ($R^1 = R^2$ = Me and R^1 = H, R^2 = ^{t}Bu) by ^{1}H-NMR and ^{13}C-NMR spectroscopies, mass spectrometry and elemental analyses were attempted. ^{1}H-NMR spectroscopy of [Ni(p-qdt^{R1,R2})] ($R^1 = R^2$ = Me and R^1 = H, R^2 = ^{t}Bu) resulted in spectra with broad features suggesting that [Ni(p-qdt^{R1,R2})] ($R^1 = R^2$ = Me and R^1 = H, R^2 = ^{t}Bu) are paramagnetic.[18] Mass spectrometric isotopic patterns were consistent with the formation of [Ni(p-qdt^{R1,R2})] ($R^1 = R^2$ = Me and R^1 = H, R^2 = ^{t}Bu), however elemental analyses suggest that each product was not pure.

The broad resonances observed in the ^{1}H-NMR spectra of [Ni(p-qdt^{R1,R2})] ($R^1 = R^2$ = Me and R^1 = H, R^2 = ^{t}Bu) may be associated with the presence of [Ni(p-qdt^{R1,R2})]$^+$ ($R_1 = R_2$ = Me and R_1 = H, R_2 = ^{t}Bu) impurities. These impurities could contain a d^7 Ni^{III} centre and consequently be paramagnetic.[19] Cobaltocene ($E_{1/2}$ = -1.3 V *vs* Fc^+/Fc), [20] a mild reducing agent, was added to a solutions of crude [Ni(p-qdt^{R1,R2})] ($R^1 = R^2$ = Me and R^1 = H, R^2 = ^{t}Bu) in deuterated chloroform in an attempt to reduce any Ni^{III} species to Ni^{II}. The addition of cobaltocene did not result in improvements in the resolution of the ^{1}H-NMR spectra and consequently it is unlikely that Ni^{III} impurities are present.

2.4.3 The syntheses of [Ni(p-q^{6,7}dt^{R1,R2})] ($R^1 = R^2$ = Me, Et, Ph and R^1 = H, R^2 = ^{t}Bu)

[Ni(p-q^{6,7}dt^{R1,R2})] ($R^1 = R^2$ = Me, Et, Ph and R^1 = H, R^2 = ^{t}Bu, Figure 2.13) were synthesised using the same approach adopted for the syntheses of [Ni(p-qdt^{R1,R2})] (Section 2.4.2). [Ni(p-q^{6,7}dt^{R1,R2})] ($R^1 = R^2$ = Me, Et, Ph and R^1 = H, R^2 = ^{t}Bu) were fully characterised by ^{1}H-NMR and ^{13}C-NMR spectroscopies, mass spectrometry and their purities confirmed by elemental analyses. The ^{1}H-NMR spectra of [Ni(p-q^{6,7}dt^{R1,R2})] ($R^1 = R^2$ = Et; R^1 = H, R^2 = ^{t}Bu) are well resolved suggesting that these complexes are diamagnetic, consistent with the Ni^{II} centre being coordinated in a square planar geometry. In contrast, the ^{1}H-NMR spectra of [Ni(p-q^{6,7}dt^{R1,R2})] ($R^1 = R^2$ = Me or Ph) possess broad features, similar to those observed for [Ni(p-qdt^{R1,R2})] ($R^1 = R^2$ = Me and R^1 = H, R^2 = ^{t}Bu) (Section 2.4.2), suggesting that these complexes

may be paramagnetic, or these features may be due to low solubility in the deuterated solvents tested (eg. CH_2Cl_2 and $(CD_3)_2SO$).

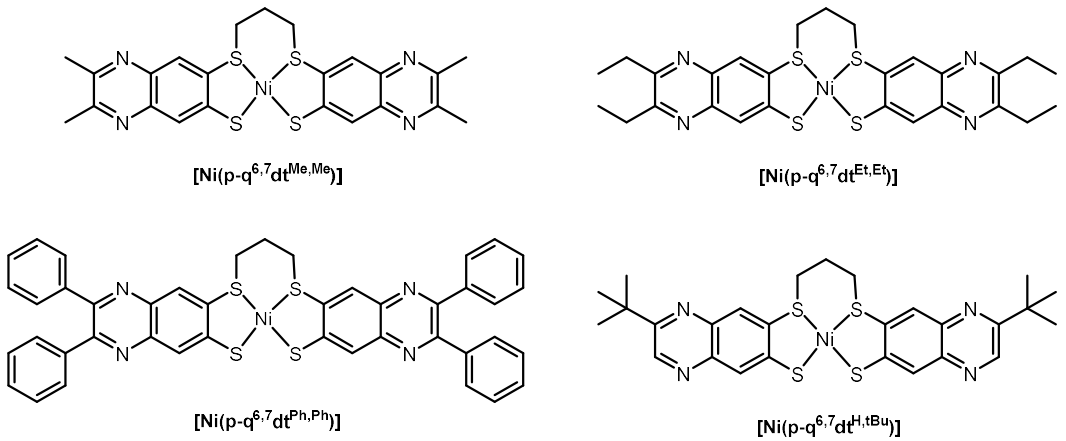


Figure 2.14: [Ni(p-$q^{6,7}dt^{R1,R2}$)] (R^1 = R^2 = Me, Et, Ph and R^1 = H, R^2 = ^{t}Bu).

^{1}H-NMR and ^{13}C-NMR spectroscopies, mass spectrometry and cyclic voltammetric studies also suggest that [Ni(p-$q^{6,7}dt^{R1,R2}$)] (R^1 = R^2 = Me, Et, Ph and R^1 = H, R^2 = ^{t}Bu) are stable as solids and in CH_2Cl_2 solution after exposure to air for one week.

2.5 The single crystal X-ray structures of [Ni(p-$q^{6,7}dt^{Et,Et}$)] and [Ni(p-$q^{6,7}dt^{H,tBu}$)] and [Ni(L^A)]

Single crystals of [Ni(p-$q^{6,7}dt^{Et,Et}$)] and [Ni(p-$q^{6,7}dt^{H,tBu}$)], suitable for X-ray crystallography, were obtained from the diffusion of methanol into solutions of the complexes in CH_2Cl_2. The complexes were isolated as orange plates and orange blocks, respectively. The X-ray crystal structures of [Ni(p-$q^{6,7}dt^{Et,Et}$)] [Ni($q^{6,7}dt^{H,tBu}$)] are shown in Figures 2.15 and 2.17, respectively, and selected bond lengths and angles are presented in Table 2.3, together with those for [Ni(L^A)].[21]

Table 2.3: Comparison of selected bonds lengths and bond angles in [Ni(p-$q^{6,7}dt^{R1,R2}$)] (R^1 = R^2 = Et, R^1 = H, R^2 = ^{t}Bu) and [Ni(L^A)].[21]

Bond Length /Å	**[Ni(p-$q^{6,7}dt^{Et,Et}$)]**	**[Ni(p-$q^{6,7}dt^{H,tBu}$)]**	**[Ni(L^A)]**
Ni(1)-S(1)	2.172(16)	2.161(4)	2.166 (2)
Ni(1)-S(2)	2.174(16)	2.178(4)	2.162(2)
Ni(1)-S(3)	2.170(16)	2.168(5)	2.175(2)
Ni(1)-S(4)	2.173(17)	2.172(4)	2.175(2)
Bond angle /º			
S(1)-Ni(1)-S(2)	91.9(6)	91.36(17)	92.3(1)
S(2)-Ni(1)-S(3)	87.3(6)	89.16(17)	90.9(1)
S(3)-Ni(1)-S(4)	91.8(6)	91.19(16)	89.9(1)
S(4)-Ni(1)-S(1)	88.9(6)	88.30(16)	88.0(1)
S(1)-Ni(1)-S(4)	177.81(7)	179.4(2)	173.48(8)
S(2)-Ni(1)-S(3)	177.42(7)	179.46(19)	169.23(8)

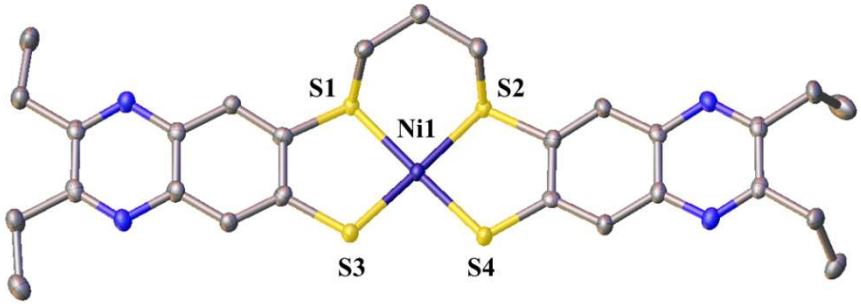


Figure 2.15: Molecular structure of [Ni(p-$q^{6,7}dt^{Et,Et}$)] with selective atom labelling. The H atoms are omitted for clarity.

[Ni(p-$q^{6,7}dt^{Et,Et}$)] crystallizes in the orthorhombic space group pbca. The Ni^{II} centre is coordinated in a distorted square planar geometry to four S donors derived from the p-$q^{6,7}dt^{Et,Et}$ ligand . The Ni-S bond distances are not significantly different from one another (average Ni-S distance = 2.172 Å) and the acute S-Ni-S bond angles range between 87.3(6) – 91.9(6)º.

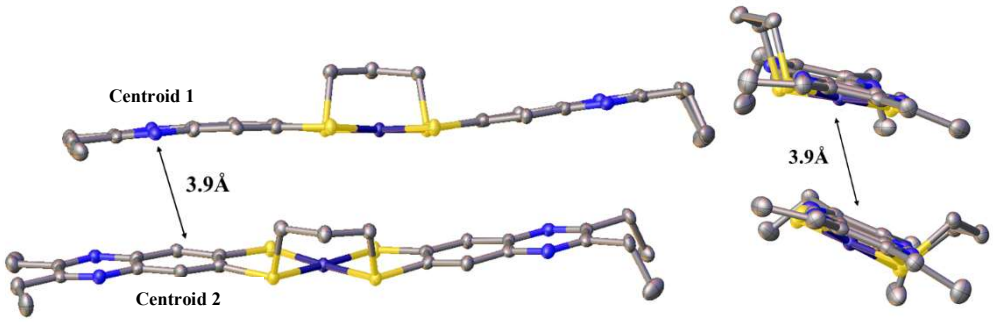


Figure 2.16: The molecular packing in the crystal structure of [Ni(p-$q^{6,7}dt^{Et,Et}$)].

The packing of the molecules of [Ni(p-$q^{6,7}dt^{Et,Et}$)] within the crystal is shown in Figure 2.16. The quinoxaline rings occupy approximately parallel planes with a plane centroid1-to-centroid2 angle of 10.7(2)° and a plane centroid-to-centroid distance of 3.958(3) Å, suggesting that π-π interactions are present in a staggered face-to-face configuration.

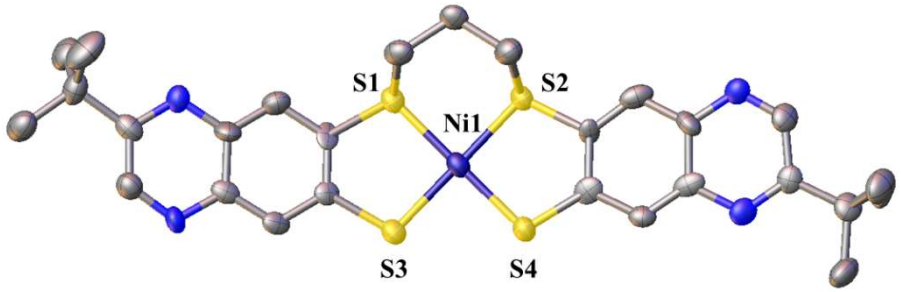


Figure 2.17: The molecular structure of [Ni(p-$q^{6,7}dt^{H,tBu}$)$_2$] with selective atom labelling. The H atoms are omitted for clarity.

[Ni(p-$q^{6,7}dt^{H,tBu}$)$_2$] crystallizes in the monoclinic space group $P2_1/c$. As in [Ni(p-$q^{6,7}dt^{Et,Et}$)], the Ni^{II} centre is coordinated by four S-donors derived from the p-$q^{6,7}dt^{H,tBu}$ ligand in a distorted square planar geometry. The Ni-S bond distances range between 2.161(4) - 2.178(4) Å and the acute S-Ni-S bond angles range between 88.30(16) and 91.36(17)°.

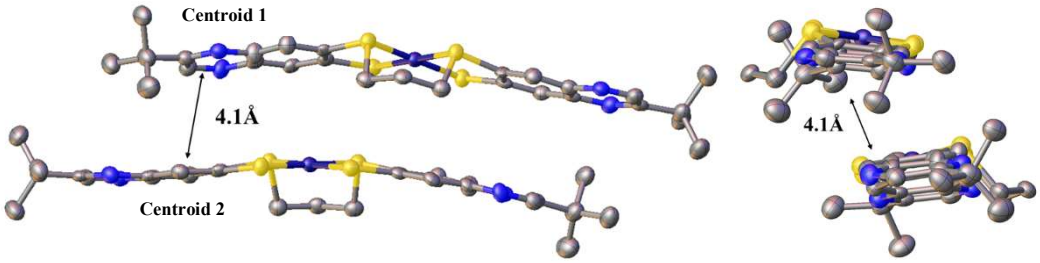


Figure 2.18: Molecule packing in the crystal structure of [Ni($q^{6,7}dt^{tBu}$)$_2$].

The packing of the [Ni(p-$q^{6,7}dt^{H,tBu}$)] molecules in the solid state (Figure 2.18) is similar to that exhibited in the solid state structure of [Ni(p-$q^{6,7}dt^{Et,Et}$)] (Figure 2.16) and involves staggered face-to-face π-π interactions, where the plane centroid1-to-centroid2 angle is 10.6(5)° and the distance is 4.101(8) Å.

The single crystal X-ray structure of [Ni(L^A)] was obtained through diffusion of methanol to a concentrated solution of [Ni(L^A)] in CH_2Cl_2, is shown in Figure 2.19

and selected bond lengths and angles are presented in Table 2.3.[21] The metrical parameters that describe the coordination sphere about the Ni^{II} centre in [Ni(L^A)] are essentially indistinguishable from those of [Ni(p-$q^{6,7}dt^{Et,Et}$)] and [Ni(p-$q^{6,7}dt^{H,tBu}$)] (Table 2.3).

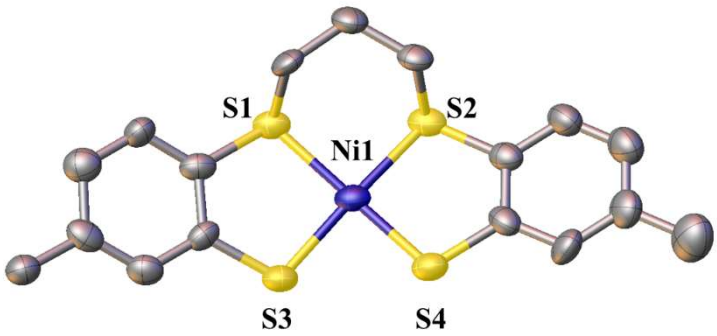


Figure 2.19: The molecular structure of [Ni(L^A)] with selective atom labelling. The H atoms are omitted for clarity.

Wang *et al.* have reported the reaction of [Ni(L^A)] with $Fe_3(CO)_{12}$ to form [Ni(L^A)$Fe_2(CO)_6$].[4] Thus, the close correspondence between the geometries of [Ni(L^A)], [Ni(p-$q^{6,7}dt^{Et,Et}$)] and [Ni(p-$q^{6,7}dt^{H,tBu}$)] would suggest that the [Ni(p-$q^{6,7}dt^{Et,Et}$)] and [Ni(p-$q^{6,7}dt^{H,tBu}$)] precursors may react with $Fe_3(CO)_{12}$ in an analogous manner to [Ni(L^A)] to generate the analogous [Ni(p-$q^{6,7}dt^{R1,R2}$)$Fe_2(CO)_6$] ($R^1 = R^2 = Et$; $R^1 = H$, $R^2 = {}^tBu$) complexes. This assumes that the reactivity of each [Ni(p-$q^{6,7}dt^{Et,Et}$)] and [Ni(p-$q^{6,7}dt^{H,tBu}$)] with $Fe_3(CO)_{12}$ is controlled primarily by the geometry about the Ni^{II} centre.

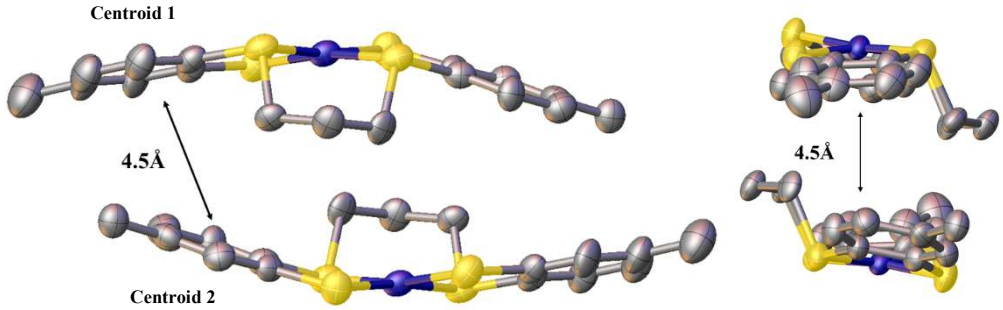


Figure 2.20: The molecular packing in the crystal structure of [Ni(L^A)].

The packing of the molecules of [Ni(L^A)] in the solid state structure (Figure 2.20) shows that the propane bridge components point inward, and that the Ni centres are bowed away from one another. The phenyl plane centroid1-to-centroid2 angle of 28.8237(18)° and phenyl plane centroid1-to-centroid2 distance of 4.53235(18) Å suggest that the phenyl rings in [Ni(L^A)] interact through weak π-π interactions in a

staggered face-to-face configuration. [Ni(p-$q^{6,7}dt^{Et,Et}$)] and [Ni(p-$q^{6,7}dt^{H,tBu}$)] appear to possess stronger π-π interactions in the solid state as revealed by their centroid1-to-centroid2 angles and distances (10.7(2) º and 3.958(3) Å, 10.6(5) º and 4.101(8) Å for [Ni(p-$q^{6,7}dt^{Et,Et}$)] and [Ni(p-$q^{6,7}dt^{H,tBu}$)], respectively). This observation may explain the higher solubility of [Ni(L^A)] in common solvents relative to the solubilities of [Ni(p-$q^{6,7}dt^{Et,Et}$)] and [Ni(p-$q^{6,7}dt^{H,tBu}$)].

We also attempted to structurally characterise [Ni(p-$q^{6,7}dt^{R1,R2}$)] (R^1 = R^2 = Me or Ph) by X-ray crystallography, but attempts to prepare crystalline material of suitable quality were unsuccessful.

2.6 Cyclic Voltammetric studies

2.6.1 Cyclic Voltametric studies of [Ni(L^A)]

The cyclic voltammogram of [Ni(L^A)] has been reported previously but has not been investigated in detail.[4,21] Electrochemical measurements were performed on [Ni(L^A)] to allow for a direct comparison with the new complexes reported in this thesis. The cyclic voltammogram of a 1 mM solution of [Ni(L^A)] was recorded at 293 K under Ar in CH_2Cl_2 containing 0.4 M [N^nBu_4][BF_4] (Figure 2.20). A full description of the cyclic voltammetry experiment is given in the Appendix.

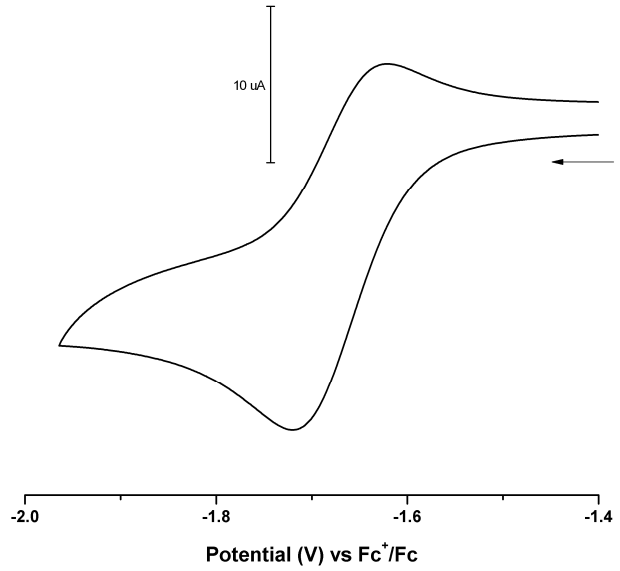


Figure 2.21: The reduction process for [Ni(L^A)] recorded at 100 mVs^{-1} in CH_2Cl_2 solution containing 0.4 M [N^nBu_4][BF_4] at 293 K.

[Ni(L^A)] exhibits a reduction process at $E_{1/2}$ = -1.66 V *vs* Fc^+/Fc with a return oxidation wave for which I_p^a decreases at slower scan rates, whist at higher scan rates a linear relationship between I_p^a and the square root of the scan rate emerges. Thus, the process at $E_{1/2}$ = -1.66 V *vs* Fc^+/Fc may be viewed as being quasireversible. A broad oxidation at -0.75 V *vs* Fc^+/Fc that is associated with the reduction also develops as the scan rate decreases to 50 mVs^{-1} suggesting that an EC process operates at these lower scan rates. The reduction at $E_{1/2}$ = -1.66 V versus Fc^+/Fc is assigned to a formal $Ni^{II/I}$ couple by comparison with the electrochemical data for [Ni{1,3-bis(2-mercaptophenylthio)-2,2-dimethylpropane}], which shows a quasi-reversible $Ni^{II/I}$ reduction process at $E_{1/2}$= - 0.91 V versus NHE.[4,22]

2.6.2 Cyclic voltammetric studies of [Ni(p-$q^{6,7}dt^{R1,R2}$)] ($R^1 = R^2$ = Me, Et, Ph; R^1 = H, R^2 = ^{t}Bu)

The cyclic voltammograms of 1 mM solutions [Ni(p-$q^{6,7}dt^{R1,R2}$)] ($R^1 = R^2$ = Me, Et, Ph and R^1 = H, R^2 = ^{t}Bu) were recorded at 293 K under Ar in CH_2Cl_2 solutions containing 0.4 M [N^nBu_4][BF_4]. The electrochemical data derived from these cyclic voltammograms is presented in Table 2.4.

Table 2.4: Potentials V *vs* Fc^+/Fc of the reduction processes for [Ni(L^A)] an [Ni(p-$q^{6,7}dt^{R1,R2}$)] (R_1 = R_2 = Me, Et, Ph and R_1 = H, R_2 = ^{t}Bu measured at 100 mVs^{-1}

Complex	[Ni(L^A)]	[Ni(p-$q^{6,7}dt^{Et,Et}$]	[Ni(p-$q^{6,7}dt^{H,tBu}$)]	[Ni(p-$q^{6,7}dt^{Me,Me}$)]	[Ni($q^{6,7}dt^{Ph,Ph}$)]
$E_{1/2}$	-1.66	-1.47	-1.45	-	-
E_p^c	-1.72	-1.51	-1.51	-1.42	-1.43

The cyclic voltammograms of [Ni(p-$q^{6,7}dt^{Me,Me}$)] and [Ni(p-$q^{6,7}dt^{Ph,Ph}$)] are similar and exhibit an irreversible reduction process at E_p^c = -1.42 V and -1.43 V *vs* Fc^+/Fc, respectively. Given the irreversible nature of these processes these compounds were not investigated further.

The cyclic voltammograms recorded for [Ni(p-$q^{6,7}dt^{Et,Et}$)] and [Ni(p-$q^{6,7}dt^{H,tBu}$)] are shown in Figures 2.22. [Ni(p-$q^{6,7}dt^{Et,Et}$)] has a electrochemical process at $E_{1/2}$ = -1.47 V *vs* Fc^+/Fc which exhibits some reversibility at faster scan rates. An oxidation process develops at E_p^a = -0.94 V *vs* Fc^+/Fc as the scan rate decreases that is associated with the reduction process with some reversibility at faster scan rates at $E_{1/2}$ = -1.47 V *vs* Fc^+/Fc. [Ni(p-$q^{6,7}dt^{H,tBu}$)], similar electrochemical behaviour to [Ni(p-$q^{6,7}dt^{Et,Et}$)] and possesses reduction process at $E_{1/2}$ = -1.45 V *vs* Fc^+/Fc with a

broad oxidation associated with the reduction at E_p^a = -0.81 *vs* Fc^+/Fc that develops at lower scan rates. Overall, [Ni(p-$q^{6,7}dt^{H,tBu}$)], [Ni(p-$q^{6,7}dt^{Et,Et}$)] and [Ni(L^A)] exhibit similar electrochemistry and possess a reduction process assigned to a formal $Ni^{II/I}$ couple that occurs between -1.66 and -1.45 V *vs* Fc^+/Fc.

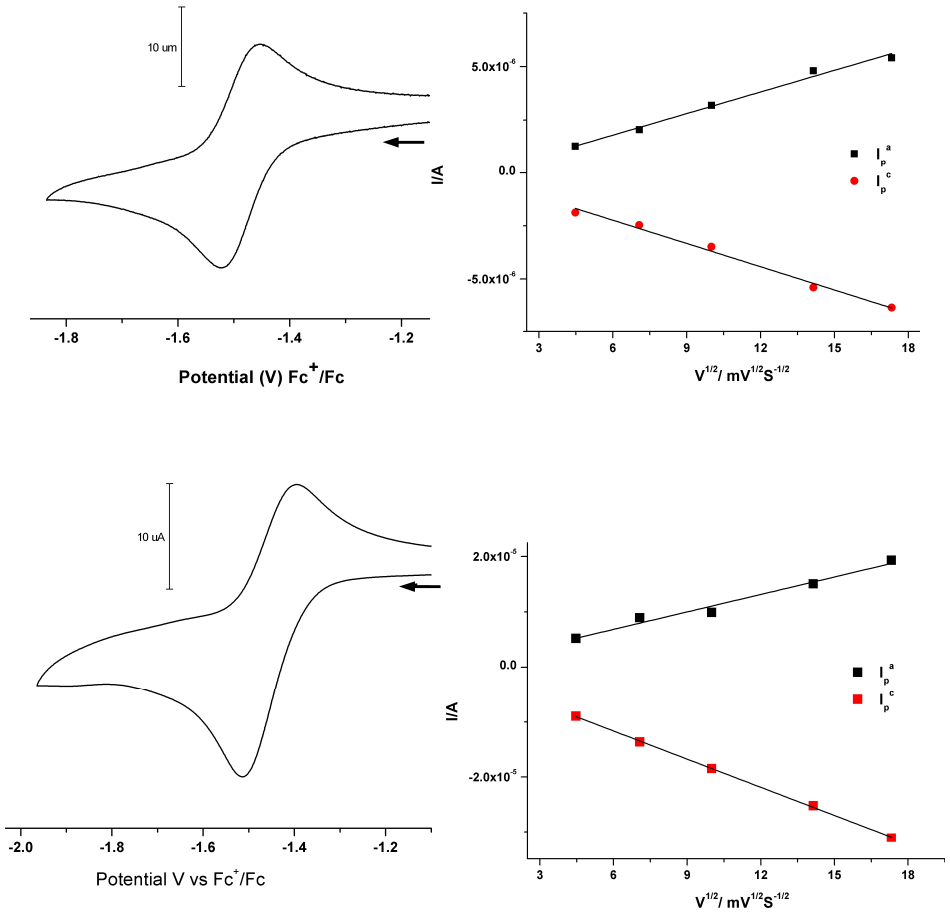


Figure 2.22: Top left: The cyclic voltammogram of [Ni(p-$q^{6,7}dt^{Et,Et}$)], Bottom left: The cyclic voltammogram of [Ni(p-$q^{6,7}dt^{H,tBu}$)] recorded at 100 mVs^{-1} in CH_2Cl_2 solution containing 0.4 M [N^nBu_4][BF_4] at 297 K. Right: Plots of I_p vs. $v^{1/2}$ for the reduction processes.

2.7 Spectroelectrochemistry of [Ni(p-$q^{6,7}dt^{R1,R2}$)] ($R^1 = R^2$ = Et, R^1 = H, R^2 = ^{t}Bu)

The changes in UV/vis spectra of 1 mM solutions of [Ni(p-$q^{6,7}dt^{Et,Et}$)] and [Ni(p-$q^{6,7}dt^{H,tBu}$)] in CH_2Cl_2 with 0.4 M [N^nBu_4][BF_4] as supporting electrolyte at 253 K, were monitored during electrolysis at -1.55 V *vs* Fc^+/Fc (Figure 2.23, Table 2.5).

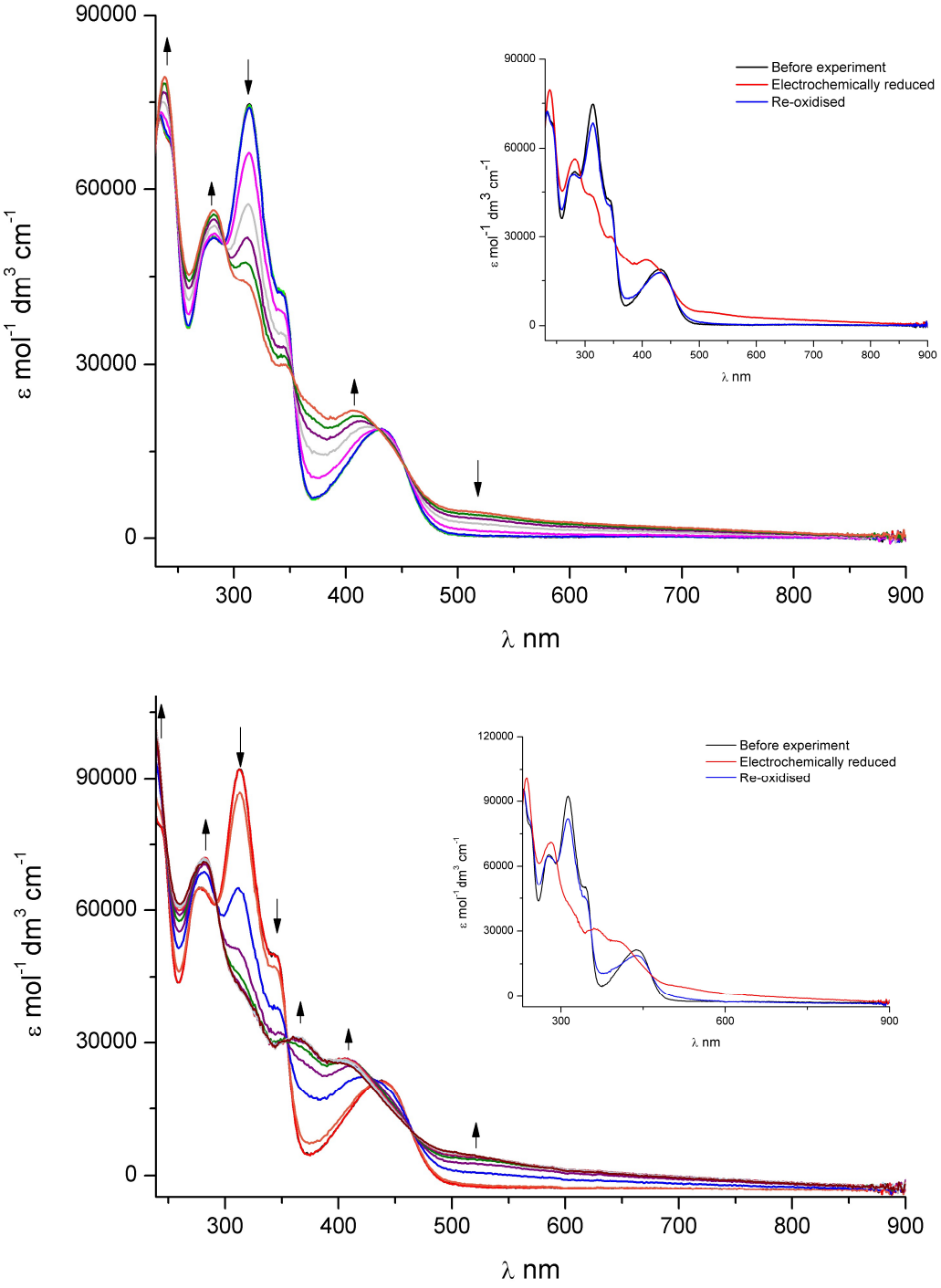


Figure 2.23: Sequential UV/vis spectra recorded during the one electron reduction of [Ni(p-$q^{6,7}dt^{Et,Et}$)] (top) and [Ni(p-$q^{6,7}dt^{H,tBu}$)] (bottom) in CH_2Cl_2 solution at 253 K containing 0.4 M [N^nBu_4][BF_4] as supporting electrolyte. The insets show the initial spectrum (black), the spectrum of the reduced species (red) and the final spectrum after re-oxidation (blue).

The spectral changes that occur during the electrolysis of solutions of [Ni(p-$q^{6,7}dt^{Et,Et}$)] and [Ni(p-$q^{6,7}dt^{H,tBu}$)] are similar. Both show decreases in the intensities of the absorptions bands associated with [Ni(p-$q^{6,7}dt^{Et,Et}$)] and [Ni(p-$q^{6,7}dt^{H,tBu}$)],

respectively and the growth of new bands at 232, 316, 351 and 408 nm associated with the formation of $[Ni(p\text{-}q^{6,7}dt^{Et,Et})]^-$ and $[Ni(p\text{-}q^{6,7}dt^{H,tBu})]^-$, respectively. Given the intensities of each band (Table 2.7) it is likely that each band results from ligand-to-metal charge transfer (LMCT) between orbitals of significant S- and Ni-character. However, we cannot rule out the presence of weaker, underlying bands resulting from transitions within the ligand-field manifold or overlaps with transitions that are localised on the 6,7-quinoxaline fragments. The presence of isobestic points at 252, 298, 355, 428 and 451nm (Table 2.7) for $[Ni(p\text{-}q^{6,7}dt^{Et,Et})]$ indicates that the reduction of $[Ni(p\text{-}q^{6,7}dt^{Et,Et})]$ proceeds directly without the formation of long-lived intermediates. The reduction of $[Ni(p\text{-}q^{6,7}dt^{H,tBu})]$ is also associated with isobestic points at 250, 298, 353 and 465nm. However, a point at 429 nm in the UV/vis spectra of $[Ni(p\text{-}q^{6,7}dt^{H,tBu})]$, corresponding to the isobestic point at 428 nm for $[Ni(p\text{-}q^{6,7}dt^{Et,Et})]$, is not isosbestic. Thus, it is uncertain if $[Ni(p\text{-}q^{6,7}dt^{H,tBu})]$ forms $[Ni(p\text{-}q^{6,7}dt^{H,tBu})]^-$ without proceeding *via* an intermediate species. The electrochemical re-oxidation of $[Ni(p\text{-}q^{6,7}dt^{Et,Et})]^-$ and $[Ni(p\text{-}q^{6,7}dt^{H,tBu})]^-$ at 0.5 V *vs* Fc^+/Fc does not result in the complete regeneration of the UV/vis spectra of $[Ni(p\text{-}q^{6,7}dt^{Et,Et})]$ and $[Ni(p\text{-}q^{6,7}dt^{H,tBu})]$. Thus, the reduction processes are not wholly chemically reversible over the time scale of the experiment (*ca.* 60 minutes).

Table 2.5: The UV/vis absorbances of $[Ni(p\text{-}q^{6,7}dt^{R1,R2})]$ and $[Ni(p\text{-}q^{6,7}dt^{R1,R2})]^-$ ($R^1 = R^2 = Et$; $R^1 = H$, $R^2 = {}^tBu$) and the isobestic points recorded in CH_2Cl_2 / 0.4 M $[N^nBu_4][BF_4]$ solution at -20 ºC.

Complex	Wavelength /nm (extinction coefficient /$mol^{-1}dm^3cm^{-1}$)	Isobestic points (nm)
$[Ni(p\text{-}q^{6,7}dt^{Et,Et})]$	241 (71000), 282 (506000), 314 (40700), 346 (41100) and 433 (18000)	252, 298, 355, 428 and 451
$[Ni(p\text{-}q^{6,7}dt^{Et,Et})]^-$	232(78600), 282 (55500), 316 (42800), 351(29700) and 408 (21900).	
$[Ni(p\text{-}q^{6,7}dt^{H,tBu})]$	238(91000), 277(64200), 314 (91000), 348 (49200) and 440 (21300)	250, 298, 353 and 465
$[Ni(p\text{-}q^{6,7}dt^{H,tBu})]^-$	240 (98800) , 282 (70400), 364 (31300) and 408 (24600)	

2.8 EPR Spectroscopy of $[Ni(p\text{-}q^{6,7}dt^{Et,Et})]^-$ and $[Ni(p\text{-}q^{6,7}dt^{H,tBu})]^-$

The X-band EPR spectra of electrochemically generated $[Ni(p\text{-}q^{6,7}dt^{Et,Et})]^-$ and $[Ni(p\text{-}q^{6,7}dt^{H,tBu})]^-$ were recorded at 77 K in CH_2Cl_2 solutions containing $[N^nBu_4][BF_4]$ (0.4 M). The frozen solution spectra are axial and may be simulated with identical spin Hamiltonian parameters $g_{11} = 2.217$ and $g_{22} = g_{33} = 2.061$ (Figure 2.24).

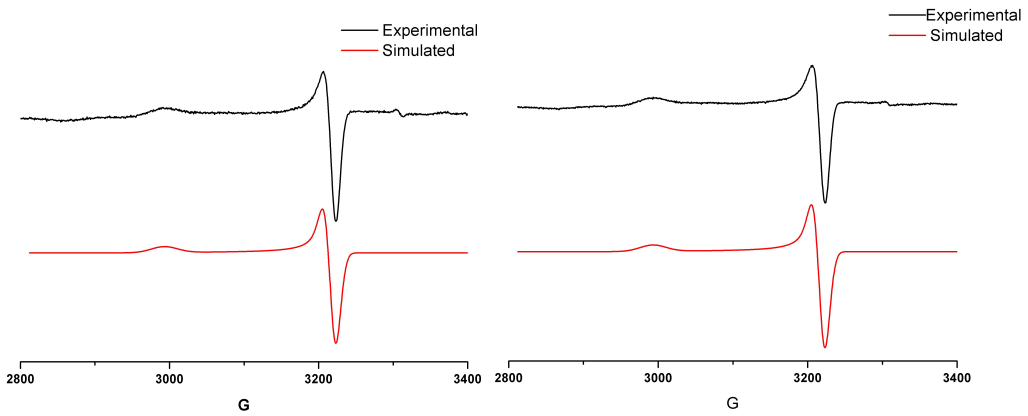


Figure 2.24: The X-band frozen solution spectrum of a) $[Ni(p\text{-}q^{6,7}dt^{Et,Et})]^-$ and b) $[p\text{-}Ni(q^{6,7}dt^{H,tBu})]^-$ in CH_2Cl_2 containing $[N^nBu_4][BF_4]$ (0.1 M) at 120 K (black), simulated spectrum (red). Spin Hamiltonian parameters g_{11} =2.217, $g_{22} = g_{33} = 2.061$, Gaussian linewidths of W_{11} =, W_{22} = and W_{33} = 10 G.

The axial EPR spectra of $[Ni(p\text{-}q^{6,7}dt^{Et,Et})]^-$ and $[Ni(p\text{-}q^{6,7}dt^{H,tBu})]^-$, where $g_{11} > g_{22} = g_{33}$, are consistent with a formal d^9 S = ½ Ni^I centre in which the single unpaired electron resides in a $d_{x^2-y^2}$ or d_{xy}-type orbital (depending on the definition of the xyz axes frame) that lies approximately in the NiS_4 plane. The large g-anisotropy implies that the unpaired electron is localised about the Ni centre and that there is little quinoxaline character in the SOMO. The frozen solution X-band EPR spectrum of $[Ni(L^A)Fe_2(CO)_6]^-$ is also axial, however, this spectrum possesses lower g-anisotropy with g_{11} = 2.099 and $g_{22} = g_{33}$ = 2.015,[4] which reflects significant differences in the nature of the SOMOs in $[Ni(p\text{-}q^{6,7}dt^{Et,Et})]^-$ and $[Ni(p\text{-}q^{6,7}dt^{H,tBu})]^-$, and $[Ni(L^A)Fe_2(CO)_6]^-$ (see Section 2.11).

2.9 Cyclic Voltammetric studies in the presence of TFA

Electrochemical experiments of $[Ni(L^A)Fe_2(CO)_6]$ in the absence and presence of trifluoroacetic acid (TFA) show that this complex catalyses the production of H_2.[23] The electrocatalytic production of H_2 by $[Ni(L^A)Fe_2(CO)_6]$ occurs at similar potentials to those for NiN_2S_2 macrocyclic complexes ($E_{1/2}$ = -0.43 to -0.78 V *vs.*

NHE; -0.83 to -1.18 V *vs*. Fc^+/Fc)[24] but at potentials that are *ca*. 900 mV more positive than those of (X)[$Fe^I(CO)_2PMe_3]_2$ [X = $2EtS^-$, edt^-, pdt^-, $xyldt^-$; *e.g*. (m-pdt)[$Fe^I(CO)_2PMe_3]_2$, $E_{1/2}$ = -1.85 V *vs*. NHE; -2.25 V *vs*. Fc^+/Fc][25] and at comparable rates of turnover (*ca*. 6–30 $ToNh^{-1}$). [$Ni(L^A)Fe_2(CO)_6$] represents the first example of a [NiFe] cluster containing biologically relevant ligands that supports the production of H_2 at comparable rates of turnover to those of analogues of the active sites of the [Fe]-only hydrogenases. In addition, [$Ni(L^A)Fe_2(CO)_6$] catalyses the production of H_2 at potentials that are more positive (*ca*. 900 mV) than (μ-pdt)[$Fe^I(CO)_2L]_2$ and which lie close to the potential window of the $Ni^{II/I}$ couples of mononuclear NiN_2S_2 macrocyclic complexes. Despite the extensive characterisation of [$Ni(L^A)Fe_2(CO)_6$], the catalytic activity of the Ni^{II} subunit [$Ni(L^A)$] towards H_2 production has not been investigated in detail. In the following sections we investigate the potential catalytic activities of [$Ni(L^A)$], [Ni(p-$q^{6,7}dt^{Et,Et}$)] and [Ni(p-$q^{6,7}dt^{H,tBu}$)], and compare them to that of [$Ni(L^A)Fe_2(CO)_6$].

The catalytic activity of the complexes discussed within this thesis is assessed electrochemically by comparing the cyclic voltammograms in the absence and presence of TFA under the same conditions employed previously to determine the electrocatalytic production of H_2 by [$Ni(L^A)Fe_2(CO)_6$].[23] A sealed cyclic voltammetric cell was used to ensure constant volume of reaction solution and fixed concentration of catalyst with CH_2Cl_2 as solvent. A control cyclic volumetric experiment was carried out with a solution of TFA (50 mM) and CH_2Cl_2 with 0.4 M [N^nBu_4][BF_4] at 298 K under Ar which showed that TFA did not give a current response within the window scanned for the complexes discussed in this thesis. A full description of the cyclic voltammetry in the presence of TFA experiment is given in the Appendix.

2.9.1 Cyclic Voltammetric studies of [$Ni(L^A)$] in the presence of TFA

Cyclic voltammograms for solutions of [$Ni(L^A)$] with the additions of known concentrations of TFA were recorded following the protocols developed previously in the group for the study of [$Ni(L^A)Fe_2(CO)_6$].[23] The cyclic voltammograms of [$Ni(L^A)$] in CH_2Cl_2 with 0.4 M [N^nBu_4][BF_4] at 298 K under Ar and with varying concentrations of TFA are shown in Figure 2.25.

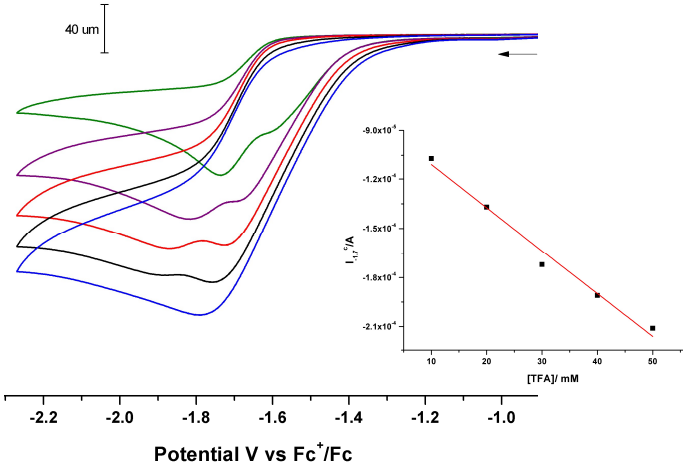


Figure 2.25: Cyclic voltammograms of [Ni(L^A)](1 mM) in CH_2Cl_2 solution at 293 K containing [N^nBu_4][BF_4] (0.4 M) and TFA at concentrations of 10 mM (green), 20 mM (purple), 30 mM (red), 40 mM (black) and 50 mM (blue).Inset: Plot of $I_{-1.7}{}^c$ *vs*. [TFA] observed in the cyclic voltammograms (100 mVs^{-1}) of [Ni(L^A)].

The cyclic voltammogram of [Ni(L^A)] in the absence of TFA (Section 2.6.1) exhibits a scan-rate dependent reduction process at -1.66 V *vs*. Fc^+/Fc. Upon the addition of TFA there is a relatively large increase in cathodic current. In addition, in the presence of TFA the return anodic peak is depressed. This observation is consistent with the removal of [Ni(L^A)]$^-$ from the diffusion layer by a mechanism other than heterogeneous electron transfer.[21,23] A plot of $I_{-1.7}{}^c$ *vs*. [TFA], (Figure 2.25) from the 100 mVs^{-1} cyclic voltammetric scans shows a linear increase in cathodic current with the increase of [TFA], and a plot of the cathodic current normalised to $\nu^{1/2}$ *vs*. scan rate (Figure 2.26) shows an increase in magnitude of $I_{-1.7}{}^c\nu^{-1/2}$ with decreasing ν. Taken together these data suggest that a catalytic mechanism operates that involves an irreversible chemical reaction that follows essentially reversible charge transfer.[26] The data is consistent with a mechanism involving the electrochemical reduction of [Ni(L^A)] to [Ni(L^A)]$^-$ that then reacts with H^+ to generate [Ni(L^A)] and H_2. A similar mechanism has been proposed for [Ni(L^A)$Fe_2(CO)_6$] that exhibits a similar voltammetric profile but at potentials -1.33 V *vs* Fc^+/Fc. [23]

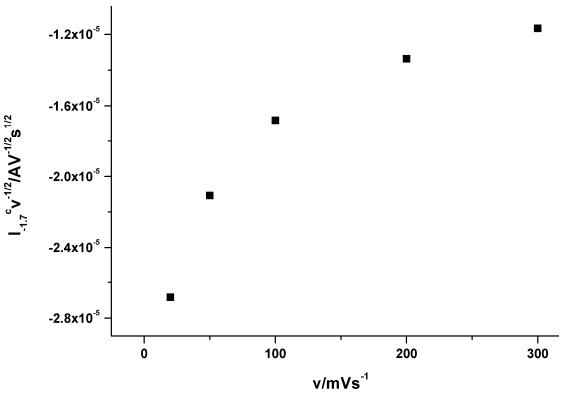


Figure 2.26: Plot of $I_{1,7}{}^{c}v^{-1/2}$ *vs*. ν for Ni(L^A) from cyclic voltammetric data at [TFA] = 50 mM.

2.9.2 Cyclic Voltammetric studies of [Ni(p-$q^{6,7}dt^{Et,Et}$)] and [Ni(p-$q^{6,7}dt^{H,tBu}$)] in the presence of TFA

The cyclic voltammograms of [Ni(p-$q^{6,7}dt^{Et,Et}$)] and [Ni(p-$q^{6,7}dt^{H,tBu}$)] were recorded in CH_2Cl_2 solution with 0.4 M [N^nBu_4][BF_4] at 298 K under Ar with increasing concentration of TFA (Figures 2.27 and 2.28).

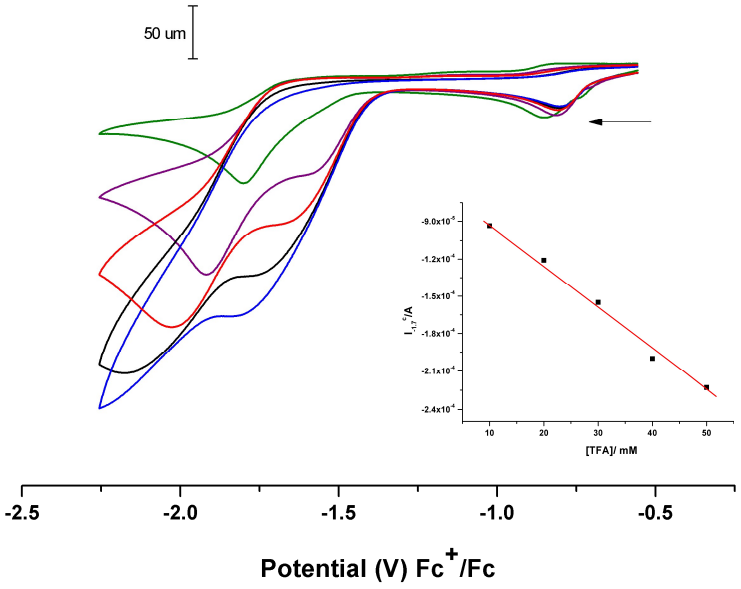


Figure 2.27: Cyclic voltammograms of [Ni(p-$q^{6,7}dt^{Et,Et}$)] (1 mM) in CH_2Cl_2 solution at 293 K containing [N^nBu_4][BF_4] (0.4 M) and TFA at concentrations of 10 mM (green), 20 mM (purple), 30 mM (red), 40 mM (black) and 50 mM (blue). Inset: Plot of $I_{1,7}{}^{c}$ *vs*. [TFA] observed in the cyclic voltammograms (100 mVs^{-1}) of [Ni(p-$q^{6,7}dt^{Et,Et}$)] .

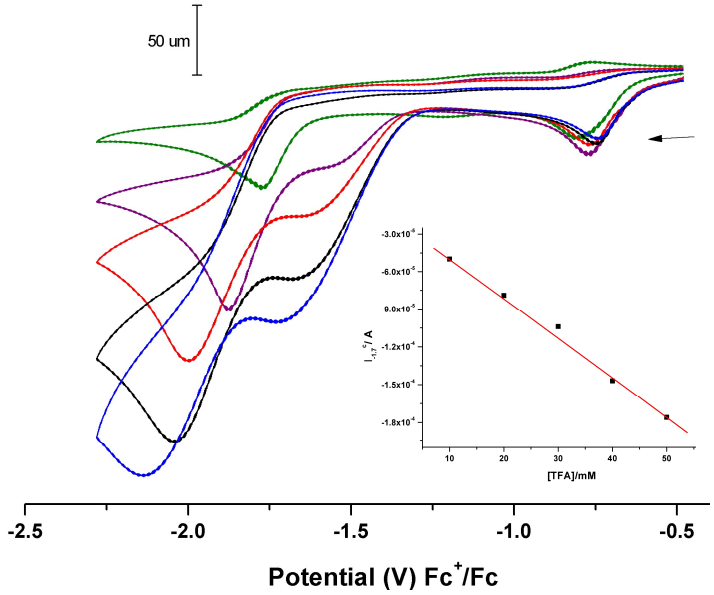


Figure 2.28: Cyclic voltammograms of [Ni(p-$q^{6,7}dt^{H,tBu}$)] (1 mM) in CH_2Cl_2 solution at 293 K containing [N^nBu_4][BF_4] (0.4 M) and TFA at concentrations of 10 mM (green), 20 mM (purple), 30 mM (red), 40 mM (black) and 50 mM (blue). Inset: Plot of $I_{-1.7}^c$ *vs.* [TFA] observed in the cyclic voltammograms (100 mVs^{-1}) of [Ni(p-$q^{6,7}dt^{H,tBu}$)].

The cyclic voltammograms of [Ni(p-$q^{6,7}dt^{Et,Et}$)] and [Ni(p-$q^{6,7}dt^{H,tBu}$)] in the absence of TFA show a scan dependent reduction process with a return oxidation at $E_{1/2}$ = - 0.94 V and -0.81 V *vs.* Fc^+/Fc , respectively (Section 2.6.2). The addition of aliquots of TFA results in a step-wise increase in the I_p^c with a shift in the potential of the reduction process from -1.51 V *vs.* Fc^+/Fc in the absence of TFA to -1.7 *vs.* Fc^+/Fc in the presence of TFA. In addition, the anodic peak is depressed on the addition of TFA, which is consistent with the removal of [Ni(p-$q^{6,7}dt^{R1,R2}$)]$^-$ ($R^1 = R^2$ = Et; R^1 = H, R^2 = ^{t}Bu) from the diffusion layer by a mechanism other than heterogeneous electron transfer as for [Ni(L^A)]. Similarly, a plot of $I_{-1.7}^c$ *vs.* [TFA] shows a linear increase in cathodic current with the increase of [TFA] (Figure 2.28) and a plot of I_p^c normalised to $\nu^{1/2}$ *vs.* scan rate shows an increase in magnitude of $I_{-1.7}^c \nu^{-1/2}$ with decreasing ν (Figure 2.29). As for [Ni(L^A)] these data suggest a catalytic mechanism involving an irreversible chemical reaction that follows a reversible charge transfer and are consistent with the electrochemical generation of [Ni(p-$q^{6,7}dt^{R1,R2}$)]$^-$ that then reacts with H^+ to yield H_2.[26]

The cyclic voltammograms of [Ni(p-$q^{6,7}dt^{R1,R2}$)] ($R^1 = R^2$ = Et; R^1 = H, R^2 = ^{t}Bu) in the presence of TFA (Figures 2.27, 2.28) also exhibit a reduction process at

ca.- 0.75 V *vs* Fc^+/Fc. The I_p^c associated with this process does not appear to vary as [TFA] is increased compared to the variation of $I_{-1.7}^c$. Given that this feature is absent in the cyclic voltammograms of [Ni(L^A)] following the addition of TFA it appears likely that this feature is associated with the 6,7-quinoxaline rings in [Ni(p-$q^{6,7}dt^{R1,R2}$)] ($R^1 = R^2 = Et$; $R^1 = H$, $R^2 = {}^tBu$) and possibly with the protonation of these species at the N atom positions of these rings (see Section 2.11.1).

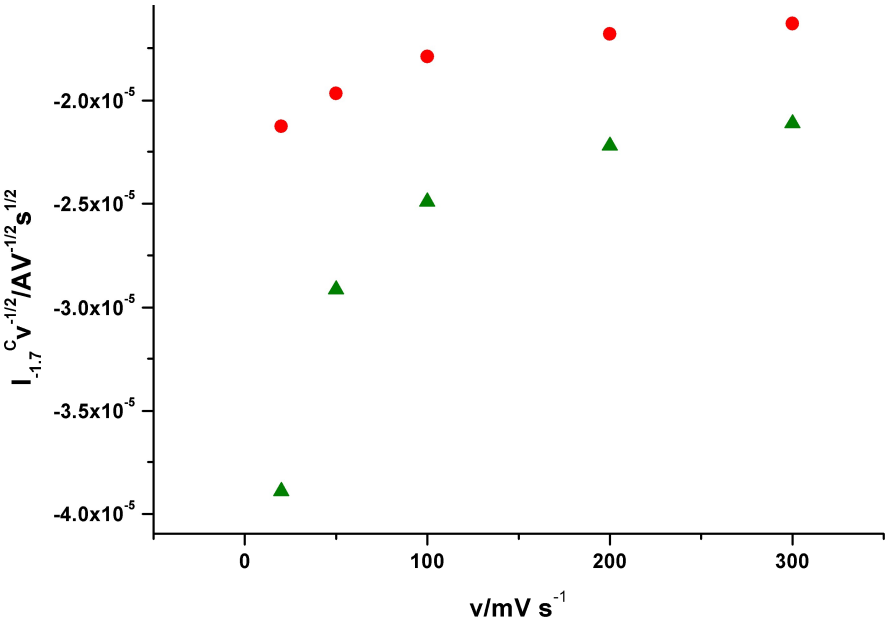


Figure 2.29: Plot of $I_{-1.7}^c v^{-1/2}$ *vs*. ν for [Ni(p-$q^{6,7}dt^{Et,Et}$)] (green) and [Ni(p-$q^{6,7}dt^{H,tBu}$)] (red) from the cyclic voltammetric data at [TFA] = 50 mM.

2.9.3 Comparison of the Cyclic Voltammetric studies of [Ni(p-$q^{6,7}dt^{Et,Et}$)], [Ni(p-$q^{6,7}dt^{H,tBu}$)] and [Ni(L^A)] in the presence of TFA

The catalytic activity of [Ni(p-$q^{6,7}dt^{Et,Et}$)], [Ni(p-$q^{6,7}dt^{H,tBu}$)] and [Ni(L^A)] were compared using a screening method developed previously within the group to compare the catalytic activity of similar [NiFe] compounds.[3] The cyclic voltammograms of the compounds at [TFA] = 0 were plotted as an internal calibration (Figure 2.30 inset). Since they have similar current responses in the absence of TFA therefore, variations in cathodic current upon addition of TFA must be due to variations in the catalytic activity. The cathodic currents at [TFA] = 50 mM for [Ni(p-$q^{6,7}dt^{Et,Et}$)], [Ni(p-$q^{6,7}dt^{H,tBu}$)] and [Ni(L^A)] are compared in Figure 2.30 and tabulated in Table 2.6.

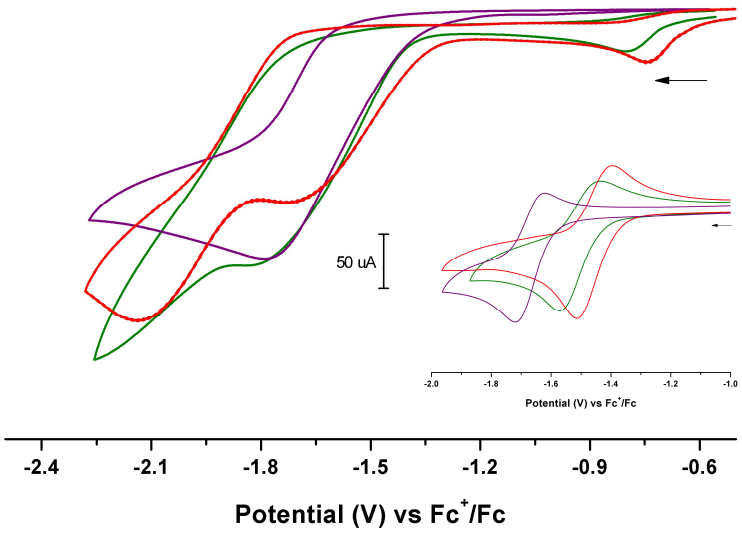


Figure 2.30: Comparison of cathodic current for [Ni(p-$q^{6,7}dt^{Et,Et}$)] (green), [Ni(p-$q^{6,7}dt^{H,tBu}$)] (red) and [Ni(L^A)] (purple) (1 mM) in CH_2Cl_2 at 293 K containing [N^nBu_4][BF_4] (0.4 M) and [TFA] = 50 (inset: [TFA] = 0, internal calibration).

Table 2.6: I_p^c at [TFA] = 50 mM for [Ni(p-$q^{6,7}dt^{Et,Et}$)] and [Ni(p-$q^{6,7}dt^{H,tBu}$)]

Complex	I_p^c (A x 10^{-4})
[Ni(p-$q^{6,7}dt^{Et,Et}$)]	-2.15
[Ni(p-$q^{6,7}dt^{H,tBu}$)]	-1.80
[Ni(L^A)]	-2.15

The cathodic current at [TFA] = 20 mM is greater for [Ni(p-$q^{6,7}dt^{Et,Et}$)] (-2.15 x 10^{-4} A) than [Ni(p-$q^{6,7}dt^{H,tBu}$)] (-1.80 x 10^{-4} A) but the same as that for [Ni(L^A)] (-2.15 x 10^{-4} A). Thus, for [Ni(p-$q^{6,7}dt^{Et,Et}$)] it appears that the incorporation of potential protonation sites at the N atoms of the pyrazine ring in the quinoxaline units has little effect on increasing the catalytic activity relative to [Ni(L^A)]. This observation suggests that the qdt ligand does not act as a proton relay site.

2.9.4 Comparison of Cyclic Voltammetric studies of [Ni(p-$q^{6,7}dt^{Et,Et}$)], [Ni(L^A)] and [Ni(L^A)$Fe_2(CO)_6$] in the presence of TFA

The catalytic activity of [Ni($q^{6,7}dt^{Et}$)$_2$], [Ni(L^A)] and [Ni(L^A)$Fe_2(CO)_6$] were compared following the same screening method employed in Section 2.9.3.[3] The cathodic currents at [TFA] = 50 mM for each complex are shown in Figure 2.31 and tabulated in Table 2.7. Cyclic voltammograms of the compounds at [TFA] = 0 were used for internal calibration and are shown in Figure 2.31 as an inset.

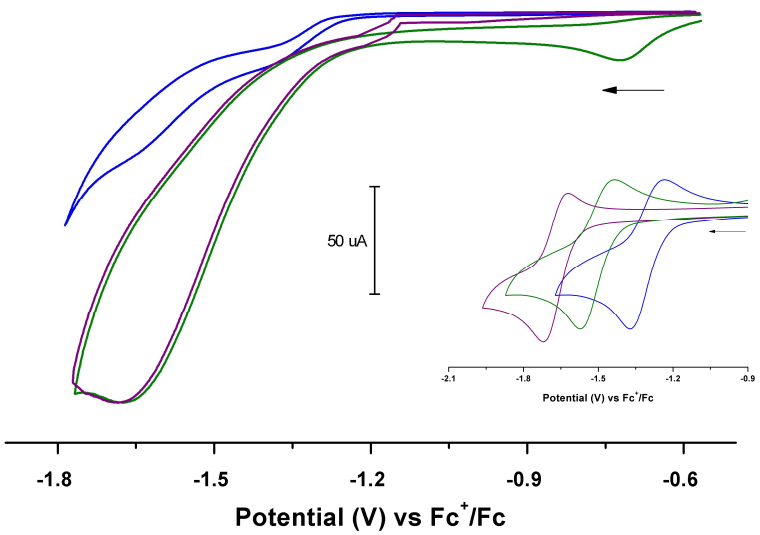


Figure 2.31: Comparison of cathodic current for [Ni(p-$q^{6,7}dt^{Et,Et}$)] (green) and [Ni(L^A)$_2$] (purple) and [Ni(L^A)$Fe_2(CO)_6$] (blue) (1 mM) in CH_2Cl_2 solutions at 293 K containing [N^nBu_4][BF_4] (0.4 M) and [TFA] = 50 (inset: [TFA] = 0, internal calibration).

Table 2.7: I_p^c at [TFA] = 50 mM for [Ni(p-$q^{6,7}dt^{Et,Et}$)], [Ni(L^A)] and [Ni(L^A)$Fe_2(CO)_6$] at -1.7 V *vs* Fc^+/Fc.

Complex	I_p^c (A x 10^{-4})
[Ni(L^A)]	-2.15
[Ni(L^A)$Fe_2(CO)_6$]	-0.73
[Ni($q^{6,7}dt^{Et}$)$_2$]	-2.15

The cathodic current at [TFA] = 50 mM at -1.7 V *vs* Fc^+/Fc, for [Ni(p-$q^{6,7}dt^{Et,Et}$)] and [Ni(L^A)] (-2.15 x 10^{-4} A) is larger than that for [Ni(L^A)$Fe_2(CO)_6$] (-0.73 x 10^{-4} A). This suggests that the mononuclear Ni^{II} complexes discussed in this Chapter have higher catalytic activity [Ni(L^A)$Fe_2(CO)_6$]. This is a somewhat surprising result given that nature employs a multinuclear [NiFe] centre in the [NiFe] hydrogenases and suggests that mononuclear Ni-complexes possessing a S-rich coordination sphere should not be overlooked as candidates as catalysts for H_2 production.

2.10 UV/vis spectroscopy of [Ni(p-$q^{6,7}dt^{Et,Et}$)] in the presence of TFA

The cyclic voltammograms of [Ni(p-$q^{6,7}dt^{Et,Et}$)], [Ni(p-$q^{6,7}dt^{H,tBu}$)] and [Ni(L^A)] demonstrated higher catalytic activity than [Ni(L^A)$Fe_2(CO)_6$]. Previous work within the group has shown that 6 M HCl can be used to displace the Ni^{II} centre to allow access to other transition metal complexes using the same ligand system. We therefore undertook preliminary UV/vis spectroscopic measurements on [Ni(p-$q^{6,7}dt^{Et,Et}$)] to (i) determine if there were any UV/vis spectroscopic changes between

solutions of [Ni(p-$q^{6,7}dt^{Et,Et}$)] in the absence or presence of TFA; (ii) assess the stability of [Ni(p-$q^{6,7}dt^{Et,Et}$)] in the presence of excess TFA.

The UV/vis spectra of [Ni($q^{6,7}dt^{Et,Et}$)$_2$] (1 mM) in CH_2Cl_2 in the absence of TFA, after 12 h following the addition of TFA ([TFA] = 50mM), and after the addition of triethylamine ([NEt_3] = 0.1 M) are shown in Figures 2.32 and 2.33.

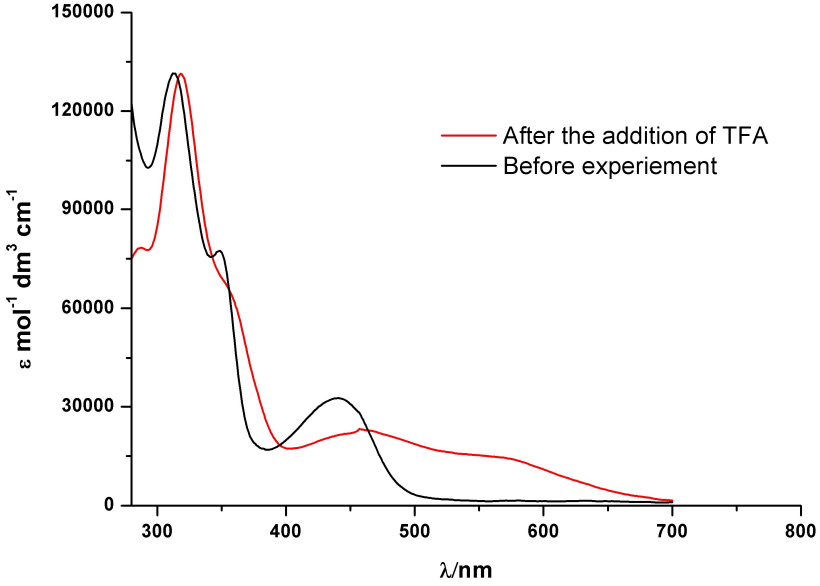


Figure 2.32: UV/vis spectra of [Ni(p-$q^{6,7}dt^{Et,Et}$)] recorded before the addition of TFA (black), the protonated species after the addition of TFA (red).

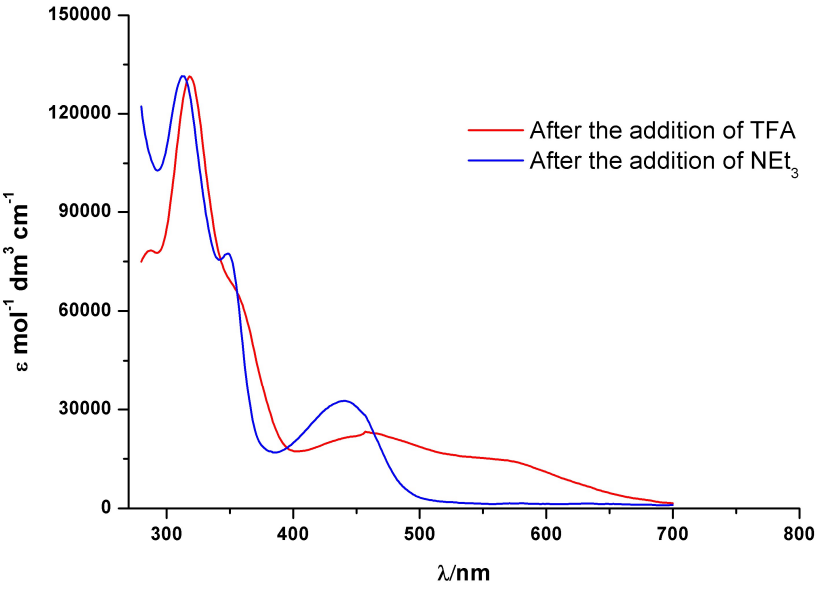


Figure 2.33: UV/vis spectra of [Ni(p-$q^{6,7}dt^{Et,Et}$)] recorded after the addition of TFA (red) and after the addition of triethylamine (blue).

Upon the addition of TFA there are decreases in the intensities of the absorption bands associated with [Ni(p-$q^{6,7}dt^{Et,Et}$)] at 350 nm (76600 $mol^{-1}dm^3cm^{-1}$) 441 nm (31500 $mol^{-1}dm^3cm^{-1}$) nm, and the shift of the band at 311 nm to 318 nm (130000 $mol^{-1}dm^3cm^{-1}$) and emergence of new bands at 464 nm (23400 $mol^{-1}dm^3cm^{-1}$) and 567 nm (15100 $mol^{-1}dm^3cm^{-1}$) were observed. The change in the UV/vis spectra are immediate and subsequent UV/Vis spectra recorded every 30 mins over 12 h remain invariant. The addition of trimethylamine ([NEt_3] = 0.1 M) regenerates the UV/vis spectrum of [Ni(p-$q^{6,7}dt^{Et,Et}$)]. These data suggest that [Ni(p-$q^{6,7}dt^{Et,Et}$)] may be protonated in a solution containing TFA and that this protonation may be reversed by the addition of NEt_3.

In order to assess the stability of [Ni(p-$q^{6,7}dt^{Et,Et}$)] and to confirm the Ni centre is not being displaced under acidic conditions. We treated a CH_2Cl_2 solution of [Ni(p-$q^{6,7}dt^{Et,Et}$)] (1 mM) with TFA or HCl ([TFA] = 50 mM, 2 M and [HCl] = 2 M and 6 M). These reaction mixtures were stirred for 2 h and then extracted with water or 10% nitric acid. We analysed the aqueous extractions by Inductively Coupled Plasma Optical Emission Spectroscopy (ICP-OES) to determine the degree of decomposition of [Ni(p-$q^{6,7}dt^{Et,Et}$)] under acidic conditions and the transfer of Ni content into an aqueous phase (Table 2.11). These results suggest that [Ni(p-$q^{6,7}dt^{Et,Et}$)] remains relatively stable up-to acid concentrations of 2 M, and that acid concentrations of 6 M are required to initiate significant decomposition of the complex.

Table 2.8: Ni content (ppm) in the aqueous washing of [Ni(p-$q^{6,7}dt^{Et,Et}$)] in CH_2Cl_2 with after the addition of TFA or HCl ([TFA] = 50 mM, 2 M and [HCl] = 2 M and 6 M) as determined by ICP-OES.

Acid concentration	Extraction medium	Ni content /ppm
[TFA] = 50 mM	water	0.2
[TFA] = 50 mM	10 % nitric acid	0.0
[TFA] = 2 M	water	0.8
[TFA] = 2 M	10 % nitric acid	1.0
[HCl] = 2 M	water	0.2
[HCl] = 2 M	10 % nitric acid	0.3
[HCl] = 6 M	water	19.8
[HCl] = 6 M	10 % nitric acid	21.1

2.11 DFT Studies

We have undertaken DFT calculations for [Ni(p-$q^{6,7}dt^{Et,Et}$)], [Ni(p-$q^{6,7}dt^{H,tBu}$)] and [Ni(L^A)] to provide a qualitative description of the structure and bonding within these complexes and to provide a framework to interpret the spectroscopic and electrochemical properties of [Ni(p-$q^{6,7}dt^{Et,Et}$)], [Ni(p-$q^{6,7}dt^{H,tBu}$)] and [Ni(L^A)]. Models of [Ni(p-$q^{6,7}dt^{Et,Et}$)], [Ni(p-$q^{6,7}dt^{H,tBu}$)] and [Ni(L^A)] were constructed from the experimentally determined crystallographic co-ordinates for [Ni(p-$q^{6,7}dt^{Et,Et}$)], [Ni(p-$q^{6,7}dt^{H,tBu}$)] and [Ni(L^A)] before being geometry optimised in the gas phase. A comparison of selected bond lengths and inter-bond angles obtained from the DFT calculations and X-ray crystallography for [Ni(p-$q^{6,7}dt^{Et,Et}$)], [Ni(p-$q^{6,7}dt^{H,tBu}$)] and [Ni(L^A)] are shown in Table 2.9 and the calculated structure of each are shown in Figure 2.34. The axis system used in the calculations places the x-axis along the bisector of the S(1)-Ni(1)-S(3) angle and the y-axis in the S(3)-Ni(1)-S(4) plane. The calculated structures broadly reproduce the experimental structures with the Ni-S distances being *ca.* 0.01Å greater in the calculated structures with the acute S-Ni-S bond angles being *ca.* 0.02º smaller. Thus, the similarity between the calculated and experimental geometries suggests that the DFT calculations at the BP86 level provide a reliable description of the electronic structures of [Ni(p-$q^{6,7}dt^{Et,Et}$)], [Ni(p-$q^{6,7}dt^{H,tBu}$)] and [Ni(L^A)].

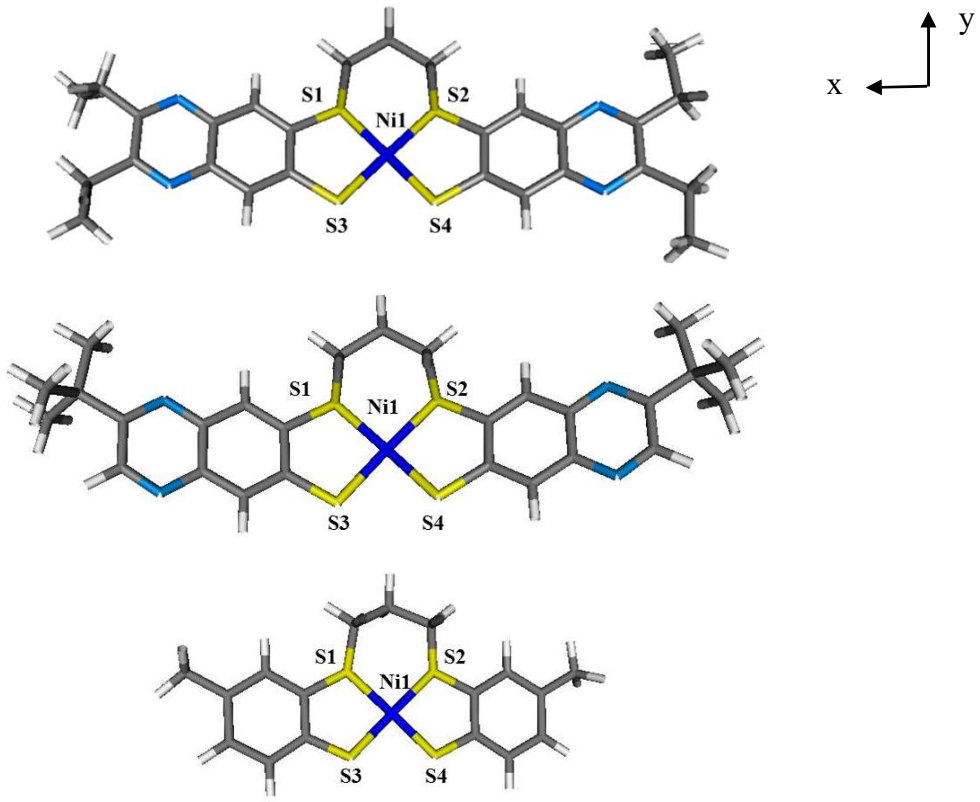


Figure 2.34: The gas-phase geometry optimised structure of [Ni(p-$q^{6,7}dt^{Et,Et}$)] (top), [Ni(p-$q^{6,7}dt^{H,tBu}$)] (middle) and [Ni(L^A)] (bottom) derived from DFT calculations using the BP86 functional.

Table 2.9: Selected metrical parameters for [Ni(p-$q^{6,7}dt^{Et,Et}$)], [Ni(p-$q^{6,7}dt^{H,tBu}$)] and [Ni(L^A)] derived from the X-ray structures and DFT models of [Ni(p-$q^{6,7}dt^{Et,Et}$)], [Ni(p-$q^{6,7}dt^{H,tBu}$)] and [Ni(L^A)].

Bond Length (Å)	**X-ray [Ni(p-$q^{6,7}dt^{Et,Et}$)]**	**BP86 [Ni(p-$q^{6,7}dt^{Et,Et}$)]**	**X-ray [Ni(p-$q^{6,7}dt^{H,tBu}$)]**	**BP86 [Ni(p-$q^{6,7}dt^{H,tBu}$)]**	**X-ray [Ni(L^A)]**	**BP86 [Ni(L^A)]**
Ni(1)-S(1)	2.172(16)	2.1801	2.161(4)	2.2185	2.166 (2)	2.0088
Ni(1)-S(2)	2.174(16)	2.1850	2.178(4)	2.2089	2.162(2)	1.9938
Ni(1)-S(3)	2.170(16)	2.1792	2.168(5)	2.2051	2.175(2)	1.9937
Ni(1)-S(4)	2.173(17)	2.1828	2.172(4)	2.2085	2.175(2)	2.0090
bond angle (°)						
S(1)-Ni(1)-S(2)	91.9(6)	91.56	91.36(17)	91.41	92.3(1)	93.18
S(2)-Ni(1)-S(3)	87.3(6)	89.54	89.16(17)	90.77	90.9(1)	91.1
S(3)-Ni(1)-S(4)	91.8(6)	91.67	91.19(16)	91.04	89.9(1)	87.85
S(4)-Ni(1)-S(1)	88.9(6)	87.21	88.30(16)	87.07	88.0(1)	87.86
S(1)-Ni(1)-S(4)	177.81(7)	177.37	179.4(2)	173.42	173.48(8)	178.81
S(2)-Ni(1)-S(3)	177.42(7)	178.80	179.46(19)	176.83	169.23(8)	178.81

The compositions and energies of the frontier orbitals of [Ni(p-$q^{6,7}dt^{Et,Et}$)], [Ni(p- $q^{6,7}dt^{H,tBu}$)] and [Ni(L^A)] calculated for the gas-phase geometry optimised structures are summarised in Table 2.10 and the frontier orbitals for [Ni(p- $q^{6,7}dt^{Et,Et}$)], [Ni(p-$q^{6,7}dt^{H,tBu}$)] and [Ni(L^A)] are illustrated in Figures 2.35.

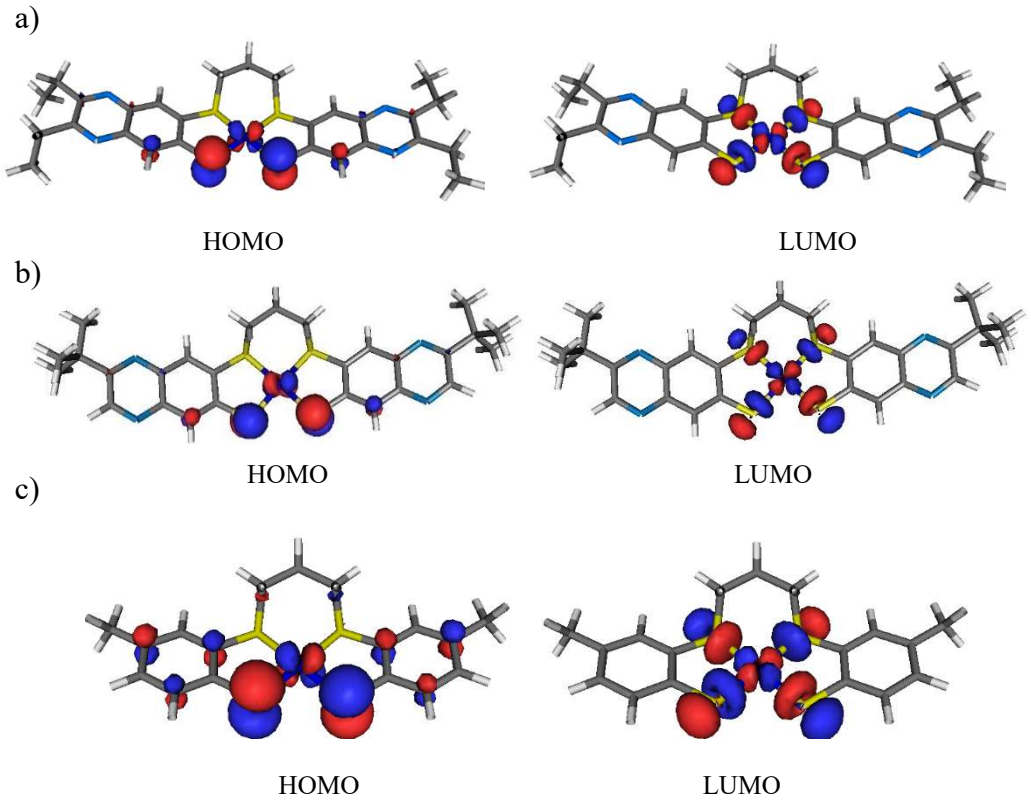


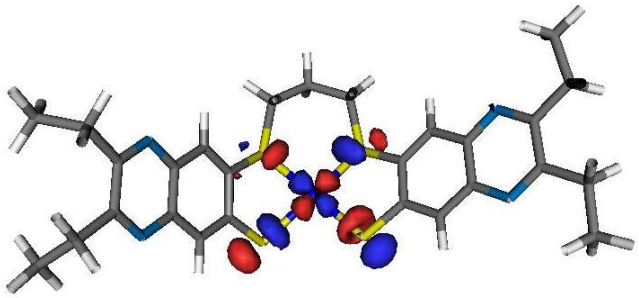
Figure 2.35: Kohn-Sham frontier orbitals for the BP86 optimised structure of a) **[**Ni(p-$q^{6,7}dt^{Et,Et}$)] b) **[**Ni(p-$q^{6,7}dt^{H,tBu}$)] c)[Ni(L^A)].

Table 2.10: The nature, energy and composition of the frontier orbitals obtained from the DFT calculations for [Ni(p-$q^{6,7}dt^{Et,Et}$)], [Ni(p-$q^{6,7}dt^{H,tBu}$)], [Ni(L^A)] and [Ni(p-$q^{6,7}dt^{Et,Et}$)]$^-$.

Compound	Designation	Orbital Nature	Energy/ Hartrees	% Contribution Ni	S	N
[Ni(p-$q^{6,7}dt^{Et,Et}$)]	157a LUMO	Ni 3d_{xy} - S σ	-0.172	24.6	47.1	1.0
	156a HOMO	Ni 3d_{xz}-S π	-0.125	38.6	52.3	0
[Ni(p-$q^{6,7}dt^{H,tBu}$)]	157a LUMO	Ni 3d_{xy} - S σ	-0.176	24.5	46.5	0
	156a HOMO	Ni 3d_{xz}-S π	-0.130	39.0	39.0	0
[Ni(L^A)]	107a LUMO	Ni 3d_{xy} - S σ	-0.141	17.0	45.3	-
	106a HOMO	Ni 3d_{xz}-S π	-0.099	33.9	45.7	-
[Ni(p-$q^{6,7}dt^{Et,Et}$)]$^-$	157a SOMO	Ni 3d_{xy} - S σ	-0.027	35.9	38.6	0

The HOMO in each of [Ni(p-$q^{6,7}dt^{Et,Et}$)], [Ni(p-$q^{6,7}dt^{H,tBu}$)] and [Ni(L^A)] is delocalised across the metalladithiolate unit and involves Ni 3d_{xz}, and dithiolate π-combinations with S (39.0 – 52.3 %) and Ni (33.9 – 39.0 %) character. The LUMO of each [Ni(p-$q^{6,7}dt^{Et,Et}$)], [Ni(p-$q^{6,7}dt^{H,tBu}$)] and [Ni(L^A)] are essentially identical and are derived from Ni 3d_{xy} and S-thiolate/thioether σ-orbital combinations. The LUMOs involve contributions from the S-donors (45.7 – 47.1 %) and the Ni centre (17.0 – 24.6 %). The relative energies of the HOMO and LUMO of [Ni(p-$q^{6,7}dt^{Et,Et}$)] and [Ni(p-$q^{6,7}dt^{H,tBu}$)] are essentially identical suggesting that the variation in substituents pendant to the 6,7-quinoxaline ring has little impact on the electronic

structures of the frontier orbitals. The energy of the LUMO for $[Ni(L^A)]$ is *ca.* 0.030 Hartrees higher in energy (Table 2.12) than those of $[Ni(p\text{-}q^{6,7}dt^{Et,Et})]$ and $[Ni(p\text{-}q^{6,7}dt^{H,tBu})]$, consistent with the more negative reduction potential of the formal $Ni^{II/I}$ couple for $[Ni(L^A)]$. An unrestricted DFT calculation for $[Ni(p\text{-}q^{6,7}dt^{Et,Et})]^-$ reveals a SOMO that possesses Ni $3d_{xy}$ and S-thiolate/thioether σ-orbital character (Table 2.12, Figure 2.36), that is in line with the axial nature of the frozen solution EPR spectra of $[Ni(p\text{-}q^{6,7}dt^{Et,Et})]^-$ and $[Ni(p\text{-}q^{6,7}dt^{H,tBu})]^-$ in which $g_{11} > g_{22} = g_{33}$ (Section 2.8). In summary, the electronic structures of $[Ni(p\text{-}q^{6,7}dt^{Et,Et})]$, $[Ni(p\text{-}q^{6,7}dt^{H,tBu})]$ and $[Ni(L^A)]$ are similar and the frontier orbitals are essentially localised about the NiS_4 unit. The electrochemical and EPR spectroscopic properties of each complex are in line with the calculated relative energies of the frontier orbitals and their compositions, respectively.



SOMO

Figure 2.36 Kohn-Sham SOMO for the BP86 optimised structure of $[Ni(p\text{-}q^{6,7}dt^{Et,Et})]^-$.

2.11.1 DFT Studies of protonation of $[Ni(p\text{-}q^{6,7}dt^{Et,Et})]$

We examined the protonated forms of $[Ni(p\text{-}q^{6,7}dt^{Et,Et})]$, $[Ni(p\text{-}q^{6,7}dt^{Et,Et})H]^+$, $[Ni(p\text{-}q^{6,7}dt^{Et,Et})H_2]^{2+}$, $[Ni(p\text{-}q^{6,7}dt^{Et,Et})H_3]^{3+}$ and $[Ni(p\text{-}q^{6,7}dt^{Et,Et})H_4]^{4+}$, which involve sequential protonation at each of the N positions of the 6,7-quinoxaline rings (see Figure 2.37). The calculated geometrical parameters for the protonated forms are similar to those of $[Ni(p\text{-}q^{6,7}dt^{Et,Et})]$ (Table 2.11) suggesting that protonation does not significantly change the geometry with the Ni^{II} unit.

Table 2.11: Selected calculated parameters for [Ni(p-$q^{6,7}dt^{Et,Et}$)] and the protonated forms of [Ni(p-$q^{6,7}dt^{Et,Et}$)H_n]$^{n+}$ (n = 1 - 4).

Bond Length/Å	[Ni(p-$q^{6,7}dt^{Et,Et}$)]	[Ni(p-$q^{6,7}dt^{Et,Et}$)H]$^{+}$	[Ni(p-$q^{6,7}dt^{Et,Et}$)H_2]$^{2+}$	[Ni(p-$q^{6,7}dt^{Et,Et}$)H_3]$^{3+}$	[Ni(p-$q^{6,7}dt^{Et,Et}$)H_4]$^{4+}$
Ni(1)-S(1)	2.1801	2.1801	2.0120	2.1911	2.0119
Ni(1)-S(2)	2.1850	2.1850	1.9939	2.1572	1.9936
Ni(1)-S(3)	2.1792	2.1792	1.9937	2.1704	1.9935
Ni(1)-S(4)	2.1828	2.1828	2.0122	2.1928	2.0119
bond angle/º					
S(1)-Ni(1)-S(2)	91.56	91.56	91.00	91.42	91.03
S(2)-Ni(1)-S(3)	89.54	89.54	87.77	90.12	87.71
S(3)-Ni(1)-S(4)	91.67	91.67	93.50	93.47	93.56
S(4)-Ni(1)-S(3)	87.21	87.21	87.73	85.27	87.70
S(1)-Ni(1)-S(4)	177.37	177.37	178.71	175.10	178.72
S(2)-Ni(1)-S(3)	178.80	178.80	178.74	173.31	178.72

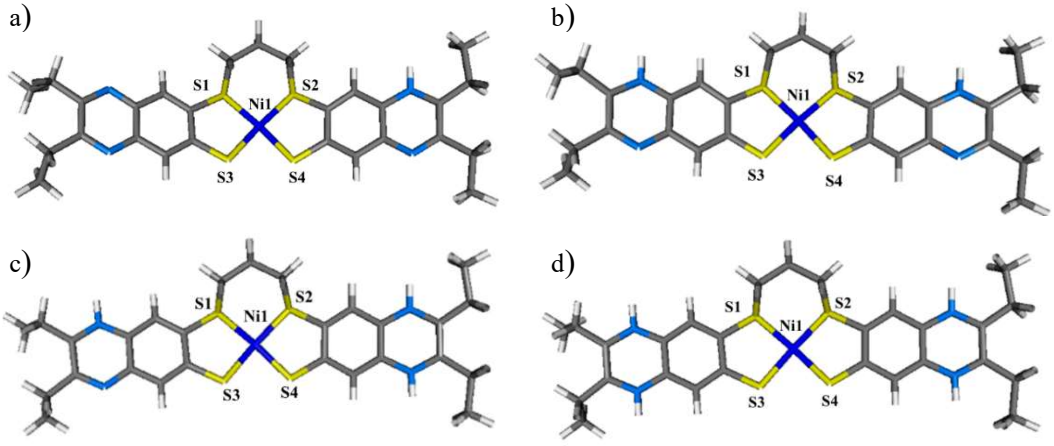


Figure 2.37: Optimised structures for a) [Ni(p-$q^{6,7}dt^{Et,Et}$)H]$^{+}$, b) [Ni(p-$q^{6,7}dt^{Et,Et}$)H_2]$^{2+}$, c) [Ni(p-$q^{6,7}dt^{Et,Et}$)H_3]$^{3+}$ and d) [Ni(p-$q^{6,7}dt^{Et,Et}$)H_4]$^{4+}$.

The Kohn-Sham frontier orbitals of the gas-phase optimised structures of [Ni(p-$q^{6,7}dt^{Et,Et}$)H_n]$^{n+}$ (n = 1–4) are shown in Figure 2.37. A comparison of the compositions of the HOMO and LUMOs of each protonated species [Ni(p-$q^{6,7}dt^{Et,Et}$)H_n]$^{n+}$ (n = 1 – 4) with those of the non-protonated species [Ni(p-$q^{6,7}dt^{Et,Et}$)] (discussed in Section 2.7.2) shows a significant change in orbital contribution. For example the LUMO of [Ni($q^{6,7}dt^{Et}$)$_2$H]$^{+}$ is of primarily C(2p) and N(2p) (38 % C, 30 % N) character derived from the atoms of one of the 6,7-quinoxaline rings. Thus, the DFT calculations suggest that protonation of the 6,7-quinoxaline ring provides a mechanism for changing the nature of the LUMO orbital such that the first reduction process is ligand-based. This suggests that the first reduction observed during the cyclic voltammetric studies of [Ni(p-$q^{6,7}dt^{Et,Et}$)] and [Ni(p-$q^{6,7}dt^{H,tBu}$)] in CH_2Cl_2 solution with TFA at –0.75 V *vs* Fc^{+}/Fc is likely ligand-based. The protonation of [Ni(p-$q^{6,7}dt^{Et,Et}$)] by 2, 3 or 4 protons presents similar LUMOs that are localised on

the 6,7-quinoxaline ligands with a progressive lowering of the energy of these orbitals (Figure 2.38, Table 2.12).

Table 2.12: The nature, energy and composition of the frontier orbitals obtained from the DFT calculations for $[Ni(p\text{-}q^{6,7}dt^{Et,Et})H]^+$, $[Ni(p\text{-}q^{6,7}dt^{Et,Et})H_2]^{2+}$, $[Ni(p\text{-}q^{6,7}dt^{Et,Et})H_3]^{3+}$ and $[Ni(p\text{-}q^{6,7}dt^{Et,Et})H_4]^{4+}$.

Compound	Designation	Orbital Nature	Energy/ Hartrees	% Contribution		
				Ni	S	N
$[Ni(p\text{-}q^{6,7}dt^{Et,Et})H]^+$,	157 LUMO	C $2p_z$ – N $2p_z$	-0.259	1.48	6.9	30.0
	156 HOMO	Ni $3d_{xz,yz}$ - S π	-0.257	16.5	40.9	9.6
$[Ni(p\text{-}q^{6,7}dt^{Et,Et})_2H_2]^{2+}$	157 LUMO	C $2p_z$ – N $2p_z$	-0.322	0	0	33.4
	156 HOMO	Ni $3d_{xz}$ - S π	-0.357	17.1	38.3	5.2
$[Ni(p\text{-}q^{6,7}dt^{Et,Et})_2H_3]^{3+}$	157 LUMO	C $2p_z$ – N $2p_z$	-0.450	4.2	16.4	24.3
	156 HOMO	Ni $3d_{xz,yz}$ - S π	-0.462	22.0	35.8	7.9
$[Ni(p\text{-}q^{6,7}dt^{Et,Et})_2H_4]^{4+}$	157 LUMO	C $2p_z$ – N $2p_z$	-0.536	0	4.5	31.1
	156 HOMO	Ni $3d_{xz}$ - S π	-0.557	30.0	19.3	7.6

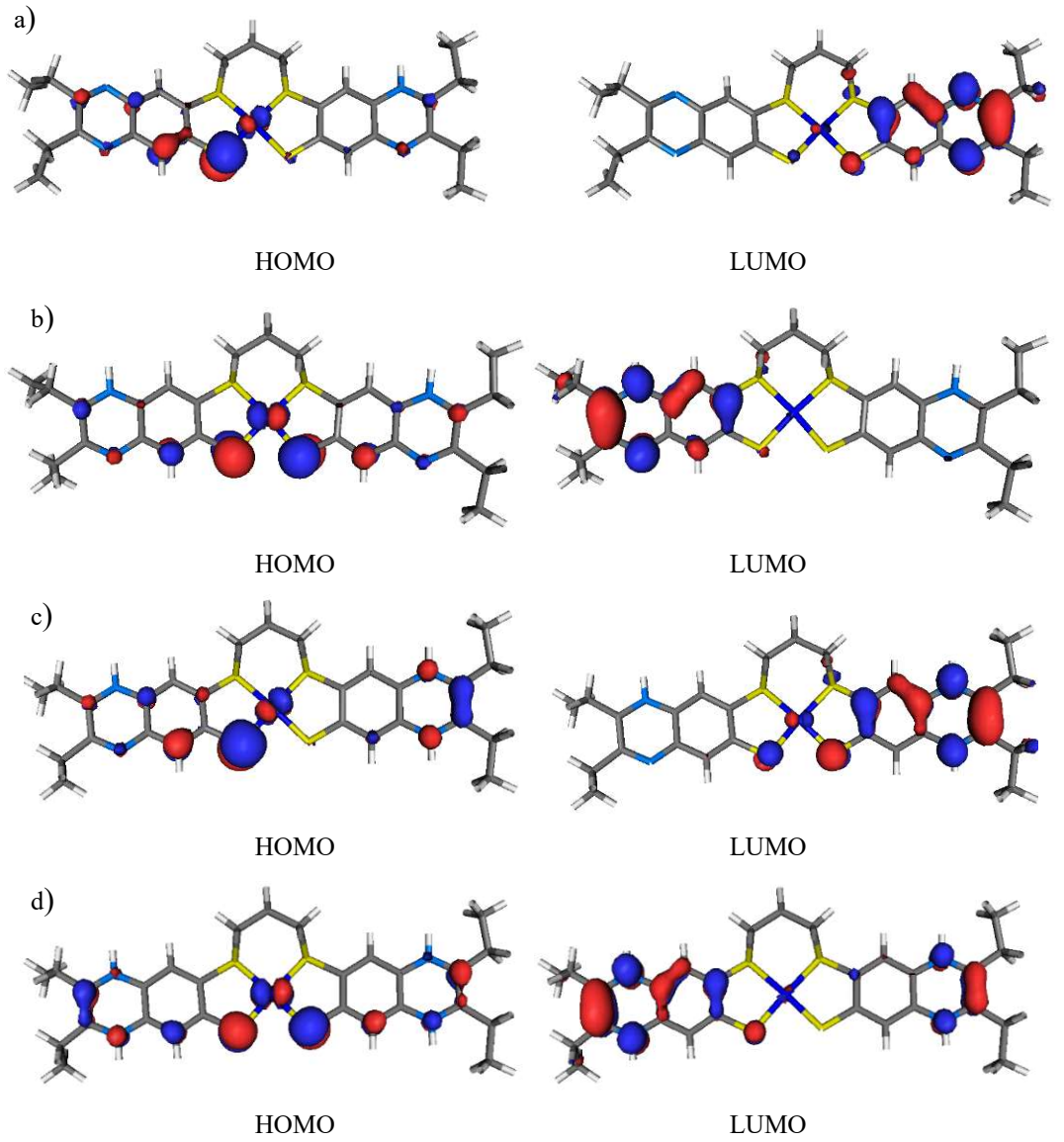


Figure 2.38: Kohn-Sham frontier orbitals for the BP optimised structure of a) $[Ni(p\text{-}q^{6,7}dt^{Et,Et})H]^+$, b) $[Ni(p\text{-}q^{6,7}dt^{Et,Et})H_2]^{2+}$, c) $[Ni(p\text{-}q^{6,7}dt^{Et,Et})H_3]^{3+}$ and d) $[Ni(p\text{-}q^{6,7}dt^{Et,Et})H_4]^{4+}$.

2.12 Conclusion

This chapter details the syntheses of the 6,7-quinoxaline-2,3-dithiols $qdt^{R1,R2}H_2$ (R^1 = R^2 = Me; R^1 = H, R^2 = ^{t}Bu) and the 2,3-quinoxaline-6,7-dithiols $q^{6,7}dt^{R1,R2}H_2$ (R^1 = R^2 = Me, Et, Ph; R^1 = H, R^2 = ^{t}Bu). The structures of the ligand precursors $q^{6,7}dt^{R1,R2}(SCN)_2$ (R^1 = R^2 = Me, Et, Ph; R^1 = H, R^2 = ^{t}Bu) were probed by X-ray crystallography and the electrochemistry of $q^{6,7}dt^{Et,Et}(SCN)_2$ was investigated in the absence and presence of TFA. The precursor $q^{6,7}dt^{Et,Et}(SCN)_2$ possesses an electrochemically irreversible reduction process at E_p^c = -1.85 V *vs* Fc^+/Fc and the potential of this process occurs a less negative potential (E_p^c = -1.15 V *vs* Fc^+/Fc) in the presence of TFA that suggests that in TFA $q^{6,7}dt^{Et,Et}(SCN)_2$ is protonated.

[Ni(L^A)] was synthesised and its electrochemical properties investigated to allow a direct comparison of the properties of this unit with [Ni(p-$qdt^{R1,R2}$)] (R^1 = R^2 = Me; R^1 = H, R^2 = ^{t}Bu and [Ni(p-$q^{6,7}dt^{R1,R2}$)] (R^1 = R^2 = Me, Et, Ph; R^1 = H, R^2 = ^{t}Bu) synthesised in this Chapter. [Ni(L^A)] possesses a reduction process at $E_{1/2}$ = -1.66 V *vs* Fc^+/Fc and cyclic voltammetric studies in solutions containing TFA indicates that [Ni(L^A)] is a potential electrocatalyst for the production of H_2.

The syntheses of [Ni(p-$qdt^{R1,R2}$)] (R^1 = R^2 =Me; R^1 = H, R^2 = ^{t}Bu) were attempted and the formation of [Ni(p-$qdt^{R1,R2}$)] (R^1 = R^2 =Me; R^1 = H, R^2 = ^{t}Bu) was confirmed by mass spectrometric studies, however elemental analysis confirmed that the complexes could not be isolated pure.

We had more success in the synthesis and characterisation of [Ni(p-$q^{6,7}dt^{R1,R2}$)] (R^1 = R^2 = Me, Et, Ph; R^1 = H, R^2 = ^{t}Bu). Electrochemical studies show that [Ni(p-$q^{6,7}dt^{Et,Et}$)] and [Ni(p-$q^{6,7}dt^{H,tBu}$)] possess a reduction process at $E_{1/2}$ = -1.47 and - 1.45 V *vs.* Fc^+/Fc, respectively that are *ca.* 0.2 V more positive than that for [Ni(L^A)]. EPR spectroscopic measurements show that this process is likely to be metal-based, localised over the NiS_4 unit in each complex and that it may be assigned to a $Ni^{II/I}$ couple.[3,4,21]

Catalytic studies of [Ni(p-$q^{6,7}dt^{Et,Et}$)], [Ni(p-$q^{6,7}dt^{H,tBu}$)] and [Ni(L^A)] show that all three complexes are potential catalysts for H_2 production. A comparison of the cathodic current of [Ni($q^{6,7}dt^{Et}$)$_2$], [Ni($q^{6,7}dt^{tBu}$)$_2$] and Ni(L^A) in the presence of TFA

in CH_2Cl_2 solution shows that the activity follows the order [Ni(p-$q^{6,7}dt^{Et,Et}$)] ≈ Ni(L^A) > [Ni(p-$q^{6,7}dt^{H,tBu}$)] and that all have a greater catalytic current than [Ni(L^A)$Fe_2(CO)_6$].[23] Thus, it appears that NiS_4 centres containing two thioether and two thiolate S-donors are capable of supporting electrochemical H_2 production. The impact of the incorporation of potential proton binding sites within the quinoxaline rings of [Ni(p-$q^{6,7}dt^{Et,Et}$)] and [Ni(p-$q^{6,7}dt^{H,tBu}$)] on the catalytic activity of NiS_4 complexes is less clear since [Ni(p-$q^{6,7}dt^{Et,Et}$)] and [Ni(p-$q^{6,7}dt^{H,tBu}$)] have a similar catalytic activity to [Ni(L^A)]. Further catalytic studies, including a quantification of the H_2 evolved by gas chromatography, will be required to investigate the potential role of the pyrazine N atoms in supporting catalysis.

We also undertook DFT calculations to provide a qualitative framework to interpret the electrochemical and EPR spectroscopic results. The frontier orbitals of [Ni(p-$q^{6,7}dt^{Et,Et}$)], [Ni(p-$q^{6,7}dt^{H,tBu}$)] and [Ni(L^A)] are similar with the LUMO orbital in each consisting of overlaps of the Ni $3d_{xy}$ orbital and a S-based σ-combination. The relative energies of the LUMOs in [Ni(p-$q^{6,7}dt^{Et,Et}$)], [Ni(p-$q^{6,7}dt^{H,tBu}$)] and [Ni(L^A)] broadly follow the trend in reduction potential of these centres with $E_{1/2}$([Ni(p-$q^{6,7}dt^{Et,Et}$)]$^{0/-}$) ≈ $E_{1/2}$([Ni(p-$q^{6,7}dt^{H,tBu}$)]$^{0/-}$) > $E_{1/2}$([Ni(L^A)]$^{0/-}$). DFT calculations on models of the protonated forms of [Ni(p-$q^{6,7}dt^{Et,Et}$)H_n]$^{n+}$ (n = 1-4) suggest protonation can make the first reduction process ligand rather than metal-based.

The research described in this Chapter demonstrates that the incorporation of 6,7-quinoxaline units can raise the potential of the formal $Ni^{II/I}$ couple in [Ni(p-$q^{6,7}dt^{R1,R2}$)] complexes relative to Ni(L^A). This is likely to be due to the more electron withdrawing nature of the 6,7-quinoxaline rings that are adjacent to the redox active NiS_4 unit. In addition, the incorporation of the 6,7-quinoxaline rings in [Ni(p-$q^{6,7}dt^{R1,R2}$)] presents up-to four protonation sites that may facilitate the catalysis of H_2 production by these centres in a process that may involve the NiS_4 centre and the 6,7-quinoxaline units. In these respects the research described in this chapter shows that [Ni(p-$q^{6,7}dt^{R1,R2}$)] are promising candidates as catalysts for H_2 production and further developments of the [p-$q^{6,7}dt^{R1,R2}$]$^{2-}$ ligand system may yield complexes with more positive $Ni^{II/I}$ reduction potentials that may make catalysis more efficient.

2.13 Experimental

2.13.1 The Synthesis of 6,7-^{R1,R2}quinoxaline-2,3-dione (3) ($R^1 = R^2 = Me$ and $R^1 = H$, $R^2 = {}^tBu$)

Representative procedure for the synthesis of 6,7-^{R1,R2}-2,3-dichloroquinoxaline 6,7-^{R1,R2}quinoxaline-2,3-dione: A mixture of 6,7- ^{R1,R2}-1,2-phenylenediamine (32.8 mmol) and diethyl oxalate (25 mL, 184 mmol) was heated to 70 °C under reduced pressure (150 mbar) for 16 h. A colourless precipitate was isolated *via* filtration and washed with diethyl ether (3 x 50 mL) to yield a colourless solid.

6,7-methyl-quinoxaline-2,3-dione: Prepared from 6,7-methyl-1,2-phenylenediamine (5.22 g, 32.8 mmol) to give a colourless powder (5.10 g, 26.0 mmol, 82 %). MS (ES^+) m/z: 191.0742 $[M+H]^+$. ^{1}H NMR δ (400 MHz, $(CD_3)_2SO$, 298 K): 7.29 (2H, s, ArH), 2.21 (6H, s, CH_3) ppm. ^{13}C-NMR δ (100 MHz, $(CD_3)_2SO$, 298 K): 128.4 (Ar-C), 120.3 (Ar-C), 116.8 (Ar-C), 113.0 (Ar-C), 18.9 (CH_3) ppm. Elemental analysis found (calculated for $C_{10}H_{10}N_2O_2$): C, 63.41 (63.15), H 5.32 (5.30), N 14.65 (14.73) %.

6-*tert*-Butyl-quinoxaline-2,3-dione: Prepared from 4-*tert*-butyl-1,2-phenylenediamine (5.00 g, 30.5 mmol) to give a colourless powder (5.90 g, 27.1 mmol, 89 %). MS (ES^+) m/z: 219.1055 $[M+H]^+$. ^{1}H NMR δ (400 MHz, $(CD_3)_2SO$, 298 K): 7.17-7.15 (2H, m, ArH), 7.08 (1H, s, ArH), 1.27 (9H, s, CH_3) ppm. ^{13}C-NMR δ (100 MHz, $(CD_3)_2SO$, 298 K): 125.6 (Ar-C), 120.8 (Ar-C), 115.2 (Ar-C), 112.2 (Ar-C), 33.4 (CCH_3), 31.61 (CCH_3) ppm. Elemental analysis found (calculated for $C_{12}H_{14}N_2O_2$): C 66.04 (66.04), H 6.47 (6.60), N 12.84 (12.72) %.

2.13.2 The Synthesis of 6,7-^{R1R2}-2,3-dichloroquinoxaline (4) ($R^1 = R^2 = Me$ and $R^1 = H$, $R^2 = {}^tBu$)

Representative procedure for the synthesis 6,7-^{R1,R2}-2,3-dichloroquinoxaline: A solution of the 6,7-R^1,R^2-quinoxaline-2,3-dione (26.0 mmol) in thionyl chloride (25.0 mL, 345 mmol) and dimethyl formamide (0.94 mL, 12.0 mmol) was heated at reflux for 20 min. Thionyl chloride (5.00 mL, 65.0 mmol) and dimethyl formamide (1.90 mL, 25.0 mmol) was added and the mixture was heated at reflux for a further 1.5 h to give a yellow solution. The mixture was reduced under vacuum to give a cream solid.

6,7-dimethyl-2,3-dichloroquinoxaline: Prepared from 6,7-methyl-quinoxaline-2,3-dione (5.00 g, 26.0 mmol) to give a cream powder (5.58 g, 24.0 mmol, 93 %). MS (ES^+) m/z: 227.0064 $[M+H]^+$. ^1H NMR δ (400 MHz, $(CD_3)_2SO$, 298 K): 7.99 – 7.87 (2H, m, ArH), 2.26 (6H, s, CH_3) ppm. ^{13}C-NMR δ (100 MHz, $(CD_3)_2SO$, 298 K): 154.6 (Ar-C), 144.3 (Ar-C), 131.3 (Ar-C), 126.8 (Ar-C), 19.0 ($C\underline{C}H_3$) ppm. Elemental analysis found (calculated for $C_{10}H_8N_2Cl_2$): C 52.99 (52.89), H 3.34 (3.55), N 12.52 (12.34) %.

6-*tert*-Butyl-2,3-dichloroquinoxaline: Prepared from 6-*tert*-butyl-quinoxaline-2,3-dione (5.00 g, 23.0 mmol) to give a cream powder (5.57 g, 22.0 mmol, 95 %). MS (ES^+) m/z: 255.0377 $[M+H]^+$. ^1H NMR δ (400 MHz, $(CD_3)_2SO$, 298 K): 8.01 – 7.94 (3H, m, ArH), 1.46 (9H, s, CH_3) ppm. ^{13}C-NMR δ (100 MHz, $(CD_3)_2SO$, 298 K): 155.2 (Ar-C), 144.6 (Ar-C), 140.7 (Ar-C), 139.0 (Ar-C), 130.3 (Ar-C), 127.5 (Ar-C), 123.5 (Ar-C), 35.5 ($\underline{C}CH_3$), 31.0 ($C\underline{C}H_3$) ppm. Elemental analysis found (calculated for $C_{12}H_{12}N_2Cl_2$): C 56.49 (56.38), H 4.74 (4.81), N 10.98 (10.96) %.

2.13.3 The Synthesis crude of $qdt^{R1,R2}H_2$ ($R^1 = R^2 = Me$ and $R^1 = H$, $R^2 = {}^tBu$)

Representative procedure for the synthesis $qdt^{R1R2}H_2$: A mixture 2,3-dichloroquinoxaline (24.4 mmol) and thiourea (10.3 g, 134 mmol) in ethanol were heated to reflux for 2 h. The resulting precipitate was filtered and washed with ethanol. The precipitate was heated to reflux in sodium hydroxide solution (8 M, 20 mL) for 30 min. The solution was then acidified with acetic acid until a precipitate formed. The brown precipitate was filtered and washed with water (3 x 30 mL) and then diethyl ether (3 x 30mL).

$qdt^{Me,Me}H_2$: Prepared from 6,7-dimethyl-2,3-dichloroquinoxaline (6.00 g, 19.7 mmol) to give a brown powder (3.9 g, 17.5 mmol, 89 %). MS (ES^+) m/z: 251.0599 $[M+H]^+$. ^1H NMR δ (400 MHz, $(CD_3)_2SO$, 298 K): 7.39 – 7.49 (3H, m, ArH), 1.28 (9H, s, CH_3) ppm. ^{13}C-NMR δ (100 MHz, $(CD_3)_2SO$, 298 K): 151.7 (Ar-C), 143.6 (Ar-C), 142.2 (Ar-C), 137.8 (Ar-C), 129.9 (Ar-C), 125.5 (Ar-C), 119.5 (Ar-C), 34.6 ($\underline{C}CH_3$), 31.3 ($C\underline{C}H_3$) ppm. Elemental analysis found (calculated for $C_{10}H_{10}N_2S_2$): C 56.26 (54.02), H 4.64 (4.53), N 11.19 (9.32) %.

$qdt^{H,tBu}H_2$: Prepared from 6-*tert*-Butyl-2,3-dichloroquinoxaline (6.00 g, 23.6 mmol) to give a brown powder (5.5 g, 21.8 mmol, 92 %). MS (ES^+) m/z: 251.0599 $[M+H]^+$. ^1H NMR δ (400 MHz, $(CD_3)_2SO$, 298 K): 7.32 – 7.29 (3H, m, ArH), 2.28 (9H, s, CH_3) ppm. ^{13}C-NMR δ (100 MHz, $(CD_3)_2SO$, 298 K): 151.7 (Ar-C), 145.3 (Ar-C), 127.8 (Ar-C), 121.5 (Ar-C), 18.3 (CH_3) ppm. Elemental analysis found (calculated for $C_{12}H_{14}N_2S_2$): C 53.52 (54.02), H 4.07 (4.53), N 11.84 (12.60) %.

2.13.4 The Synthesis of Crude [Ni(p-$qdt^{R1,R2}$)] ($R^1 = R^2 = Me$ and $R^1 = H$, $R^2 = {}^tBu$)

Representative procedure for the synthesis of [Ni(p-$qdt^{R1,R2}$)]: Sodium methoxide (1.90 g, 35.0 mmol) was added to a solution of $qdt^{Me,Me}H_2$ (4.00 g, 15.9 mmol) in methanol (50 mL). The solution was stirred for 30 min at room temperature. A solution of nickel acetate (1.90 g, 7.90 mmol) in methanol (50 mL) was added to the reaction mixture drop wise. The reaction was stirred for 1 h at room temperature. 1,3-diiodopropane (1.20 mL, 9.90 mmol) was added under darkness. The reaction was left to stir 16 h at room temperature. The precipitate was collected *via* filtration to give a dark brown powder dried under *vacuo*. Purified by column chromatography CH_2Cl_2/methanol (100:0-98:2) with the addition of 3% trimethylamine.

[Ni(p-$qdt^{Me,Me}$)]: Prepared from $qdt^{Me,Me}H_2$ (4.00 g, 16.0 mmol) to give a brown powder (1.36 g, 2.50 mmol, 16 %). MS (ES^+) m/z: 540.0081 $[M+H]^+$. Elemental analysis found (calculated for $C_{23}H_{22}N_4NiS_4$): C, 48.15 (51.03); H, 4.35 (4.10); N, 9.12 (10.35) %.

[Ni(p-$qdt^{H,tBu}$)]: Prepared from $qdt^{H,tBu}H_2$ (4.00 g, 16 mmol) to give a brown powder (0.58 g, 0.96 mmol, 6 %). MS (ES^+) m/z: 597.0716 $[M+H]^+$ ^1H-NMR δ (400 MHz, $(CD_3)_2SO$, 298 K): 7.90- 7.23(m, 4H, ArH), 3.03 (q, 2H, CH_2), 1.39-1.13 (m, 20H, CH_2 and CH_3) ppm. Elemental analysis found (calculated for $C_{27}H_{30}N_4NiS_4$): C, 56.22 (54.28); H, 4.72 (5.06); N, 8.11 (9.38) %.

2.13.5 The Synthesis of 3,3-dimethyl-2-oxobutanal

Typical procedure: Bromopinacolone (10 g, 56 mmol) in dimethylsulfoxide (60 mL, 845 mmol) was heated at 80 ^{o}C for 3 h. The resulting orange solution was diluted with water (150 mL) and extracted with diethyl ether (3 x 20 mL). The combined diethyl ether washings were dried with $MgSO_4$ and filtered. The yellow filtrate was distilled under reduced pressure to give a yellow oil (60 ^{o}C, 90 mmHg) and was used without any further purification.

2.13.6 The Synthesis of $q^{6,7}dt^{R1,R2}(SCN)_2$ ($R^1 = R^2$ = Me, Et, Ph; R^1 = H, R^2 = ^{t}Bu)

Representative procedure for the synthesis of $q^{6,7}dt^{R1,R2}(SCN)_2$: A solution of the subsituted 3,4-butanedione (1.40 mL, 16.2 mmol), 4,5-thiocynanatobenzene-1,2-diamine (3.00 g, 13.5 mmol) and iodine (0.50 g, 3.90 mmol) in acetonitrile (30 mL) was stirred at room temperature for 1 h. The mixture was filtered and washed with acetonitrile. The filtrate was removed under vacuum leaving a brown oil. The oil was washed with pentane (2 x 50 mL) to give a crystalline powder.

$q^{6,7}dt^{Me,Me}(SCN)_2$: Prepared from 3,4-butanedione (1.40 mL, 16.2 mmol) to give a brown crystalline powder (3.12 g, 11.0 mmol, 85 %). MS (ES^+) m/z: 273.0191 $[M+H]^+$. ^{1}H-NMR δ (400 MHz, $(CD_3)_2SO$, 298 K): 8.49 (2H, s, ArH), 2.74 (6H, s, CH_3) ppm. ^{13}C- NMR δ (100 MHz, $(CD_3)_2SO$, 298 K): 157.90 (Ar-C), 140.99 (Ar-C), 133.43 (Ar-C), 127.50 (Ar-C), 110.95 (S-C), 23.26 (CH_3) ppm. Elemental analysis found (calculated for $C_{12}H_8N_4S_2$): C 53.29 (52.92), H 2.84 (2.96), N 20.14 (20.57) %.

$q^{6,7}dt^{Et,Et}(SCN)_2$: Prepared from 3,4-hexanedione (1.90 mL, 16.2 mmol) to give a red crystalline powder (3.60 g, 12.0 mmol, 89 %). MS (ES^+) m/z: 301.0510 $[M+H]^+$. ^{1}H-NMR δ_H (400 MHz, $(CD_3)_2SO$, 298 K): 8.50 (2H, s, ArH), 3.06-3.11 (4H, q, CH_2), 1.33-1.37 (6H, t, CH_3) ppm. ^{13}C-NMR δ (100 MHz, $(CD_3)_2SO$, 298 K): 160.41 (Ar-C), 140.35 (Ar-C), 133.16 (Ar-C), 127.02 (Ar-C), 110.53 (S-C), 27.23 (CH_2), 10.72 (CH_3) ppm. Elemental analysis found (calculated for $C_{14}H_{12}N_4S_2$): C 56.13 (55.98), H 3.89 (4.03), N 19.06 (18.65) %.

$q^{6,7}dt^{H,tBu}(SCN)_2$: Prepared from 3,3-dimethyl-2-oxobutanal (crude product from previous step) to give a brown crystalline powder (3.40 g, 12.0 mmol, 86 %). MS (ES^+) m/z: 301.0510 $[M+H]^+$. ^1H NMR δ (400 MHz, $(CD_3)_2SO$, 298 K): 9.36 (1H, s, ArH), 8.62 (1H, s, ArH) 8.52 (1H, s, ArH), 1.47 (9H, s, C-$(CH_3)_3$) ppm. ^{13}C-NMR δ (100 MHz, $(CD_3)_2SO$, 298 K): 166.61 (Ar-C), 147.10 (Ar-C), 141.03 (Ar-C), 140.44 (Ar-C), 134.24 (Ar-C), 133.32 (Ar-C), 129.35 (Ar-C), 127.51 (Ar-C), 110.72 (S-C), 110.64 (S-C), 37.58 (C-$(CH_3)_3$), 28.99 (CH_3) ppm. Elemental analysis found (calculated for $C_{14}H_{12}N_4S_2$): C 55.63 (55.98), H 4.08 (4.03), N 18.47 (18.65) %.

$q^{6,7}dt^{Ph,Ph}(SCN)_2$: Prepared from benzil (3.40 g, 16.0 mmol) to give a pink crystalline powder (4.20 g, 11.0 mmol, 79 %). MS (ES^+) m/z: 397.0601 $[M+H]^+$ ^1H NMR δ (400 MHz, $(CD_3)_2SO$, 298 K): 8.67 (2H, s, ArH), 7.53-7.37 (10H, m, ArH) ppm. ^{13}C-NMR δ (100 MHz, $(CD_3)_2SO$, 298 K): 155.66 (Ar-C), 140.66 (Ar-C), 137.89 (Ar-C), 133.67 (ArC), 129.77 (Ar-C), 129.48 (Ar-C), 128.98 (Ar-C), 128.15 (Ar-C), 110.69 (S-C) ppm. Elemental analysis found (calculated for $C_{22}H_{12}N_4S_2$): C 66.28 (66.65), H 3.18 (3.05) N 14.21 (14.13) %.

2.13.7 The Synthesis of crude $q^{6,7}dt^{R1,R2}H_2$ ($R^1 = R^2$ = Me, Et, Ph; R^1 = H, R^2 = ^{t}Bu)

Representative procedure for the synthesis of $q^{6,7}dt^{R1,R2}H_2$**:** A solution of $Na_2S{\cdot}9H_2O$ (1.82 g, 7.60 mmol) in water (150 mL) was added to $q^{6,7}dt^{Me,Me}(SCN)_2$ (3. 00 g, 11.0 mmol). The mixture was heated at 80 °C for 5 h. The resulting solution was cooled to room temperature and 10 % HCl (20 mL) was added drop wise to afford a precipitate. The precipitate was collected *via* filtration and dried under vacuum to give a powder which is reacted forward without further purification.

$q^{6,7}dt^{Me,Me}H_2$: Prepared from $q^{6,7}dt^{Me,Me}(SCN)_2$ (3. 00 g, 11.0 mmol) to give a pink powder MS (ES^+) m/z: 221.0285 $[M-H]^-$. ^1H NMR δ (400 MHz, $(CD_3)_2SO$, 298 K): 8.48 (2H, s, ArH), 2.76 (6H, s, CH_3) ppm. Elemental analysis found (calculated for $C_{10}H_{10}N_2S_2$): C 51.98 (54.02), H 5.21 (4.53), N 7.64 (9.32) %.

$q^{6,7}dt^{Et,Et}H_2$: Prepared from $q^{6,7}dt^{Et,Et}(SCN)_2$ (3. 00 g, 10.0 mmol) to give a purple powder MS (ES^+) m/z: 249.0598 $[M-H]^-$. ^1H NMR δ (400 MHz, $(CD_3)_2SO$, 298 K): 8.53 (2H, s, ArH), 3.05-3.11 (4H, q, CH_2), 1.42-1.46 (6H, t, CH_3) ppm. Elemental

analysis found (calculated for $C_{12}H_{14}N_2S_2$): C 54.61 (57.57), H 5.32 (5.64), N 9.72 (11.19) %.

$q^{6,7}dt^{H,tBu}H_2$: Prepared from $q^{6,7}dt^{H,tBu}(SCN)_2$ (3.00 g, 10.0 mmol) to give a pink powder MS (ES^+) m/z: 249.0598 $[M-H]^-$. ^1H NMR δ (400 MHz, $(CD_3)_2SO$, 298 K): 8.48 (2H, s, ArH), 1.35 (9H, s, CH_3) ppm. Elemental analysis found (calculated for $C_{12}H_{14}N_2S_2$): C 55.11 (57.57), H 5.99 (5.64), N 9.46 (11.19) %.

$q^{6,7}dt^{Ph,Ph}H_2$: Prepared from $q^{6,7}dt^{Ph,Ph}(SCN)_2$ (3.00 g, 7.6 mmol) to give a green powder MS (ES^+) m/z: 347.05 $[M-H]^-$. ^1H NMR δ (400 MHz, $(CD_3)_2SO$, 298 K): 8.49 (2H, s, ArH), 8.03 (2H, d, ArH), 7.46 (2H, s, ArH), 7.21 (4H, d, ArH) ppm. Elemental analysis found (calculated for $C_{20}H_{14}N_2S_2$): C 64.82 (69.33), H 5.12 (4.07), N 7.34 (8.09) %.

2.12.8 Synthesis of [Ni(p-$q^{6,7}dt^{R1,R2}$)] ($R^1 = R^2$ = Me, Et, Ph; R^1 = H, $R^2 = {}^t$Bu)

Representative procedure for the synthesis of [Ni(p-$q^{6,7}dt^{R1,R2}$)]: Sodium methoxide (0.141 g, 2.60 mmol) was added to a solution of $q^{6,7}dt^{R1,R2}H_2$ (0.231 g, 1.00 mmol) in methanol (20 mL). The solution was stirred for 30 min at room temperature. A solution of nickel acetate (0.093 g, 0.39 mmol) in methanol (20 mL) was added to the reaction mixture drop wise. The reaction was stirred for 1 h at room temperature. 1,3-diiodopropane (0.06 mL, 0.50 mmol) was added under darkness. The reaction was left to stir 16 h at room temperature. The precipitate was collected via filtration to give a light brown powder dried and under vacuum. The product was purified by column chromatography dichloromethane/methanol (99:1 and 100:0-98:2) and recrystallised from layering a solution of the product in dichloromethane and by layering with methanol.

[Ni(p-$q^{6,7}dt^{Me,Me}$)]: Prepared from $q^{6,7}dt^{MeMe}H_2$ (1.0 g, 4.61 mmol) to give an orange powder (0.55 g, 1.0 mmol, 22 %). MS (ES^+) m/z: 541.0081 $[M+H]^+$. ^1H NMR δ (400 MHz, $(CD_3)_2SO$, 298 K): 8.32 (s, 2H, ArH), 7.76 (s, 2H, ArH), 2.64 (q, 8H, CH_2), 2.61 (t, 4H, CH_2), 1.23 (t, 12H, CH_3) ppm. Elemental analysis found (calculated for $C_{23}H_{22}N_4NiS_4$): C, 48.15 (51.03); H, 4.35 (4.10); N, 9.12 (10.35) %.

[Ni(p-$q^{6,7}dt^{Et,Et}$)]: Prepared from $q^{6,7}dt^{Et,Et}H_2$ (1.80 g, 7.00 mmol) to give an orange powder (1.2g, 2.00 mmol, 29 %). MS (ES^+) m/z: 597.0716 $[M+H]^+$. ^1H NMR δ (400

MHz, $(CD_3)_2SO$, 298 K): 8.05 (s, 2H, ArH), 7.99 (s, 2H, ArH), 3.01 (q, 8H, CH_2), 2.75 (t, 4H, CH_2), 1.67 (m, 2H, CH_2), 1.40 (t, 12H, CH_3) ppm. Elemental analysis found (calculated for $C_{27}H_{30}N_4NiS_4$ CH_2Cl_2): C, 53.69 (53.69); H 4.99 (5.02); N 8.96 (9.24) %.

[Ni(p-$q^{6,7}dt^{H,tBu}$)]: Prepared from $q^{6,7}dt^{H,tBu}H_2$ (1.40 g, 5.00 mmol) to give an orange powder (1.00 g, 1.70 mmol, 34 %). MS (ES^+) m/z: 597.0716 $[M+H]^+$. ^1H NMR δ (400 MHz, $(CD_3)_2SO$, 298 K): 8.89 (s, 2H, ArH), 8.05 (s, 2H, ArH), 7.98 (s, 2H, ArH), 3.59 (q, 2H, CH_2), 1.68 (m, 2H, CH_2), 1.46 (s, 18H, CH_3) ppm. Elemental analysis found (calculated for $C_{27}H_{30}N_4NiS_4$): C 54.14 (54.28); H, 4.98 (5.06); N 9.25 (9.38) %.

[Ni(p-$q^{6,7}dt^{Ph,Ph}$)]: Prepared from $q^{6,7}dt^{Ph,Ph}H_2$ (1.6 g, 4 mmol) to give an orange powder (0.72 g, 1 mmol, 23 %). MS (ES+, m/z): 789.0710 $[M+H]^+$ NMR δ (400 MHz, $(CD_3)_2SO$, 298 K): 8.56 (s, 4H, ArH), 7.85 (m, 8H, ArH), 7.47 (m, 12H, ArH), 3.64 (q, 4H, CH_2), 1.67 (m, 2H, CH_2) ppm. Elemental analysis found (calculated for $C_{43}H_{30}N_4NiS_4$): C 64.97 (65.40); H 3.92 (3.83); N, 7.23 (7.10) %.

2.13 References

1 Y. Ohki and K. Tatsumi, *Eur. J. Inorg. Chem.*, 2011, **2011**, 973–985.

2 A. Marr, *Coord. Chem. Rev.*, 2001, **219**–**221**, 1055–1074.

3 J. Dawson, University of Nottingham, 2010.

4 Q. Wang, J. E. Barclay, A. J. Blake, E. S. Davies, D. J. Evans, A. C. Marr, E. J. L. McInnes, J. McMaster, C. Wilson and M. Schröder, *Chem. Eur. J.*, 2004, **10**, 3384–3396.

5 G. Durgaprasad and S. Das, *J. Chem. Sci.*, 2015, **127**, 295–305.

6 C. L. Linfoot, P. Richardson, K. L. McCall, J. R. Durrant, A. Morandeira and N. Robertson, *Sol. Energy*, 2011, **85**, 1195–1203.

7 S. Lo Schiavo, F. Nicolò, R. Scopelliti, G. Tresoldi and P. Piraino, *Inorg. Chim. Acta*, 2000, **304**, 108–113.

8 G. Peyronel, A. Pignedoli and W. Malavasi, *Spectrochim. Acta Part A Mol. Spectrosc.*, 1976, **32**, 1015–1020.

9 C. L. Linfoot, P. Richardson, K. L. McCall, J. R. Durrant, A. Morandeira and N. Robertson, *Sol. Energy*, 2011, **85**, 1195–1203.

10 R. Bolligarla, G. Durgaprasad and S. K. Das, *Inorg. Chem. Commun.*, 2011, **14**, 809–813.

11 J.Dawson, *Unpublished work*, 2012.

12 F. B. Mallory, C. W. Mallory, C. K. Regan, R. J. Aspden, A. B. Ricks, J. M. Racowski, A. I.

Nash, A. V. Gibbons, P. J. Carroll and J. M. Bohen, *J. Org. Chem.*, 2013, **78**, 2040–2045.

13 X. Qiao, M. A. Padula, D. M. Ho, N. J. Vogelaar, C. E. Schutt and R. A. Pascal, *J. Am. Chem. Soc.*, 1996, **118**, 741–745.

14 R. Bolligarla, S. N. Reddy, G. Durgaprasad, V. Sreenivasulu and S. K. Das, *Inorg. Chem.*, 2013, **52**, 66–76.

15 M. G. Fraser, A. G. Blackman, G. I. S. Irwin, C. P. Easton and K. C. Gordon, *Inorg. Chem.*, 2010, **49**, 5180–5189.

16 E. V. Anslyn and D. A. Dougherty, *Modern Physical Organic Chemistry*, University Science Books, 2006.

17 *Encyclopedia of Reagents for Organic Synthesis*, John Wiley & Sons, Ltd, Chichester, UK, 2001.

18 C. Belle, C. Bougault, M.-T. Averbuch, A. Durif, J.-L. Pierre, J.-M. Latour and L. Le Pape, *J. Am. Chem. Soc.*, 2001, **123**, 8053–8066.

19 A. G. Lappin, C. K. Murray and D. W. Margerum, *Inorg. Chem.*, 1978, **17**, 1630–1634.

20 N. G. Connelly and W. E. Geiger, *Chem. Rev.*, 1996, **96**, 877–910.

21 A.Perra, University of Nottingham, 2007.

22 D. Sellmann, D. Häussinger, F. Knoch and M. Moll, *J. Am. Chem. Soc.*, 1996, **118**, 5368–5374.

23 A. Perra, E. S. Davies, J. R. Hyde, Q. Wang, J. McMaster and M. Schröder, *Chem. Commun.*, 2006, **10**, 1103–1105.

24 G. Musie, J. H. Reibenspies and M. Y. Darensbourg, *Inorg. Chem.*, 1998, **37**, 302–310.

25 R. Mejia-Rodriguez, D. Chong, J. H. Reibenspies, M. P. Soriaga and M. Y. Darensbourg, *J. Am. Chem. Soc.*, 2004, **126**, 12004–12014.

26 R. S. Nicholson and I. Shain, *Anal. Chem.*, 1964, **36**, 706–723.

CHAPTER THREE

NiS_2P_2 Complexes Containing a Quinoxaline unit: Synthesis, Characterisation and Catalytic Studies.

3.1 Introduction

Research undertaken by DuBois *et al.* on the activation of H_2 by transition metal complexes has highlighted that Ni^{II} complexes containing phosphine donor ligands can act as efficient catalysts for H^+ reduction or the oxidation of H_2 (see Section 1.7).[1] The introduction of a basic site, strategically positioned in close proximity to the catalytic metal centre, facilitates the proton-transfer process and the formation of metal-hydride species involved in H_2 activation.[2] Thus, the synthesis of $[Ni(P^{Ph}_2N^{Ph})_2](BF_4)_2$ ($P^{Ph}_2N^{Ph}$ = 1,3,6-triphenyl-1-aza-3,6-diphosphacycloheptane) (Figure 3.1a) has been reported, which exhibits a turnover frequency above 100,000 s^{-1} for electrocatalytic H_2 production; this turnover frequency is significantly greater than that of the native [NiFe] hydrogenase enzyme.[3] Research into transition metal complexes possessing phosphine donor ligands has grown significantly with the focus of researchers shifting to other mononuclear Ni complexes, Fe-only and Fe-Fe systems incorporating pendant amine bases as well as diphosphine ligands.[4–6]

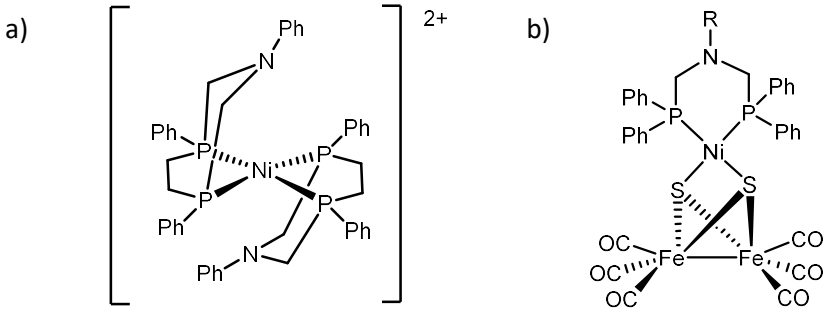


Figure 3.1: a) $[Ni(P^{Ph}_2N^{Ph})_2]^{2+}$, the first catalyst to show rates for H_2 production greater than those of the [NiFe] hydrogenase enzyme.[3] b) The structure of the $[Fe_2(CO)_6(\mu_3\text{-}S)_2Ni(Ph_2PCH_2)_2NR]$ (R = ^{n}Bu, Ph) reported by Sun *et al.*[7]

[NiFe] complexes containing pendant bases are less well-known, however Sun *et al.* have reported the trinuclear complex, $[Fe_2(CO)_6(\mu_3\text{-}S)_2Ni(Ph_2PCH_2)_2NR]$ (R = ^{n}Bu, Ph) (Figure 3.1b).[7] $[Fe_2(CO)_6(\mu_3\text{-}S)_2Ni(Ph_2PCH_2)_2NR$ consists of a NiS_2P_2 centre bound to a $Fe_2(CO)_6$ fragment through bridging S donors.[7,8] $[Fe_2(CO)_6(\mu_3\text{-}S)_2Ni(Ph_2PCH_2)_2NR]$ (R = ^{n}Bu) exhibits two reduction processes at −1.73 and –2.00 V *vs* Ag/AgCl that are assigned to reduction at the Fe_2S_2 centre. The addition of two equivalents of trifluoroacetic acid (TFA) to a solution of $[Fe_2(CO)_6(\mu_3\text{-}$

$S)_2Ni(Ph_2PCH_2)_2NR]$ (R = ^nBu) in CH_3CN generates a new reduction peak at *ca.* −1.42 V *vs* Ag/AgCl, which is assigned to the formation of a metal-hydride *in situ.*[7]

The research described in this chapter focuses on the design of NiS_2P_2 centres that contain the dppe [dppe = 1,2-bis(diphenylphosphino)ethane] ligand and the quinoxaline $[qdt^{R1,R2}]^{2-}$ ($R^1 = R^2 =$ Me and $R^1 =$ H, $R^2 = {}^tBu$) and $[q^{6,7}dt^{R1,R2}]^{2-}$ ($R^1 = R^2 =$ Me, Et, Ph; $R^1 =$ H, $R^2 = {}^tBu$) ligands discussed in Chapter 2. [(dppe)Ni(dt)] (dt = sdt, 2-pedt, 3-pedt, 4-pedt) complexes have been reported previously by the group (Figure 3.2).[9] Electrochemical and spectroelectrochemical studies have shown that [(dppe)Ni(dt)] complexes undergo a one-electron reduction at *ca.* -1.94 V *vs* Fc^+/Fc. The more negative reduction potentials associated with these centres, when compared to those of the NiS_4 complexes discussed in Chapter 2 ($E_{1/2}$ = -1.51 to -1.66 V *vs.* Fc^+/Fc), are consistent with the substitution of two S π-donors for two P π-acceptors. While the shift to a more negative potential for these NiS_2P_2 is not necessarily desirable, these centres may support a higher catalytic turnover.

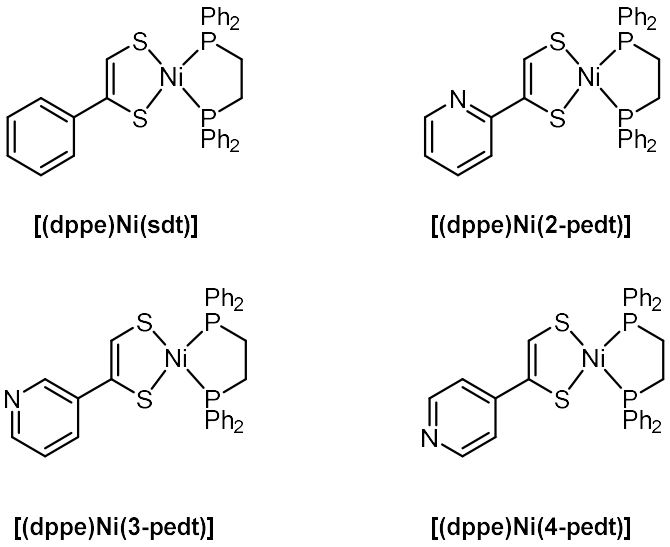
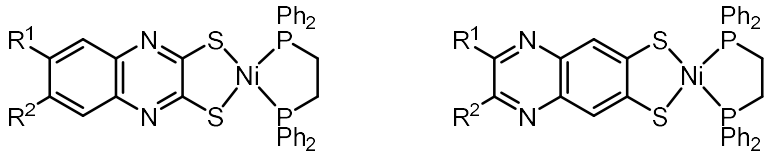


Figure 3.2: The range of [(dppe)Ni(dt)] complexes synthesised previously within the group.[9]

The quinoxaline-2,3-dithioate (qdt^{2-}) and quinoxaline-6,7-dithiolate ($q^{6,7}dt^{2-}$) ligands each contain potential protonation sites at the N-atoms associated with each quinoxaline ring. The incorporation of these units into a NiS_2P_2 framework (Figure 3.3) may modulate the reduction potential and/or catalytic turnover of the Ni^{II} centre. In addition, the incorporation of bulky substituents onto the backbone of the quinoxaline-ligand framework may also improve the solubility of the Ni^{II} species,

as discussed in Chapter 2. We will compare the structural and electronic properties of the NiS_2P_2 compounds synthesised and characterised in this chapter with those of other [(dppe)Ni(dt)] complexes and with those of the NiS_4 complexes discussed in Chapter 2. We will also assess the electrocatalytic activity of the NiS_2P_2 centres synthesised in this chapter towards H_2 production.

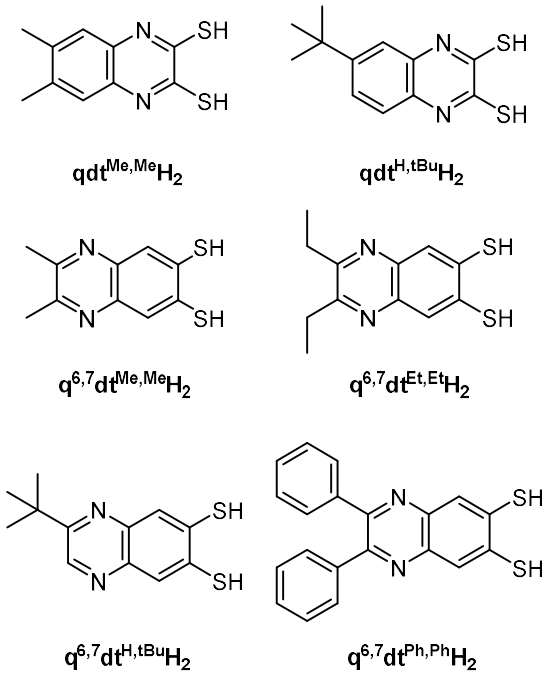


[Ni(qdt^{R1,R2})(dppe)] **[Ni(q^{6,7}dt^{R1,R2})(dppe)]**

Figure 3.3: The structures of the [Ni(qdt^{R1,R2})(dppe)] ($R^1 = R^2$ = Me; R^1 = H, R^2 = ^{t}Bu) and [Ni(q^{6,7}dt^{RR1,R2})(dppe)] ($R^1 = R^2$ = Me, Et, Ph; R^1 = H, R^2 = ^{t}Bu) complexes discussed in this chapter.

3.2 Ligand Synthesis

The 6,7-*R^1,R^2*-quinoxaline-2,3-dithiols qdt^{R1,R2}H$_2$ ($R^1 = R^2$ = Me; R^1 = H, R^2 = ^{t}Bu) and 2,3-*R^1,R^2*-quinoxaline-6,7-dithiols q^{6,7}dt^{R1,R2}H$_2$ ($R^1 = R^2$ = Me, Et, Ph; R^1 = H, R^2 = ^{t}Bu) (Figure 3.4) were synthesised following the preparations described previously in Chapter 2, Section 2.3.



qdt^{Me,Me}H$_2$ **qdt^{H,tBu}H$_2$**

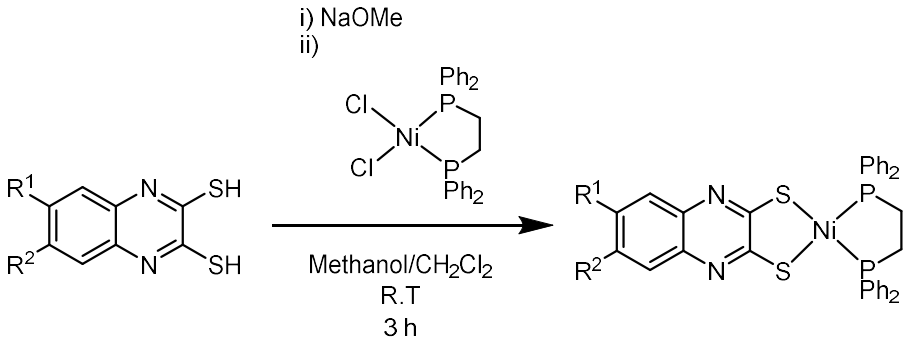
q^{6,7}dt^{Me,Me}H$_2$ **q^{6,7}dt^{Et,Et}H$_2$**

q^{6,7}dt^{H,tBu}H$_2$ **q^{6,7}dt^{Ph,Ph}H$_2$**

Figure 3.4: The ligands synthesised in Chapter 2.

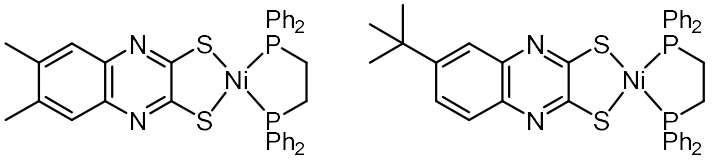
3.3 The Syntheses of Ni^{II} Complexes

3.3.1 The synthesis of [Ni(qdt^{R1,R2})(dppe)] ($R^1 = R^2 = Me$; $R^1 = H$, $R^2 = {}^tBu$)



Scheme 3.1: The synthetic route to give [Ni(qdt^{R1,R2})(dppe)] ($R^1 = R^2 = Me$; $R^1 = H$, $R^2 = {}^tBu$).

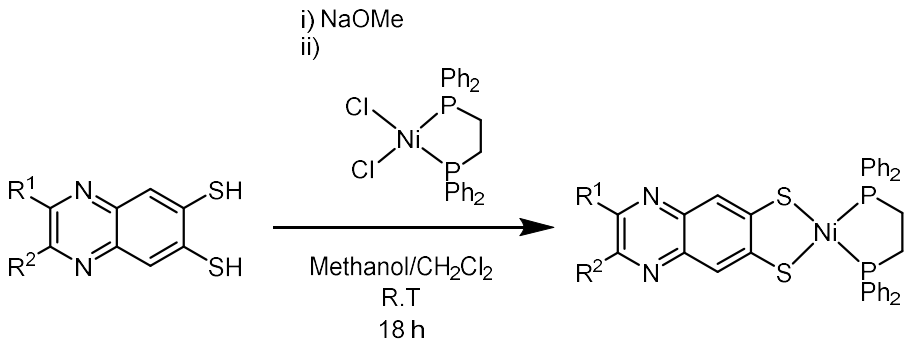
[Ni(qdt^{R1,R2})(dppe)] ($R^1 = R^2 = Me$; $R^1 = H$, $R^2 = {}^tBu$) (Figure 3.5) were prepared by the deprotonation of the corresponding qdt$^{R1,R2}H_2$ ($R^1 = R^2 = Me$; $R^1 = H$, $R^2 = {}^tBu$) ligand with sodium methoxide in methanol followed by the addition of 1,2-bis(diphenylphosphino)ethanedichloronickel(II) ([$NiCl_2$(dppe)]) in CH_2Cl_2 at room temperature and stirring for 3 h (Scheme 3.1).[9] The removal of the solvent under vacuum and a subsequent recrystallisation from CH_2Cl_2/pentane solutions gave Ni(qdt^{R1,R2})(dppe)] ($R^1 = R^2 = Me$; $R^1 = H$, $R^2 = {}^tBu$) (Figure 3.5) as crystalline orange solids. The formulation of each complex was confirmed by ^{1}H-NMR, ^{13}C-NMR and ^{31}P-NMR spectroscopies, mass spectrometric studies, by X-ray diffraction and by elemental analyses.



[Ni(qdt^{Me,Me})(dppe)] **[Ni(qdt^{H,tBu})(dppe)]**

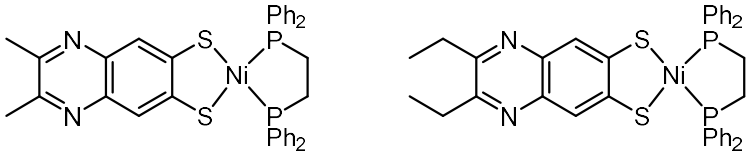
Figure 3.5: The structures of [Ni(qdt^{R1,R2})(dppe)] ($R^1 = R^2 = Me$; $R^1 = H$, $R^2 = {}^tBu$).

3.3.2 The synthesis of [Ni($q^{6,7}dt^{R1,R2}$)(dppe)] ($R^1 = R^2$ = Me, Et, Ph; R^1 = H, R^2 = ^{t}Bu)



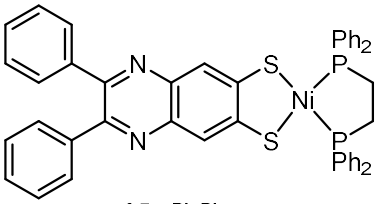
Scheme 3.2: The general synthetic route to [Ni($q^{6,7}dt^{R1,R2}$)(dppe)] ($R^1 = R^2$ = Me, Et, Ph; R^1 = H, R^2 = ^{t}Bu).

[Ni($q^{6,7}dt^{R1,R2}$)(dppe)] ($R^1 = R^2$ = Me, Et, Ph; R^1 = H, R^2 = ^{t}Bu) were prepared using the same procedure described above for [Ni($qdt^{R1,R2}$)(dppe)] ($R^1 = R^2$ = Me; R^1 = H, R^2 = ^{t}Bu) (Scheme 3.2). Recrystallisation from CH_2Cl_2/pentane solutions gave [Ni($q^{6,7}dt^{R1,R2}$)(dppe)] ($R^1 = R^2$ = Me, Et, Ph; R^1 = H, R^2 = ^{t}Bu) (Figure 3.6) as crystalline red solids, which were analysed by ^{1}H-NMR, ^{13}C-NMR, ^{31}P-NMR spectroscopies, mass spectrometric studies, X-ray diffraction and confirmed to be pure by elemental analyses.

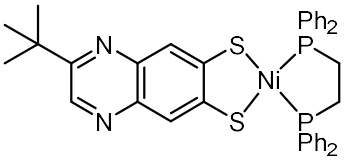


[Ni($q^{6,7}dt^{Me,Me}$)(dppe)]

[Ni($q^{6,7}dt^{Et,Et}$)(dppe)]



[Ni($q^{6,7}dt^{Ph,Ph}$)(dppe)]



[Ni($q^{6,7}dt^{H,tBu}$)(dppe)]

Figure 3.6: The structures of [Ni($q^{6,7}dt^{R1,R2}$)(dppe)] ($R^1 = R^2$ = Me, Et, Ph; R^1 = H, R^2 = ^{t}Bu)

3.4 Single Crystal X-ray structures

3.4.1 The Single Crystal X-ray Structures of [Ni(qdt^{R1,R2})(dppe)] ($R^1 = R^2 = Me$; $R^1 = H$, $R^2 = {}^tBu$)

Single crystals of [Ni(qdt^{Me,Me})(dppe)] and [Ni(qdt^{H,tBu})(dppe)], suitable for X-ray diffraction studies, were grown by layering pentane on to a concentrated solution of the each Ni^{II} complex in CH_2Cl_2. The X-ray structures of [Ni(qdt^{Me,Me})(dppe)] and [Ni(qdt^{H,tBu})(dppe)] are shown in Figures 3.7 and 3.8, respectively, with selected bond lengths and angles presented in Table 3.1.

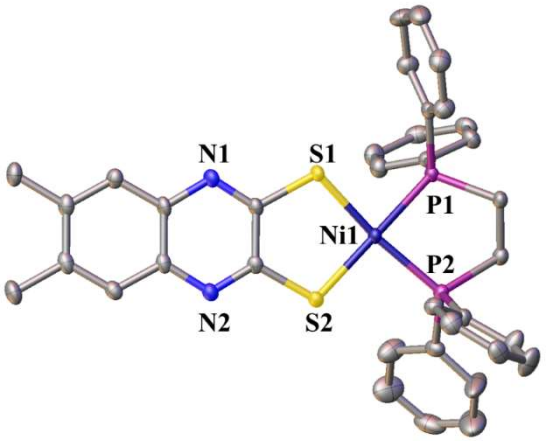


Figure 3.7: The structure of [Ni(qdt^{Me,Me})(dppe)] with selective atom labelling. The H atoms are omitted for clarity.

In [Ni(qdt^{Me,Me})(dppe)] and [Ni(qdt^{H,tBu})(dppe)] the Ni centre adopts a distorted square planar geometry bound to two phosphine donors from the dppe unit and two sulfur donors from the quinoxaline-2,3-dithiolate ligand. The angles about the Ni centre for [Ni(qdt^{Me,Me})(dppe)] and [Ni(qdt^{H,tBu})(dppe)] are close to 90° with S(2)-Ni(1)-P(2) = 93.26(6)° and 92.594(18)°, respectively, and P(2)-Ni(1)-P(1) = 86.31(6)° and 86.542(19)°, respectively. It is likely that distortions from 90° are due to the constrained bite angles of the dppe and $[qdt]^{2-}$ ligands.[10] The average Ni-S and Ni-P bond lengths are 2.1702 ($R^1 = R^2 = Me$) and 2.1598 Å ($R^1 = H$, $R^2 = {}^tBu$) and 2.1735 ($R^1 = R^2 = Me$) and 2.1610 Å ($R^1 = H$, $R^2 = {}^tBu$) and are within *ca.* 0.01 Å of each other suggesting that the addition of bulky solubilising groups on the $[qdt]^{2-}$ ligand does not affect the geometry of the Ni^{II} centre significantly. This observation is consistent with the solid state structures of the NiS_4 units, discussed in Chapter 2.

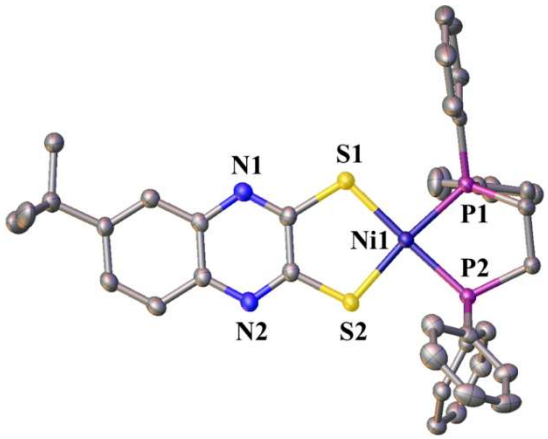


Figure 3.8: View of the structure of [Ni($qdt^{H,tBu}$)(dppe)] with selective atom labelling. The H atoms are omitted for clarity.

Selected bond lengths and angles for the unsubstituted $[qdt]^{2-}$ complex, [Ni(dppe)(qdt)], are tabulated in Table 3.1.[11] In [Ni(dppe)(qdt)], the Ni centre is coordinated to two P atoms from the dppe ligand and two S atoms from the $[qdt]^{2-}$ ligand to give a distorted square planar geometry. The S-Ni-S and P-Ni-P bond angles in [Ni(dppe)(qdt)] are 91.96(6) and 86.29(6)°, respectively.[11] These angles are within *ca.* 1.0° (S-Ni-S) and *ca.* 0.2° (P-Ni-P) of those observed for [Ni($qdt^{R1,R2}$)(dppe)]. Similarly, the average Ni-S and Ni-P bond distances in [Ni(dppe)(qdt)] are 2.166 Å and 2.179 Å, respectively;[11] the Ni-S and Ni-P distances for [Ni($qdt^{R1,R2}$)(dppe)] ($R^1 = R^2 = Me$; $R^1 = H$, $R^2 = {}^tBu$) are within 0.01 Å and 0.02 Å. Thus, the geometrical parameters about the Ni centre are similar to those for [Ni($qdt^{R1,R2}$)(dppe)] ($R^1 = R^2 = Me$; $R^1 = H$, $R^2 = {}^tBu$), an observation that further supports that the addition of substituents on the back of the quinoxaline ring does not greatly impact the geometry about the Ni^{II} centre in [Ni($qdt^{R1,R2}$)(dppe)] ($R^1 = R^2 = Me$; $R^1 = H$, $R^2 = {}^tBu$) complexes.

Table 3.1: Selected bond lengths (Å) and angles (°) with s.u. for [Ni(dppe)(qdt)], [Ni($qdt^{Me,Me}$)(dppe)] and [Ni($qdt^{H,tBu}$)(dppe)].[11]

Bond Length /Å	**Ni(dppe)(qdt)**	**[Ni($qdt^{Me,Me}$)(dppe)]**	**[Ni($qdt^{H,tBu}$)(dppe)]**
Ni(1)-S(1)	2.1656(15)	2.1639(17)	2.1601(5)
Ni(1)-S(2)	2.1671(14)	2.1765(10)	2.1594(5)
Ni(1)-P(1)	2.1791(14)	2.1662(10)	2.1614(5)
Ni(1)-P(2)	2.1791(15)	2.1809(14)	2.1607(5)
Bond Angle /°			
S(2)-Ni(1)-S(1)	91.96(5)	92.76(6)	92.594(18)
S(1)-Ni(1)-P(1)	89.41(6)	88.50(6)	90.005(18)
S(2)-Ni(1)-P(2)	93.06(6)	93.26(6)	90.843(18)
S(1)-Ni(1)-P(2)	175.21(6)	171.05(4)	176.54(2)
S(2)-Ni(1)-P(1)	170.01(6)	173.17(4)	176.23(2)
P(2)-Ni(1)-P(1)	86.29(6)	86.31(6)	86.542(19)

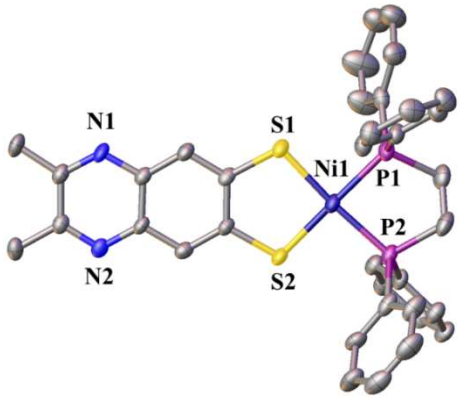
3.4.2 The Single Crystal X-ray Structures of [Ni($q^{6,7}dt^{R1,R2}$)(dppe)] (R^1 = R^2 = Me, Et, Ph; R^1 = H, R^2 = ^{t}Bu)

Single crystals of [Ni($q^{6,7}dt^{Me,Me}$)(dppe)], [Ni($q^{6,7}dt^{Et,Et}$)(dppe)] and [Ni($q^{6,7}dt^{H,tBu}$)(dppe)], suitable for X-ray crystallography, were grown by layering pentane on to a concentrated solution of each Ni^{II} complex in CH_2Cl_2. Single crystals of [Ni($q^{6,7}dt^{Ph,Ph}$)(dppe)] were grown by the evaporation of a solution of [Ni($q^{6,7}dt^{Ph,Ph}$)(dppe)] in $CHCl_3$.

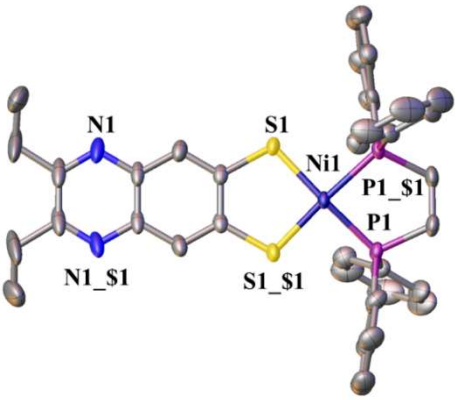
The X-ray structures of [Ni($q^{6,7}dt^{Me,Me}$)(dppe)], [Ni($q^{6,7}dt^{Et,Et}$)(dppe)], [Ni($q^{6,7}dt^{H,tBu}$)(dppe)] and [Ni($q^{6,7}dt^{Ph,Ph}$)(dppe)] are shown in Figure 3.9 and selected bond lengths and angles are presented in Table 3.2. The Ni^{II} centres are bound by two S donors derived from the $[q^{6,7}dt^{R1,R2}]^{2-}$ ligand and two P donors from the dppe unit, to give a NiS_2P_2 centre that possesses a distorted square planar geometry. The S(1)-Ni(1)-S(2) and P(1)-Ni(1)-P(2) bond angles approach 90° with S(1)-Ni(1)-S(2) = 93.20(6)° (R^1 = R^2 = Me), 93.20(6)° (R^1 = R^2 = Et), 92.594(18)° (R^1 = H, R^2 = ^{t}Bu) and 92.275(18)° (R^1 = R^2 = Ph) and P(1)-Ni(1)-P(2) = 87.06(6)° (R^1 = R^2 = Me), 87.06(6)° (R^1 = R^2 = Et), 86.542(19)° (R^1 = H, R^2 = ^{t}Bu) and 87.817(18)° (R^1 = R^2 = Ph). The average Ni-S and Ni-P distances are within 0.01 Å of one another for each [Ni($q^{6,7}dt^{R1,R2}$)(dppe)] [Ni-S_{av} = 2.1553 (R^1 = R^2 = Me), 2.1513 (R^1 = R^2 = Et), 2.1597 (R^1 = H, R^2 = ^{t}Bu) and 2.1607 Å (R^1 = R^2 = Ph); Ni-P_{av} = 2.1548 (R^1 = R^2 = Me), 2.1530 (R^1 = R^2 = Et), 2.1610 (R^1 = H, R^2 = ^{t}Bu) and 2.1707 Å (R^1 = R^2 = Ph)] and similar to those of [Ni(dppe)(qdt)][11] and [Ni(dppe)($qdt^{R1,R2}$)] (R^1 = R^2 = Me; R^1 = H, R^2 = ^{t}Bu, Table 3.2).

The relatively small differences between the metrical parameters about each Ni^{II} centre suggests that the nature of the quinoxaline-1,2-dithiolate ligand does not significantly affect the geometry of each NiP_2S_2 unit in [Ni(dppe)($qdt^{R1,R2}$)] (R^1 = R^2 = Me; R^1 = H, R^2 = ^{t}Bu) and [Ni(dppe)($q^{6,7}dt^{R1,R2}$)] (R^1 = R^2 = Me, Et and Ph; R^1 = H, R^2 = ^{t}Bu).

a)



b)



d)

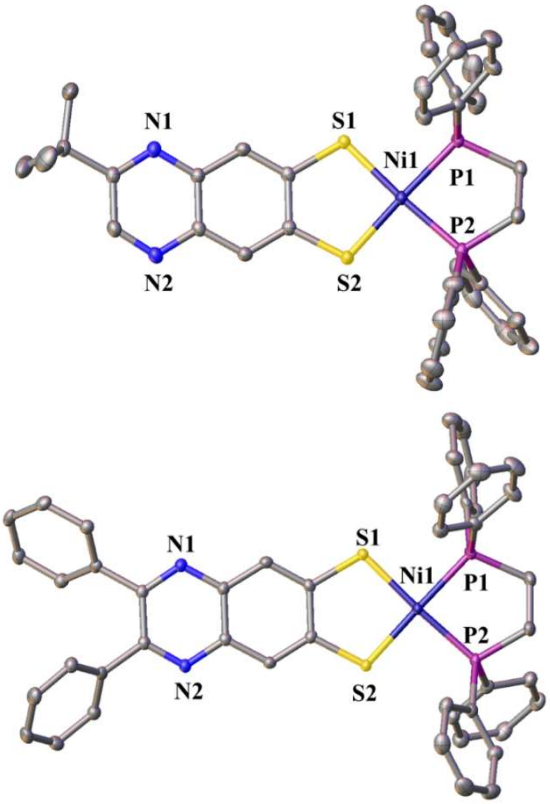


Figure 3.9: The molecular structure of a) [Ni($q^{6,7}dt^{Me,Me}$)(dppe)] and b) [Ni($q^{6,7}dt^{Et,Et}$)(dppe)] c)[Ni($q^{6,7}dt^{H,tBu}$)(dppe)] d) [Ni($q^{6,7}dt^{Ph,Ph}$)(dppe)] with H atoms omitted for clarity.

Table 3.2: A comparison of selected bond lengths and angles in [Ni(qdt)(dppe)][11] and [Ni($q^{6,7}dt^{R1,R2}$)(dppe)] (R^1 = R^2 = Me, Et, Ph; R^1 = H, R^2 = ^{t}Bu).

Bond Length/Å	**[Ni(qdt)(dppe)]**	**[Ni($q^{6,7}dt^{Me,Me}$)(dppe)]**	**[Ni($q^{6,7}dt^{H,tBu}$)(dppe)]**	**[Ni($q^{6,7}dt^{Ph,Ph}$)(dppe)]**	**[Ni($q^{6,7}dt^{Et,Et}$)(dppe)]**
Ni1-S1	2.1656(15)	2.1478(6)	2.1601(5)	2.1664(5)	2.1514(10)
Ni1-S2	2.1671(14)	2.1626(7)	2.1594(5)	2.1550(5)	2.1514(10)
Ni1-P1	2.1791(14)	2.1538(7)	2.1614(5)	2.1664(5)	2.1530(10)
Ni1-P2	2.1791(15)	2.1559(6)	2.1607(5)	2.1750(5)	2.1530(10)
Bond Angle/º					
S2-Ni1-S1	91.96(5)	93.35(2)	92.594(18)	92.275(18)	93.20(6)
S1-Ni1-P1	89.41(6)	89.64(2)	90.005(18)	89.242(18)	91.03(4)
S2-Ni1-P2	93.06(6)	90.89(2)	90.843(18)	90.918(18)	91.03(4)
S1-Ni1-P2	175.21(6)	172.66(3)	176.54(2)	175.47(2)	168.02(4)
S2-Ni-P1	170.01(6)	169.29(3)	176.23(2)	175.44(2)	168.02(4)
P2-Ni1-P1	86.29(6)	87.27(2)	86.542(19)	87.817(18)	87.06(6)

3.4.2 Summary of the X-ray Crystal Structures of [Ni($qdt^{R1,R2}$)(dppe)] (R^1 = R^2 = Me; R^1 = H, R^2 = ^{t}Bu) and [Ni($q^{6,7}dt^{R1,R2}$)(dppe)] (R^1 = R^2 = Me, Et, Ph; R^1 = H, R^2 = ^{t}Bu)

The X-ray structures of [Ni($qdt^{R1,R2}$)(dppe)] (R^1 = R^2 = Me; R^1 = H, R^2 = ^{t}Bu) and [Ni($q^{6,7}dt^{R1,R2}$)(dppe)] (R^1 = R^2 = Me, Et, Ph; R^1 = H, R^2 = ^{t}Bu) are similar and each consist of a NiS_2P_2 centre in an approximate square planar geometry. The acute

angles around each Ni^{II} centre approach 90° and the Ni-S and Ni-P bond lengths average to *ca.* 2.16 and 2.16 Å, respectively. The similarities in the solid states structures of [Ni(qdt^{R1,R2})(dppe)] (R^1 = R^2 = Me; R^1 = H, R^2 = ^{t}Bu) and [Ni(q^{6,7}dt^{R1,R2})(dppe)] (R^1 = R^2 = Me, Et, Ph; R^1 = H, R^2 = ^{t}Bu) suggest that the relative positions of the N atoms within the [qdt^{R1,R2}]$^{2-}$ or [q^{6,7}dt^{R1,R2}]$^{2-}$ ligand does not impact significantly on the geometry about each Ni^{II} centre. The X-ray crystal structures of [(dppe)Ni(dt)] (dt = sdt, 2-pedt, 3-pedt, 4-pedt) (Section 3.1, Table 3.3)[9] are also similar to those of [Ni(qdt^{R1,R2})(dppe)] (R^1 = R^2 = Me; R^1 = H, R^2 = ^{t}Bu) and [Ni(q^{6,7}dt^{R1,R2})(dppe)] (R^1 = R^2 = Me, Et, Ph; R^1 = H, R^2 = ^{t}Bu). Each NiS_2P_2 unit in [(dppe)Ni(dt)] (dt = sdt, 2-pedt, 3-pedt, 4-pedt) is close to planar and the average S-Ni-S and P-Ni-P interbond angles = 92.1° and 87.4°, respectively. These averages are within 1.0° of those observed for [Ni(qdt^{R1,R2})(dppe)] (R^1 = R^2 = Me; R^1 = H, R^2 = ^{t}Bu) and [Ni(q^{6,7}dt^{R1,R2})(dppe)] (R^1 = R^2 = Me, Et, Ph; R^1 = H, R^2 = ^{t}Bu). The Ni(1)-S(1) and Ni(1)-S(2) bond distances in [(dppe)Ni(dt)] (dt = sdt, 2-pedt, 3-pedt, 4-pedt) range from 2.1511(10) to 2.1648(5) Å and are within 0.01 Å of [Ni(qdt^{R1,R2})(dppe)] and [Ni(q^{6,7}dt^{R1,R2})(dppe)].[9] Similarly the Ni(1)-P(1) and Ni(1)-P(1) bond distances range from 2.1585(10) to 2.1843(5) Å and are within 0.02 Å of the Ni(1)-P(1) and Ni(1)-P(2) distances of [Ni(qdt^{R1,R2})(dppe)] and [Ni(q^{6,7}dt^{R1,R2})(dppe)].[9]

Table 3.3: Table of Selected bond lengths and angles for [(dppe)Ni(dt)].[9]

Bond Length/Å	**[(dppe)Ni(sdt)]**	**[(dppe)Ni(2-pedt)]**	**[(dppe)Ni(3-pedt)]**	**[(dppe)Ni(4-pedt)]**
Ni(1)-S(1)	2.1511(10)	2.1579(7)	2.1513(5)	2.1606(6)
Ni(1)-S(2)	2.1570(10)	2.1541(7)	2.1648(5)	2.1519(6)
Ni(1)-P(1)	2.1585(10)	2.1741(7)	2.1843(5)	2.1644(6)
Ni(1)-P(2)	2.1727(10)	2.1720(7)	2.1648(5)	2.1687(6)
Bond Angle/°				
S(2)-Ni(1)-S(1)	91.93(4)	92.14(3)	91.731(19)	92.55(2)
P(2)-Ni(1)-P(1)	87.85(4)	86.90(3)	88.006(19)	86.70(2)

3.5 Cyclic Voltammetric Studies of [Ni(qdt^{R1,R2})(dppe)] (R^1 = R^2 = Me; R^1 = H, R^2 = ^{t}Bu) and [Ni(q^{6,7}dt^{R1,R2})(dppe)] (R^1 = R^2 = Me, Et; R^1 = H, R^2 = ^{t}Bu)

The electrochemical properties of [Ni(qdt^{R1,R2})(dppe)] (R^1 = R^2 = Me; R^1 = H, R^2 = ^{t}Bu) and [Ni(q^{6,7}dt^{R1,R2})(dppe)] (R^1 = R^2 = Me, Et; R^1 = H, R^2 = ^{t}Bu) were examined by cyclic voltammetry. The cyclic voltammograms of 1 mM solutions of [Ni(qdt^{R1,R2})(dppe)] (R^1 = R^2 = Me; R^1 = H, R^2 = ^{t}Bu) and [Ni(q^{6,7}dt^{R1,R2})(dppe)] (R^1

= R^2 = Me, Et; R^1 = H, R^2 = ^{t}Bu) were recorded at 293 K under Ar in CH_2Cl_2 containing 0.4 M [N^nBu_4][BF_4] and a full description of the cyclic voltammetric experiments is given in the Appendix. We did not investigate [Ni($q^{6,7}dt^{Ph,Ph}$)(dppe)] because this complex is insoluble in 0.4 M [N^nBu_4][BF_4] solutions in CH_2Cl_2, CH_3CN or orthodichlorobenzene. The cyclic voltammograms of [Ni($qdt^{R1,R2}$)(dppe)] (R^1 = R^2 = Me; R^1 = H, R^2 = ^{t}Bu) and [Ni($q^{6,7}dt^{R1,R2}$)(dppe)] (R^1 = R^2 = Me, Et; R^1 = H, R^2 = ^{t}Bu) are shown in Figures 3.10 and 3.11, respectively, with electrochemical data tabulated in Table 3.4.

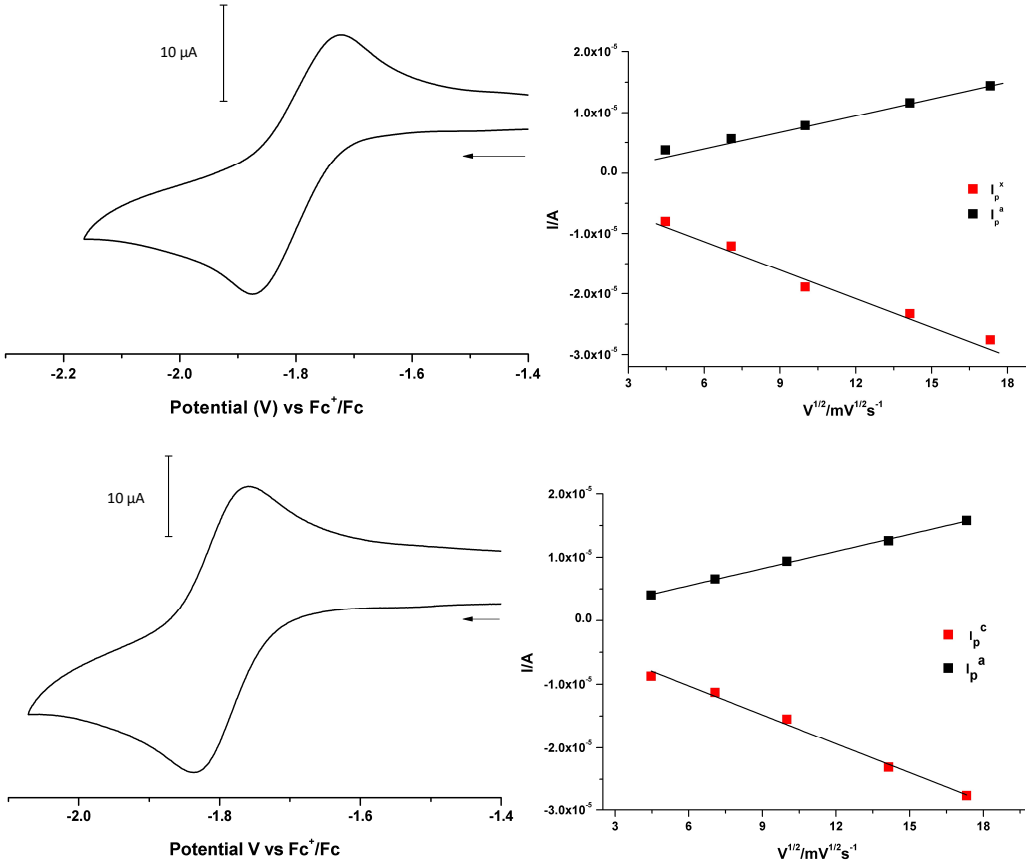


Figure 3.10: Cyclic voltammograms of 1 mM solutions of top: [Ni($qdt^{Me,Me}$)(dppe)] (left) and plots of I_p^a /I_p^c. (right) bottom: [Ni($qdt^{H,tBu}$)(dppe)](left) and plots of I_p^a /I_p^c. (right), in CH_2Cl_2 at 293 K containing [N^nBu_4][BF_4] (0.4 M) as supporting electrolyte at 100 mVs^{-1}.

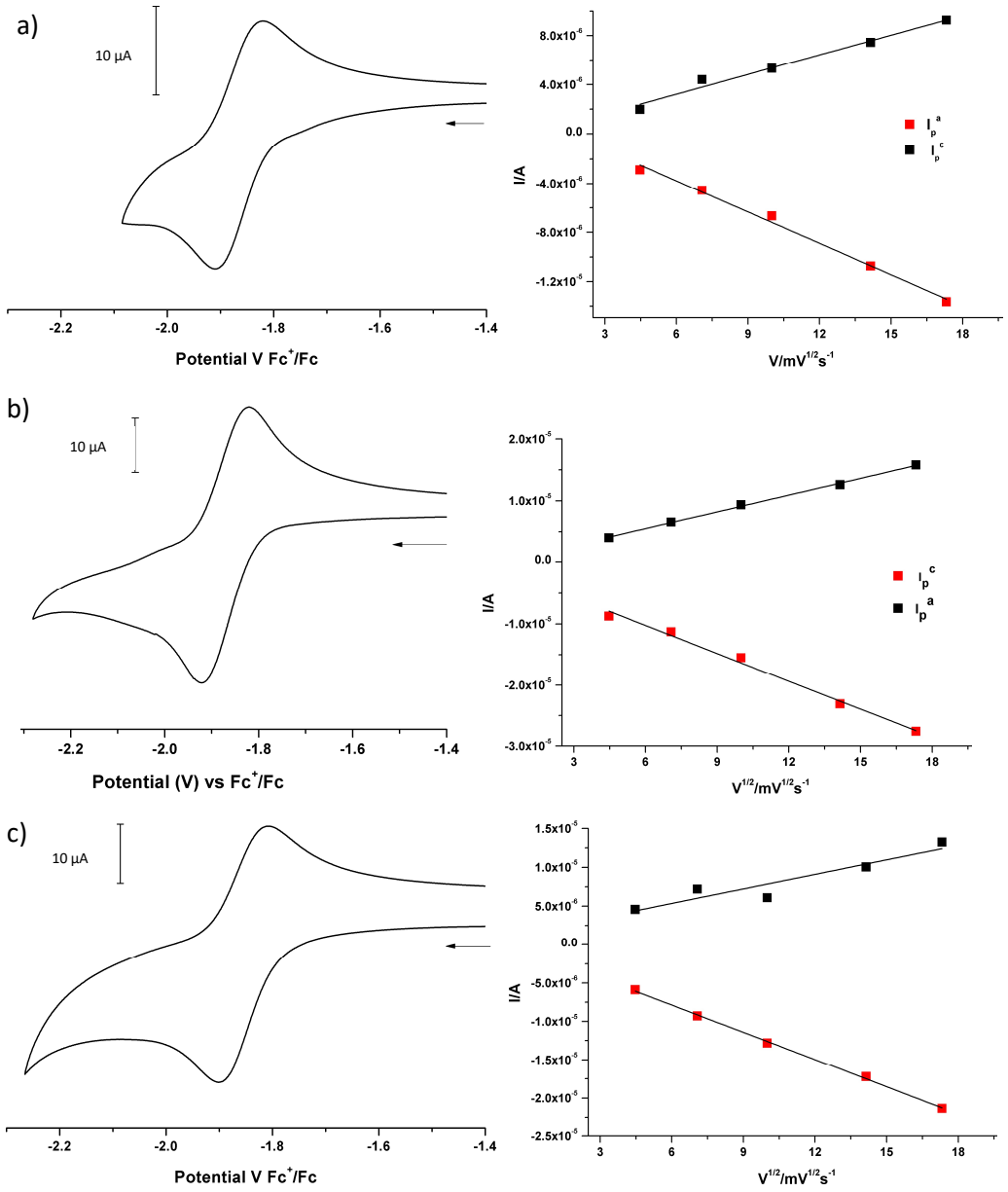


Figure 3.11: Left: Cyclic voltammograms of 1 mM solutions of a) [Ni($q^{6,7}dt^{Me,Me}$)(dppe)] b) [Ni($q^{6,7}dt^{Et,Et}$)(dppe)] c) [Ni($q^{6,7}dt^{H,tBu}$)(dppe)] and in CH_2Cl_2 at 293 K containing [N^nBu_4][BF_4] (0.4 M) as supporting electrolyte at 100 mVs^{-1}. With plots of I_p^a /I_p^c. to the right.

Table 3.4: Electrochemical data for [Ni($qdt^{R1,R2}$)(dppe)] (R^1 = R^2 = Me; R^1 = H, R^2 = ^{t}Bu) and [Ni($q^{6,7}dt^{R1,R2}$)(dppe)] (R^1 = R^2 = Me, Et, Ph; R^1 = H, R^2 = ^{t}Bu) measured at 100 mVs^{-1}.

Complex	$E_{1/2}$ (V vs Fc^+/Fc)
[Ni($qdt^{Me,Me}$)(dppe)]	-1.79
[Ni($qdt^{H,tBu}$)(dppe)]	-1.79
[Ni($q^{6,7}dt^{Me,Me}$)(dppe)]	-1.86
[Ni($q^{6,7}dt^{Et,Et}$)(dppe)]	-1.87
[Ni($q^{6,7}dt^{H,tBu}$)(dppe)]	-1.85

[Ni(qdt^{R1,R2})(dppe)] ($R^1 = R^2 = Me$; $R^1 = H$, $R^2 = {}^tBu$) exhibit a reduction process at $E_{1/2}$ = -1.79 V *vs* Fc^+/Fc and [Ni(q^{6,7}dt^{R1,R2})(dppe)] ($R^1 = R^2 = Me$, Et, Ph; $R^1 = H$, $R^2 = {}^tBu$) possess a reduction process at $E_{1/2}$ = -1.86, -1.87 and -1.85 V *vs* Fc^+/Fc, respectively. Each process exhibits a linear correlation between I_p^c and I_p^a, and the square root of scan rate (Figures 3.10 and 3.11), $I_p^a / I_p^c \approx 1.0$ and $E_p^c - E_p^a$ = 0.10 mV, which compares well to that of the Fc^+/Fc couple ($E_p^c - E_p^a$ = 0.11 mV) recorded under the same conditions as an internal standard. Taken together these data demonstrate that each reduction process for [Ni(qdt^{R1,R2})(dppe)] ($R^1 = R^2 = Me$; $R^1 = H$, $R^2 = {}^tBu$) and [Ni(q^{6,7}dt^{R1,R2})(dppe)] ($R^1 = R^2 = Me$, Et; $R^1 = H$, $R^2 = {}^tBu$) is electrochemically reversible.

3.5.1 A Comparison of the Cyclic Voltammetric Studies of [Ni(qdt^{R1,R2})(dppe)] ($R^1 = R^2 = Me$; $R^1 = H$, $R^2 = {}^tBu$) and [Ni(q^{6,7}dt^{R1,R2})(dppe)] ($R^1 = R^2 = Me$, Et; $R^1 = H$, $R^2 = {}^tBu$)

The potential of the [Ni(qdt^{R1,R2})(dppe)]$^{0/-}$ ($R^1 = R^2 = Me$; $R^1 = H$, $R^2 = {}^tBu$) couple is *ca.* 0.1 V more positive than those of the [Ni(q^{6,7}dt^{R})(dppe)]$^{0/-}$ ($R^1 = R^2 = Me$, Et; $R^1 = H$, $R^2 = {}^tBu$) couple (Table 3.5) consistent with the position of the electron-withdrawing N atoms in each complex.

The electrochemical properties of [Ni(qdt^{R1,R2})(dppe)]$^{0/-}$ ($R^1 = R^2 = Me$; $R^1 = H$, $R^2 = {}^tBu$) and [Ni(q^{6,7}dt^{R1,R2})(dppe)]$^{0/-}$ ($R^1 = R^2 = Me$, Et; $R^1 = H$, $R^2 = {}^tBu$) are similar to those of [(dppe)Ni(dt)] (dt = dt = sdt, 2-pedt, 3-pedt, 4-pedt, Table 3.5) Each [(dppe)Ni(dt)] possesses a reduction process at $E_{1/2}$ = -1.90 to -1.97 V *v*s Fc^+/Fc.[9] Thus, the potentials of the [Ni(qdt^{R1,R2})(dppe)]$^{0/-}$ ($R^1 = R^2 = Me$; $R^1 = H$, $R^2 = {}^tBu$) and [Ni(q^{6,7}dt^{R1,R2})(dppe)]$^{0/-}$ ($R^1 = R^2 = Me$, Et; $R^1 = H$, $R^2 = {}^tBu$) couples are *ca.* 0.1 – 0.2 V less negative than those of [(dppe)Ni(dt)]$^{0/-}$ reflecting the more distant N and fewer N substitutions in [(dppe)Ni(dt)].

The electrochemistries of [Ni(qdt^{R1,R2})(dppe)] ($R^1 = R^2 = Me$; $R^1 = H$, $R^2 = {}^tBu$) and [Ni(q^{6,7}dt^{R1,R2})(dppe)] ($R^1 = R^2 = Me$, Et; $R^1 = H$, $R^2 = {}^tBu$) are significantly different to those of [Ni(p-q^{6,7}dt^{R1,R2})] (Chapter 2, Section 2.6.2). There is a notable shift in reduction potential to more negative potentials for [Ni(qdt^{R1,R2})(dppe)] and [Ni(q^{6,7}dt^{R1,R2})(dppe)] relative to those of [Ni(p-q^{6,7}dt^{R1,R2})] ($R^1 = R^2 = Et$; $R^1 = H$, $R^2 = {}^tBu$) (Table 3.5). Thus, it appears that the coordination of one quinoxaline unit

and one π-accepting dppe ligand is insufficient to raise the potential of the formal $Ni^{II/I}$ couple in [Ni(qdt^{R1,R2})(dppe)] ($R^1 = R^2$ = Me; R^1 = H, R^2 = ^{t}Bu) and [Ni(q^{6,7}dt^{R1,R2})(dppe)] ($R^1 = R^2$ = Me, Et; R^1 = H, R^2 = ^{t}Bu) over those of [Ni(p-q^{6,7}dt^{R1,R2})] ($R^1 = R^2$ = Me, Et, Ph; R^1 = H, R^2 = ^{t}Bu). However, the [Ni(qdt)(dppe)] frameworks appears to uniformly support reversible electrochemistry in contrast to that found for [Ni(p-q^{6,7}dt^{R1,R2})] ($R^1 = R^2$ = Me, Et, Ph; R^1 = H, R^2 = ^{t}Bu, Chapter 2) that demonstrate quasireversible ($R^1 = R^2$ = Et; R^1 = H, R^2 = ^{t}Bu) or irreversible ($R^1 = R^2$ = Me and Ph) electrochemistry.

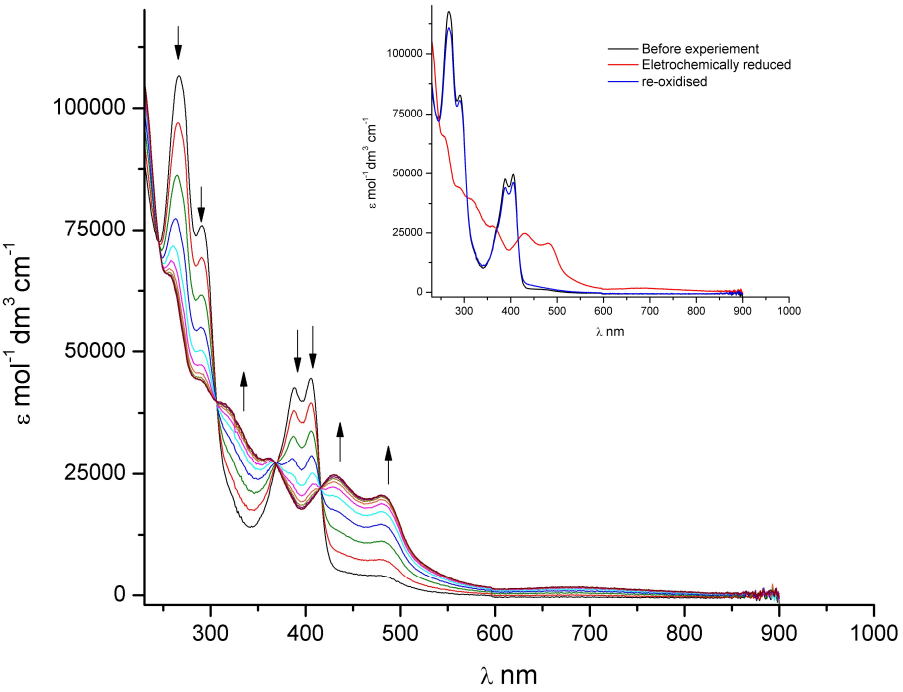
Table 3.5: Electrochemistry of [Ni(qdt^{R1,R2})(dppe)] ($R^1 = R^2$ = Me; R^1 = H, R^2 = ^{t}Bu) and [Ni(q^{6,7}dt^{R1,R2})(dppe)] ($R^1 = R^2$ = Me, Et; R^1 = H, R^2 = ^{t}Bu) to compared to [Ni(q^{6,7}dt^{R})$_2$] (R = Me, Et and ^{t}Bu) and [(dppe)Ni(dt)] (dt = sdt, 2-pedt, 3-pedt, 4-pedt), measured at 100 mVs^{-1}.

Complex	$E_{1/2}$ (V vs Fc^+/Fc)	E_{pc} (V vs Fc^+/Fc)
[Ni(qdt^{Me})(dppe)]	-1.79	-1.87
[Ni(qdt^{tBu})(dppe)]	-1.79	-1.84
[Ni(q^{6,7}dt^{Me})(dppe)]	-1.86	-1.91
[Ni(q^{6,7}dt^{Et})(dppe)]	-1.87	-1.92
[Ni(q^{6,7}dt^{tBu})(dppe)]	-1.85	-1.90
[(dppe)Ni(sdt)]	-1.97	-
[(dppe)Ni(2-pedt)]	-1.94	-
[(dppe)Ni(3-pedt)]	-1.92	-
[(dppe)Ni(4-pedt)]	-1.90	-
[Ni(p-q^{6,7}dt^{Et,Et})]	-1.47	-1.51
[Ni(p-q^{6,7}dt^{tBu,tBu})]	-1.45	-1.51
[Ni(p-q^{6,7}dt^{Me,Me})]	-	-1.42
[Ni(p-q^{6,7}dt^{Ph,Ph})]	-	-1.43

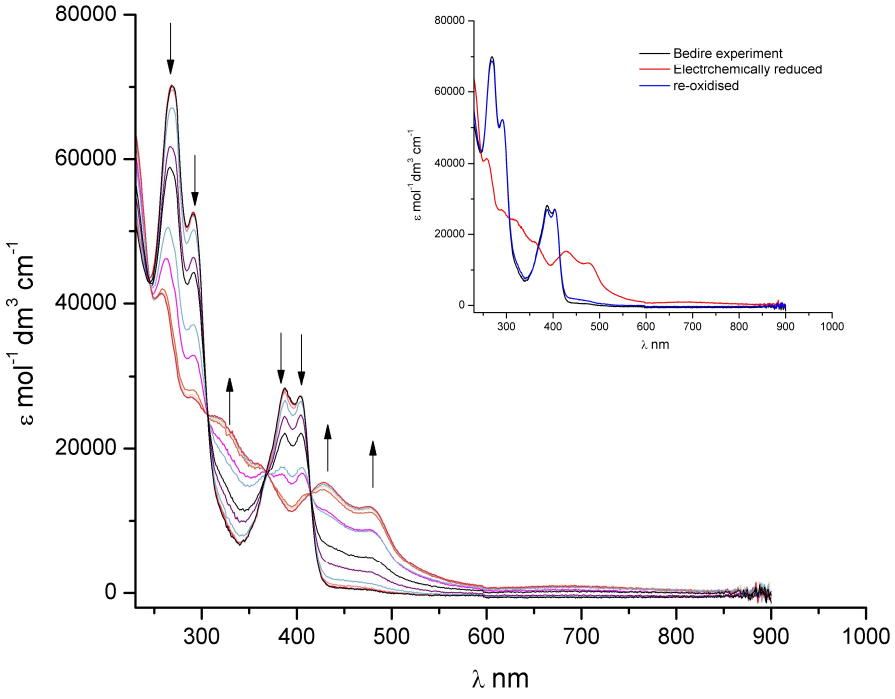
3.6 Spectroelectrohemistry of [Ni(qdt^{R1,R2})(dppe)] ($R^1 = R^2$ = Me; R^1 = H, R^2 = ^{t}Bu)) and [Ni(q^{6,7}dt^{R1,R2})(dppe)] ($R^1 = R^2$ = Me, Et; R^1 = H, R^2 = ^{t}Bu)

The electrochemical reduction processes of [Ni(qdt^{R1,R2})(dppe)] ($R^1 = R^2$ = Me; R^1 = H, R^2 = ^{t}Bu) and [Ni(q^{6,7}dt^{R1,R2})(dppe)] ($R^1 = R^2$ = Me, Et; R^1 = H, R^2 = ^{t}Bu) were explored by spectroelectrochemical methods to determine if these processes were chemically reversible. The changes in the UV/vis spectra of 1mM solutions of [Ni(qdt^{R1,R2})(dppe)] ($R^1 = R^2$ = Me; R^1 = H, R^2 = ^{t}Bu) and [Ni(q^{6,7}dt^{R1,R2})(dppe)] ($R^1 = R^2$ = Me, Et; R^1 = H, R^2 = ^{t}Bu) in CH_2Cl_2 with [N^{n}Bu$_4$][BF_4] as supporting electrolyte at 253 K, were monitored during the electrochemical reductions. The spectra observed during the reductions of [Ni(qdt^{R1,R2})(dppe)] ($R^1 = R^2$ = Me; R^1 = H, R^2 = ^{t}Bu) and [Ni(q^{6,7}dt^{R1,R2})(dppe)] ($R^1 = R^2$ = Me, Et; R^1 = H, R^2 = ^{t}Bu) are shown in Figure 3.12.

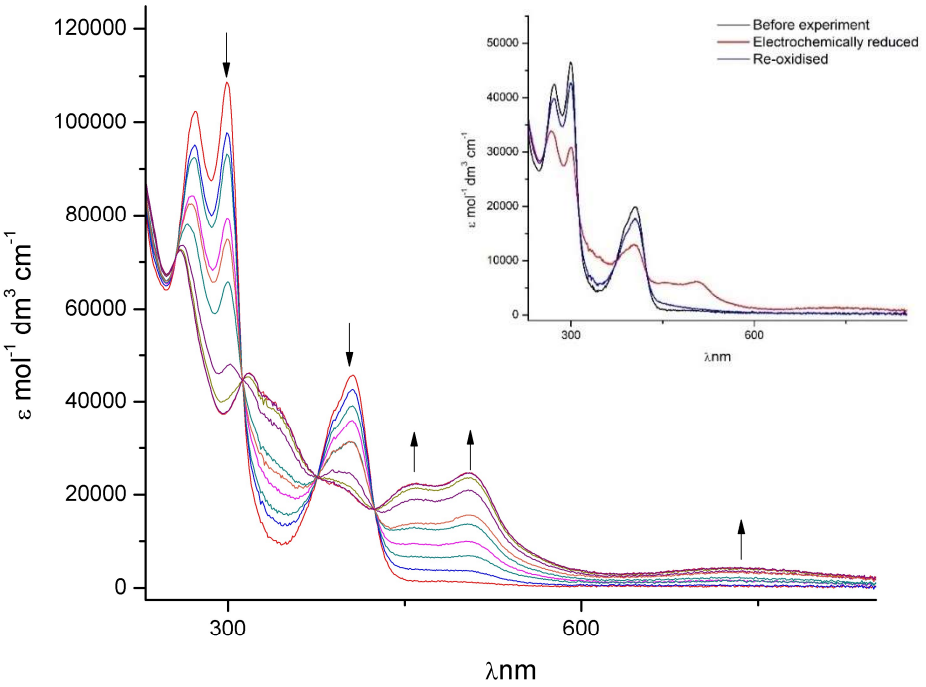
a)


Before experiement
Eletrochemically reduced
re-oxidised
ε mol-1 dm3 cm-1
λ nm

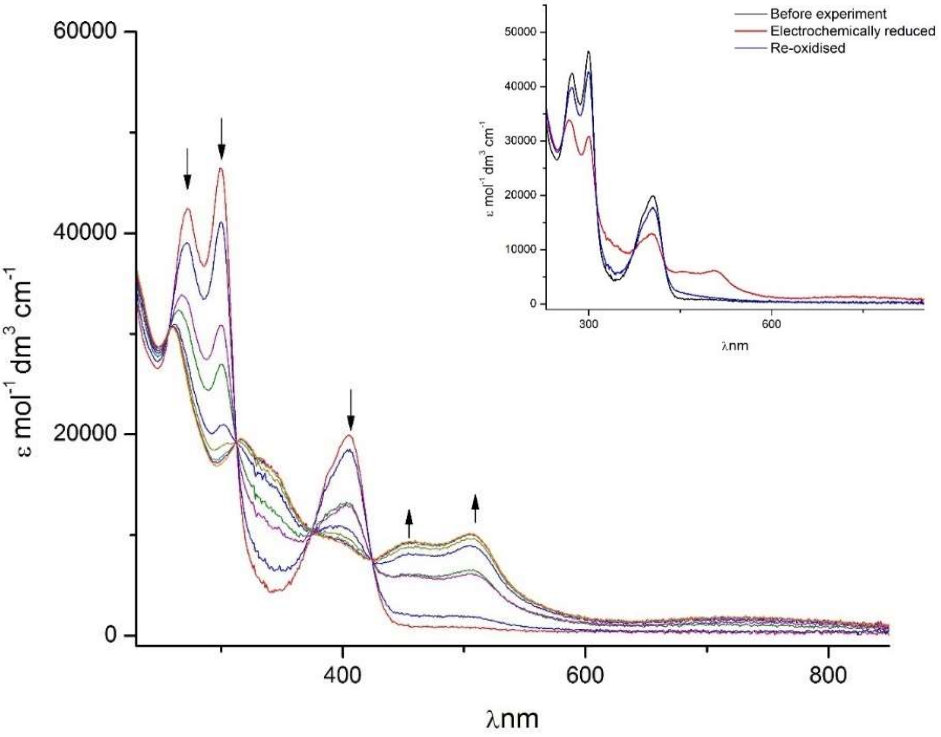
b)


Bedire experiment
Electrchemically reduced
re-oxidised
ε mol-1 dm3 cm-1
λ nm

c)


120000
100000
80000
60000
40000
20000
0
ε mol-1 dm3 cm-1
300
600
λnm
Before experiment
Electrochemically reduced
Re-oxidised
50000
40000
30000
20000
10000
0
ε mol-1 dm3 cm-1
300
600
λnm

d)


60000
40000
20000
0
ε mol-1 dm3 cm-1
400
600
800
λnm
Before experiment
Electrochemically reduced
Re-oxidised
50000
40000
30000
20000
10000
0
ε mol-1 dm3 cm-1
300
600
λnm

e)

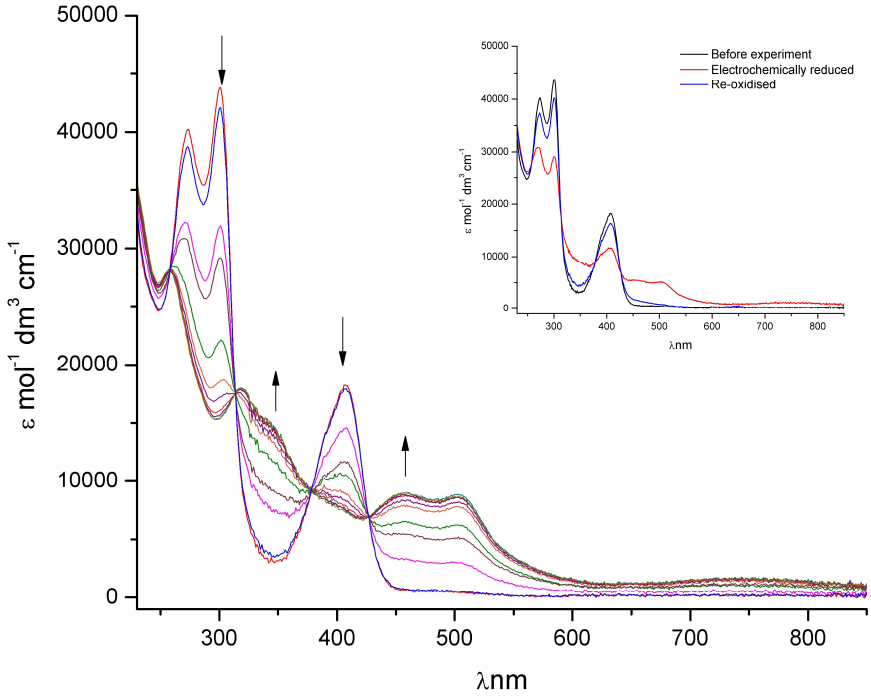


Figure 3.12: Sequential UV/Vis spectra recorded during the reduction of a solution of a) [Ni(qdt^{Me,Me})(dppe)], b) [Ni(qdt^{H,tBu})(dppe)], c) [Ni(q^{6,7}dt^{Me,Me})(dppe)] , d) [Ni(q^{6,7}dt^{Et,Et})(dppe)] and e) [Ni(q^{6,7}dt^{H,tBu})(dppe)] in CH_2Cl_2 at 253 K containing [N^{n}Bu$_4$][BF_4] (0.4 M) as supporting electrolyte. Insert shows the initial spectrum (black), the spectrum of the reduced species (red) and the final spectrum upon re-oxidised (blue).

Within each series of spectra the absorption bands associated with [Ni(qdt^{R1,R2})(dppe)] ($R^1 = R^2 = Me$; $R^1 = H$, $R^2 = {}^tBu$) and [Ni(q^{6,7}dt^{R1,R2})(dppe)] ($R^1 = R^2 = Me$, Et; $R^1 = H$, $R^2 = {}^tBu$) decrease in intensity and those associated with [Ni(qdt^{R1,R2})(dppe)]$^-$ and [Ni(q^{6,7}dt^{R1,R2})(dppe)]$^-$ grow in. The UV/vis spectra of [Ni(qdt^{R1,R2})(dppe)] ($R^1 = R^2 = Me$; $R^1 = H$, $R^2 = {}^tBu$) and [Ni(q^{6,7}dt^{R1,R2})(dppe)] ($R^1 = R^2 = Me$, Et; $R^1 = H$, $R^2 = {}^tBu$) are similar to one another; [Ni(qdt^{R1,R2})(dppe)] ($R^1 = R^2 = Me$; $R^1 = H$, $R^2 = {}^tBu$) exhibit four clearly resolved absorption bands at *ca.* 269, 292, 386 and 406 nm whereas [Ni(q^{6,7}dt^{R1,R2})(dppe)] ($R^1 = R^2 = Me$, Et; $R^1 = H$, $R^2 = {}^tBu$) exhibit bands at *ca.* 273, 301 and 409 nm with the band at 409 nm possessing a shoulder at higher energy. The relative intensities of each band (Table 3.6) suggest that those transitions at wavelengths <300 nm may be assigned to intraligand π→π* processes whereas those between *ca.* 386-406 nm may be assigned to ligand-to-metal charge transfer (LMCT). The HOMO calculated for each complex (see Section 3.7) reveals significant Sπ character and it is likely that the lowest

energy LMCT process involves this orbital. The UV/vis spectra of [Ni(qdt^{R1,R2})(dppe)] ($R^1 = R^2 = Me$; $R^1 = H$, $R^2 = {}^tBu$) and [Ni(q^{6,7}dt^{R1,R2})(dppe)] ($R^1 = R^2 = Me$, Et; $R^1 = H$, $R^2 = {}^tBu$) are also similar to one another with the notable differences in the UV/vis spectra of their reduced counterparts being the development of two bands at *ca.* 433 and 485 nm for [Ni(qdt^{R1,R2})(dppe)]$^-$ ($R^1 = R^2 = Me$; $R^1 = H$, $R^2 = {}^tBu$) and at *ca.* 456 and 505 nm for [Ni(q^{6,7}dt^{R1,R2})(dppe)]$^-$ ($R^1 = R^2 = Me$, Et; $R^1 = H$, $R^2 = {}^tBu$). The relative intensities of these transitions (Table 3.6) also indicates that they may be assigned to LMCT. The spectroelectrochemical reductions are also associated with the growth of a weak band at *ca.* 740-760 nm (ε = 110-650 mol^{-1} dm^3 cm^{-1}), which, based on its relative energy and intensity, is likely to be associated with a primarily *d-d* transition localized on the Ni centre. The isosbestic points (Table 3.6) for each series of spectra indicate that the reduction of [Ni(qdt^{R1,R2})(dppe)] ($R^1 = R^2 = Me$; $R^1 = H$, $R^2 = {}^tBu$) and [Ni(q^{6,7}dt^{R1,R2})(dppe)] ($R^1 = R^2 = Me$, Et; $R^1 = H$, $R^2 = {}^tBu$) generates [Ni(qdt^{R1,R2})(dppe)]$^-$ and [Ni(q^{6,7}dt^{R1,R2})(dppe)]$^-$, respectively, directly and without the involvement of any long-lived intermediates. The electrochemical reoxidation of [Ni(qdt^{H,tBu})(dppe)]$^-$, [Ni(q^{6,7}dt^{Me,Me})(dppe)]$^-$ and [Ni(q^{6,7}dt^{H,tBu})(dppe)]$^-$ leads to spectra that are essentially identical to [Ni(qdt^{H,tBu})(dppe)], [Ni(q^{6,7}dt^{Me,Me})(dppe)] and [Ni(q^{6,7}dt^{H,tBu})(dppe)], respectively. Thus, the reduction process for these complexes is chemically reversible on the time-scale of the electrochemical experiment. The electrochemical reoxidations of [Ni(qdt^{Me,Me})(dppe)]$^-$ and [Ni(q^{6,7}dt^{Et,Et})(dppe)]$^-$ do not show a complete regeneration of the UV/vis spectra of [Ni(qdt^{Me,Me})(dppe)] or [Ni(q^{6,7}dt^{Et,Et})(dppe)]$^-$, respectively. However, the UV/vis spectral profiles for the oxidised and reduced forms are similar so, while the reduction process for these complexes is not completely chemically reversible, oxidation does appear to regenerate the neutral forms of the complexes.

Table 3.6: The UV-Vis absorbance of [Ni(qdt^{R1,R2})(dppe)] and [Ni(qdt^{R1,R2})(dppe)]$^-$ ($R^1 = R^2$ = Me; R^1 = H, R^2 = ^{t}Bu) and [Ni(q^{6,7}dt^{R1,R2})(dppe)] and [Ni(q^{6,7}dt^{R1,R2})(dppe)]$^-$ ($R^1 = R^2$ = Me, Et; R^1 = H, R^2 = ^{t}Bu) with the isobestic points CH_2Cl_2 / 0.4 M [N^{n}Bu$_4$][BF_4] at -20 ºC.

Complex	Absorbance / nm (extinction coefficient /mol^{-1}dm^{3}cm^{-1})	Isobestic points (nm)
[Ni(qdt^{Me,Me})(dppe)]	267 (116000), 290 (82400), 388 (46200) and 407 (49200)	245, 308, 371 and 415
[Ni(qdt^{Me,Me})(dppe)]$^-$	263 (64900), 298 (43100), 321 (37900), 368 (28300), 433 (23900) and 485 (20000), 692 (2100)	
[Ni(qdt^{H,tBu})(dppe)]	269 (69700), 292 (52500), 386 (27900) and 406 (26400)	244, 307, 366 and 415
[Ni(qdt^{H,tBu})(dppe)]$^-$	261 (40900), 293 (27100), 366 (18200), 432 (15200) and 480 (11800), 683 (685)	
[Ni(q^{6,7}dt^{Me,Me})(dppe)]	273 (10200), 301 (10700) and 409 (4600)	256, 313, 374 and 425
[Ni(q^{6,7}dt^{Me,Me})(dppe)]$^-$	260 (7210), 321(4480), 346 (38500), 456 (2150), 505(2490) and 7733 (501)	
[Ni(q^{6,7}dt^{Et,Et})(dppe)]	273(41700), 301 (46200) and 404 (19700)	259, 310, 375 and 426
[Ni(q^{6,7}dt^{Et,Et})(dppe)]$^-$	269(33500), 301(30300), 404 (12500) and 508 (6550), 737 (1300)	
[Ni(q^{6,7}dt^{H,tBu})(dppe)]	273 (4020), 304 (4340) and 407 (1840)	259, 313, 379 and 426
[Ni(q^{6,7}dt^{H,tBu})(dppe)]$^-$	259 (3020), 317 (2880) 409 (1150) and 505 (520), 746 (110)	
[Ni(p-q^{6,7}dt^{Et,Et})]	232 (78600), 282 (55500), 316 (42800), 351(29700) and 408 (21900).	252, 298, 355, 428 and 451
[Ni(p-q^{6,7}dt^{Et,Et})]$^-$	241 (71000), 282 (506000), 314 (40700), 346 (41100) and 433 (18000)	
[Ni(p-q^{6,7}dt^{H,tBu})]	232 (78700), 282 (55600), 316 (42900), 351 (29800) and 408 (21900).	250, 298, 353 and 465
[Ni(p-q^{6,7}dt^{H,tBu})]$^-$	238 (91100), 277 (64300), 314 (91100), 348 (49200) and 440 (21300)	

The UV/vis spectroelectrochemical properties of [Ni(qdt^{R1,R2})(dppe)] ($R^1 = R^2$ = Me; R^1 = H, R^2 = ^{t}Bu) and [Ni(q^{6,7}dt^{R1,R2})(dppe)] ($R^1 = R^2$ = Me, Et; R^1 = H, R^2 = ^{t}Bu) are similar to those of [Ni(p-q^{6,7}dt^{R1,R2})] ($R^1 = R^2$ = Et; R^1 = H, R^2 = ^{t}Bu, Chapter 2, Section 2.7, Table 3.6). Each series shows bands that may be assigned to ligand-to-metal charge transfer involving orbitals of significant S- and Ni-character. [Ni(qdt^{R1,R2})(dppe)] ($R^1 = R^2$ = Me; R^1 = H, R^2 = ^{t}Bu) and [Ni(q^{6,7}dt^{R1,R2})(dppe)] (R^1

= R^2 = Me, Et; R^1 = H, R^2 = ^{t}Bu) demonstrate the growth of low-energy bands at *ca.* 740 – 760 nm that may be assigned to transitions with significant *d-d* character. A clear difference in the spectroelectrochemical behaviours of [Ni(qdt^{R1,R2})(dppe)] (R^1 = R^2 = Me; R^1 = H, R^2 = ^{t}Bu) and [Ni(q^{6,7}dt^{R1,R2})(dppe)] (R^1 = R^2 = Me, Et; R^1 = H, R^2 = ^{t}Bu) and [Ni(p-q^{6,7}dt^{R1,R2})] (R^1 = R^2 = Et; R^1 = H, R^2 = ^{t}Bu) is that the reduction processes for [Ni(qdt^{R1,R2})(dppe)] (R^1 = R^2 = Me; R^1 = H, R^2 = ^{t}Bu) and [Ni(q^{6,7}dt^{R1,R2})(dppe)] (R^1 = R^2 = Me, Et; R^1 = H, R^2 = ^{t}Bu) are essentially chemically reversible on the timescale of the experiment whereas those for [Ni(p-q^{6,7}dt^{R1,R2})] (R^1 = R^2 = Et; R^1 = H, R^2 = ^{t}Bu) do not appear to be chemically reversible. Thus, given the chemical and electrochemical reversibility of the [Ni(qdt^{R1,R2})(dppe)]$^{0/-}$ (R^1 = R^2 = Me; R^1 = H, R^2 = ^{t}Bu) and [Ni(q^{6,7}dt^{R1,R2})(dppe)] $^{0/-}$ (R^1 = R^2 = Me, Et; R^1 = H, R^2 = ^{t}Bu) couples, these complexes may show promise as more robust catalysts for H_2 production relative to their [Ni(p-q^{6,7}dt^{R1,R2})] (R^1 = R^2 = Et; R^1 = H, R^2 = ^{t}Bu) counterparts.

2.7 EPR Studies of [Ni(qdt^{R1,R2})(dppe)]$^-$ (R^1 = R^2 = Me; R^1 = H, R^2 = ^{t}Bu) and [Ni(q^{6,7}dt^{R1,R2})(dppe)]$^-$ (R^1 = R^2 = Me, Et, Ph; R^1 = H, R^2 = ^{t}Bu)

X-band EPR spectra of electrochemically generated of [Ni(qdt^{R1,R2})(dppe)] (R^1 = R^2 = Me; R^1 = H, R^2 = ^{t}Bu) and [Ni(q^{6,7}dt^{R1,R2})(dppe)] (R^1 = R^2 = Me, Et; R^1 = H, R^2 = ^{t}Bu) were recorded at room temperature and at 77 K in CH_2Cl_2 containing [N^{n}Bu$_4$][BF$_4$] (0.4 M) (Figures 3.13 – 3.16). The spin Hamiltonian parameters derived from the simulation of each spectrum are shown in Table 3.7.

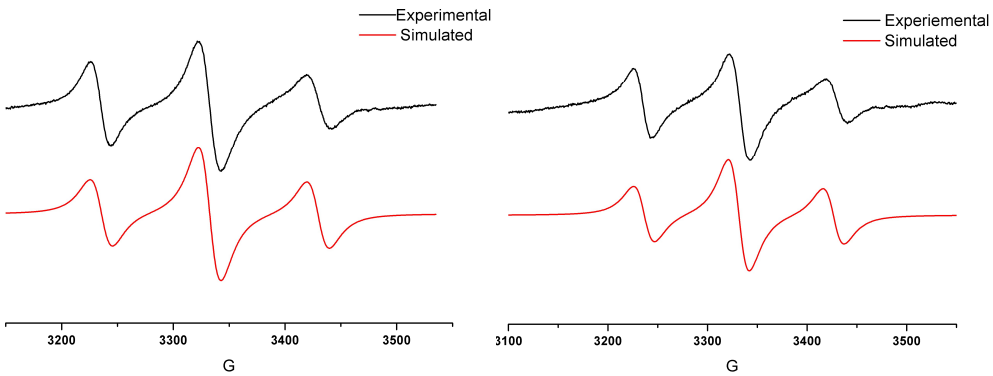


Figure 3.13: The X-band fluid spectrum of [Ni(qdt^{Me,Me})(dppe)]$^-$ b)[Ni(qdt^{H,tBu})(dppe)]$^-$ in CH_2Cl_2 containing [N^{n}Bu$_4$][BF$_4$] (0.1 M) at 120 K (black), simulated spectrum (red).

.

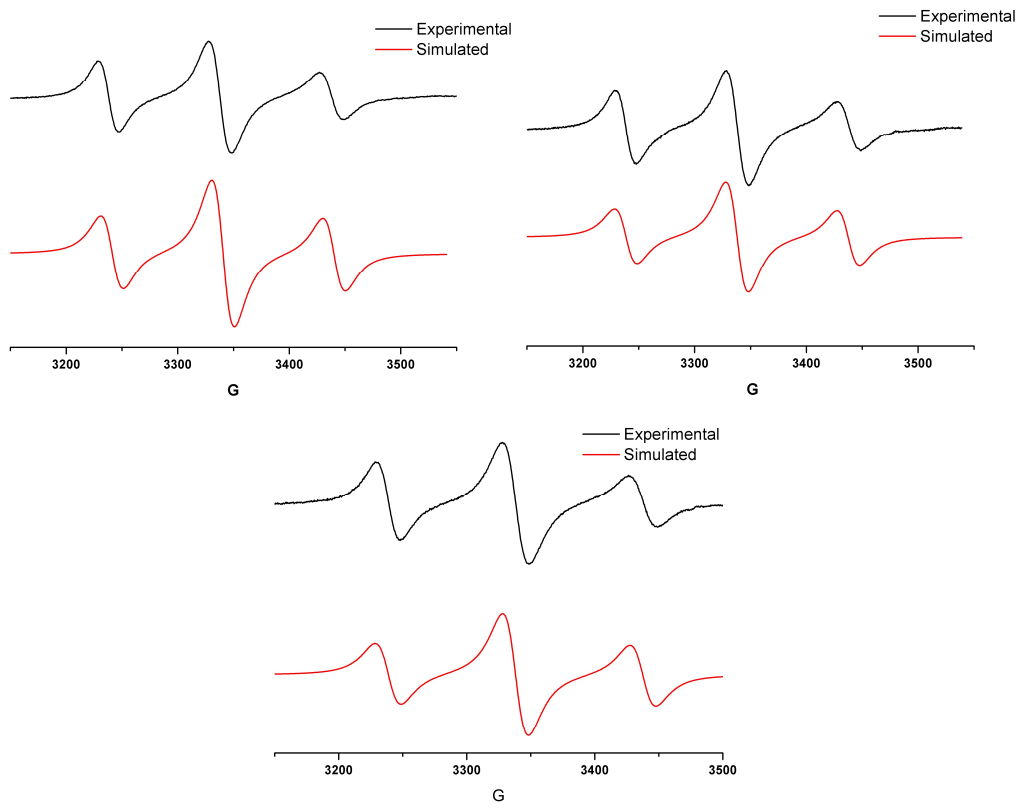


Figure 3.14: The X-band fluid spectrum of a) $[Ni(q^{6,7}dt^{Me,Me})(dppe)]^-$ b)$[Ni(q^{6,7}dt^{Et,Et})(dppe)]^-$ and c) $[Ni(q^{6,7}dt^{H,tBu})(dppe)]^-$ in CH_2Cl_2 containing $[N^nBu_4][BF_4]$ (0.1 M) at 120 K (black), simulated spectrum (red).

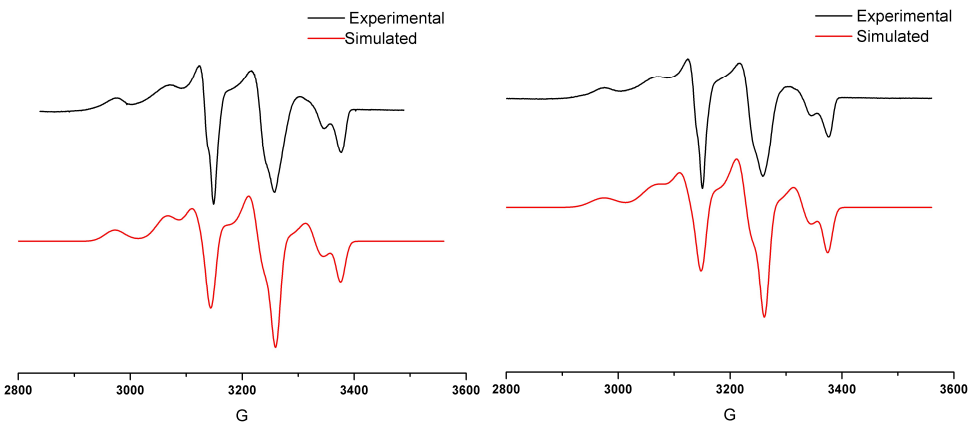


Figure 3.15: The X-band frozen spectrum of a) $[Ni(qdt^{Me,Me})(dppe)]^-$ b)$[Ni(qdt^{H,tBu})(dppe)]^-$ in CH_2Cl_2 containing $[N^nBu_4][BF_4]$ (0.1 M) at 120 K (black), simulated spectrum (red).

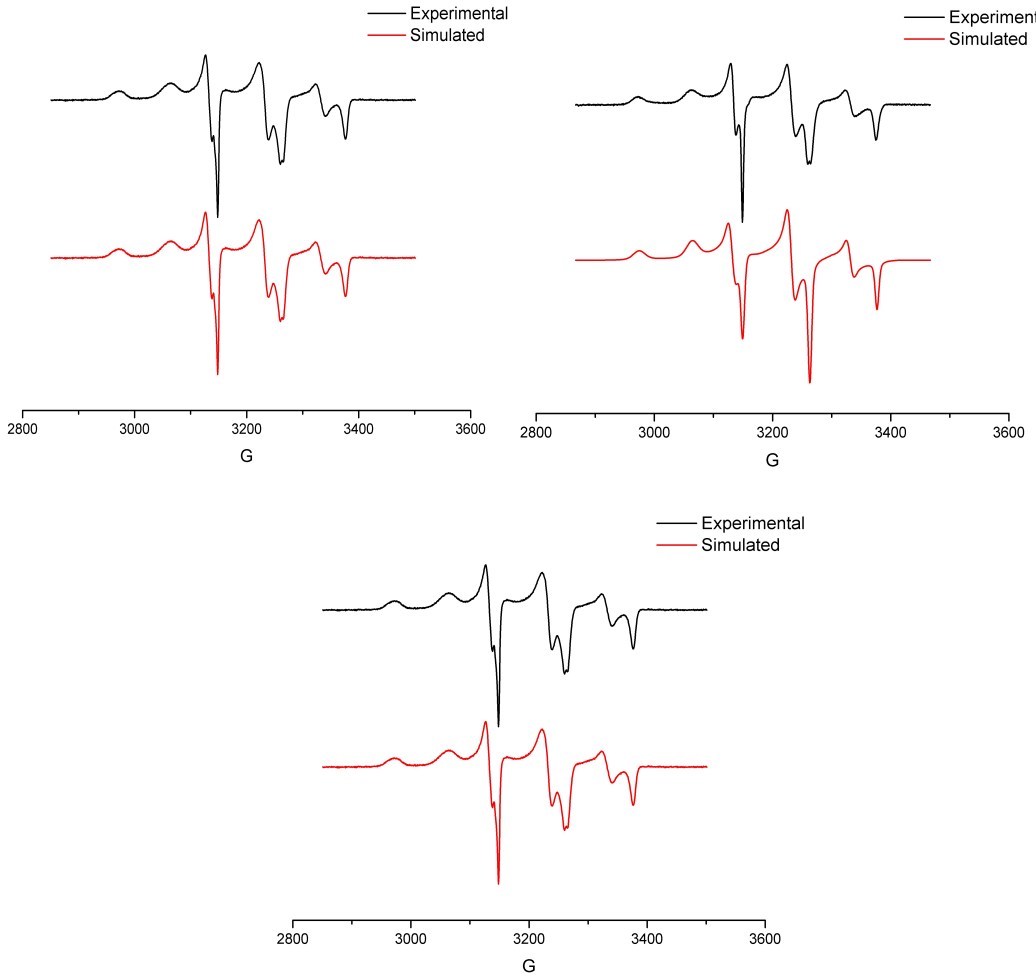


Figure 3.16: The X-band frozen spectrum of a) $[Ni(q^{6,7}dt^{Me,Me})(dppe)]^-$ b)$[Ni(q^{6,7}dt^{Et,Et})(dppe)]^-$ and c) $[Ni(q^{6,7}dt^{H,tBu})(dppe)]^-$ in CH_2Cl_2 containing $[N^nBu_4][BF_4]$ (0.1 M) at 120 K (black), simulated spectrum (red).

Table 3.7: Spin Hamiltonian parameters derived from simulations of the X-band room temperature frozen solutions of $[Ni(qdt^{R1,R2})(dppe)]^-$ ($R^1 = R^2 = Me$; $R^1 = H$, $R^2 = {}^tBu$) and $[Ni(q^{6,7}dt^{R1,R2})(dppe)]^-$ ($R^1 = R^2 = Me$, Et; $R^1 = H$, $R^2 = {}^tBu$). The ^{31}P hyperfine coupling constants, a_{iso}, a_{11}, a_{22} and a_{33}, are in units of x 10^{-4} cm^{-1}.

Complex	g_{iso}	g_{11}	g_{22}	g_{33}	a_{iso}	a_{11}	a_{22}	a_{33}
$[Ni(qdt^{Me,Me})(dppe)]^-$	2.0909	2.166	2.057	2.035	95.1	92.0	102.0	113.0
$[Ni(qdt^{H,tBu})(dppe)]^-$	2.0900	2.165	2.057	2.036	97.0	92.0	102.0	116.0
$[Ni(q^{6,7}dt^{Me,Me})(dppe)]^-$	2.068	2.217	2.061	2.0613	99.5	90.0	100.0	113.7
$[Ni(q^{6,7}dt^{Et,Et})(dppe)]^-$	2.0866	2.163	2.051	2.035	99.5	90.0	99.0	113.7
$[Ni(q^{6,7}dt^{H,tBu})(dppe)]^-$	2.0836	2.165	2.053	2.033	99.5	90.0	100.0	113.7
$[Ni^I(dppe)((CN)_2C_2S_2)]^{-12}$	2.094	2.177	2.045	2.045	98.5	92.7	102.6	102.6

The fluid solution EPR spectrum of each of $[Ni(qdt^{R1,R2})(dppe)]^-$ ($R^1 = R^2 = Me$; $R^1 = H$, $R^2 = {}^tBu$) and $[Ni(q^{6,7}dt^{R1,R2})(dppe)]^-$ ($R^1 = R^2 = Me$, Et; $R^1 = H$, $R^2 = {}^tBu$) present three lines with features in an approximate intensity ratio of 1:2:1 that result from the coupling of the unpaired electron with two equivalent ^{31}P nuclei (I = 1/2 ; natural abundance 100%) derived from the dppe ligand in each complex. Each spectrum is similar with only small variations in g_{iso} (2.068-2.0909) and a_{iso} (95.1-99.5). The frozen solution EPR spectra of $[Ni(qdt^{R1,R2})(dppe)]^-$ ($R^1 = R^2 = Me$; $R^1 = H$, $R^2 = {}^tBu$) and $[Ni(q^{6,7}dt^{R1,R2})(dppe)]^-$ ($R^1 = R^2 = Me$, Et; $R^1 = H$, $R^2 = {}^tBu$) are complex. Nevertheless, each spectrum could be simulated satisfactorily by assuming a rhombic symmetry and coupling to two equivalent ^{31}P nuclei with associated g_{11}, g_{22}, g_{33}, a_{11}, a_{22} and a_{33} spin Hamiltonian parameters (Table 3.7).

The frozen solution EPR spectra of $[(dppe)Ni(dt)]^-$ (dt = sdt, 2-pedt, 3-pedt, 4-pedt[10] and $S_2C_4N_2$[15]) have been reported previously and the frozen solution EPR spectrum of $[(dppe)Ni(S_2C_4N_2)]^-$ is shown in Figure 3.17 as an example.[12] The spectrum possesses a similar profile to those of $[Ni(qdt^{R1,R2})(dppe)]^-$ ($R^1 = R^2 = Me$; $R^1 = H$, $R^2 = {}^tBu$) and $[Ni(q^{6,7}dt^{R1,R2})(dppe)]^-$ ($R^1 = R^2 = Me$, Et; $R^1 = H$, $R^2 = {}^tBu$) (Figure 3.15 and 3.16). The frozen solution EPR spectra of $[Ni(qdt^{R1,R2})(dppe)]^-$ ($R^1 = R^2 = Me$; $R^1 = H$, $R^2 = {}^tBu$) and $[Ni(q^{6,7}dt^{R1,R2})(dppe)]^-$ are significantly different from the frozen solution EPR spectra of $[Ni(p\text{-}q^{6,7}dt^{Et,Et})]^-$ and $[Ni(p\text{-}q^{6,7}dt^{H,tBu})]^-$. These differences arise from (i) the lack of ^{31}P coordination in $[Ni(p\text{-}q^{6,7}dt^{Et,Et})]^-$ and $[Ni(p\text{-}q^{6,7}dt^{H,tBu})]^-$ and (ii) the lower local symmetry about the Ni centre in $[Ni(qdt^{R1,R2})(dppe)]^-$ ($R^1 = R^2 = Me$; $R^1 = H$, $R^2 = {}^tBu$) and $[Ni(q^{6,7}dt^{R1,R2})(dppe)]^-$ ($R^1 = R^2 = Me$, Et; $R^1 = H$, $R^2 = {}^tBu$), which contain π-acceptor dppe and π-donor

dithiolate ligands, relative to $[Ni(p\text{-}q^{6,7}dt^{Et,Et})]^-$ and $[Ni(p\text{-}q^{6,7}dt^{H,tBu})]^-$, which contain π-donor ligands only.

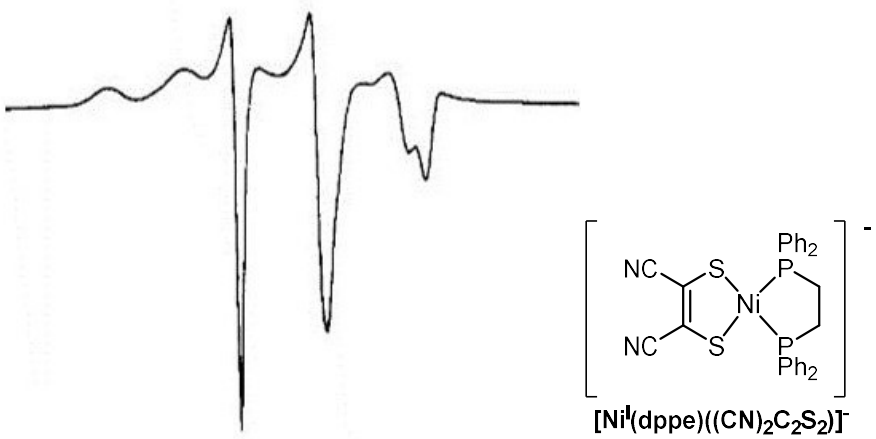


Figure 3.17: The X-band frozen spectrum (left) of $[Ni^I(dppe)((CN)_2C_2S_2)]^-$ (right) reported by Bowmaker *et al.*[12]

DFT calculations (Section 3.7) on $[Ni(qdt^{R1,R2})(dppe)]^-$ ($R^1 = R^2 = Me$; $R^1 = H$, $R^2 = {}^tBu$) and $[Ni(q^{6,7}dt^{R1,R2})(dppe)]^-$ ($R^1 = R^2 = Me$, Et; $R^1 = H$, $R^2 = {}^tBu$) reveal a SOMO in these complexes that results from Ni d_{xy} and S-thiolate/P-phosphine σ-orbital combinations. The contributions to the SOMO are *ca.* 24.9 (Ni), 30.3 (S) and 15.1 % (P); the significant P contribution to the SOMO results in well-resolved ^{31}P couplings in the frozen and solution spectra.

3.8 Cyclic Voltammetric Studies of $[Ni(qdt^{R1,R2})(dppe)]^-$ ($R^1 = R^2 = Me$; $R^1 = H$, $R^2 = {}^tBu$) and $[Ni(q^{6,7}dt^{R1,R2})(dppe)]^-$ ($R^1 = R^2 = Me$, Et, Ph; $R^1 = H$, $R^2 = {}^tBu$) in the presence of TFA

The potential of $[Ni(qdt^{R1,R2})(dppe)]$ ($R^1 = R^2 = Me$; $R^1 = H$, $R^2 = {}^tBu$) and $[Ni(q^{6,7}dt^{R1,R2})(dppe)]$ ($R^1 = R^2 = Me$, Et, Ph; $R^1 = H$, $R^2 = {}^tBu$) as catalysts for H^+ reduction was investigated following the electrochemical protocols developed at Nottingham.[13] Cyclic voltammograms of $[Ni(qdt^{R1,R2})(dppe)]$ ($R^1 = R^2 = Me$; $R^1 = H$, $R^2 = {}^tBu$) and $[Ni(q^{6,7}dt^{R1,R2})(dppe)]$ ($R^1 = R^2 = Me$, Et, Ph; $R^1 = H$, $R^2 = {}^tBu$) in $[N^nBu_4][BF_4]$ (0.4 M) in CH_2Cl_2 at 293 K under Ar and with increasing concentrations of TFA are shown in Figures 3.18 and 3.19, respectively.

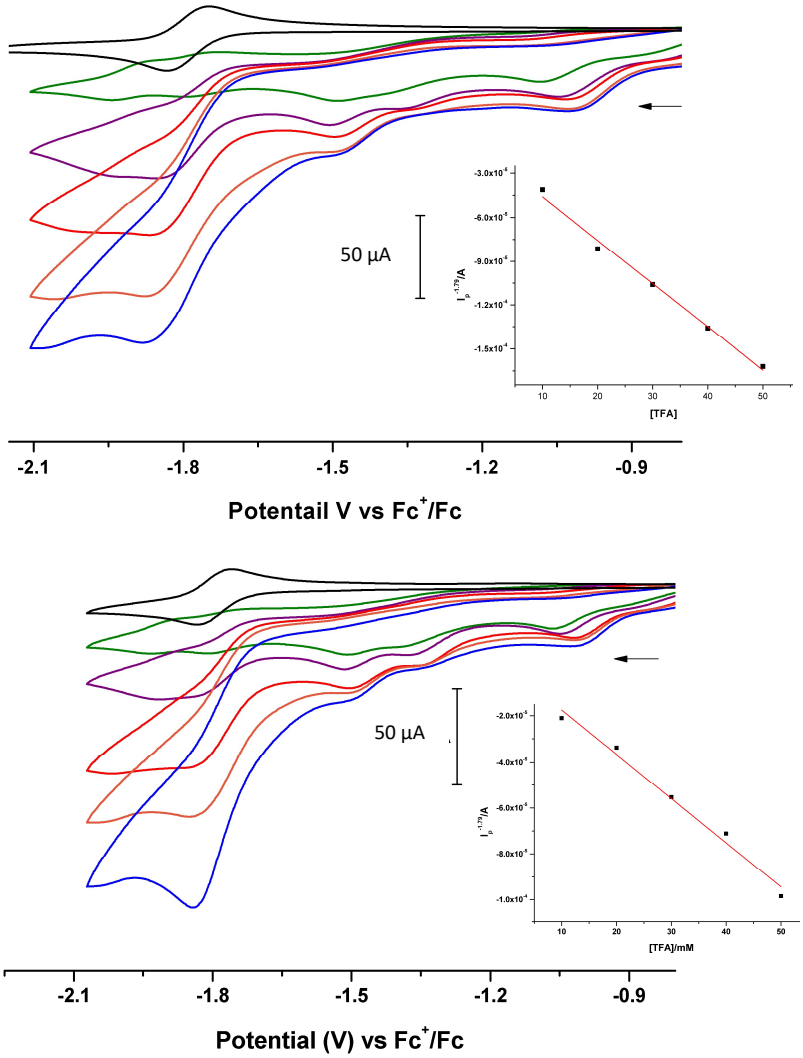


Figure 3.18: Cyclic voltammograms of 1 mM [Ni($qdt^{Me,Me}$)(dppe)] (top) and [Ni($qdt^{H,tBu}$)(dppe)] (bottom) in CH_2Cl_2 at 293 K containing 0.4 mM [N^nBu_4][BF_4] and increasing concentrations of TFA at of 0 mM (black), 10mM (green), 20 mM (purple), 30 mM (red), 40 mM (orange) and 50 mM (blue). Inset: Plots of I_p^c vs. [TFA] observed in the cyclic voltammograms (100 mVs^{-1}).

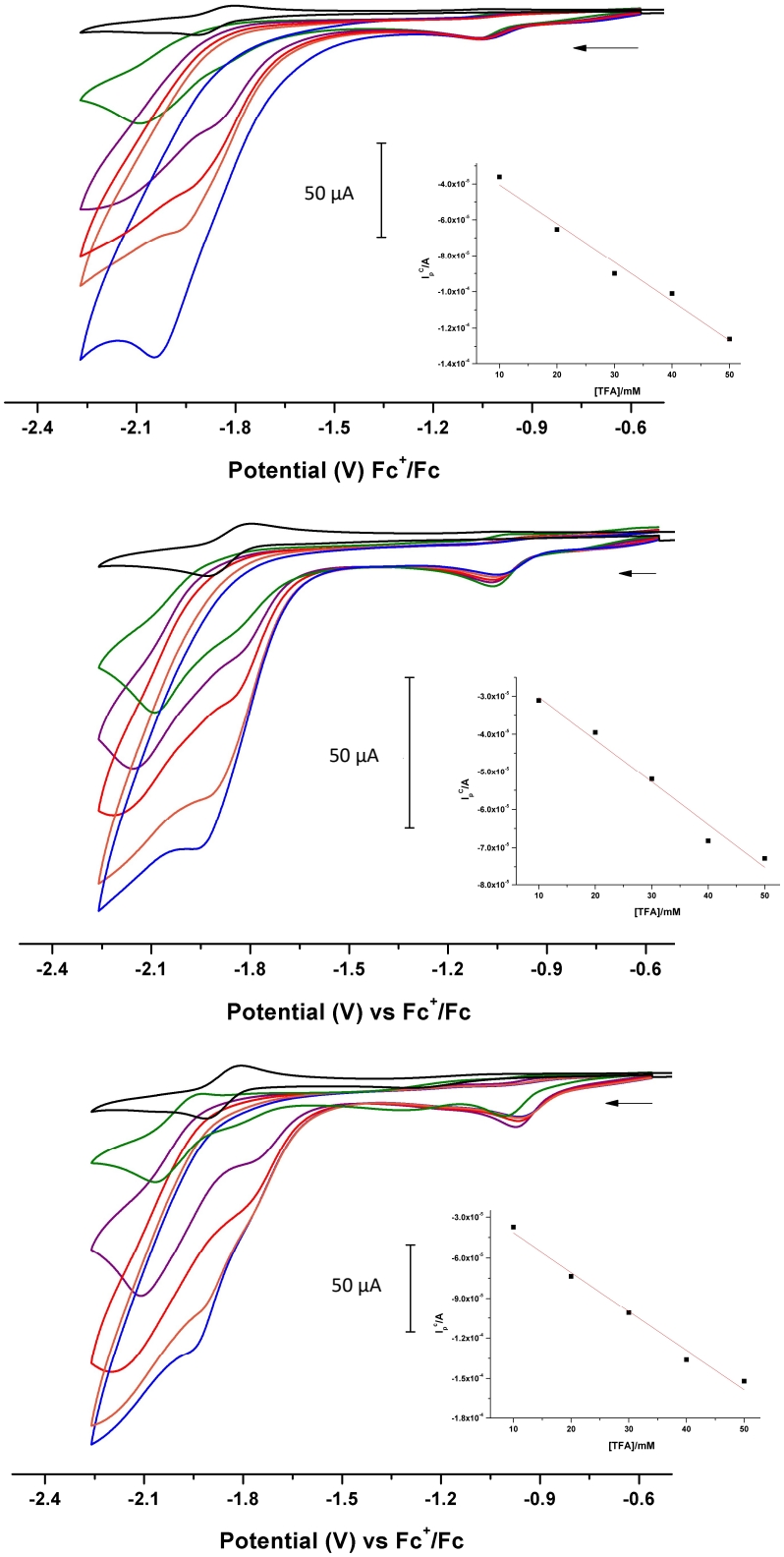


Figure 3.19: Cyclic voltammograms of 1 mM [Ni($q^{6,7}dt^{Me,Me}$)(dppe)] (Top), [Ni($q^{6,7}dt^{Et,Et}$)(dppe)] (middle) [Ni($q^{6,7}dt^{H,tBu}$)(dppe)] (bottom) in CH_2Cl_2 at 293 K containing 0.4 mM [N^nBu_4][BF_4] and increasing concentrations of TFA of 0 mM (black), 10mM (green), 20 mM (purple), 30 mM (red), 40 mM (orange) and 50 mM (blue). Inset: Plots of $I_p^{-1.8}$ vs. [TFA] observed in the cyclic voltammograms (100 mVs^{-1}).

In the absence of TFA each cyclic voltammogram of [Ni(qdt^{R1,R2})(dppe)] (R^1 = R^2 = Me; R^1 = H, R^2 = ^{t}Bu) exhibits a reversible reduction process at $E_{1/2}$ = -1.79 V *vs* Fc^+/Fc (Section 3.5). Upon the addition of TFA to the solution two additional reduction processes at -1.0 and -1.5 V vs Fc^+/Fc and three additional processes at -1.0, -1.3 and -1.5 V vs Fc^+/Fc were observed for [Ni(qdt^{Me,Me})(dppe)] and [Ni(qdt^{H,tBu})(dppe)], respectively. The original reduction at $E_{1/2}$ = -1.79 V vs Fc^+/Fc shifts to more negative potential at E_p^c = -1.84 and -1.83 V *vs* Fc^+/Fc for [Ni(qdt^{Me,Me})(dppe)] and [Ni(qdt^{H,tBu})(dppe)], respectively. The cyclic voltammograms of [Ni(q^{6,7}dt^{R1,R2})(dppe)] (R^1 = R^2 = Me, Et; R^1 = H, R^2 = ^{t}Bu) (Figure 3.19) in the presence of TFA show the appearance of a new reduction at *ca.*-1.0 V *vs* Fc^+/Fc, which remains essentially invariant as the concentration of TFA is varied. The reduction at $E_{1/2}$ = -1.86, -1.87 and -1.85 V *vs* Fc^+/Fc, respectively in the absence of TFA shifts to more negative potential at E_p^c = -2.0, -1.94 and -2.0 V *vs* Fc^+/Fc for [Ni(q^{6,7}dt^{R1,R2})(dppe)] (R^1 = R^2 = Me, Et; R^1 = H, R^2 = ^{t}Bu) respectively, in the presence of TFA.

All of the cyclic voltammograms exhibit a suppression of the return wave following reduction, consistent with the removal of [Ni(qdt^{R1,R2})(dppe)]$^-$ or [Ni(q^{6,7}dt^{R1,R2})(dppe)]$^-$ from the diffusion layer by a mechanism other than heterogeneous electron transfer.[13] Plots of I_p^c vs. [TFA] from cyclic voltammograms recorded at 100 mVs^{-1} (Figure 3.18 and 3.19, insets) show a linear increase in peak cathodic current with increasing concentration of acid for each complex.

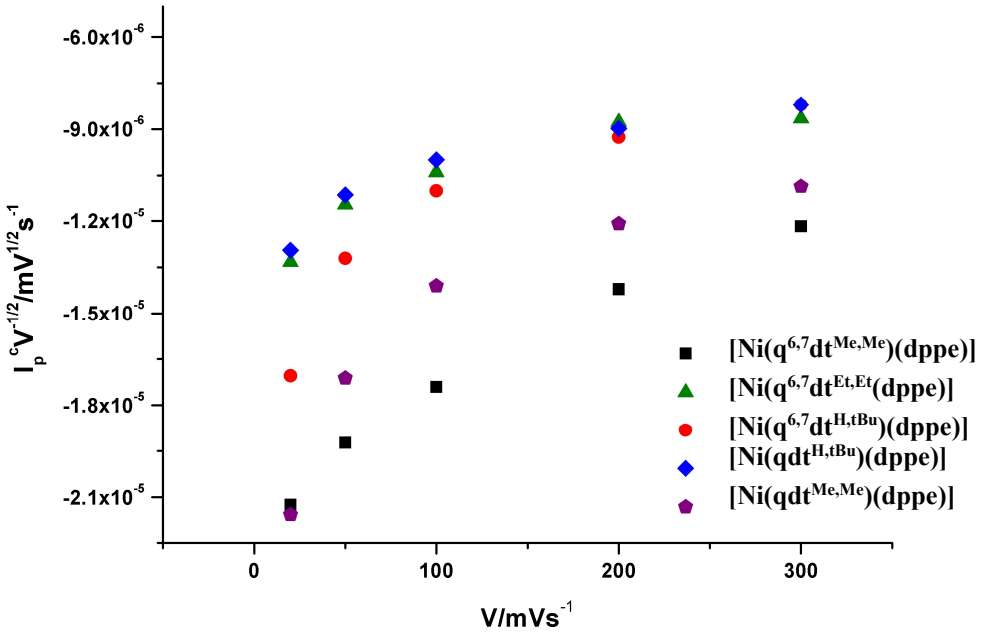


Figure 3.20: Plot of $I_p^c v^{-1/2}$ *vs*. v at [TFA] = 50 mM for [Ni(qdt^{Me,Me})(dppe)] (purple), [Ni(qdt^{H,tBu})(dppe)] (blue) [Ni(q^{6,7}dt^{Me,Me})(dppe)] (black), [Ni(q^{6,7}dt^{Et,Et})(dppe)] (green) and [Ni(q^{6,7}dt^{H,tBu})(dppe)] (red).

Plots of cathodic current normalised to $v^{1/2}$ *vs*. scan rate of [Ni(qdt^{R1,R2})(dppe)] ($R^1 = R^2 = Me$; $R^1 = H$, $R^2 = {}^tBu$) and [Ni(q^{6,7}dt^{R1,R2})(dppe)] ($R^1 = R^2 = Me$, Et; $R^1 = H$, $R^2 = {}^tBu$) are shown in Figure 3.20. Each plot shows an increase in $I_p^c v^{-1/2}$ with decreasing v that indicates a catalytic mechanism that involves an irreversible chemical reaction that follows reversible charge transfer.[14] Thus, based upon these experiments and published studies on [Ni(L^A)$Fe_2(CO)_6$],[13] we suggest that [Ni(qdt^{R1,R2})(dppe)] ($R^1 = R^2 = Me$; $R^1 = H$, $R^2 = {}^tBu$) and [Ni(q^{6,7}dt^{R1,R2})(dppe)] ($R^1 = R^2 = Me$, Et; $R^1 = H$, $R^2 = {}^tBu$) are reduced to [Ni(qdt^{R1,R2})(dppe)]$^-$ and [Ni(q^{6,7}dt^{R1,R2})(dppe)]$^-$ respectively. These anions react with H^+ to generate [Ni(qdt^{R1,R2})(dppe)] and [Ni(q^{6,7}dt^{R1,R2})(dppe)], respectively, and H_2. Future work could include a full quantification of H_2 gas evolved using gas chromatography using a protocol employed previously in our laboratory.[15]

3.8.1 Comparisons of the Cyclic Voltammetric Studies of $[Ni(qdt^{R1,R2})(dppe)]^-$ ($R^1 = R^2 = Me$; $R^1 = H$, $R^2 = {}^tBu$) and $[Ni(q^{6,7}dt^{R1,R2})(dppe)]^-$ ($R^1 = R^2 = Me$, Et; $R^1 = H$, $R^2 = {}^tBu$), $[Ni(L^A)Fe_2(CO)_6]$, $[Ni(p\text{-}q^{6,7}dt^{Et,Et})]$ and $[Ni(L^A)]$ in the presence of TFA

The catalytic activities of $[Ni(qdt^{R1,R2})(dppe)]^-$ ($R^1 = R^2 = Me$; $R^1 = H$, $R^2 = {}^tBu$) and $[Ni(q^{6,7}dt^{R1,R2})(dppe)]^-$ ($R^1 = R^2 = Me$, Et; $R^1 = H$, $R^2 = {}^tBu$) to $[Ni(p\text{-}q^{6,7}dt^{Et,Et})]$ were compared using a screening method developed previously at Nottingham.[16] The comparison of cyclic voltammograms is shown in Figure 3.21 and 3.22 and comparisons of $I_{-1.8}{}^c$ at [TFA] = 50 mM are shown in Table 3.8.

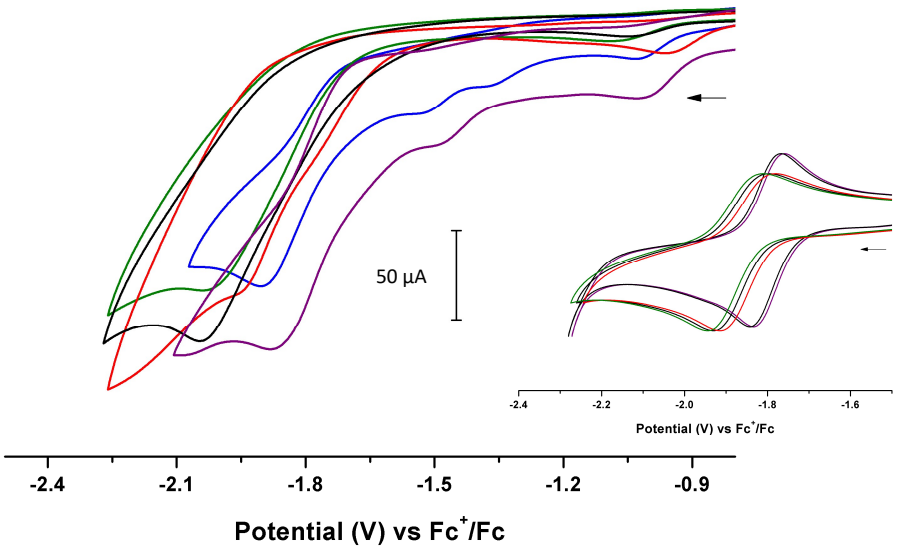


Figure 3.21: Comparison of cathodic currents for $[Ni(qdt^{Me,Me})(dppe)]$ (purple), $[Ni(qdt^{H,tBu})(dppe)]$ (blue) $[Ni(q^{6,7}dt^{Me,Me})(dppe)]$ (black), $[Ni(q^{6,7}dt^{Et,Et})(dppe)]$ (green) and $[Ni(q^{6,7}dt^{H,tBu})(dppe)]$ (red) (1 mM) in CH_2Cl_2 at 293 K containing $[N^nBu_4][BF_4]$ (0.4 M) and [TFA] = 50 (inset: Cyclic voltammograms recorded at [TFA] = 0, internal calibration).

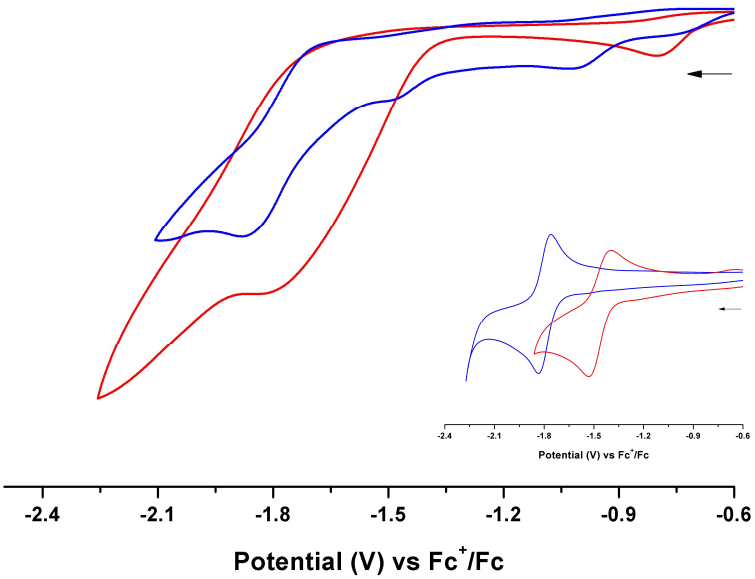


Figure 3.22: Comparison of cathodic currents for [for [Ni(qdt^{Me,Me})(dppe)] (blue) to [Ni(p-q^{6,7}dt^{Et,Et})] (red) (1 mM) in CH_2Cl_2 at 293 K containing [N^{n}Bu$_4$][BF$_4$] (0.4 M) and [TFA] = 50 (inset: Cyclic voltammograms recorded at [TFA] = 0, internal calibration).

Table 3.8: $I_{-1.8}{}^c$ at [TFA] = 50 mM for [Ni(qdt^{R1,R2})(dppe)]$^-$ (R^1 = R^2 = Me; R^1 = H, R^2 = ^{t}Bu) and [Ni(q^{6,7}dt^{R1,R2})(dppe)]$^-$ (R^1 = R^2 = Me, Et, Ph; R^1 = H, R^2 = ^{t}Bu).

Complex	$I_p{}^c$ (x 10^{-4} A)
[Ni(qdt^{Me,Me})(dppe)]	-1.91
[Ni(qdt^{H,tBu})(dppe)]	-1.56
[Ni(q^{6,7}dt^{Me,Me})(dppe)]	-1.89
[Ni(q^{6,7}dt^{Et,Et})(dppe)]	-1.58
[Ni(q^{6,7}dt^{H,tBu})(dppe)]	-1.66
[Ni(p-q^{6,7}dt^{Et,Et})]	-2.37

Within the [Ni(qdt^{R1,R2})(dppe)] and [Ni(q^{6,7}dt^{R1,R2})(dppe)] series of compounds the cathodic current at [TFA] = 50 mM appears to be greatest for [Ni(qdt^{Me,Me})(dppe)] (-1.91 x 10^{-4} A), the cathodic current for [Ni(p-q^{6,7}dt^{Et,Et})] (-2.37 x 10^{-4} A) recorded under identical conditions is larger than the cathodic current for [Ni(qdt^{Me,Me})(dppe)]. An effect that is consistent with a greater number of protonation sites associated with the [p-q^{6,7}dt]$^{2-}$ ligands relative to those in [qdt^{R1,R2}]$^{2-}$ and [q^{6,7}dt^{R1,R2}]$^{2-}$.

3.8.2 Comparisons of The Cyclic Voltammetric Studies of [Ni(qdt^{Me,Me})(dppe)] to [Ni(L^A)Fe$_2$(CO)$_6$] in the presence of TFA

A comparison of the catalytic activity of [Ni(qdt^{Me,Me})(dppe)] relative to that of [Ni(L^A)Fe$_2$(CO)$_6$] was attempted using the same screening method as described

above (Section 3.6.2). The cathodic current at [TFA] = 50 mM of [Ni(qdt^{Me,Me})(dppe)] and [Ni(L^{A})Fe$_2$(CO)$_6$], after the first reduction and then over the same potential window scanned for [Ni(qdt^{Me,Me})(dppe)] have been compared. The cyclic voltammograms are presented in Figure 3.23 and the cathodic currents are tabulated in Table 3.9.

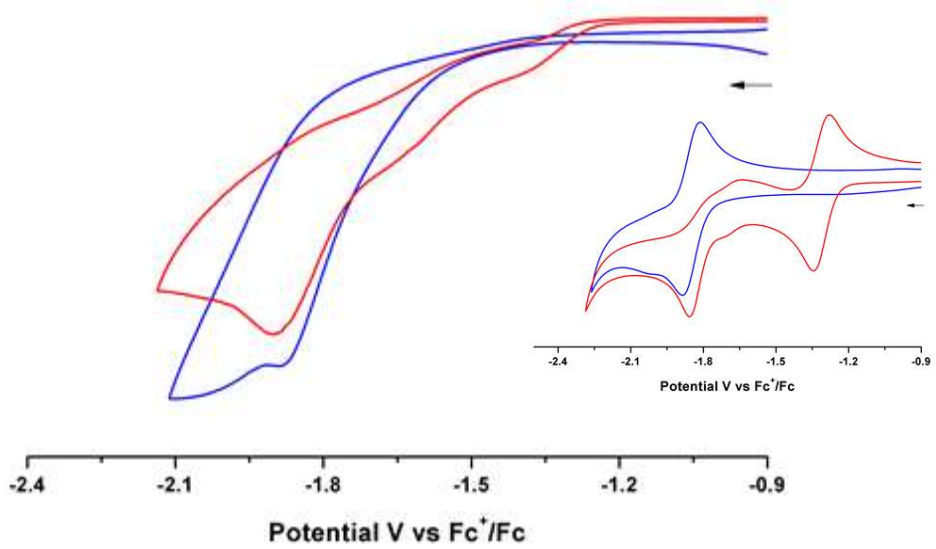


Figure 3.23: Comparison of cathodic currents for [Ni(qdt^{Me,Me})(dppe)] (Blue) to [Ni(L^{A})Fe$_2$(CO)$_6$] (red) (1 mM) in CH_2Cl_2 at 293 K containing [N^{n}Bu$_4$][BF$_4$] (0.4 M) and [TFA] = 50 (inset: Cyclic voltammograms recorded at [TFA] = 0, internal calibration).

The cathodic current at [TFA] = 50 mM for [Ni(qdt^{Me,Me})(dppe)] (-1.91 x 10^{-4} A) at -1.8 V *vs* Fc^+/Fc is larger than that associated with the first reduction of [Ni(L^{A})Fe$_2$(CO)$_6$] (-0.24 x 10^{-4} A) at –1.33 V *vs* Fc^+/Fc.[13] Given the significant difference in potential between the reduction potentials for each complex we widened the potential window for [Ni(L^{A})Fe$_2$(CO)$_6$] to reveal a second irreversible reduction process for [Ni(L^{A})Fe$_2$(CO)$_6$] (Figure 3.23). At -1.79 V *vs* Fc^+/Fc. The cathodic current in the presence of TFA (50 mM) for [Ni(qdt^{Me,Me})(dppe)] (-1.91 x 10^{-4} A) remains larger than that for [Ni(L^{A})Fe$_2$(CO)$_6$] (-1.43 x 10^{-4} A) under the same conditions. We note that the second reduction process for [Ni(L^{A})Fe$_2$(CO)$_6$] is irreversible, which may indicate that catalysis at this potential (-1.79 V *vs* Fc^+/Fc) might not be sustainable using [Ni(L^{A})Fe$_2$(CO)$_6$] as the catalyst. Future research must include an assessment of the robustness of the [Ni(L^{A})Fe$_2$(CO)$_6$] complex when the potential is cycled to-2.1 V *vs* Fc^+/Fc in the presence of TFA.

Table 3.9: I_p^c at [TFA] = 50 mM for $[Ni(qdt^{Me,Me})(dppe)]$, $[Ni(L^A)Fe_2(CO)_6]^-$ $[Ni(L^A)Fe_2(CO)_6]^{2-}$ and $[Ni(p\text{-}q^{6,7}dt^{Et,Et})]$.

Complex	I_p^c (A x 10^{-4})
$[Ni(qdt^{Me})(dppe)]$	-1.91
$[Ni(L^A)Fe_2(CO)_6]^-$	-0.24
$[Ni(L^A)Fe_2(CO)_6]^{2-}$	-1.43

3.9 DFT Studies

We have undertaken DFT calculations for $[Ni(qdt^{R1,R2})(dppe)]$ ($R^1 = R^2 = Me$; $R^1 = H$, $R^2 = {}^tBu$) and $[Ni(q^{6,7}dt^{R1,R2})(dppe)]$ ($R^1 = R^2 =$ Me, Et, Ph; $R^1 = H$, $R^2 = {}^tBu$) to provide a qualitative description of the structure and bonding within these complexes and to provide a framework to interpret the spectroscopic and electrochemical properties of the Ni^{II} complexes discussed within this chapter. Models of $[Ni(qdt^{R1,R2})(dppe)]$ ($R^1 = R^2 = Me$; $R^1 = H$, $R^2 = {}^tBu$) and $[Ni(q^{6,7}dt^{R1,R2})(dppe)]$ ($R^1 = R^2 =$ Me, Et, Ph; $R^1 = H$, $R^2 = {}^tBu$) were constructed from the experimentally determined crystallographic co-ordinates of the corresponding complex before being geometry optimised in the gas phase. The calculated geometries about each Ni centre within each series of $[Ni(qdt^{R1,R2})(dppe)]$ ($R^1 = R^2 = Me$; $R^1 = H$, $R^2 = {}^tBu$) and $[Ni(q^{6,7}dt^{R1,R2})(dppe)]$ ($R^1 = R^2 =$ Me, Et, Ph; $R^1 = H$, $R^2 = {}^tBu$) are similar. The calculated structures of $[Ni(qdt^{Me,Me})(dppe)]$ and $[Ni(q^{6,7}dt^{Et,Et})(dppe)]$ are shown in Figure 3.24 as representative examples and a comparison of selected bond lengths and angles obtained from X-ray crystallography and by calculation are shown in Table 3.10.

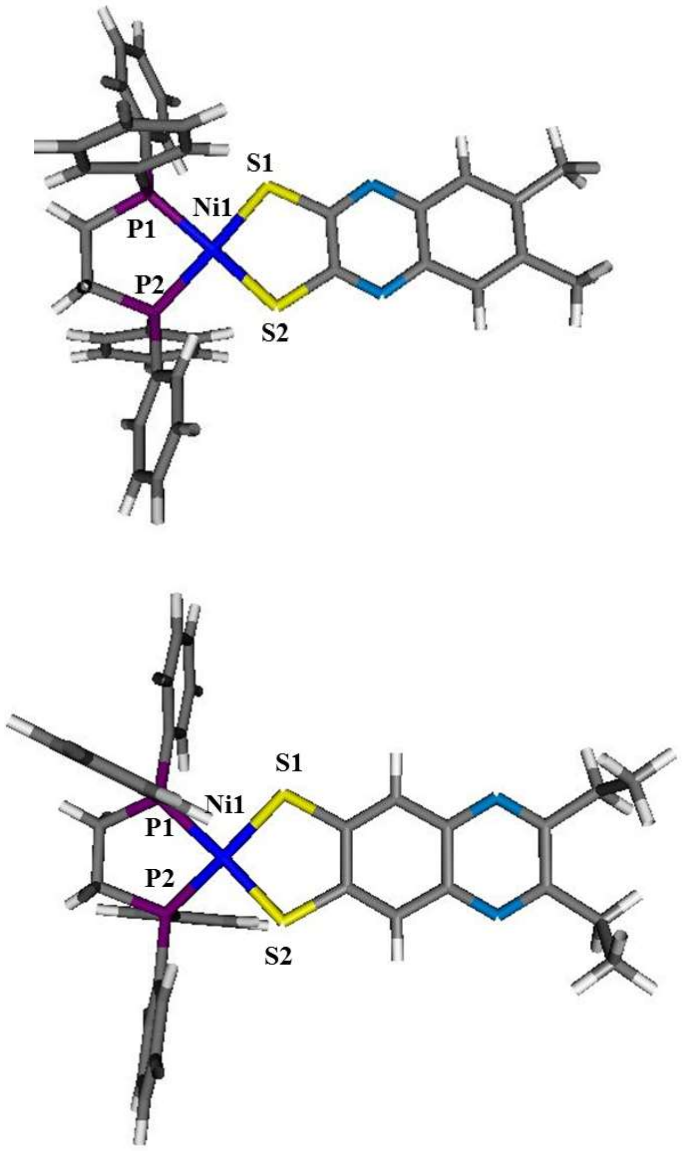


Figure 3.24: The geometry optimised structure of a) [Ni($qdt^{Me,Me}$)(dppe)] and b) [Ni($q^{6,7}dt^{Et,Et}$)(dppe)] using the BP86 functional.

Table 3.10: Selected structural parameters for [Ni(qdt^{Me,Me})(dppe)] and [Ni(^{6,7}qdt^{Et,Et})(dppe)] from the experimental X-ray crystal structures and the calculated DFT models.

Bond Length/Å	**[Ni(qdt^{Me,Me})(dppe)] X-ray crystallography**	**[Ni(qdt^{Me,Me})(dppe)] BP86**	**[Ni(q^{6,7}dt^{Et,Et})(dppe)] X-ray crystallography**	**[Ni(q^{6,7}dt^{Et,Et})(dppe)] BP86**
Ni(1)-S(1)	2.1639(17)	2.1795	2.1513(10)	2.1722
Ni(1)-S(2)	2.1765(10)	2.1807	2.1514(10)	2.1682
Ni(1)-P(1)	2.1662(10)	2.1708	2.1530(10)	2.1654
Ni(1)-P(2)	2.1809(14)	2.1731	2.1530(10)	2.1524
Bond Angle/º				
S(2-Ni(1)-S(1)	92.76(6)	92.96	93.20(6)	92.72
S(1)-Ni(1)-P(1)	88.50(6)	90.90	168.02(4)	165.31
S(2)-Ni(1)-P(2)	93.26(6)	91.10	168.02(4)	164.19
S(1)-Ni(1)-P(2)	171.05(4)	166.38	91.03(4)	89.99
S(2)-Ni(1)-P(1)	173.17(4)	165.16	91.03(4)	92.39
P(2)-Ni(1)-P(1)	86.31(6)	88.45	87.06(6)	88.83

The DFT calculations broadly reproduce the principal structural features of [Ni(qdt^{Me,Me})(dppe)] and [Ni(q^{6,7}dt^{Et,Et})(dppe)] revealed by X-ray crystallography, notably an approximate square planar geometry about each Ni^{II} centre. The average Ni-S and Ni-P bond distances are overestimated by *ca.* 0.01 – 0.02 Å in each calculation and the average calculated acute bond angles are within *ca.* 0.5º of the experimental structures. Thus, the close agreement between the experimental and calculated geometries suggests that the DFT calculations provide a reliable framework for a qualitative description of the electronic structures of [Ni(qdt^{R1,R2})(dppe)] ($R^1 = R^2 = Me$; $R^1 = H$, $R^2 = {}^tBu$) and [Ni(q^{6,7}dt^{R1,R2})(dppe)] ($R^1 = R^2 = Me$, Et, Ph; $R^1 = H$, $R^2 = {}^tBu$).

The compositions and energies of the frontier orbitals calculated for [Ni(qdt^{R1,R2})(dppe)] ($R^1 = R^2 = Me$; $R^1 = H$, $R^2 = {}^tBu$) and [Ni(q^{6,7}dt^{R1,R2})(dppe)] ($R^1 = R^2 = Me$, Et, Ph; $R^1 = H$, $R^2 = {}^tBu$), and for the anions [Ni(qdt^{Me,Me})(dppe)]$^-$ and [Ni(q^{6,7}dt^{Et,Et})(dppe)], as representative examples, are summarised in Table 3.11. Isosurface plots of the HOMO and LUMO for orbitals for [Ni(qdt^{Me,Me})(dppe)] and

[Ni(qdt^{Et,Et})(dppe)], and of the SOMOs for [Ni(qdt^{Me,Me})(dppe)]$^-$ and [Ni(qdt^{Et,Et})(dppe)]$^-$ are illustrated in Figure 3.25.

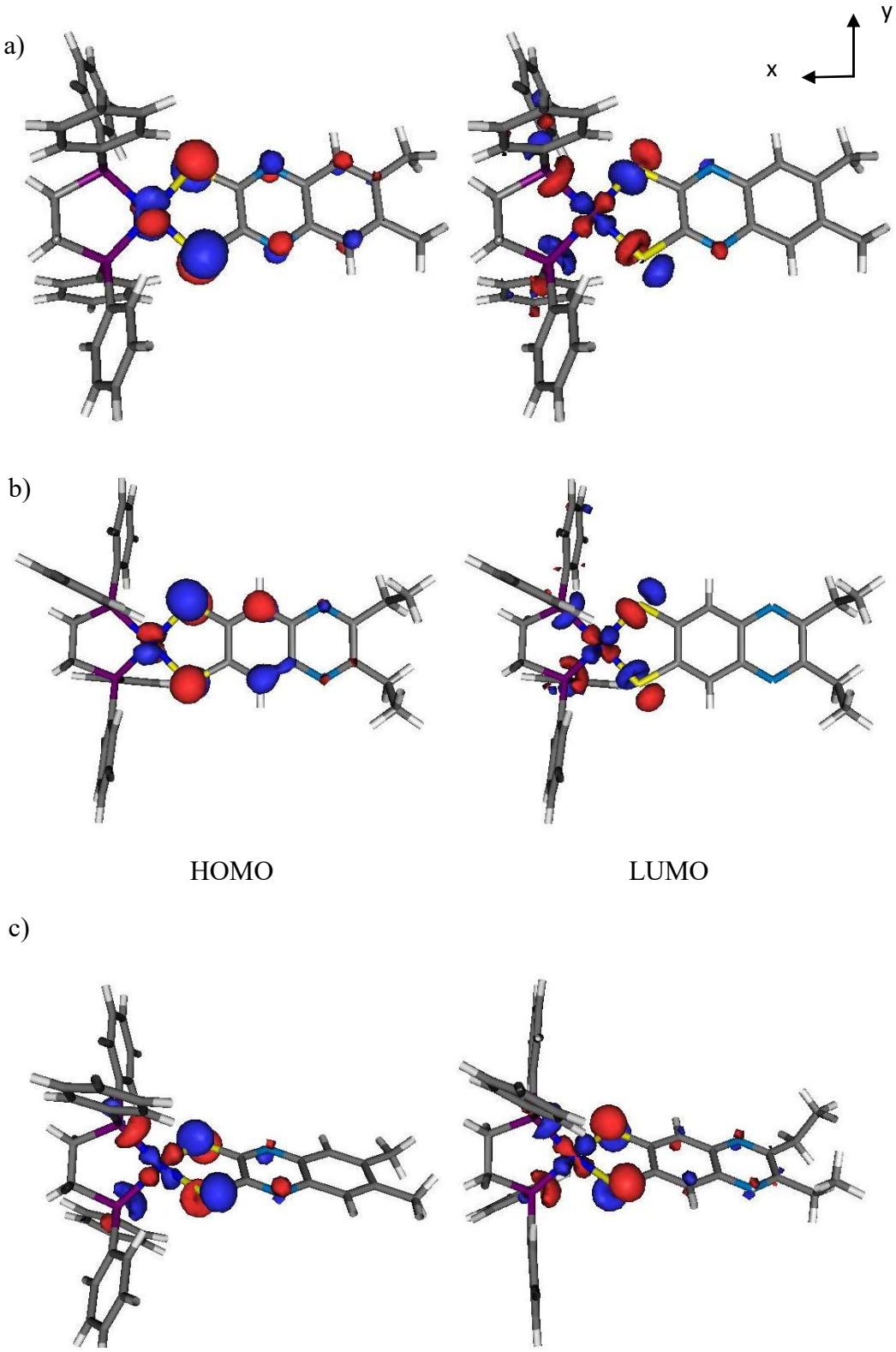


Figure 3.25: Kohn-Sham frontier orbitals of a) [Ni(qdt^{Me,Me})(dppe)] b) [Ni(q^{6,7}dt^{Et,Et})(dppe)] and c) the SOMOs for [Ni(qdt^{Me,Me})(dppe)]$^-$ (left) and [Ni(q^{6,7}dt^{Et,Et})(dppe)]$^-$ (right).

Table 3.11: The nature, energy and composition of the frontier orbitals obtained from the DFT calculations for [Ni(qdt^{R1,R2})(dppe)] ($R^1 = R^2$ = Me; R^1 = H, R^2 = ^{t}Bu) and [Ni(q^{6,7}dt^{R1,R2})(dppe)] ($R^1 = R^2$ = Me, Et, Ph; R^1 = H, R^2 = ^{t}Bu), and [Ni(qdt^{Me,Me})(dppe)]$^-$ and [Ni(q^{6,7}dt^{Et,Et})(dppe)]$^-$.

Compound	Designation	Orbital Nature	Energy/ Hartrees	% Contribution Ni	S	N	P
[Ni(qdt^{Me,Me})(dppe)]	177a LUMO	Ni d_{xy} - S/P σ	-0.172	23.8	23.5	0	15.4
	176a HOMO	Ni d_{xz}-S π	-0.106	35.3	37.6	8	0
[Ni(qdt^{H,tBu})(dppe)]	185a LUMO	Ni d_{xy} - S/P σ	-0.174	23.9	23.2	0	15.5
	184a HOMO	Ni d_{xz}-S π	-0.107	36.8	35.1	6.8	0
[Ni(qdt^{Me,Me})(dppe)]$^-$	177 SOMO	Ni d_{xy} - S/P σ	-0.0324	21.6	29.6	3.2	14.1
[Ni(q^{6,7}dt^{Me,Me})(dppe)]	177a LUMO	Ni d_{xy} - S/P σ	-0.166	24.1	24.2	0	17
	176a HOMO	Ni d_{xz}-S π	-0.107	25.6	38.7	2.5	0
[Ni(q^{6,7}dt^{Et,Et})(dppe)]	185a LUMO	Ni d_{xy} - S/P σ	-0.165	24.3	24.5	0	16.7
	184a HOMO	Ni d_{xz}-S π	-0.106	24.4	38.5	2.4	0
[Ni(q^{6,7}dt^{H,tBu,})(dppe)]	185a LUMO	Ni d_{xy} - S/P σ	-0.167	24.3	25.4	0	16.6
	184a HOMO	Ni d_{xz}-S π	-0.108	25.4	41.2	1.4	0
[Ni(q^{6,7}dt^{Ph,Ph})(dppe)]	209a LUMO	Ni d_{xy} - S/P σ	-0.169	23.1	24.5	0	17.3
	208a HOMO	Ni d_{xz}-S π	-0.110	25.5	34.1	2.6	0
[Ni(q^{6,7}dt^{Et,Et})(dppe)]$^-$	185 SUMO	Ni d_{xy} - S/P σ	-0.0353	24.9	30.3	0	15.1

The HOMOs within [Ni(qdt^{R1,R2})(dppe)] ($R^1 = R^2$ = Me; R^1 = H, R^2 = ^{t}Bu) and [Ni(q^{6,7}dt^{R1,R2})(dppe)] ($R^1 = R^2$ = Me, Et, Ph; R^1 = H, R^2 = ^{t}Bu) series are essentially the same and involve Ni 3d_{xz}, Sπ and quinoxaline π combinations. Each HOMO possesses similar contributions from the Ni centre (23.1-24.3 %) and the S-dithiolate donors (23.3-25.4 %) and as such the HOMO is delocalised across the whole metallodithiolate unit. The LUMOs of [Ni(qdt^{R1,R2})(dppe)] ($R^1 = R^2$ = Me; R^1 = H, R^2 = ^{t}Bu) and [Ni(q^{6,7}dt^{R1,R2})(dppe)] ($R^1 = R^2$ = Me, Et, Ph; R^1 = H, R^2 = ^{t}Bu) are derived from Ni 3d_{xy}, S-σ and P- σ combinations with little contributions from the quinoxaline ring system (Table 3.11). As expected unrestricted calculations on models of [Ni(qdt^{Me,Me})(dppe)]$^-$ and [Ni(q^{6,7}dt^{Et,Et})(dppe)]$^-$ reveals SOMOs that have similar compositions to the LUMOs of the parent [Ni(qdt^{Me,Me})(dppe)] and [Ni(q^{6,7}dt^{Et,Et})(dppe)] complexes and which are composed of Ni 3d_{xy}, S-σ and P- σ combinations. The compositions of these SOMOs is in line with the EPR spectra of the anions discussed in Section 3.5.5.

The similarities in compositions and the relative energies of the HOMOs, LUMOs and SOMOs within the [Ni(qdt^{R1,R2})(dppe)] ($R^1 = R^2$ = Me; R^1 = H, R^2 = ^{t}Bu) and [Ni(q^{6,7}dt^{R1,R2})(dppe)] ($R^1 = R^2$ = Me, Et, Ph; R^1 = H, R^2 = ^{t}Bu) series suggests that the substituents pendant to the quinoxaline dithiolate ligand backbone do not

significantly affect the nature of these orbitals and thus the redox properties of these centres.

3.9.1 DFT Studies of Protonation of [Ni(qdt^{Me,Me})(dppe)] and [Ni(q^{6,7}dt^{Et,Et})(dppe)]

We examined the protonated forms of [Ni(qdt^{Me,Me})(dppe)] and [Ni(q^{6,7}dt^{Et,Et})(dppe)]; [Ni(qdt^{Me,Me})(dppe)H$_n$]$^{n+}$ and [Ni(q^{6,7}dt^{Et,Et})(dppe)H$_n$]$^{n+}$ (n = 1 or 2), that involve protonation at the N positions of the quinoxaline rings (see Figure 3.26). The calculated geometrical parameters of [Ni(qdt^{Me,Me})(dppe)] and [Ni(q^{6,7}dt^{Et,Et})(dppe)] are similar to those of [Ni(qdt^{Me,Me})(dppe)H$_n$]$^{n+}$ and [Ni(q^{6,7}dt^{Et,Et})(dppe)H$_n$]$^{n+}$ (n = 1 or 2) (Tables 3.12 and 3.13) suggesting that protonation does not significantly change the geometry of the Ni^{II} unit. Comparison of the data presented in Table 3.12 and 3.13 indicates that the sequential protonation to give a mono- and di-cation is accompanied by the sequential lengthening of the Ni-S and Ni-P bonds by *ca.* 0.01 and 0.02 Å, respectively, for each protonation.

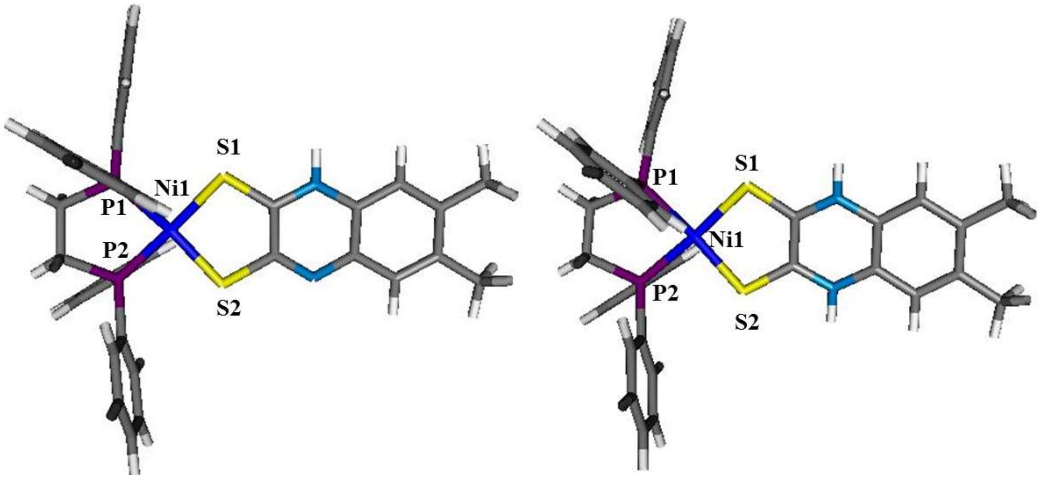


Figure 3.26: Geometry optimised structures for a) [Ni(qdt^{Me,Me})(dppe)H]$^+$ and b) [Ni(qdt^{Me,Me})dppe)H$_2$]$^{2+}$.

Table 3.12: Selected calculated parameters for [Ni($qdt^{Me,Me}$)(dppe)] and the protonated forms of [Ni($qdt^{Me,Me}$)(dppe)].

Bond Length/Å	**[Ni($qdt^{Me,Me}$)(dppe)]**	**[Ni($qdt^{Me,Me}$)(dppe)H]$^+$**	**[Ni($qdt^{Me,Me}$)(dppe)H_2]$^{2+}$**
Ni(1)-S(1)	2.1795	2.1883	2.2101
Ni(1)-S(2)	2.1807	2.1919	2.2105
Ni(1)-P(1)	2.1708	2.1843	2.2107
Ni(1)-P(2)	2.1731	2.1940	2.2142
Bond Angle/º			
S(2)-Ni(1)-S(1)	92.96	93.30	92.51
S(1)-Ni(1)-P(1)	90.90	89.11	91.06
S(2)-Ni(1)-P(2)	91.10	91.46	91.15
S(1)-Ni(1)-P(2)	166.38	170.15	170.32
S(2)-Ni(1)-P(1)	165.16	170.52	171.79
P(2)-Ni(1)-P(1)	88.45	87.59	86.51

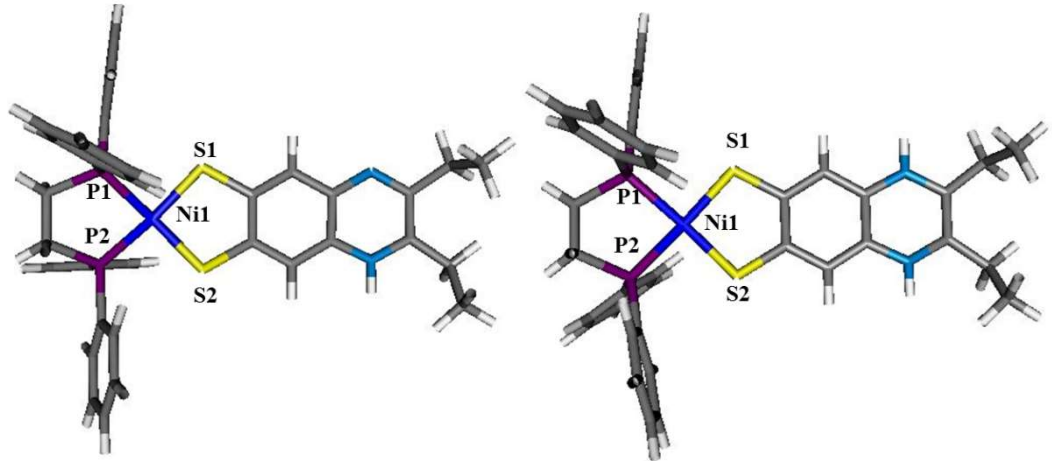


Figure 3.27: Geometry optimised structures for a) [Ni($q^{6,7}dt^{Et,Et}$)(dppe)H] $^+$, b) [Ni($q^{6,7}dt^{Et,Et}$)(dppe)H_2]$^{2+}$.

Table 2.13: Selected calculated parameters for [Ni($q^{6,7}dt^{Et,Et}$)(dppe)] and the protonated forms of [Ni($q^{6,7}dt^{Et,Et}$)(dppe)].

Bond Length/Å	**[Ni($qdt^{Me,Me}$)(dppe)]**	**[Ni($qdt^{Me,Me}$)(dppe)H]$^+$**	**[Ni($qdt^{Me,Me}$)(dppe)H_2]$^{2+}$**
Ni(1)-S(1)	2.1722	2.1830	2.1926
Ni(1)-S(2)	2.1682	2.1783	2.1924
Ni(1)-P(1)	2.1654	2.1888	2.2209
Ni(1)-P(2)	2.1624	2.1897	2.2197
Bond Angle/º			
S(2)-Ni(1-S(1)	92.72	92.23	91.56
S(1)-Ni(1-P(1)	165.31	169.41	173.17
S(2)-Ni(1-P(2)	164.19	168.31	174.12
S(1)-Ni(1-P(2)	89.99	89.15	90.93
S(2)-Ni(1)-P(1)	92.39	92.72	91.11
P(2)-Ni(1)-P(1)	88.83	87.90	86.95

The Kohn-Sham frontier orbitals of $[Ni(qdt^{Me,Me})(dppe)H_n]^{n+}$ and $[Ni(q^{6,7}dt^{Et,Et})(dppe)H_n]^{n+}$ are shown in Figure 3.28 and 3.29, respectively. There appears to be a significant reconfiguration in the compositions and energies of the frontier orbitals on protonation in each species relative to their unprotonated forms, $[Ni(qdt^{Me,Me})(dppe)]$ and $[Ni(q^{6,7}dt^{Et,Et})(dppe)]$ (Section 3.5). The HOMOs of $[Ni(qdt^{Me,Me})(dppe)H_n]^{n+}$ and $[Ni(q^{6,7}dt^{Et,Et})(dppe)H_n]^{n+}$ (n = 1, 2) are essentially a combination of Ni dz^2 with varying Sπ contributions while the LUMOs of $[Ni(qdt^{Me,Me})(dppe)H_n]^{n+}$ and $[Ni(q^{6,7}dt^{Et,Et})(dppe)H_n]^{n+}$ (n = 1, 2) are quinoxaline based with little or no Ni contribution. This suggests that on protonation the first reduction process for $[Ni(qdt^{Me,Me})(dppe)H_n]^{n+}$ and $[Ni(q^{6,7}dt^{Et,Et})(dppe)H_n]^{n+}$ shifts from being metal based to quinoxaline-based as suggested for $[Ni(p\text{-}q^{6,7}dt^{Et,Et})]$ (Chapter 2, Section 2.11).

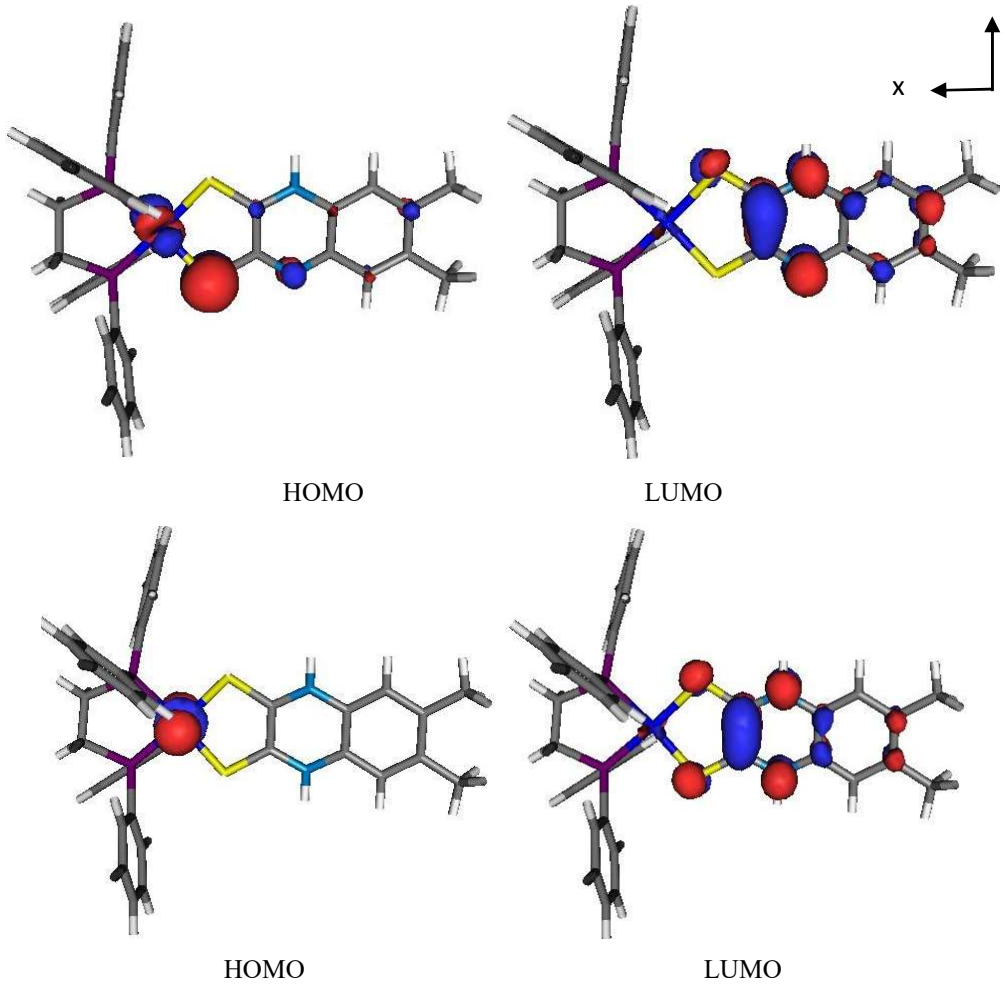
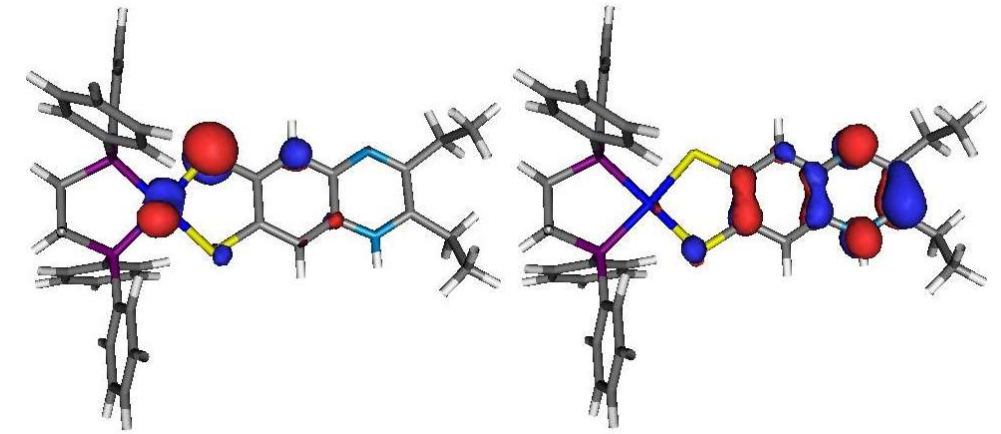
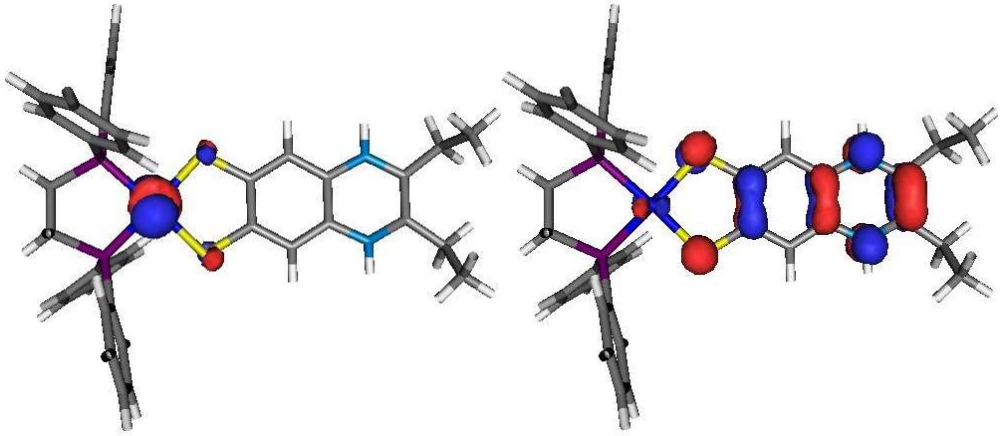


Figure 3.28: Kohn-Sham frontier orbitals for the BP86 optimised structures of a) $[Ni(qdt^{Me,Me})H(dppe)]^{+}$ and b) $[Ni(qdt^{Me,Me})H_2(dppe)]^{2+}$.



HOMO LUMO



HOMO LUMO

Figure 3.29: Kohn-Sham frontier orbitals for the BP86 optimised structures of a) $[Ni(q^{6,7}dt^{Et,Et})H(dppe)]^+$ b) $[Ni(q^{6,7}dt^{Et,Et})H_2(dppe)]^{2+}$.

Table 3.14: The nature, energy and composition of the frontier orbitals obtained from the DFT calculations for $[Ni(qdt^{Me.Me})(dppe)H_n]^{n+}$ and $[Ni(q^{6,7}dt^{Et,Et})(dppe)H_n]^{n+}$ (n = 1 or 2).

Compound	Designation	Orbital Nature	Energy/ Hartrees	% Contribution Ni	S	N	P
$[Ni(qdt^{Me,Me})(dppe)H]^+$	177a LUMO	Quinoxaline	-0.219	1.1	9.9	33.0	0
	176a HOMO	Ni dz^2 - Sπ	-0.280	40.0	34.7	3.9	0
$[Ni(qdt^{Me,Me})(dppe)H_2]^{2+}$	177a LUMO	Quinoxaline	-0.354	1.34	7.9	26.8	0
	176a HOMO	Ni dz^2	-0.392	100	0	0	0
$[Ni(q^{6,7}dt^{Et,Et})(dppe)H]^+$	185a LUMO	Quinoxaline	-0.227	0	6.5	34.8	0
	184a HOMO	Ni dz^2 – Sπ	-0.269	44.1	32.3	0	0
$[Ni(q^{6,7}dt^{Et,Et})(dppe)H_2]^{2+}$	185a LUMO	Quinoxaline	-0.354	4.3	19.7	23.4	0
	184a HOMO	Ni dz^2 - Sπ	-0.377	78.3	9.3	0	0

3.10 Conclusions

This chapter discusses the synthesis and characterisation of a series of [Ni(qdt^{R1,R2})(dppe)] ($R^1 = R^2 = Me$; $R^1 = H$, $R^2 = {}^tBu$) and [Ni(q^{6,7}dt^{R1,R2})(dppe)] ($R^1 = R^2 = Me$, Et, Ph; $R^1 = H$, $R^2 = {}^tBu$) complexes. The potential of these complexes to behave as catalysts for the electrocatalytic production of H_2 has been assessed.

X-ray crystallography has shown that [Ni(qdt^{R1,R2})(dppe)] ($R^1 = R^2 = Me$; $R^1 = H$, $R^2 = {}^tBu$) and [Ni(q^{6,7}dt^{R1,R2})(dppe)] ($R^1 = R^2 = Me$, Et, Ph; $R^1 = H$, $R^2 = {}^tBu$) adopt distorted square planar geometries with bond lengths and angles about the Ni^{II} centre that are comparable to those of [(dppe)Ni(dt)] (dt = sdt, 2-pedt, 3-pedt, 4-pedt) and [Ni(qdt)(dppe)].[9,11] Electrochemical and spectroelectrochemical studies show that [Ni(qdt^{R1,R2})(dppe)] ($R^1 = R^2 = Me$; $R^1 = H$, $R^2 = {}^tBu$) and [Ni(q^{6,7}dt^{R1,R2})(dppe)] ($R^1 = R^2 = Me$, Et; $R^1 = H$, $R^2 = {}^tBu$) possess a reversible reduction process at *ca.* -1.79 and *ca.* -1.87 V *vs* Fc^+/Fc, respectively. The positive potential shift of *ca.* 100 mV relative to the redox potentials for [(dppe)Ni(dt)] (dt = sdt, 2-pedt, 3-pedt, 4-pedt, $E_{1/2}$ *ca.* -1.94 *vs* Fc^+/Fc)[9] appears to reflect the proximity and number of N atoms to the metal centre in this series of compounds.

The X-band fluid and frozen solution EPR spectra of [Ni(qdt^{R1,R2})(dppe)]$^-$ and [Ni(q^{6,7}dt^{R1,R2})(dppe)]$^-$ exhibit ^{31}P hyperfine couplings and the anisotropic nature of the frozen solution spectra are consistent with a SOMO with a significant Ni contribution. The details of the electronic structures of these centres revealed by EPR spectroscopy are in line with those calculated by DFT.

Cyclic voltametric studies in the presence of TFA suggest that [Ni(qdt^{R1,R2})(dppe)] ($R^1 = R^2 = Me$; $R^1 = H$, $R^2 = {}^tBu$) and [Ni(q^{6,7}dt^{R1,R2})(dppe)] ($R^1 = R^2 = Me$, Et; $R^1 = H$, $R^2 = {}^tBu$) are electrocatalysts towards proton reduction and comparisons with [Ni(L^A)$Fe_2(CO)_6$] suggest that [Ni(qdt^{R1,R2})(dppe)] ($R^1 = R^2 = Me$; $R^1 = H$, $R^2 = {}^tBu$) and [Ni(q^{6,7}dt^{R1,R2})(dppe)] ($R^1 = R^2 = Me$, Et; $R^1 = H$, $R^2 = {}^tBu$) may be more effective catalysts for H_2 production. Further quantification of H_2 production by gas chromatography must be undertaken in order to complete a full assessment of [Ni(qdt^{R1,R2})(dppe)] and [Ni(q^{6,7}dt^{R1,R2})(dppe)] as potential catalysts for H_2 production. Nevertheless, the synthetic accessibility of [Ni(qdt^{R1,R2})(dppe)] and [Ni(q^{6,7}dt^{R1,R2})(dppe)] and their long-term stability relative to complexes based on

the $[Ni(L^A)Fe_2(CO)_6]$ framework makes them promising candidates for future investigations.

3.11 Experimental

3.11.1 The Synthesis of [Ni(qdt^{R1,R2})(dppe)] ($R^1 = R^2 = Me$; $R^1 = H$, $R^2 = {}^tBu$)

Representative procedure for the synthesis for [Ni(qdt^{R1,R2})(dppe)]: Sodium methoxide (5.00 mmol) was added to a solution of qdt$^{R1,R2}H_2$ ($R^1 = R^2 = Me$; $R^1 = H$, $R^2 = {}^tBu$) (2.00 mmol) in methanol (20 mL). The solution was stirred for 30 min at room temperature. A solution of [1,2-bis(diphenylphosphino)ethane]dichloronickel(II) (1.00 mmol) in CH_2Cl_2 (20 mL) was added to the reaction mixture drop wise. The reaction was stirred for 3 h at room temperature. The solvent was removed under vacuum to give a red solid which was then recrystallised from a CH_2Cl_2 solution layered with pentane.

[Ni(qdt^{Me,Me})(dppe)] was prepared from q^{6,7}dt$^{Me,Me}H_2$ (0.44 g, 2.00 mmol) to give red crystals (1.15 g, 1.61 mmol, 85 %). MS (ESI^+) m/z: 677.0836 $[M+H]^+$. ^1H NMR (400 MHz $CDCl_3$, 298 K): δH 7.84-7.78 (18H, m, Ar-H), 7.59-7.44 (4H, m, Ar-H), 2.42-2.47 (4H, m, CH_2), 2.36 (6H, s, CH_3). ^{13}C NMR (100 MHz, $CDCl_3$, 298 K): δC 133.5 (Ar-C), 132.1 (Ar-C), 131.6 (Ar-C), 129.1 (Ar-C), 77.4 (Ar-C), 77.0 (Ar-C), 76.6 (Ar-C), 26.6 (CH), 20.2 (CH_2), 19.8 (CH_3). ^{31}P-{^1H}NMR (400 MHz, CD_3Cl_3, 298 K): δP 59.1 (s). Elemental analysis found (calculated for $C_{36}H_{32}N_2NiP_2S_2$): C 63.42 (63.83), H 4.46 (4.76), N 3.83 (4.14) %.

[Ni(qdt^{H,tBu})(dppe)] was prepared from q^{6,7}dt$^{H,tBu}H_2$ (0.50 g, 2.00 mmol) to give red crystals (1.17 g, 1.66 mmol, 83 %). MS (ESI^+) m/z: 705.1148 $[M+H]^+$. ^1H NMR δ (400 MHz, $CDCl_3$, 298 K): 8.66 (s, 1H, ArH), 8.00 (s, 2H, ArH), 7.85 (q, 8H, J = 17.5 Hz, ArH), 7.57-7.47 (m, 12H, ArH), 2.40 (d, 4H, J = 17.5 Hz, CH_2), 1.42 (s, 9H, CH_3). ^{13}C NMR δ (100 MHz, $CDCl_3$, 298 K): 160.60 (Ar-C), 140.45 (Ar-C), 138.19 (Ar-C), 133.85 (Ar-C), 131.78 (Ar-C), 129.326 (Ar-C), 129.18 (Ar-C), 124.98 (Ar-C), 53.73 (CH_2), 37.08 (C-$(CH_3)_3$), 30.17 (CH_3). ^{31}P-{^1H}NMR δ (162 MHz, $CDCl_3$, 298 K) 58.05 (s, 1P, PPh_2). Elemental analysis found (calculated for $C_{38}H_{36}N_2NiP_2S_4$): C: 64.73 (64.70) H: 4.97 (5.14) N: 3.95 (3.97) %.

3.11.2 The Synthesis of [Ni($q^{6,7}dt^{R1,R2}$)(dppe)] (R^1 = R^2 = Me, Et, Ph; R^1 = H, R^2 = ^{t}Bu)

Typical procedure: Sodium methoxide (5.00 mmol) was added to a solution of $q^{6,7}dt^{R1,R2}H_2$ (2.00 mmol) in methanol (20 mL). The solution was stirred for 30 min at room temperature. A solution of [1,2-bis(diphenylphosphino)ethane]dichloronickel(II) (1.00 mmol) in CH_2Cl_2 (20 mL) was added to the reaction mixture drop wise. The reaction was stirred for 3 h at room temperature. The solvent was removed under vacuum to give a red solid which was then recrystallised from a CH_2Cl_2 solution layered with pentane.

[Ni($q^{6,7}dt^{Me,Me}$)(dppe)] was prepared from $q^{6,7}dt^{Me,Me}H_2$ (0.44 g, 2.00 mmol) to give red crystals (1.14 g, 1.68 mmol, 84 %). MS (ESI^+) m/z: 677.0836 $[M+H]^+$. ^{1}H NMR δ (400 MHz, $CHCl_3$, 298 K): 7.85 (q, 8H, *J* = 17.7 Hz, ArH), 7.80 (s, 2H, ArH), 7.62-7.48 (m, 12H, ArH), 2.64 (d, 4H, *J* = 17.7 Hz CH_2), 1.23 (s, 6H, CH_3). ^{13}C NMR δ (100 MHz, $CHCl_3$, 298 K): 159.52 (Ar-C), 140.02 (Ar-C), 138.34 (Ar-C), 133.21 (Ar-C), 131.67 (Ar-C), 129.44 (Ar-C), 128.61 (Ar-C), 125.05 (Ar-C), 53.57 (CH_2), 24.13 (CH_3).^{31}P-{^{1}H}NMR δ (162 MHz, $CHCl_3$, 298 K) 59.38 (s, 1P, PPh_2). Elemental analysis found (calculated for $C_{36}H_{32}N_2NiP_2S_2$): C: 63.67 (63.83), H: 4.58 (4.76), N: 4.20 (4.14) %.

[Ni($q^{6,7}dt^{Et,Et}$)(dppe)] was prepared from $q^{6,7}dt^{Et,Et}H_2$ (0.50 g, 2.00 mmol) to give red crystals (1.24 g, 1.76 mmol, 88 %). MS (ESI^+) m/z: 705.1148 $[M+H]^+$. ^{1}H NMR δ (400 MHz, $CDCl_3$, 298 K): 7.86 (q, 8H, *J* = 18.7 Hz, ArH), 7.63 (s, 2H, ArH)7.59-7.47 (m, 12H, *J* = 26.8 Hz ArH), 2.88 (q, 4H, *J*= 7.4 Hz, CH_2), 2.60 (d, 4H, *J* = 18.7 Hz, CH_2), 1.24 (t, 6H, *J*= 15.1 Hz CH_3). ^{13}C NMR δ (100 MHz, $CDCl_3$, 298 K): 131.43 (Ar-C), 129.62 (Ar-C), 128.49 (Ar-C), 124.35 (Ar-C), 52.87 (CH_2), 28.98 (C-$(CH_3)_3$), 26.23 (CH_3). ^{31}P-{^{1}H}NMR δ (162 MHz, $CDCl_3$, 298 K) 59.12 (s, 1P, PPh_2). Elemental analysis found (calculated for $C_{38}H_{36}N_2NiP_2S_4$): C: 64.86 (64.70), H: 5.02 (5.14), N: 3.83 (3.97) %.

[Ni($q^{6,7}dt^{H,tBu}$)(dppe)] was prepared from $q^{6,7}dt^{H,tBu}H_2$ (0.50 g, 2.00 mmol) to give red crystals (1.15 g, 1.64 mmol, 82 %). MS (ESI^+) m/z: 705.1148 $[M+H]^+$. ^{1}H NMR δ (400 MHz, $CDCl_3$, 298 K): 8.75 (s, 1H, ArH), 7.82 (t, 8H, *J* =17.6 Hz, ArH), 7.71

(s, 1H, ArH), 7.64-7.51 (m, 12H, ArH), 2.62 (d, 4H, *J* =17.6 Hz, CH_2), 1.38 (s,9, CH_3). ^{13}C NMR δ (100 MHz, $CDCl_3$, 298 K): 160.60 (Ar-C), 140.45 (Ar-C), 138.19 (Ar-C), 133.85 (Ar-C), 131.78 (Ar-C), 129.326 (Ar-C), 129.18 (Ar-C), 124.98 (Ar-C), 53.73 (CH_2), 37.08 (C-$(CH_3)_3$), 30.17 (CH_3). ^{31}P-{^1H}NMR δ (162 MHz, $CDCl_3$, 298 K) 59.22 (s, 1P, PPh_2). Elemental analysis found (calculated for $C_{38}H_{36}N_2NiP_2S_4$): C: 64.73 (64.70), H: 4.97 (5.14), N: 3.95 (3.97) %.

[Ni($q^{6,7}dt^{Ph,Ph}$)(dppe)] was prepared from $q^{6,7}dt^{Ph,Ph}H_2$ (0.69 g, 2.00 mmol) to give red crystals (1.2 g, 1.53 mmol, 76 %). MS (ESI^+) m/z: 801.1148 $[M+H]^+$. ^1H NMR δ (400 MHz, $CDCl_3$, 298 K): 8.12 (s, 2H, ArH), 7.87 (q, 8H, *J* = 17.3 Hz, ArH), 7.75 (m, 4H, ArH) 7.56-7.47 (m, 18H, ArH), 2.62 (d, 4H, *J* = 17.3 Hz, CH_2), ^{13}C NMR δ (100 MHz, $CDCl_3$, 298 K): ^{31}P-{^1H}NMR δ (162 MHz, $CDCl_3$, 298 K) 59.23 (s, 1P, PPh_2). Elemental analysis found (calculated for $C_{46}H_{36}N_2NiP_2S_2$): C: 62.95 (68.93), H: 5.86 (4.53) N: 5.01 (3.49) %.

3.12 References

1 M. Rakowski DuBois and D. L. DuBois, *Chem. Soc. Rev.*, 2009, **38**, 62–72.

2 D. E. Berning, A. Miedaner, C. J. Curtis, B. C. Noll, M. C. Rakowski DuBois and D. L. DuBois, *Organometallics*, 2001, **20**, 1832–1839.

3 M. L. Helm, M. P. Stewart, R. M. Bullock, M. R. DuBois and D. L. DuBois, *Science*, 2011, **333**, 863–6.

4 J. Y. Yang, R. M. Bullock, W. J. Shaw, B. Twamley, K. Fraze, M. R. DuBois and D. L. DuBois, *J. Am. Chem. Soc.*, 2009, **131**, 5935–5945.

5 G. M. Jacobsen, R. K. Shoemaker, M. Rakowski DuBois and D. L. DuBois, *Organometallics*, 2007, **26**, 4964–4971.

6 N. Wang, M. Wang, J. Liu, K. Jin, L. Chen and L. Sun, *Inorg. Chem.*, 2009, **48**, 11551–11558.

7 L. Duan, M. Wang, P. Li, N. Wang, F. Wang and L. Sun, *Inorg. Chim. Acta*, 2009, **362**, 372–376.

8 L.-C. Song, X.-J. Sun, G.-J. Jia, M.-M. Wang and H.-B. Song, *J. Organomet. Chem.*, 2014, **761**, 10–19.

9 Adam Taylor, University of Nottingham, 2010.

10 W. Zhu, A. C. Marr, Q. Wang, F. Neese, D. J. E. Spencer, A. J. Blake, P. A. Cooke, C. Wilson and M. Schröder, *Proc. Natl. Acad. Sci. U. S. A.*, 2005, **102**, 18280–18285.

11 C. Ni, Y. Li, Z. Ni, D. Dang and Q. Meng, *Acta Crystallogr. Sect. E Struct. Reports Online*, 2004, **60**, m410–m412.

12 G. A. Bowmaker, P. D. W. Boyd and G. K. Campbell, *Inorg. Chem.*, 1982, **21**, 2403–2412.

13 A. Perra, E. S. Davies, J. R. Hyde, Q. Wang, J. McMaster and M. Schröder, *Chem. Commun.*, 2006, **10**, 1103–1105.

14 R. S. Nicholson and I. Shain, *Anal. Chem.*, 1964, **36**, 706–723.

15 A. Perra, Q. Wang, A. J. Blake, E. S. Davies, J. McMaster, C. Wilson and M. Schröder, *Dalton Trans.*, 2009, **373**, 925–931.

16 J. Dawson, University of Nottingham, 2010.

CHAPTER FOUR

Synthesis Towards [NiFe] Complexes Incorporating Quinoxaline-based Ligands: Synthesis and Characterisation

4.1 Introduction

[NiFe] hydrogenase are enzymes that catalyse the interconversion of H^+/H_2 with high efficiency.[1] The active site of the enzyme contains a sulfur-rich dinuclear Ni-Fe cluster with cyanide and carbonyl ligands bound to the Fe centre.[2,3] Synthetic and functional analogues of the active site of [NiFe] hydrogenase have been explored in the development of low molecular weight catalysts for H_2 production.[4–7] A common strategy for the synthesis of structural analogues of the active site of the [NiFe] hydrogenases to synthesise mononuclear Ni^{II}-thiolate complexes and use them as metallothiolate ligands to organometallic iron centres. Various [NiS_4] and [NiS_2P_2] complexes have been used as precursors to [NiFe] compounds including: [$Ni(L^A)Fe_2(CO)_6$],[7] [(dppe)Ni(μu-pdt)FeCp(CO)]PF_6,[8] [(dppe)Ni(pdt)$(Fe(CO)_3]$[9] and [Cp*M(μ-1κ^{3}SSS′:^{2}κ2SS-tpdt)Ni(dppe)].10

In Chapters Two and Three we expanded research into [NiS_4] and [NiS_2P_2] precursors by incorporating quinoxaline-dithiolate ligands as potential protonation and/or proton relay sites (Figure 4.1).

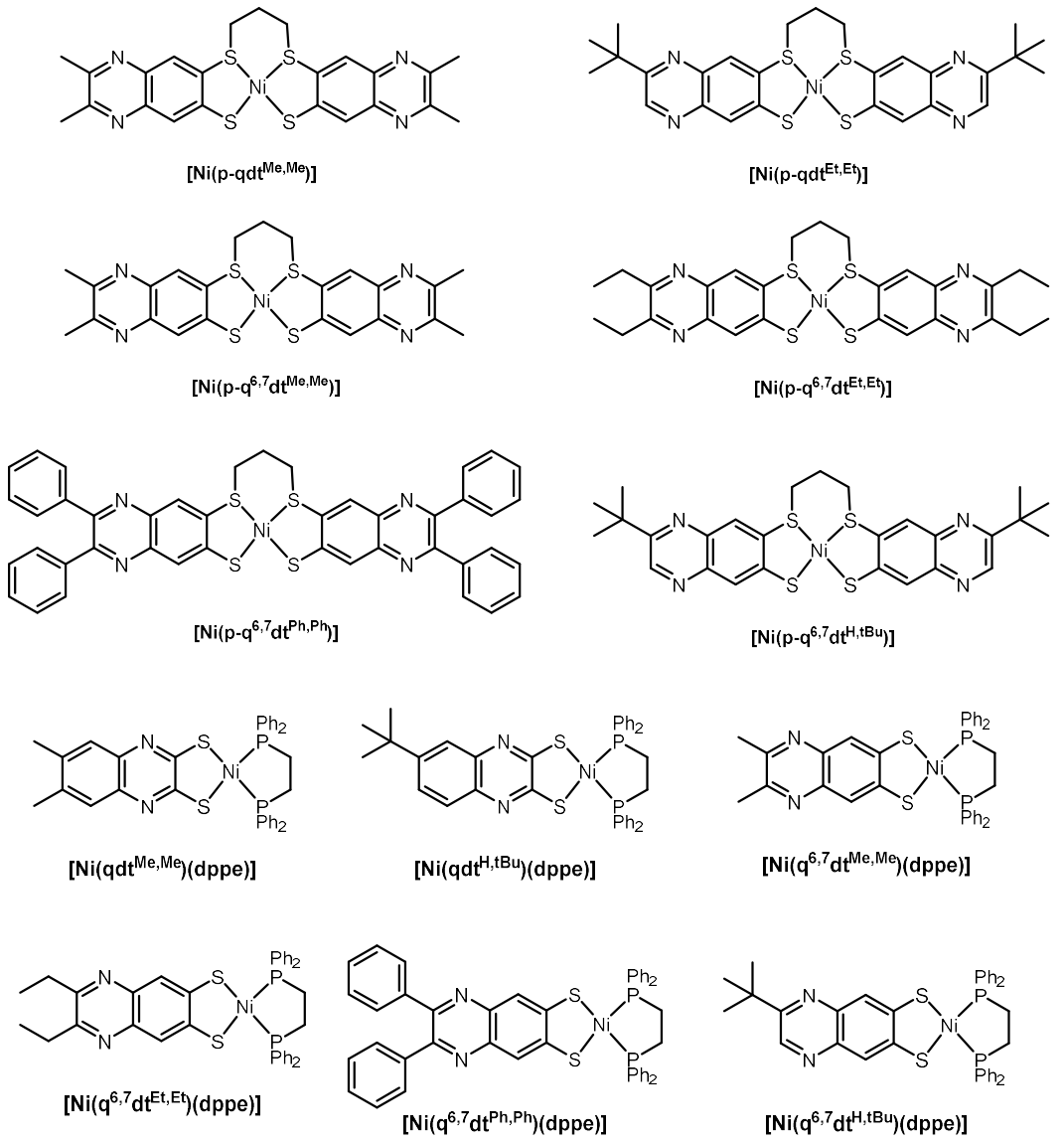


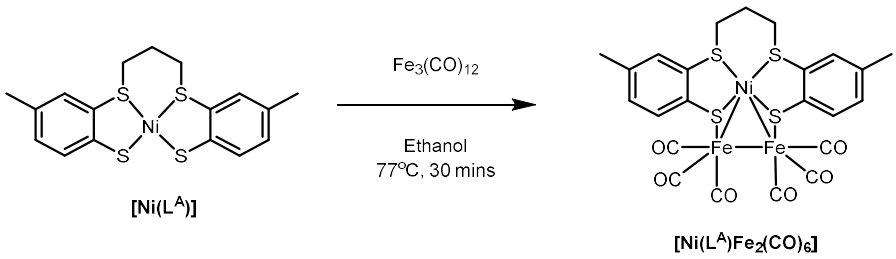
Figure 4.1: The Ni^{II} quinoxaline-based complexes synthesised in Chapters Two and Three.

Two of the complexes discussed in Chapter Two, [Ni(p-$q^{6,7}dt^{Et,Et}$)] and [Ni(p-$q^{6,7}dt^{H,tBu}$)] exhibit reversible electrochemical $Ni^{II/I}$ reduction processes at -1.51 V *vs.* Fc^+/Fc, and may be electrocatalysts for the production of H_2. [Ni(qdt^{R1,R2})(dppe)] ($R^1 = R^2 =$ Me and $R_1 =$ H, $R_2 =$ ^{t}Bu) and [Ni(p-$q^{6,7}dt^{R1,R2}$)(dppe)] ($R^1 = R^2 =$ Me, Et, Ph and R_1 = H, R_2 = ^{t}Bu) discussed in Chapter Three also exhibit reversible electrochemical $Ni^{II/I}$ reduction processes over the range -1.79 to -1.87 V *vs.* Fc^+/Fc and may be electrocatalysts. Previous work at Nottingham has shown that the addition of a $Fe_2(CO)_6$ unit to [Ni(L^A)] shifts the first redox process to a more positive potential from $E_{1/2}$ = -1.66 V *vs* Fc^+/Fc for [Ni(L^A)] to $E_{1/2}$ = -1.31 V *vs* Fc^+/Fc for [Ni(L^A)$Fe_2(CO)_6$]. Thus, the syntheses of [NiFe] compounds using the

Ni^{II} quinoxaline-based complexes described in Chapters Two and Three could result in the formation of [NiFe] compounds with more positive reduction potentials than their respective Ni^{II} precursors. Furthermore, these new [NiFe] compounds may exhibit further increases in reduction potential, following protonation at the N-atoms associated with the quinoxaline ligands in each complex in acidic solutions. These increases in reduction potential could lead to the development of more efficient electrocatalysts for the production of H_2 when compared to previously reported compounds such as; $[Ni(L^A)Fe_2(CO)_6]$[7] and $[Cp^*Fe(\mu\text{-}1\kappa^3SSS':2\kappa^2SS\text{-}tpdt)Ni(dppe)][PF_6]$ [tpdt = 3-thiapentane-1,5-dithiolate, $S(CH_2CH_2S^-)_2$].[10]

4.2 Aims

The aims of the work in this Chapter were to synthesise and characterise new [NiFe] compounds from the Ni^{II} complexes described in Chapters Two and Three (Figure 4.1). We investigated reactions with all eleven Ni^{II} complexes with [Fe]-containing precursors [*e.g.* $Fe_3(CO)_{12}$] with our initial attempts focussed on the reactions of the three precursor complexes $[Ni(p\text{-}qdt^{H,tBu})]$ (crude product), $[Ni(p\text{-}q^{6,7}dt^{Et,Et})]$ and $[Ni(q^{6,7}dt^{Et,Et})(dppe)]$ under a variety of reaction conditions.



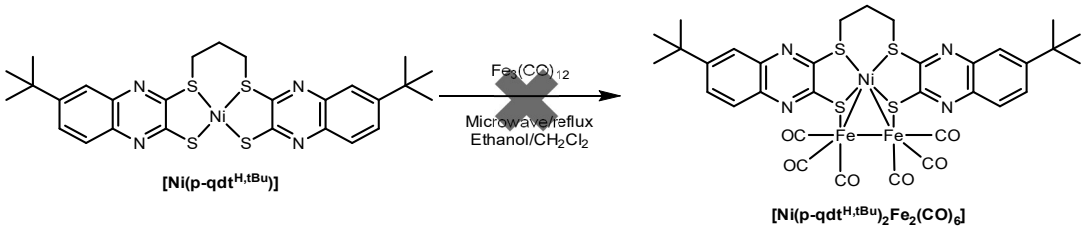
Scheme 4.1: The synthesis of $[Ni(L^A)Fe_2(CO)_6]$.[7]

Our first attempts utilized the [Fe]-containing precursor, $Fe_3(CO)_{12}$, since this compound has been used previously for the successful synthesis of $[Ni(L^A)Fe_2(CO)_6]$ (Scheme 4.1).[7,11] Following the absence of any desired [NiFe] products following the reactions between $[Ni(p\text{-}qdt^{H,tBu})]$, $[Ni(q^{6,7}dt^{Et,Et})(dppe)]$ and $Fe_3(CO)_{12}$, we also explored the use of other [Fe]-carbonyl precursors, including $[FeCp(CO)_2I]$ and $[FeCp(CO)_2(THF)][BF_4]$. The use of $[FeCp(CO)_2(THF)][BF_4]$ allowed access to [NiFe] compounds containing the $[Ni(q^{6,7}dt^{R1,R2})(dppe)]$ ($R^1 = R^2$ = Me, Et and R^1 = H R_2 = ^{t}Bu) unit. However, the isolation of analytically pure

[NiFe] compounds formed from the reactions with these Ni^{II} complexes proved difficult.

4.3 Attempted Syntheses of [NiFe] complexes using [Ni(p-qdt^{H,tBu})] as the Ni^{II} precursor

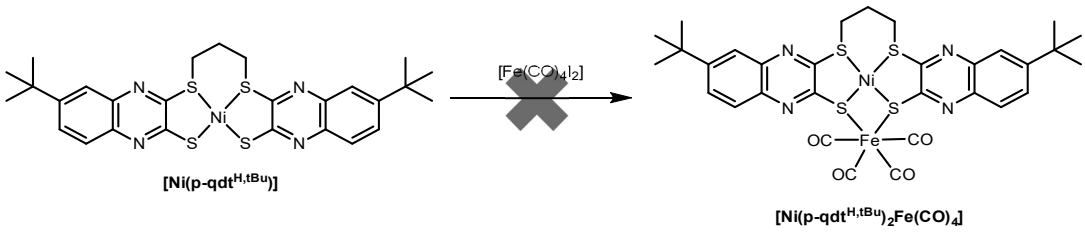
4.3.1 The reaction between [Ni(p-qdt^{H,tBu})] and $Fe_3(CO)_{12}$



Scheme 4.2: The attempted synthesis of [Ni(p-qdt^{H,tBu})$Fe_2(CO)_6$].

We carried out reactions of [Ni(p-qdt^{H,tBu})] with $Fe_3(CO)_{12}$ under a range of reaction conditions in an attempt to synthesise [Ni(p-qdt^{H,tBu})$Fe_2(CO)_6$]. We explored stirring the reaction mixture at room temperature, heating the reaction mixture to reflux and we attempted to carry out the reaction in microwave reactor using ethanol or CH_2Cl_2 as the solvent; all of these conditions have been used previously for the successful syntheses of [$NiFe_2$] complexes such as, [Ni(L^A)$Fe_2(CO)_6$].[7,12–14] We were unable to isolate [Ni(p-qdt^{H,tBu})$Fe_2(CO)_6$]; only unreacted [Ni(p-qdt^{H,tBu})] and the by-product $Fe(CO)_5$ were identified by mass spectrometry, and ^{1}H-NMR and IR spectroscopies.

4.3.2 The reaction between [Ni(p-qdt^{H,tBu})] and $[Fe(CO)_4I_2]$

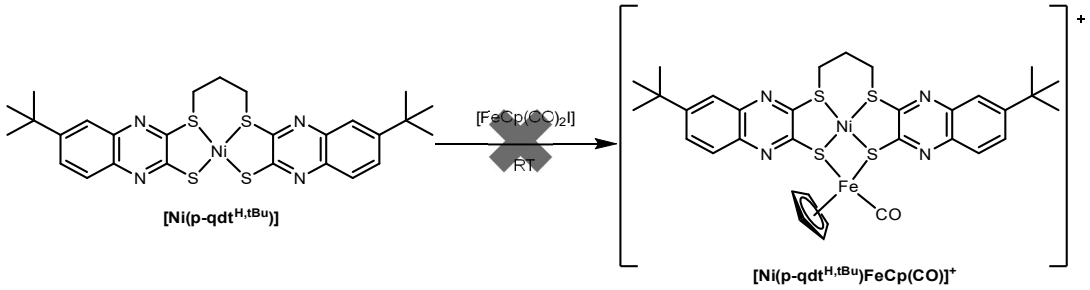


Scheme 4.3: The attempted synthesis of [Ni(p-qdt^{H,tBu})$Fe(CO)_4$].

Given that the reactions between [Ni(p-qdt^{H,tBu})] and $Fe_3(CO)_{12}$ were unsuccessful, we attempted a reaction between [Ni(p-qdt^{H,tBu})] and $[Fe(CO)_4I_2]$ as the [Fe]-containing precursor, using reaction conditions used previously for the synthesis of [Ni($L^1N_2S_2$)$Fe(CO)_3I$][BPh_4].[15] A mixture of [Ni(p-qdt^{H,tBu})] and $[Fe(CO)_4I_2]$ was stirred in CH_2Cl_2 at room temperature in the absence of light and the progress of the

reaction was monitored by IR spectroscopy, focusing on the carbonyl containing region (*ca.* 1700- 2200 cm^{-1}). The reaction was monitored for up to 120 h and only absorptions associated with the $[Fe(CO)_4I_2]$ starting material were observed. Unreacted [Ni(p-$qdt^{H,tBu}$)] and $[Fe(CO)_4I_2]$ were identified by mass spectrometry.

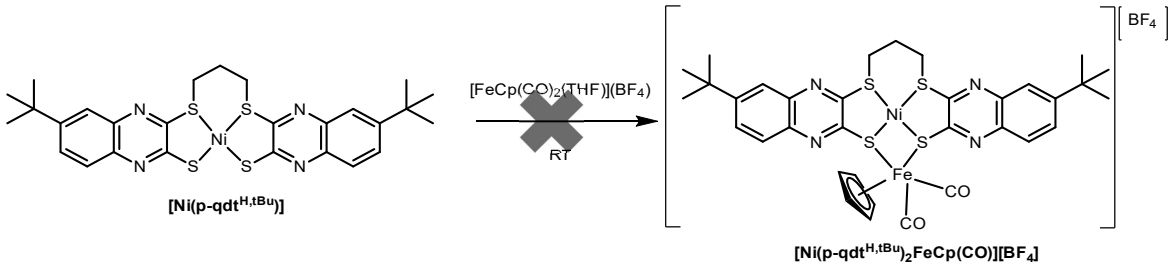
4.3.3 The reaction between [Ni(p-$qdt^{H,tBu}$)] and $[FeCp(CO)_2I]$



Scheme 4.4: The attempted synthesis of $[Ni(qdt^{tBu})_2FeCp(CO)]I$.

We also attempted a reaction between [Ni(p-$qdt^{H,tBu}$)] and $[FeCp(CO)_2I]$; Zhu *et al.* have previously used $[FeCp(CO)_2I]$ as a reagent to produce a [NiFe] compound.[8] A mixture of [Ni(p-$qdt^{H,tBu}$)] and $[FeCp(CO)_2I]$ were stirred in CH_2Cl_2 at room temperature and the reaction mixture was monitored using IR spectroscopy. After 120 h only ν(CO) absorptions for $[FeCp(CO)_2I]$ at 2041 and 1996 cm^{-1} were observed and mass spectrometry confirmed the presence of $[FeCp(CO)_2I]$ and unreacted [Ni(p-$qdt^{H,tBu}$)] in the reaction mixture.

4.3.4 The reaction between [Ni(p-$qdt^{H,tBu}$)] and $[FeCp(CO)_2(THF)][BF_4]$



Scheme 4.5 The attempted synthesis of [Ni(p-$qdt^{H,tBu}$)$FeCp(CO)_2(THF)][BF_4]$.

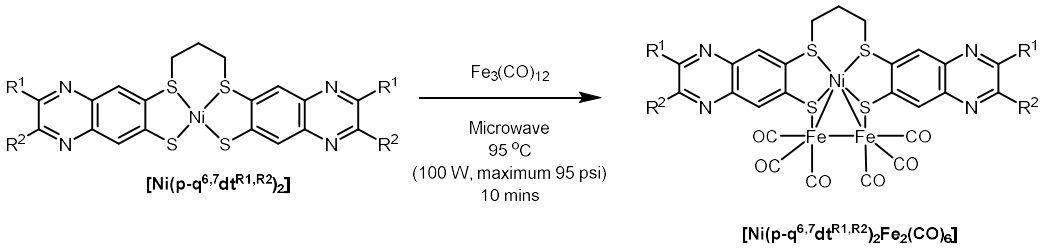
The precursor, $[FeCp(CO)_2I]$, used in Section 4.3.2, may not contain a sufficiently labile iodide ligand to promote its reaction with [Ni(p-$qdt^{H,tBu}$)]. Therefore, we prepared $[FeCp(CO)_2(THF)][BF_4]$ from $[FeCp(CO)_2I]$ by treatment with $AgBF_4$ in THF.[16] The reaction of [Ni(p-$qdt^{H,tBu}$)] with $[FeCp(CO)_2(THF)][BF_4]$ in CH_2Cl_2 at room temperature in the absence of light was followed by IR spectroscopy and mass

spectrometry for up to 48 h. However, only unreacted [Ni(p-qdt^{H,tBu})] and [FeCp(CO)$_2$(THF)][BF$_4$] [ν(CO) = 2071 and 2026 cm^{-1}] were identified. The reactions were attempted at room temperature in the absence of light due to the temperature and light sensitive nature of [FeCp(CO)$_2$(THF)][BF$_4$] and the corresponding products formed from reactions with other Ni^{II} precursors explored previously in the group.[17]

Thus, while [Ni(p-qdt^{H,tBu})] pocesses a similar coordination about the Ni^{II} as in [Ni(L^A)], it appears that the incorporation of quinoxaline unit pendant to the S-donors in [Ni(p-qdt^{H,tBu})] may deactivate the thiolate donors towards reactions with [Fe]-containing precursors. We therefore focussed on reactions involving Ni^{II} precursors containing functionalised q^{6,7}dt-based ligands to investigate whether the position of the N atoms within the quinoxaline framework effects the reactivity of these precursors towards [Fe]-containing complexes.

4.4 The synthesis of [NiFe] complexes using [Ni(p-q^{6,7}dt^{R1,R2})] (R^1 = R^2 = Me, Et and Ph; R^1 = H, R^2 = ^{t}Bu)

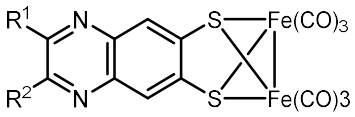
4.4.1 The synthesis of [Ni(p-q^{6,7}dt^{R1,R2})Fe$_2$(CO)$_6$] (R^1 = R^2 = Me, Et and Ph; R^1 = H, R^2 = ^{t}Bu)



Scheme 4.6: Synthetic route for [Ni(p-q^{6,7}dt^{R1,R2})Fe$_2$(CO)$_6$] (R^1 = R^2 = Me, Et and Ph; R^1 = H, R^2 = ^{t}Bu).

The syntheses of [Ni(p-q^{6,7}dt^{R1,R2})Fe$_2$(CO)$_6$] (R^1 = R^2 = Me, Et and Ph; R^1 = H, R^2 = ^{t}Bu) in 10-18 % crude yields were achieved *via* the reaction of [Ni(p-q^{6,7}dt^{R1,R2})] and Fe$_3$(CO)$_{12}$ in CH$_2$Cl$_2$ in a microwave reactor for 10 mins using a method previously explored within our group.[14] In each reaction the ν(CO) bands for Fe$_3$(CO)$_{12}$ at 2053 cm^{-1} decreased in intensity and new bands grew in over the course of the reaction. The ν(CO) bands at 1959-2038 cm^{-1} are assigned to the product [Ni(p-q^{6,7}dt^{R1,R2})Fe$_2$(CO)$_6$] (R^1 = R^2 = Me, Et, Ph and R^1 = H and R^2 = ^{t}Bu) from comparison of ν(CO) bands recorded for [Ni(L^A)Fe$_2$(CO)$_6$] (2035 (s), 1995 (s) and

1955 cm^{-1}), The ν(CO) bands at 1997-2079 cm^{-1} were assigned to $[(q^{6,7}dt^{R1,R2})Fe_2(CO)_6]$ (R^1=R^2 = Me, Et, Ph and R^1= H and R^2 = ^{t}Bu) on the basis of comparisons with $[Fe_2\{\mu\text{-Hqdt}\}(CO)_6][CF_3SO_3]$[18] [2116 (s), 2064(s) and 2011(s) cm^{-1}] and those at 1995 and 2018 cm^{-1} to $[Fe(CO)_5]$ that also forms as a by-product.[19] The mass spectra of the reaction mixtures, recorded after 10 minutes of reaction, possessed peaks assigned to the $[Ni(p\text{-}q^{6,7}dt^{R1,R2})]$ (R^1 = R^2 = Me, Et, Ph; R^1 = H and R^2 = ^{t}Bu) starting material, the $[Ni(p\text{-}q^{6,7}dt^{R1,R2})Fe_2(CO)_6]$ (R^1 = R^2 = Me, Et, Ph; R^1= H and R^2 = ^{t}Bu) product and the $[(q^{6,7}dt^{R1,R2})Fe_2(CO)_6]$ (R^1 = R^2 = Me, Et, Ph; R^1= H and R^2 = ^{t}Bu) by-product (Figure 4.2).



$[(p\text{-}q^{6,7}dt^{R1,R2})Fe_2(CO)_6]$

Figure 4.2 The structure of the $[(q^{6,7}dt^{R1,R2})Fe_2(CO)_6]$ (R^1 = R^2 = Me, Et, Ph; R^1 = H and R^2 = ^{t}Bu) by-product.

Crude $[Ni(p\text{-}q^{6,7}dt^{R1,R2})Fe_2(CO)_6]$ (R_1 = R_2 = Me, Et, Ph; R_1= H and R_2 = ^{t}Bu) could be isolated from the reaction mixture by the removal of the solvent and the $Fe(CO)_5$ by-product under vacuum followed by the washing of the resulting brown precipitate with diethyl ether to remove $[(q^{6,7}dt^{R1,R2})Fe_2(CO)_6]$. A variety of column chromatographic conditions were investigated in attempts to isolate analytically pure samples of $[Ni(p\text{-}q^{6,7}dt^{R1,R2})Fe_2(CO)_6]$. These included performing column chromatography in the absence of light and air, with silica or alumina gels and with a range of eluents including CH_2Cl_2, ethyl acetate, methanol and pentane. For R^1 = R^2 = Me, recrystallisation of the columned mixture from CH_2Cl_2, followed by

manual separation, yielded crystals of [Ni(p-$q^{6,7}dt^{Me,Me}$)$Fe_2(CO)_6$] suitable for X-ray crystallography.

Table 4.1: IR ν(CO) recorded for [Ni(p-$q^{6,7}dt^{R1,R2}$)$Fe_2(CO)_6$] ($R^1 = R^2$ = Me, Et, Ph; R^1 = H and R^2 = ^{t}Bu) and [Ni(L^A)$Fe_2(CO)_6$] in CH_2Cl_2 solutions.[7]

Complex	ν(CO) bands /cm^{-1}
[Ni(p-$q^{6,7}dt^{Me,Me}$)$Fe_2(CO)_6$]	2038, 1998 and 1959
[Ni(p-$q^{6,7}dt^{Et,Et}$)$Fe_2(CO)_6$]	2038, 1999 and 1960
[Ni(p-$q^{6,7}dt^{H,tBu}$)$Fe_2(CO)_6$]	2037, 1997 and 1961
[Ni(p-$q^{6,7}dt^{Ph,Ph}$)$Fe_2(CO)_6$]	2038,1998 and 1960
[Ni(L^A)$Fe_2(CO)_6$]	2035, 1995 and 1955

Table 4.1 shows a comparison of the ν(CO) recorded for [Ni(p-$q^{6,7}dt^{R1,R2}$)$_2Fe_2(CO)_6$] ($R^1 = R^2$ = Me, Et, Ph; R^1 = H and R^2 = ^{t}Bu) and [Ni(L^A)$Fe_2(CO)_6$]. The IR spectra of [Ni(p-$q^{6,7}dt^{R1,R2}$)$_2Fe_2(CO)_6$] are similar and do not exhibit a significant variation in ν(CO) as R^1 and R^2 are varied. A comparison of ν(CO) for [Ni(p-$q^{6,7}dt^{R1,R2}$)$Fe_2(CO)_6$] with those of [Ni(L^A)$Fe_2(CO)_6$][7] shows that ν(CO) for [Ni(p-$q^{6,7}dt^{R1,R2}$)$Fe_2(CO)_6$] are each shifted by *ca.* 5 cm^{-1} to higher wavenumber. This shift suggests that there is less π-back bonding in [Ni(p-$q^{6,7}dt^{R1,R2}$)$Fe_2(CO)_6$] that may reflect the more electron-withdrawing nature of the [p-$q^{6,7}dt^{R1,R2}$]$^{2-}$ relative to [L^A]^2.

4.4.2 The reactions between [Ni(p-$q^{6,7}dt^{R1,R2}$)] and [FeCp(CO)$_2$(THF)](BF$_4$)

The reactions of [Ni(p-$q^{6,7}dt^{R1,R2}$)] ($R^1 = R^2$ = Me, Et, Ph; R^1= H and R^2 = ^{t}Bu) with [FeCp(CO)$_2$(THF)][BF$_4$] in CH_2Cl_2 at room temperature in the absence of light were monitored by IR spectroscopy. During the course of the reaction the ν(CO) bands associated with [FeCp(CO)$_2$(THF)][BF$_4$] (2071 and 2026 cm^{-1}) decrease in intensity and bands at *ca.* 2040 and 1998 cm^{-1} (Figure 4.3 Table 4.2) grow in. The development of these ν(CO) features mirrors those found for [Ni(xbsms)FeCp(CO)$_2$](BF$_4$) [H$_2$xbsms = 1,2-bis(4-mercapto-3,3-dimethyl-2-thiabutyl)benzene][20] that occur at 2006 and 2053 cm^{-1}. Mass spectroscopic data is consistent with the formation of [Ni(p-$q^{6,7}dt^{R1,R2}$)FeCp(CO)$_2$][BF$_4$] ($R^1 = R^2$ = Me, Et, Ph; R^1 = H and R^2 = ^{t}Bu).

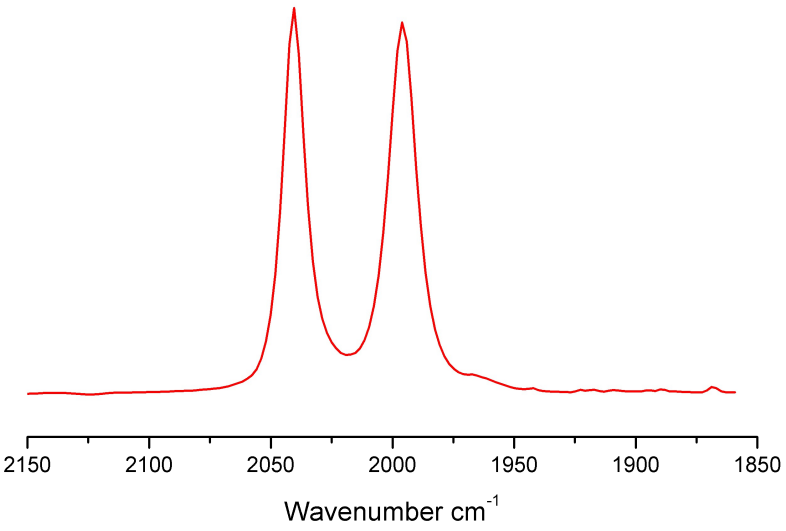


Figure 4.3: The IR spectrum of [Ni(p-q^{6,7}dt^{Et,Et})FeCp(CO)$_2$][BF$_4$] in CH_2Cl_2 solution.

Table 4.2 IR ν(CO) bands [Ni(p-q^{6,7}dt^{R1,R2})$_2$FeCp(CO)$_2$][BF$_4$] (R_1 = R_2 = Me, Et, Ph; R_1 = H and R_2 = ^{t}Bu) recorded in CH_2Cl_2.

Complex	ν(CO) bands /cm^{-1}
[Ni(p-q^{6,7}dt^{Me,Me})FeCp(CO)$_2$][BF$_4$]	2046 and 1998
[Ni(p-q^{6,7}dt^{Et,Et})FeCp(CO)$_2$][BF$_4$]	2040 and 1995
[Ni(p-q^{6,7}dt^{H,tBu})FeCp(CO)$_2$][BF$_4$]	2049 and 2001
[Ni(p-q^{6,7}dt^{Ph,Ph})FeCp(CO)$_2$][BF$_4$]	2046 and 1998

Solid materials were precipitated from the reaction mixtures by the addition of pentane and attempts were made to isolate pure [Ni(p-q^{6,7}dt^{R1,R2})FeCp(CO)$_2$][BF$_4$] from this crude material. These included recrystallisation from CH_2Cl_2 with a range of antisolvents and column chromatography with silica and alumina gels under anaerobic conditions and in the absence of light. However, IR spectroscopy on the isolated residues showed the development of new ν(CO) bands at *ca.* 2010 cm^{-1}, which may be associated with the decomposition of the products, and elemental analyses confirmed that [Ni(p-q^{6,7}dt^{R1,R2})FeCp(CO)$_2$][BF$_4$] could not be isolated pure.

4.4.3 The deactivation of the thiolate S-donors in [Ni(p-qdt^{R1,R2})]

The reactions above suggest that [Ni(p-qdt^{H,tBu})] does not react with [Fe]-containing compounds under those conditions usually employed for the syntheses of [Ni(L^A)Fe$_2$(CO)$_6$] and [Ni(xbsms)FeCp(CO)$_2$][BF$_4$].[20] In contrast, [Ni(p-q^{6,7}dt^{R1,R2})] (R_1 = R_2 = Me, Et, Ph; R_1= H and R_2 = ^{t}Bu) reacts with $Fe_3(CO)_{12}$ to form [Ni(p-

$q^{6,7}dt^{R1,R2})Fe_2(CO)_6]$ (Section 4.4.1) and appears to react with $[FeCp(CO)_2(THF)][BF_4]$ to form unstable $[Ni(p\text{-}q^{6,7}dt^{R})FeCp(CO)_2][BF_4]$ ($R^1 = R^2$ = Me, Et, Ph; R^1= H and R^2 = ^{t}Bu) products. We suspect that the nature of the quinoxaline components may be modulating the reactivity of the thiolate S-lone pairs in these complexes and we looked to DFT calculations previously accomplished for $[Ni(p\text{-}qdt^{H,tBu})]$, $[Ni(q^{6,7}dt^{Et,Et})]$ and $[Ni(L^A)]$ (Chapter 2, Section 2.11) to provide some insight. Representations of the HOMOs calculated by DFT for the gas-phase geometry optimised structures of $[Ni(p\text{-}qdt^{H,tBu})]$, $[Ni(q^{6,7}dt^{Et,Et})]$ and $[Ni(L^A)]$ are shown in Figure 4.3 and may be used to rationalise the difference in reactivities of these compounds with [Fe]-containing precursors.

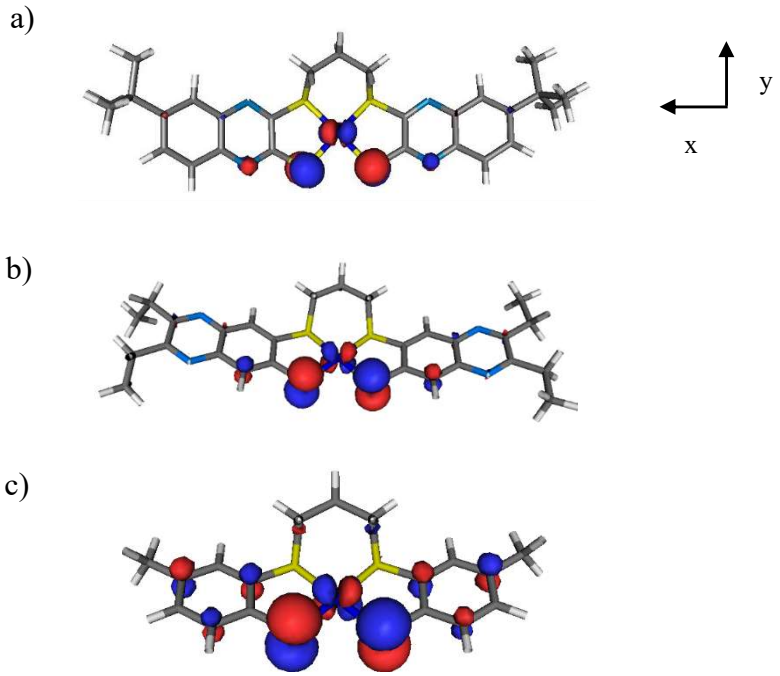


Figure 4.4: Kohn-Sham HOMOs for the BP86 gas-phase optimised structures of a) $[Ni(p\text{-}qdt^{HtBu})]$ b) $[Ni(q^{6,7}dt^{Et,Et})]$ c) $[Ni(L^A)]$.

Each HOMO has contributions principally derived from the Ni $3d_{xz}$ orbital and a dithiolate-S $3p(\pi)$ combination. Assuming that the reactivity of the Ni^{II} precursors with [Fe]-containing precursors involves an overlap of their HOMO with the antibonding LUMO orbitals of the [Fe]-precursors, then a contributor to the relative differences in reactivity for each Ni^{II} precursor will be the differences in dithiolate-

S 3*p*(π) contributions in each HOMO. The relative dithiolate-S 3*p*(π) characters vary as [Ni(L^A)] (48% S, 24 % Ni character) ≈ [Ni(p-$q^{6,7}dt^{Et,Et}$)] (47% S, 25% Ni character) > [Ni(p-$qdt^{H,tBu}$)] (42% S, 32% Ni character). Thus, the lower dithiolate-S 3*p*(π) (42%) contribution in the HOMO of [Ni(p-$qdt^{H,tBu}$)] may be sufficient to deactivate the thiolate S-donors in [Ni(p-$qdt^{H,tBu}$)] towards reactions with [Fe]-precursors.

4.4.4 The single crystal X-ray structure of [Ni($q^{6,7}dt^{Me}$)$_2$Fe$_2$(CO)$_6$]

Single blue-block crystals of [Ni(p-$q^{6,7}dt^{Me,Me}$)$Fe_2(CO)_6$] suitable for X-ray diffraction were obtained through the diffusion of hexane into a concentrated solution of [Ni(p-$q^{6,7}dt^{Me,Me}$)$Fe_2(CO)_6$] in CH_2Cl_2. The X-ray crystal structure of [Ni(p-$q^{6,7}dt^{Me,Me}$)$Fe_2(CO)_6$] in shown in Figure 4.5 and selective bond lengths and angles are presented in Table 4.3.

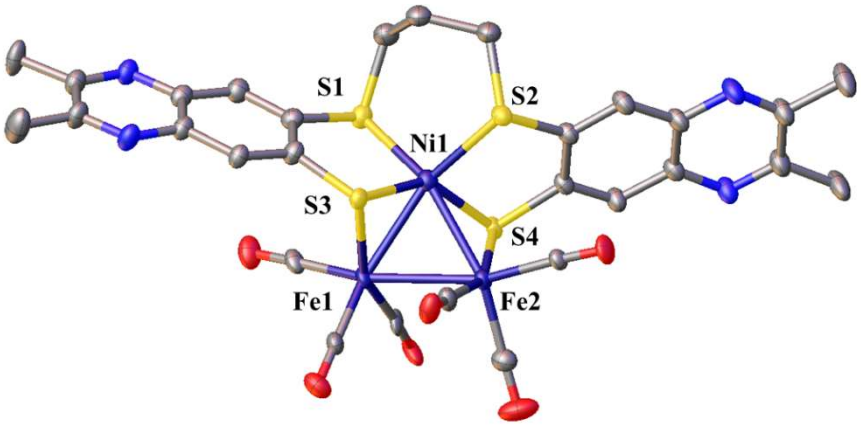


Figure 4.5: The molecular structure of [Ni(p-$q^{6,7}dt^{Me,Me}$)$Fe_2(CO)_6$] with atoms selectively labelled. The H atoms are omitted for clarity.

The Ni^{II} centre is coordinated to four S-donors derived from the [p-$q^{6,7}dt^{Me,Me}$]$^{2-}$ ligand framework and two Fe centres derived from the [$Fe_2(CO)_6$] fragment. The coordination of each thiolate S-donor to the Fe centres completes an NiS_4Fe_2 core in which each metal centre possesses a distorted octahedral geometry. This is consistent

with the molecular structure of $[Ni(L^A)Fe_2(CO)_6]$ and other $[Ni(S_4)Fe_2(CO)_6]$ compounds reported within the group.[7,12,13,21,22]

The Ni(1)-S(3) and Ni(1)-S(4) distances are ~ 2.18 Å (Table 4.3) and are typical of formal Ni^{II}-S(thiolate) bonds ([Ni-S] = 2.17 Å; σ= 0.02 Å).[23] The Ni(1)-S(1) and Ni(1)-S(2) distances are ~ 2.25 Å (Table 4.3) and lie within the range for Ni^{II}-S(thioether) interations ([Ni-S] = 2.36 Å; σ = 0.11 Å).[23] The S(1)-Ni(1)-S(3) [92.65(14) °] and S(2)-Ni(1)-S(4) [93.06(13) °] (Table 4.3) are close to 90° and the S(3)-Ni(1)-S(4) and S(1)-Ni(1)-S(2) angles are greater than 90° [S(3)-Ni(1)-S(4) = 141.95(15)° and S(1)-Ni(1)-S(2) = 104.28(15)°, Table 4.3]. The dihedral angle between the planes defined by S(1)-Ni(1)-S(3) and the S(2)-Ni(1)-S(4) [86.64(6)°] is similar to that for $[Ni(L^A)Fe_2(CO)_6]$ [84.04(4)°][7] and a comparison of the metrical parameters about the Ni centres in $[Ni(q^{6,7}dt^{Me,Me})_2Fe_2(CO)_6]$ and $[Ni(L^A)Fe_2(CO)_6]$ (Table 4.3) shows that the geometry of the two Ni centres are similar.[7]

As discussed in Chapter Two the geometries of $[Ni(p\text{-}q^{6,7}dt^{R1,R2})]$ appear to be distorted square planar. Thus, the geometry of the NiS_4 unit in $[Ni(p\text{-}q^{6,7}dt^{Me,Me})Fe_2(CO)_6]$ distorts further away from the approximate square-planar geometry of $[Ni(p\text{-}q^{6,7}dt^{Me,Me})]$ in order to accommodate the $[Fe_2(CO)_6]$ fragment.[7] This distortion, together with the inclusion of two Fe atoms in the coordination sphere of the Ni centre, leads to a coordination geometry about the Ni atom that may be regarded as distorted octahedral.

The two Fe centres in $[Ni(p\text{-}q^{6,7}dt^{Me,Me})Fe_2(CO)_6]$ are each coordinated by one thiolate S-donor, one Fe atom and three CO ligands. The Fe-S distances [Fe(1)-S(3) = 2.258(3) and Fe(2)-S(4) = 2.269(4) Å] are within the range of those for complexes containing $[Fe_2(CO)_6]$ units coordinated by thiolate ligands ([Fe-S] = 2.263 Å; σ = 0.021 Å).[23] The Fe(1)-S(4) and Fe(2)-S(3) distances (3.270(4) and 3.297(4) Å, respectively) suggest that the thiolate donor atoms do not bridge between the Fe atoms. The Fe(1)-Fe(2) distance 2.608(3) Å is shorter than that for $[Ni(L^A)Fe_2(CO)_6]$ (2.6435(9) Å),[7] suggesting that a stronger Fe-Fe bonding interaction is present in $[Ni(p\text{-}q^{6,7}dt^{Me,Me})Fe_2(CO)_6]$. The Ni-Fe distances (Ni(1)-Fe(1) = 2.504(3) and Ni(1)-Fe(2) = 2.481(3) Å) are shorter than the sum of the emperical atomic radii for Ni and Fe (1.35 and 1.40 Å, respectively)[24] and are similar to those in $[Ni(L^A)Fe_2(CO)_6]$

(Ni(1)-Fe(1) = 2.4789(9) and Ni(1)-Fe(2) = 2.6435(9) Å) suggesting that Ni-Fe bonding interactions are present in [Ni(p-$q^{6,7}dt^{Me,Me}$)$Fe_2(CO)_6$].

Table 4.3: Comparison of selected bond lengths and angles in [Ni(p-$q^{6,7}dt^{Me,Me}$)$Fe_2(CO)_6$] with [Ni(L^A)$Fe_2(CO)_6$] and the gas-phase geometry optimized structure of [Ni(p-$q^{6,7}dt^{Me,Me}$)$Fe_2(CO)_6$].

Bond Length (Å)	**[Ni(p-$q^{6,7}dt^{Me,Me}$)$Fe_2(CO)_6$]**	**[Ni(L^A)$Fe_2(CO)_6$]**	**BP86**
Ni(1)-S(1)	2.251(4)	2.1877(13)	2.2546
Ni(1)-S(2)	2.274(4)	2.2495(12)	2.2635
Ni(1)-S(3)	2.182(4)	2.1784(12)	2.1894
Ni(1)-S(4)	2.181(4)	2.2371(13)	2.1877
Fe(1)-S(3)	2.258(3)	2.2580(14)	2.2916
Fe(2)-S(4)	2.269(4)	2.2532(14)	2.2920
Fe(2)··S(3)	3.297(4)	3.3408(14)	3.375
Fe(1)··S(4)	3.270(4)	3.3690(14)	3.335
Ni(1)-Fe(1)	2.504(3)	2.4789(9)	2.5047
Ni(1)-Fe(2)	2.481(3)	2.4904(8)	2.5007
Fe(1)-Fe(2)	2.608(3)	2.6435(9)	2.6850
Bond angle (°)			
S(1)-Ni(1)-S(2)	104.28(15)	104.39(5)	103.48
S(1)-Ni(1)-S(4)	109.17(15)	109.96(5)	106.83
S(2)-Ni(1)-S(4)	93.06(13)	92.95(5)	94.56
S(1)-Ni(1)-S(3)	92.65(14)	93.07(5)	93.82
S(2)-Ni(1)-S(3)	111.78(14)	106.97(5)	108.41
S(3)-Ni(1)-S(4)	141.95(15)	144.88(5)	144.66
Fe(1)-Ni(1)-Fe(2)	63.08(9)	64.28(3)	64.88
Ni(1)-Fe(2)-Fe(1)	58.90(8)	57.65(2)	57.49
Ni(1)-Fe(1)-Fe(2)	58.02(8)	58.07(2)	57.63

The gas phase geometry optimised DFT calculated structure of [Ni(p-$q^{6,7}dt^{Me,Me}$)$Fe_2(CO)_6$] is shown in Figure 4.6 and the metrical parameters are shown in Table 4.3. There is a good agreement between the calculated and experimental parameters that characterise the geometry of the Ni^{II} centre; the average Ni-S bond distances (av. 2.2097 Å) calculated by DFT model are essentially indistinguishable from those of the X-ray structure (av. 2.2275 Å). There is good agreement with the

Ni-S, Ni-Fe bonds whereas the calculated Fe-Fe bond distance (2.6850 Å) is 0.065 Å than the experimental bond length (2.608(3) Å).

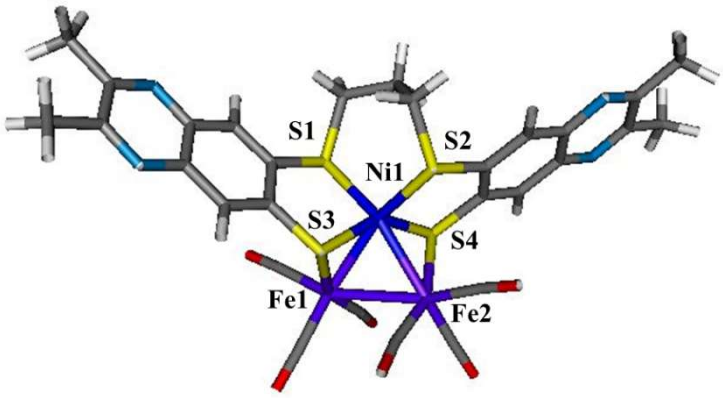


Figure 4.6: The gas-phase DFT geometry optimised structure of [Ni(p-q^{6,7}dt^{Me,Me})Fe$_2$(CO)$_6$] using the BP86 functional.

4.5 Cyclic voltametric studies of [Ni(p-q^{6,7}dt^{R1,R2})Fe$_2$(CO)$_6$] (R^1 = R^2 = Et; R^1 = H, R^2 = ^{t}Bu)

Cyclic voltammetric studies on of [Ni(p-q^{6,7}dt^{R1,R2})Fe$_2$(CO)$_6$] (R^1 = R^2 = Et; R^1 = H, R^2= ^{t}Bu) were obtained before decomposition was observed. Satisfactory cyclic voltammetry for [Ni(p-q^{6,7}dt^{Me,Me})Fe$_2$(CO)$_6$] could not be obtained before decomposition occurred. Further synthetic attempts for these complexes will be required to carry out complete electrochemical studies.

The cyclic voltammograms of 1 mM solutions of [Ni(p-q^{6,7}dt^{R1,R2})Fe$_2$(CO)$_6$] (R^1 = R^2 = Et; R^1 = H, R^2 = ^{t}Bu) in CH_2Cl_2 solution with [N^{n}Bu$_4$][BF$_4$] as supporting electrolyte are shown in Figure 4.7.

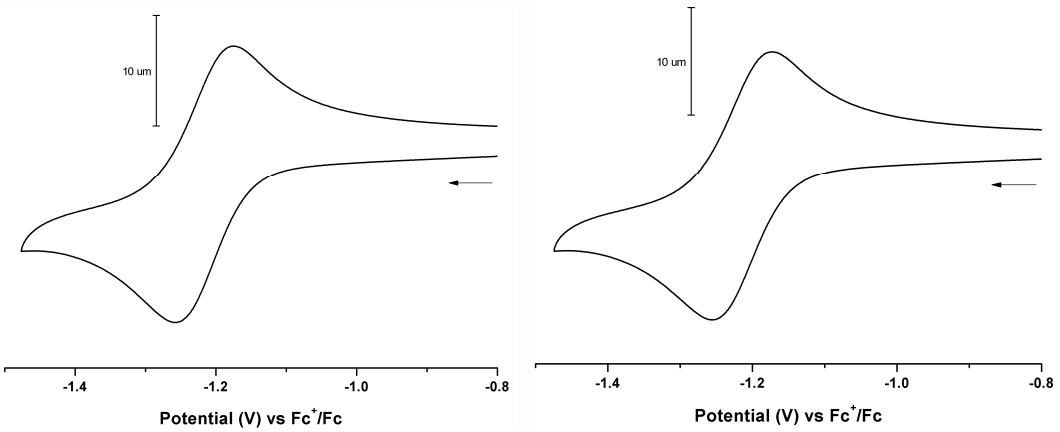


Figure 4.7: Cyclic voltammograms of [Ni(p-$q^{6,7}dt^{Et,Et}$)$Fe_2(CO)_6$] (Left) and [Ni(p-$q^{6,7}dt^{H,tBu}$)$Fe_2(CO)_6$] (Right) in CH_2Cl_2 at 293 K containing [N^nBu_4][BF_4] (0.4M) as supporting electrolyte at a scan rate of 100 mVs^{-1}.

[Ni(p-$q^{6,7}dt^{R1,R2}$)$Fe_2(CO)_6$] (R^1 = R^2 = Et; R^1 = H, R^2 = ^{t}Bu) exhibit electrochemically reversible reduction processes at $E_{1/2}$ = -1.22 and -1.21 V *vs* Fc^+/Fc, respectively. [Ni(p-$q^{6,7}dt^{R1,R2}$)$Fe_2(CO)_6$] (R^1 = R^2 = Et; R^1 = H, R^2 = ^{t}Bu) also exhibit a second reduction process at E_p^c = -1.78 and -1.77 V *vs* Fc^+/Fc, respectively, together with an associated oxidation process at E_p^a = -0.92 and -0.91 V *vs* Fc^+/Fc, respectively. [Ni(L^A)$_2Fe_2(CO)_6$] possesses an electrochemically reversible reduction process at $E_{1/2}$= -1.31 V *vs* Fc^+/Fc, assigned to the formation of [Ni(L^A)$_2Fe_2(CO)_6$]$^-$ in which the unpaired electron is delocalised across the [$NiFe_2$] core as evidenced by EPR, IR and UV/vis spectroscopic studies, supported by DFT calculations. In the absence of spectroelectrochemical data for [Ni(p-$q^{6,7}dt^{R1,R2}$)$Fe_2(CO)_6$] (R_1 = R_2 = Et; R_1 = H, R_2 = ^{t}Bu), we used the DFT calculations on [Ni(p-$q^{6,7}dt^{Me,Me}$)$Fe_2(CO)_6$] and comparisons to [Ni(L^A)$_2Fe_2(CO)_6$] to assign the first redox process at $E_{1/2}$ = -1.22 and -1.21 V *vs* Fc^+/Fc for these species.

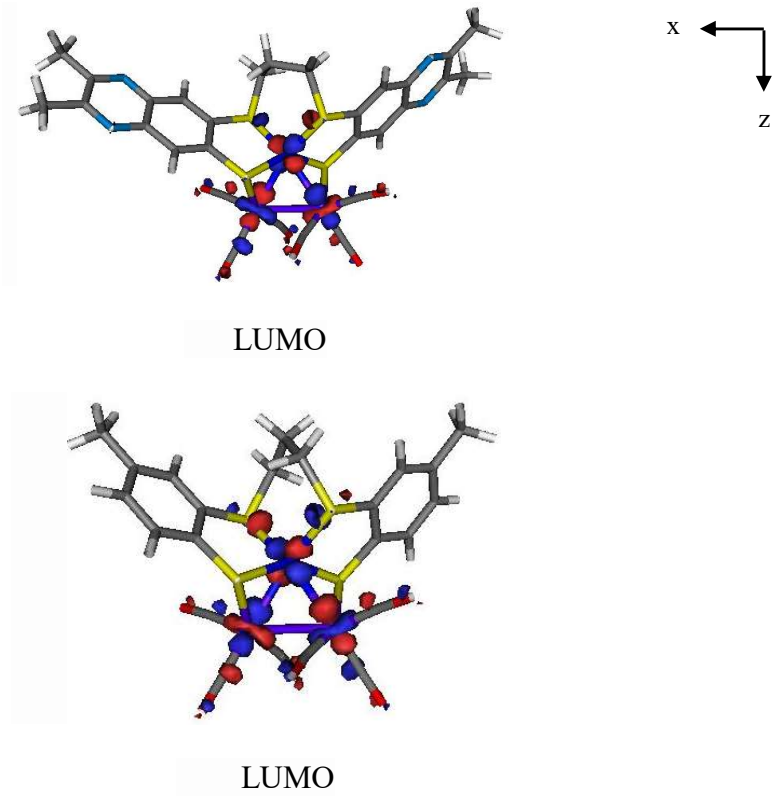


Figure 4.8: Kohn-Sham LUMOs for the BP86 optimised structures of a)[Ni(p-$q^{6,7}dt^{Me,Me}$)$Fe_2(CO)_6$] and b) [Ni(L^A)$Fe_2(CO)_6$]

The composition and energies of the redox active LUMOs of [Ni(p- $q^{6,7}dt^{Me,Me}$)$Fe_2(CO)_6$] and [Ni(L^A)$Fe_2(CO)_6$] from restricted DFT calculation of the corresponding geometry optimised models are shown in Table 4.4 Isosurface plots of the Kohn-Sham LUMOs for [Ni(p-$q^{6,7}dt^{Me,Me}$)$Fe_2(CO)_6$] and [Ni(L^A)$Fe_2(CO)_6$] are shown in Figure 4.8. The results of both calculations support a delocalised LUMO involving the metal and ligand donor atoms across the $NiS_4Fe_2(CO)_6$ core. The principal metal contributions are $3d_{xz}$ in character with small admixtures of $3d_{yz}$ for Ni and $3d_z^2$ and $3d_{yz}$ for Fe. There is also contribution from the thioether and thiolate S-donors along with delocalisation of electron density into the π* orbitals of the CO ligands.

The Ni contribution to the LUMO for [Ni(p-$q^{6,7}dt^{Me,Me}$)$_2Fe_2(CO)_6$] and [Ni(L^A)$Fe_2(CO)_6$] are 17.8% and 20.3%, respectively, and the Fe contributions are 37.8 and 55.2%, respectively. Thus, given the similarity in natures of the LUMOs of [Ni($q^{6,7}dt^{Me,Me}$)$Fe_2(CO)_6$] and [Ni(L^A)$Fe_2(CO)_6$], then the first reduction process for [Ni(p-$q^{6,7}dt^{R1,R2}$)$Fe_2(CO)_6$] ($R^1 = R^2 = Et$; $R^1 = H$, $R^2 = {}^tBu$) at $E_{1/2}$ = -1.22 and -1.21 V *vs* Fc^+/Fc, respectively, may be assigned to the addition of an electron to the

LUMO of [Ni(p-q^{6,7}dt^{R1,R2})Fe$_2$(CO)$_6$] (R^1 = R^2 = Et; R^1 = H, R^2 = ^{t}Bu) that is delocalised across the [NiFe$_2$] core. Future spectroelectrochemical EPR, IR and UV/vis spectroscopic studies need to be undertaken in order to establish experimentally, the nature of the redox active orbitals in [Ni(p-q^{6,7}dt^{R1,R2})Fe$_2$(CO)$_6$] (R^1 = R^2 = Et; R^1 = H, R^2 = ^{t}Bu) for direct comparisons with those derived from DFT calculations.

Table 4.4: The nature, energy and composition of the frontier orbitals obtained from the DFT calculations for [Ni(q^{6,7}dt^{Et})$_2$Fe$_2$(CO)$_6$] and [Ni(L^A)Fe$_2$(CO)$_6$].

Compound	Designation	Orbital Nature	Energy /Hartrees	% Contribution		
				Ni	S	Fe
[Ni(p-q^{6,7}dt^{Me,Me})Fe$_2$(CO)$_6$]	209a LUMO	Ni 3d_{xz} , 3d_{yz} Fe 3d_z^2, 3d_{yz}	-0.148	17.8	4.6	37.8
[Ni(L^A)Fe$_2$(CO)$_6$]	175a LUMO	Ni 3d_{xz} , 3d_{yz} Fe 3d_z^2, 3d_{yz}	-0.141	20.3	6.3	55.15

The relative energies of the LUMOs calculated for [Ni(p-q^{6,7}dt^{Me,Me})Fe$_2$(CO)$_6$] and [Ni(L^A)Fe$_2$(CO)$_6$] (-0.148 and -0.141 Hartrees) and the increase in the potential of the first reduction of [Ni(p-q^{6,7}dt^{R1,R2})Fe$_2$(CO)$_6$] (R$_1$ = R$_2$ = Et; R$_1$ = H, R$_2$ = ^{t}Bu) relative to [Ni(L^A)Fe$_2$(CO)$_6$] are consistent with the incorporation of the electron withdrawing [p-q^{6,7}dt^{R1,R2}]$^{2-}$ ligand in [Ni(p-q^{6,7}dt^{Me,Me})Fe$_2$(CO)$_6$]. Thus, the incorporation of quinoxaline units has achieved the desired aim of increasing the potential of the first reduction process by *ca.* 0.1 V. Further electrochemical and catalytic studies are required to fully evaluate complexes of the type [Ni(p-q^{6,7}dt^{R1,R2})Fe$_2$(CO)$_6$] as potential catalysts for H$_2$ production.

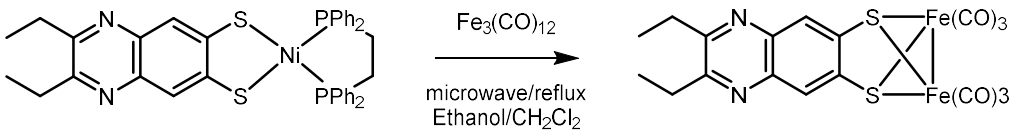
4.6 The Synthesis of [NiFe] Compounds from [Ni(q^{6,7}dt^{R1,R2})(dppe)] (R^1 = R^2 = Me, Et, Ph and R^1 = H R^2 = ^{t}Bu) and [Ni(qdt^{R1,R2})(dppe)] (R^1 = R^2 = Me, and R^1 = H R^2 = ^{t}Bu) precursors

We selected the [Ni(q^{6,7}dt^{Et,Et})(dppe)] complex to explore the reactions between a [Ni(q^{6,7}dt^{R1,R2})(dppe)] precursor and [Fe]-containing fragments because it demonstrates good solubility in a range of solvents (e.g. CH_2Cl_2), which allows for a wide range of reaction conditions to be considered.

4.6.1 The reaction between [Ni($q^{6,7}dt^{Et,Et}$)dppe] and $Fe_3(CO)_{12}$

Reactions between [Ni($q^{6,7}dt^{Et,Et}$)(dppe)] and $Fe_3(CO)_{12}$ were investigated in an attempt to synthesise [Ni($q^{6,7}dt^{Et,Et}$)(dppe)$Fe_2(CO)_6$]. The reaction conditions investigated were stirring the reaction mixture at room temperature, at reflux and in a microwave reactor using either ethanol or CH_2Cl_2 as the solvent. The reactions were monitored by solution IR spectroscopy to track the loss and growth of CO bands associated with the $Fe_3(CO)_{12}$ precursor and any potential products.

In all cases only unreacted [Ni($q^{6,7}dt^{Et,Et}$)(dppe)] starting material and the by-product [($q^{6,7}dt^{Et,Et}$)$Fe_2(CO)_6$] (Scheme 4.7) were identified by mass spectrometry and IR spectroscopy. It has been proposed that the Ni^{II} subunit should be sufficiently flexible to be able to distort away from a square-planar geometry to adopt a distorted tetrahedral geometry in order to coordinate a {$Fe_2(CO)_6$} fragment.[14] Our X-ray crystallographic studies of [Ni($q^{6,7}dt^{R1,R2}$)(dppe)] ($R^1 = R^2$ = Me, Et, Ph; R^1 = H, R^2 = ^{t}Bu and Ph, Chapter Three, Section 3.4.2) have shown that these complexes adopt an approximate square planar geometry about the Ni^{II} centre. Thus, the steric and electronic properties of [Ni($q^{6,7}dt^{Et,Et}$)(dppe)] may mean that the coordination geometry about the Ni^{II} centre in this unit remains locked in an approximate square plane, which prevents the coordination of a {$Fe_2(CO)_6$} fragment during its reaction with $Fe_3(CO)_{12}$.



[Ni($q^{6,7}dt^{Et,Et}$)(dppe)] [($q^{6,7}dt^{Et,Et}$)$Fe_2(CO)_6$]

Scheme 4.7: The reaction of [Ni($q^{6,7}dt^{Et,Et}$)(dppe)] with $Fe_3(CO)_{12}$ to form the by-product [($q^{6,7}dt^{Et,Et}$)$Fe_2(CO)_6$].

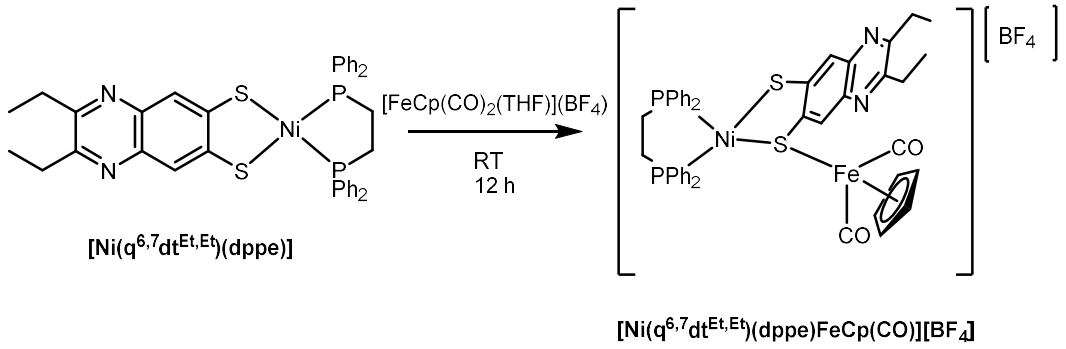
4.6.2 The reaction between [Ni(p-$q^{6,7}dt^{Et,Et}$)(dppe)] and [$FeCp(CO)_2I$]

Given that the reactions involving [Ni($q^{6,7}dt^{Et,Et}$)(dppe)] and $Fe_3(CO)_{12}$ were unsuccessful, we investigated the reaction between [Ni($q^{6,7}dt^{Et,Et}$)(dppe)] and [$FeCp(CO)_2I$] in CH_2Cl_2 at room temperature. The reaction was monitored using IR spectroscopy and after 120 hours only ν(CO) bands at 2041 and 1996 cm^{-1}, associated with [$FeCp(CO)_2I$],[17] were observed. Mass spectrometry confirmed only [$FeCp(CO)_2I$] and unreacted [Ni($q^{6,7}dt^{Et,Et}$)(dppe)] were present in the reaction

mixture. Therefore we decided to attempt reactions using the iodide-free iron-carbonyl precursor, $[FeCp(CO)_2(THF)][BF_4]$.

4.6.3 The reaction between $[Ni(q^{6,7}dt^{Et,Et})(dppe)]$ and $[FeCp(CO)_2(THF)][BF_4]$

The reaction of $[Ni(q^{6,7}dt^{Et,Et})dppe]$ and $[FeCp(CO)_2(THF)][BF_4]$ (1:1 molar ratio) in CH_2Cl_2 at room temperature affords $[Ni(q^{6,7}dt^{Et,Et})(dppe)FeCp(CO)_2][BF_4]$ (Scheme 4.8).



Scheme 4.8: Synthetic route to form $[Ni(q^{6,7}dt^{Et,Et})(dppe)FeCp(CO)_2][BF_4]$.

The progress of the reaction was monitored by IR spectroscopy and as the reaction progresses the ν(CO) stretches at 2071 and 2026 cm^{-1}, associated with $[FeCp(CO)_2(THF)][BF_4]$,[17] decrease in intensity. The reaction appeared to be complete after 24 h. We assign the new ν(CO) stretches at 2045 and 1996 cm^{-1} to $[Ni(q^{6,7}dt^{Et,Et})(dppe)FeCp(CO)_2][BF_4]$, which are shifted *ca.* 26 – 30 cm^{-1} to lower wavenumber compared to those of $[FeCp(CO)_2(THF)][BF_4]$. This shift to lower wavenumber is consistent with the displacement of the THF ligand in $[FeCp(CO)_2(THF)][BF_4]$ with a more strongly electron-donating $[Ni(q^{6,7}dt^{Et,Et})(dppe)]$ group that coordinates to the Fe centre through a thiolate S-donor. Mass spectrometry of the reaction mixture confirmed the formation of $[Ni(q^{6,7}dt^{Et,Et})(dppe)FeCp(CO)_2][BF_4]$ by the presence of a peak at 881.07 associated with the cation $[Ni(q^{6,7}dt^{Et,Et})(dppe)FeCp(CO)_2]^+$. We attempted to isolate the $[Ni(q^{6,7}dt^{Et,Et})(dppe)FeCp(CO)_2][BF_4]$ product by column chromatography using ethyl acetate and petroleum ether as the eluent. Recrystallization of the first fraction by slow evaporation from a CH_2Cl_2 solution gave crystalline material from which crystals of $[Ni(q^{6,7}dt^{Et,Et})(dppe)FeCp(CO)_2][BF_4]$, suitable for X-ray crystallography could be separated.

4.6.4 The syntheses of [Ni(qdt^{R1,R2})(dppe)FeCp(CO)$_2$][BF$_4$] (R^1 = R^2 = Me; R^1 = H, R^2 = ^{t}Bu) and [Ni(q^{6,7}dt^{R1,R2})(dppe)FeCp(CO)$_2$][BF$_4$] (R^1 = R^2 = Me, Ph; R^1 = H, R^2 = ^{t}Bu)

Given our success in the synthesis of [Ni(q^{6,7}dt^{Et,Et})(dppe)FeCp(CO)$_2$](BF$_4$) we attempted the syntheses [Ni(qdt^{R1,R2})(dppe)FeCp(CO)$_2$][BF$_4$] (R^1 = R^2 = Me; R^1 = H, R^2 = ^{t}Bu) and [Ni(q^{6,7}dt^{R1,R2})(dppe)FeCp(CO)$_2$][BF$_4$] (R^1 = R^2 = Me, Ph; R^1 = H, R^2 = ^{t}Bu) using the same approach. The progress of each reaction was followed by IR spectroscopy and the ν(CO) bands observed after a 12 h reaction time are presented in Table 4.5. The development of two ν(CO) bands at similar wavenumbers to those of [Ni(q^{6,7}dt^{Et,Et})(dppe)FeCp(CO)$_2$][BF$_4$] supports the formation of similar [Ni(qdt^{R1,R2})(dppe)FeCp(CO)$_2$][BF$_4$] and [Ni(q^{6,7}dt^{R1,R2})(dppe)FeCp(CO)$_2$][BF$_4$] compounds in each case. We attempted to purify the reaction mixtures using a variety of different chromatographic conditions that included variations in eluents (*e.g.* CH_2Cl_2 with pentane/ methanol), column materials (silica and alumina) and performing the column in the absence of light and air. The growth of new ν(CO) bands at 2126 cm^{-1} in the solutions of the fractions suggest that [Ni(qdt^{R1,R2})(dppe)FeCp(CO)$_2$][BF$_4$] and [Ni(q^{6,7}dt^{R1,R2})(dppe)FeCp(CO)$_2$][BF$_4$] can decompose under the conditions used for column chromatography, with elemental analyses of the isolated products following this procedure being generally inconsistent with [Ni(qdt^{R1,R2})(dppe)FeCp(CO)$_2$][BF$_4$] and [Ni(q^{6,7}dt^{R1,R2})(dppe)FeCp(CO)$_2$][BF$_4$] formulations. Nevertheless, the recrystallization of product from an ethyl acetate/pentane column fraction of [Ni(q^{6,7}dt^{H,tBu})(dppe)FeCp(CO)$_2$][BF$_4$] from a

CH_2Cl_2 solution layered with pentane gave crystals of $[Ni(q^{6,7}dt^{H,tBu})(dppe)FeCp(CO)_2](BF_4)$ that were suitable for X-ray crystallography.

Table 4.5: IR spectroscopic data recorded for reactions attempted in the syntheses of $[Ni(qdt^{R1,R2})(dppe)FeCp(CO)_2][BF_4]$ and $[Ni(q^{6,7}dt^{R1,R2})(dppe)FeCp(CO)_2][BF_4]$ recorded in CH_2Cl_2 solutions.

Complex	ν(CO) /cm^{-1}
$[Ni(qdt^{Me,Me})(dppe)FeCp(CO)_2][BF_4]$	2001 and 2048
$[Ni(qdt^{H,tBu})(dppe)FeCp(CO)_2][BF_4]$	2002 and 2049
$[Ni(q^{6,7}dt^{Me,Me})(dppe)FeCp(CO)_2][BF_4]$	2002 and 2049
$[Ni(q^{6,7}dt^{Et,Et})(dppe)FeCp(CO)_2][BF_4]$	2001 and 2048
$[Ni(q^{6,7}dt^{H,tBu})(dppe)FeCp(CO)_2][BF_4]$	2001 and 2048
$[Ni(q^{6,7}dt^{Ph,Ph})(dppe)FeCp(CO)_2][BF_4]$	2003 and 2050

4.6.5 The single crystal X-ray structures of $[Ni(q^{6,7}dt^{R1,R2})(dppe)FeCp(CO)_2][BF_4]$ ($R^1 = R^2 = Et$; $R^1 = H$, $R^2 = {}^tBu$)

The X-ray crystal structures of $[Ni(q^{6,7}dt^{Et,Et})(dppe)FeCp(CO)_2][BF_4]$ and $[Ni(q^{6,7}dt^{H,tBu})(dppe)FeCp(CO)_2][BF_4]$ are shown in Figures 4.10 and 4.11, respectively, with selected bond lengths and angles presented in Table 4.5.

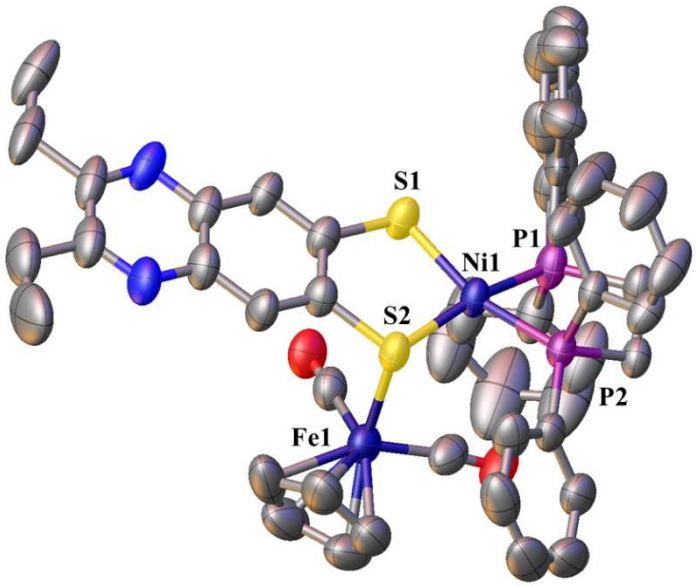


Figure 4.9: The molecular structure of $[Ni(q^{6,7}dt^{Et,Et})(dppe)FeCp(CO)_2]^+$ in the $[BF_4]^-$ salt with atoms selectively labelled. The H atoms are omitted for clarity.

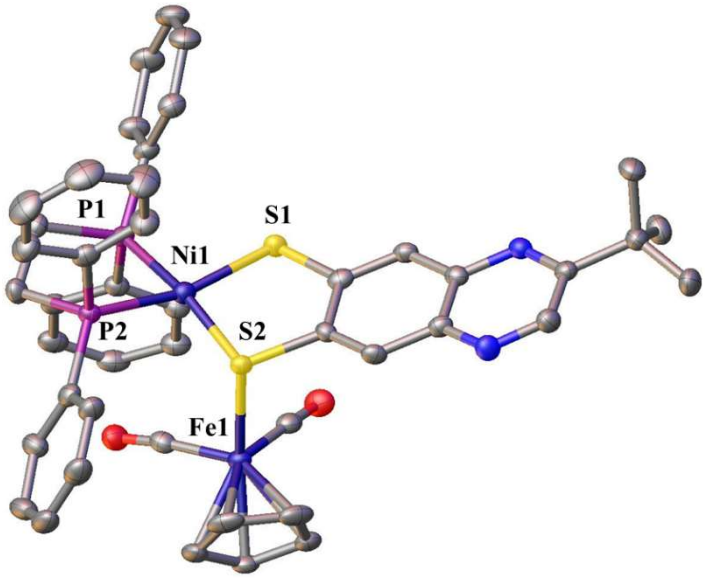


Figure 4.10: Molecular structure of $[Ni(q^{6,7}dt^{H,tBu})(dppe)FeCp(CO)_2]^+$ in the $[BF_4]^-$ salt with atoms selectively labelled. The H atoms are omitted for clarity.

In each $[Ni(q^{6,7}dt^{R1,R2})(dppe)FeCp(CO)_2]^+$ ($R^1 = R^2 = Et$; $R^1 = H$, $R^2 = {}^tBu$) complex the $[Ni(q^{6,7}dt^{R1,R2})(dppe)]$ group is coordinated to the $[CpFe(CO_2)]^+$ unit *via* one of the thiolate S donors (Figure 4.10 and 4.11). The angle between the P(1)-Ni(1)-P(2) plane and the S(1)-Ni(1)-S(2) plane is 23.36° and 22.12° in $[Ni(q^{6,7}dt^{Et,Et})(dppe)FeCp(CO)_2]^+$ and $[Ni(q^{6,7}dt^{H,tBu})(dppe)FeCp(CO)_2]^+$, respectively. Therefore in each $[Ni(q^{6,7}dt^{R1,R2})(dppe)FeCp(CO)_2]^+$ cation the approximate square planar geometry of the precursor, $[Ni(q^{6,7}dt^{R1,R2})(dppe)]$ (Chapter Three, Section 3.4.2) is maintained. The Ni(1)-S(1), Ni(1)-P(1) and Ni(1)-P(2) distances in $[Ni(q^{6,7}dt^{R1,R2})(dppe)FeCp(CO)_2]^+$ are similar to those of the parent $[Ni(q^{6,7}dt^{R1,R2})(dppe)]$ precursors (Tables 4.5 and 4.6). However, in each $[Ni(q^{6,7}dt^{R1,R2})(dppe)FeCp(CO)_2]^+$ there is a significant elongation of the Ni(1)-S(2) bond (*ca.* 0.015 – 0.020 Å) consistent with the coordination of the $[FeCp(CO)_2]^+$ fragment to this donor. The Ni(1)-Fe(1) distances in $[Ni(q^{6,7}dt^{Et,Et})(dppe)FeCp(CO)_2]^+$ [3.515(17) Å] and $[Ni(q^{6,7}dt^{H,tBu})(dppe)FeCp(CO)_2]^+$ [3.465(9) Å] are greater than the sum of the Ni

and Fe atomic radii (2.75 Å) and consequently it is unlikely that there are any significant direct interactions between the Ni and Fe atoms.[24]

Table 4.5: Selected metrical parameters for $[Ni(q^{6,7}dt^{Et,Et})(dppe)FeCp(CO)_2][BF_4]$, $[Ni(q^{6,7}dt^{H,tBu})(dppe)FeCp(CO)_2][BF_4]$.

Bond Length/Å	**$[Ni(q^{6,7}dt^{Et,Et})(dppe)FeCp(CO)_2]^+$**	**$[Ni(q^{6,7}dt^{H,tBu})(dppe)FeCp(CO)_2]^+$**
Ni(1)-S(1)	2.1577(16)	2.1590(9)
Ni(1)-S(2)	2.1704(17)	2.1816(9)
Ni(1)-P(1)	2.1715(17)	2.1756(10)
Ni(1)-P(2)	2.1841(15)	2.1811(9)
Fe(1)-S(2)	2.3122(19)	2.3230(9)
Ni(1)-Fe(1)	3.515(17)	3.465(9)
Bond angle/°		
S(1)-Ni(1)-S(2)	92.64(6)	92.60(3)
P(1)-Ni(1)-P(2)	86.83(6)	86.75(4)
P(1)-Ni(1)-S(1)	91.17(7)	90.63(4)
P(2)-Ni(1)-S(2)	94.01(6)	92.65(3)
Ni(1)-S(2)-Fe(1)	103.25(7)	100.52(4)
S(1)-Ni(1)-P(2)	161.70(8)	163.87(4)
P(1)-Ni(1)-S(2)	164.84(9)	170.14(4)

Table 4.6.: Selected bond lengths and angles in $[Ni(q^{6,7}dt^{Et,Et})(dppe)]$ and $[Ni(q^{6,7}dt^{H,tBu})(dppe)]$ discussed in Chapter Three, Section 3.4.2.

Bond Length/Å	**$[Ni(q^{6,7}dt^{Et})(dppe)]$**	**$[Ni(q^{6,7}dt^{tBu})(dppe)]$**
Ni(1)-S(1)	2.1513(10)	2.1601(5)
Ni(1)-S(2)	2.1513(10)	2.1594(5)
Ni(1)-P(1)	2.1530(10)	2.1614(5)
Ni(1)-P(2)	2.1530(10)	2.1607(5)
Bond Angle/º		
S(1)-Ni(1)-S(2)	93.20(6)	92.594(18)
P(1)-Ni(1)-P(2)	87.06(6)	86.542(19)
P(1)-Ni(1)-S(1)	91.03(4)	90.005(18)
P(2)-Ni(1)-S(2)	91.03(4)	90.843(18)
S(1)-Ni(1)-P(2)	168.02(4)	176.54(2)
P(1)-Ni(1)-S(2)	168.02(4)	176.23(2)

4.7 Conclusion

This chapter describes the different approaches undertaken in an attempt to synthesise and characterise [NiFe] compounds containing Ni^{II} units bound by quinoxaline-containing ligands. We attempted reactions between the Ni^{II} $[Ni(p\text{-}qdt^{R1,R2})]$ ($R^1 = R^2 = Me$; $R^1 = H$, $R^2 = {}^tBu$), $[Ni(p\text{-}q^{6,7}dt^{R1,R2})]$ ($R^1 = R^2 = Me$, Et and Ph; $R^1 = H$, $R^2 = {}^tBu$) and $[Ni(p\text{-}q^{6,7}dt^{R1,R2})(dppe)]$ ($R^1 = R^2 = Me$, Et and Ph; $R^1 = H$, $R^2 = {}^tBu$) precursors and a range of [Fe]-containing fragments in attempts to synthesise [NiFe] compounds. These reactions were monitored by IR spectroscopy

to follow changes within the ν(CO) region (*ca.* 1700-2200 cm^{-1}). [Ni(p-$qdt^{H,tBu}$)] precursors do not appear to react with $Fe_3(CO)_{12}$ whereas we had some success with [Ni(p-$q^{6,7}dt^{R1,R2}$)] precursors; we were able to isolate [Ni(p-$q^{6,7}dt^{R1,R2}$)$Fe_2(CO)_6$] (R^1 = R^2 = Me, Et; R^1 = H, R^2 = ^{t}Bu) albeit in low yields. We also note that [Ni(p-$q^{6,7}dt^{R1,R2}$)$Fe_2(CO)_6$] decompose in CH_2Cl_2 solution over prolonged period. DFT calculations on [Ni(p-$qdt^{H,tBu}$)], [Ni(p-$q^{6,7}dt^{Et,Et}$)] and [Ni(L^A)] suggest that the thiolate S-donors in [Ni(p-$qdt^{H,tBu}$)] may be deactivated towards reaction with [Fe]-containing precursors due to the electron withdrawing properties of the quinoxaline units within the ligands bound to the Ni^{II} centres. These DFT calculations support the observation that [Ni(p-$qdt^{R1,R2}$)] does not react with $Fe_3(CO)_{12}$ whereas [Ni(p-$q^{6,7}dt^{R1,R2}$)] and [Ni(L^A)] do react under the same conditions.

[Ni(p-$q^{6,7}dt^{R1,R2}$)$Fe_2(CO)_6$] (R^1 = R^2 = Me; R^1 = H, R^2 = ^{t}Bu) possess an electrochemically reversible reduction process at $E_{1/2}$ = -1.22 and -1.21 V *vs* Fc^+/Fc, respectively, that occur at *ca.* 0.1 V more positive potentials than the first reduction of [Ni(L^A)$Fe_2(CO)_{12}$] ($E_{1/2}$ = -1.31 V *vs* Fc^+/Fc),[7] consistent with the incorporation of electron-withdrawing quinoxaline units in [Ni(p-$q^{6,7}dt^{R1,R2}$)$Fe_2(CO)_6$]. These preliminary electrochemical results are promising, however, the instability of these complexes over prolonged periods in solution may present some challenges in the assessment of the catalytic activity of these species towards the production of H_2.

Reactions between [Ni($q^{6,7}dt^{R1,R2}$)(dppe)] (R^1 = R^2 = Me, Et, Ph; R^1 = H, R^2 = ^{t}Bu) and [FeCp$(CO)_2$(THF)][BF_4] gave [Ni($q^{6,7}dt^{R1,R2}$)(dppe)FeCp$(CO)_2$][BF_4] as confirmed by IR spectroscopy, mass spectrometry and X-ray crystallography studies of [Ni($q^{6,7}dt^{R1,R2}$)(dppe)FeCp$(CO)_2$][BF_4] (R^1 = R^2 = Et and R^1 = H, R^2 = ^{t}Bu). The structures show that each [Ni($q^{6,7}dt^{R1,R2}$)(dppe)] unit coordinates to a $[FeCp(CO)_2]^+$ fragment through one of the thiolate S-donors. Future work will involve the optimisations of the syntheses of [Ni($q^{6,7}dt^{R1,R2}$)(dppe)FeCp$(CO)_2$][BF_4] in order to prepare material sufficient for electrochemical, spectroelectrochemical and catalytic studies in order to gain insight into the electronic structures of these complexes and to assess their catalytic activity towards the production of H_2.

4.8 Experimental

4.8.1 The attempted Synthesis of [Ni(p-qdt^{H,tBu})Fe$_2$(CO)$_6$]

Method 1

Typical procedure: [Ni(p-qdt^{H,tBu})] (30.0 mg, 0.05 mmol) and $Fe_3(CO)_{12}$ (25.0 mg, 0.05 mmol) were stirred in ethanol (3 mL) or CH_2Cl_2 (3 mL) or 1,2-dichlorobenzene (3 mL) in a 10 mL microwave reactor vessel. In the microwave reactor, the reaction mixture was heated at 95 °C (100 W, maximum 95 psi) for up to 30 min. The reactions were monitored using *ex situ* infrared spectroscopy and mass spectrometry. No spectroscopic data consistent with a [NiFe] compound were obtained.

Method 2

Typical procedure: [Ni(p-qdt^{H,tBu})] (30.0 mg, 0.05 mmol) and $Fe_3(CO)_{12}$ (25.0 mg, 0.05 mmol) were stirred in ethanol (10 mL) at room temperature, CH_2Cl_2 (10 mL) at room temperature or CH_2Cl_2 (10 mL) under reflux for up to 96 h. The reactions were monitored using *ex situ* infrared spectroscopy and mass spectrometry. No spectroscopic data consistent with a [NiFe] compound were obtained.

4.8.2 The Attempted Synthesis of [Ni(p-qdt^{H,tBu})FeCp(CO)]I

Typical procedure: A solution of [$FeCp(CO)_2I$] (0.01 g, 0.04 mmol) in CH_2Cl_2 (10 mL) was added to a suspension of [Ni(p-qdt^{H,tBu})$_2$] (0.03 g, 0.04 mmol) in CH_2Cl_2 (10 mL) and the mixture stirred at room temperature for up to 48 h. The reactions were monitored using *ex situ* infrared spectroscopy and mass spectrometry. No change in wavenumber for the ν(CO) bands were observed during the reaction and only bands at 2040(s) and 1996(s) cm^{-1}, associated with [$FeCp(CO)_2I$] were found.

4.8.3 The Synthesis of [CpFe(CO)$_2$(THF)][BF$_4$]

A solution of $AgBF_4$ (1.9 g, 10.0 mmol) and [$FeCp(CO)_2I$] (3.00 g, 9.80 mmol) in CH_2Cl_2 (50 mL) was stirred for 3 h in the dark. The solvent was removed and the residue extracted with chloroform (6 x 15 mL). The chloroform fractions were reduced to 20 mL and layered with hexane (50 mL) and kept at 0 °C for 16 h. The resulting red crystals were collected by filtration and washed in hexane (3.05 g, 9.31

mmol, 95 %). IR (CH_2Cl_2, cm^{-1}, ν(CO)): 2070 (s), 2024 (s). Elemental analysis, found (calculated for $C_{11}H_{13}BF_4FeO_3$): C 39.38 (39.34), H 3.85 (3.90) %.

4.8.4 The Attempted Synthesis of [Ni(p-qdt^{H,tBu})FeCp(CO)][BF_4]

Typical procedure A solution of [$CpFe(CO)_2(THF)$][BF_4] (0.025 g, 0.075 mmol) and [Ni(p-qdt^{H,tBu})] (0.045 g, 0.075 mmol) in CH_2Cl_2 (5 mL) was stirred for up to 72 h at room temperature in the dark. The reactions were monitored using *ex situ* infrared spectroscopy and mass spectrometry. No consistent spectroscopic data could be obtained for a [NiFe] compound.

4.8.5 The Synthesis of crude [Ni(p-q^{6,7}dt^{R1,R2})$Fe_2(CO)_6$] ($R^1 = R^2$ = Me, Et, Ph; R^1 = H, R^2 = ^{t}Bu)

Method 1

Representative procedure for the synthesis of [Ni(p-q^{6,7}dt^{R1,R2})$Fe_2(CO)_6$]: [Ni(p-q^{6,7}dt^{R1,R2})] (0.05 mmol) and $Fe_3(CO)_{12}$ (25.0 mg, 0.05 mmol) were stirred in ethanol (3 mL) or CH_2Cl_2 (3 mL) in a 10 mL microwave reactor vessel. In the microwave reactor, the reaction mixture was heated at 95 °C (100 W, maximum 95 psi) for 10 mins. The reactions were monitored using *ex situ* infrared spectroscopy and mass spectrometry. The solvent was removed in *vacuo* to give a brown solid which was washed with diethyl ether (3x10 mL). The resulting brown solid was chromatographed on an alumina column under anaerobic conditions in a range of eluents.

[Ni(p-q^{6,7}dt^{Me,Me})$Fe_2(CO)_6$]: MS (ESI^+) m/z: 820.8474 $[M+H]^+$. IR (CH_2Cl_2, cm^{-1}, ν_{CO}): 2038 (s), 1998 (s), 1959 (s). Elemental analysis found (calculated for $C_{29}H_{22}Fe_2N_4NiO_6S_4$): C: 55.78 (50.46), H: 4.91 (3.94), N: 6.98 (8.12) %.

[Ni(p-q^{6,7}dt^{Et,Et})$Fe_2(CO)_6$]: MS (ESI^+) m/z: 876.9100 $[M+H]^+$. IR (CH_2Cl_2, cm^{-1}, ν_{CO}): 2038 (s), 1999 (s), 1960 (s). Elemental analysis found (calculated for $C_{33}H_{30}Fe_2N_4NiO_6S_4$): C: 45.49 (45.18), H: 3.13 (3.45), N: 6.47 (6.39) %.

[Ni(p-q^{6,7}dt^{H,tBu})$Fe_2(CO)_6$]: MS (ESI^+) m/z: 876.9100 $[M+H]^+$. IR (CH_2Cl_2, cm^{-1}, ν_{CO}): 2037 (s), 1997 (s), 1961 (s). Elemental analysis found (calculated for $C_{33}H_{30}Fe_2N_4NiO_6S_4$): C: 44.89 (45.18), H: 3.56 (3.45), N: 6.47 (6.39) %.

[Ni(p-q^{6,7}dt^{Ph,Ph})Fe$_2$(CO)$_6$]: MS (ESI$^+$) m/z: 1068.9100 [M+H]$^+$. IR (CH_2Cl_2, cm^{-1}, ν_{CO}): 2038 (s), 1998 (s), 1960 (s). Elemental analysis found (calculated for $C_{49}H_{30}Fe_2N_4NiO_6S_4$): C: 60.15 (55.03), H: 3.99 (2.83), N: 6.54 (5.24) %.

4.8.6 Attempted Syntheses of [Ni(p-q^{6,7}dt^{R1,R2})FeCp(CO)$_2$][BF$_4$] (R^1 = R^2 = Me, Et, Ph; R^1 = H, R^2 = ^{t}Bu)

Representative procedure for the synthesis of [Ni(p-q^{6,7}dt^{R1,R2})FeCp(CO)$_2$][BF$_4$]: A solution of [CpFe(CO)$_2$(THF)][BF$_4$] (25.1 mg, 0.075 mmol) and [Ni(p-q^{6,7}dt^{R1,R2})] (0.075 mmol) in CH_2Cl_2 (10 mL) was stirred for 12 h at room temperature in the dark. Pentane (10 mL) was added to precipitate the product which was isolated by filtration and washed with pentane (3 x 10 mL) and dried *in vacuo* to afford a red/brown powder.

[Ni(p-q^{6,7}dt^{Me,Me})FeCp(CO)$_2$][BF$_4$]: m/z: 716.9719 [M]$^+$. IR (CH_2Cl_2, cm^{-1}, ν_{CO}): 2046 (s), 1998 (s). Elemental analysis found (calculated) for $C_{30}H_{27}FeN_4NiO_2S_4BF_4$: C: 53.18 (47.31), H: 5.20 (4.32), N: 7.28 (6.49) %.

[Ni(p-q^{6,7}dt^{Et,Et})FeCp(CO)$_2$][BF$_4$]: m/z: 773.0345 [M]$^+$. IR (CH_2Cl_2, cm^{-1}, ν_{CO}): 2040 (s), 1995 (s). Elemental analysis found (calculated for $C_{34}H_{35}FeN_4NiO_2S_4BF_4$): C: 47.78 (49.64), H: 4.12 (4.93), N: 7.18 (6.09) %.

[Ni(p-q^{6,7}dt^{H,tBu})FeCp(CO)$_2$][BF$_4$]: m/z: 773.0345 [M]$^+$. IR (CH_2Cl_2, cm^{-1}, ν_{CO}): 2049 (s), 2001 (s). Elemental analysis found (calculated for $C_{34}H_{35}FeN_4NiO_2S_4BF_4$): C: 45.34 (49.64), H: 4.23 (4.93), N: 7.01 (6.09) %.

[Ni(p-q^{6,7}dt^{Ph,Ph})FeCp(CO)$_2$][BF$_4$]: m/z: 965.0346 [M]$^+$. IR (CH_2Cl_2, cm^{-1}, ν_{CO}): 2046 (s), 1998 (s). Elemental analysis found (calculated for $C_{50}H_{35}FeN_4NiO_2S_4BF_4$): C: 60.54 (62.13), H: 5.76 (3.65), N: 6.58 (5.80) %.

4.8.7 The Attempted Synthesis of [Ni(q^{6,7}dt^{Et,Et})(dppe)Fe$_2$(CO)$_6$]

Method 1

Typical procedure: [Ni(q^{6,7}dt^{Et,Et})(dppe)] (35.0 mg, 0.05 mmol) and $Fe_3(CO)_{12}$ (25.0 mg, 0.05 mmol) were stirred in ethanol (3 mL) or CH_2Cl_2 (3 mL) in a 10 mL microwave reactor vessel. In the microwave reactor, the reaction mixture was heated at 95 ˚C (100 W, maximum 95 psi) for up to 30 min. The reactions were monitored

using *ex situ* infrared spectroscopy and mass spectrometry. No spectroscopic data could be attained consistent with a [NiFe] compound.

Method 2

Typical procedure: [Ni($q^{6,7}dt^{Et,Et}$)(dppe)] (35.0 mg, 0.05 mmol) and $Fe_3(CO)_{12}$ (25.0 mg, 0.05 mmol) were stirred in ethanol (10 mL) at room temperature, CH_2Cl_2 (10 mL) at room temperature or CH_2Cl_2 (10 mL) under reflux for up to 96 h. The reactions were monitored using *ex situ* infrared spectroscopy and mass spectrometry. No consistent spectroscopic data could be attained for a [NiFe] compound.

4.8.8 The Reaction between [Ni($q^{6,7}dt^{Et,Et}$)(dppe)$Fe_2(CO)_6$] and [$FeCp(CO)_2I$]

A solution of [$FeCp(CO)_2I$] (0.161 g, 0.43 mmol) in CH_2Cl_2 (15 mL) was added to a suspension of [Ni($q^{6,7}dt^{Et,Et}$)(dppe)] (0.37 g, 0.43 mmol) in CH_2Cl_2 (15 mL) and the mixture stirred at room temperature for 48 h. The resulting mixture was filtered, and the red filtrate reduced to 15 mL and layered with diethyl ether, precipitating a red/brown solid at RT over 16 h. The solid was collected by filtration and washed with diethyl ether and dried *in vacuo* overnight to give a red/brown powder. No consistent spectroscopic data could be obtained consistent with a [NiFe] compound.

4.8.9 The Syntheses of crude [Ni($qdt^{R1,R2}$)(dppe)$FeCp(CO)_2$][BF_4] (R^1 = R^2 = Me; R^1 = H, R^2 = ^{t}Bu) and [Ni($q^{6,7}dt^{R1,R2}$)(dppe)$FeCp(CO)_2$][BF_4] (R^1 = R^2 = Me, Et, Ph R^1 = H, R^2 = ^{t}Bu)

Representative procedure for the synthesis of [Ni($qdt^{R1,R2}$)(dppe)$FeCp(CO)_2$][BF_4]/ [Ni($q^{6,7}dt^{R1,R2}$)(dppe)$FeCp(CO)_2$][BF_4]: A solution of [$(Cp)Fe(CO)_2(THF)$][BF_4] (25.0 mg, 0.075 mmol) and [Ni($q^{6,7}dt^{R}$)(dppe)] (0.075 mmol) in CH_2Cl_2 (5 mL) was stirred for 12 - 24 h at room temperature in the dark. The product was then precipitated with pentane, isolated by filtration, washed with pentane and dried *in vacuo* to afford a red/brown powder.

[Ni($qdt^{Me,Me}$)(dppe)$FeCp(CO)_2$][BF_4]: m/z: 916.9916 $[M]^+$. IR (CH_2Cl_2, cm^{-1}, ν_{CO}): 2048 (s), 2001 (s). Elemental analysis found (calculated for $C_{43}H_{37}FeN_2NiO_2P_2S_2BF_4$): C: 52.86 (53.87), H: 4.86 (3.96), N: 3.78 (2.98) %.

[Ni(qdt^{H,tBu})(dppe)FeCp(CO)$_2$][BF$_4$]: m/z: 945.0229 $[M]^+$. IR (CH_2Cl_2, cm^{-1}, ν_{CO}): 2049 (s), 2002 (s). Elemental analysis found (calculated for $C_{45}H_{41}FeN_2NiO_2P_2S_2BF_4$): C: 51.87 (55.76), H: 4.89 (4.26), N: 4.45 (2.89) %.

[Ni(q^{6,7}dt^{Me,Me})(dppe)FeCp(CO)$_2$][BF$_4$]: m/z: 916.9916 $[M]^+$. IR (CH_2Cl_2, cm^{-1}, ν_{CO}): 2049 (s), 2002 (s). Elemental analysis found (calculated for $C_{43}H_{37}FeN_2NiO_2P_2S_2BF_4$): C: 56.36 (53.87), H: 4.68 (3.96), N: 3.91 (2.98) %.

[Ni(q^{6,7}dt^{Et,Et})(dppe)FeCp(CO)$_2$][BF$_4$]: m/z: 945.0229 $[M]^+$. IR (CH_2Cl_2, cm^{-1}, ν_{CO}): 2048 (s), 2001 (s). Elemental analysis found (calculated for $C_{45}H_{41}FeN_2NiO_2P_2S_2BF_4$): C: 57.92 (55.76), H: 2.99 (4.26), N: 5.12 (2.89) %.

[Ni(q^{6,7}dt^{H,tBu})(dppe)FeCp(CO)$_2$][BF$_4$]: m/z: 945.0229 $[M]^+$. IR (CH_2Cl_2, cm^{-1}, ν_{CO}): 2048 (s), 2001 (s). Elemental analysis found (calculated for $C_{45}H_{41}FeN_2NiO_2P_2S_2BF_4$): C: 51.78 (55.76), H: 3.68 (4.26), N: 4.15 (2.89) %.

[Ni(q^{6,7}dt^{Ph,Ph})(dppe)FeCp(CO)$_2$][BF$_4$]: m/z: 1041.0229 $[M]^+$. IR (CH_2Cl_2, cm^{-1}, ν_{CO}): 2050 (s), 2003 (s). Elemental analysis found (calculated for $C_{53}H_{41}FeN_2NiO_2P_2S_2BF_4$): C: 54.78 (59.75), H: 5.11 (3.88), N: 3.89 (2.63) %.

4.9 References

1 R. R. Richard Cammack, Michel Frey, *Hydrogen as a Fuel: Learning from Nature*, CRC Press, London, 2002.

2 A. Volbeda, M. H. Charon, C. Piras, E. C. Hatchikian, M. Frey, J. C. Fontecilla-Camps, Y. Higuchi, T. Yagi and N. Yasuoka, *Nature*, 1995, **5**, 580–587.

3 A. Volbeda, E. Garcin, C. Piras, A. L. de Lacey, V. M. Fernandez, E. C. Hatchikian, M. Frey and J. C. Fontecilla-Camps, *J. Am. Chem. Soc.*, 1996, **118**, 12989–12996.

4 C. Tard and C. J. Pickett, *Chem. Rev.*, 2009, **109**, 2245–2274.

5 E. Bouwman and J. Reedijk, *Coord. Chem. Rev.*, 2005, **249**, 1555–1581.

6 D. J. Evans and C. J. Pickett, *Chem. Soc. Rev.*, 2003, **32**, 268.

7 Q. Wang, J. E. Barclay, A. J. Blake, E. S. Davies, D. J. Evans, A. C. Marr, E. J. L. McInnes, J. McMaster, C. Wilson and M. Schröder, *Chem. Eur. J.*, 2004, **10**, 3384–3396.

8 W. Zhu, A. C. Marr, Q. Wang, F. Neese, D. J. E. Spencer, A. J. Blake, P. A. Cooke, C. Wilson and M. Schröder, *Proc. Natl. Acad. Sci. U. S. A.*, 2005, **102**, 18280–18285.

9 B. E. Barton, C. M. Whaley, T. B. Rauchfuss and D. L. Gray, *J. Am. Chem. Soc.*, 2009, **131**, 6942–6943.

10 P. Sun, D. Yang, Y. Li, Y. Zhang, L. Su, B. Wang and J. Qu, *Organometallics*, 2016, **35**, 751–757.

11 A. Perra, E. S. Davies, J. R. Hyde, Q. Wang, J. McMaster and M. Schröder, *Chem. Commun.*, 2006, **10**, 1103–1105.

12 A. Perra, Q. Wang, A. J. Blake, E. S. Davies, J. McMaster, C. Wilson and M. Schröder, *Dalton Trans.*, 2009, **373**, 925–931.

13 P. A. Summers, J. A. Calladine, F. Ghiotto, J. Dawson, X.-Z. Sun, M. L. Hamilton, M. Towrie, E. S. Davies, J. McMaster, M. W. George and M. Schröder, *Inorg. Chem.*, 2016, **55**, 527–536.

14 J.Dawson, *Unpublished work*, 2012.

15 Carlos Perotto, University of Nottingham, 2013.
16 D. L. Reger and C. Coleman, *J. Organomet. Chem.*, 1977, **131**, 153–162.
17 Charlene Sodipo, University of Nottingham.
18 G. Durgaprasad and S. Das, *J. Chem. Sci.*, 2015, **127**, 295–305.
19 D. J. Curran, P. B. Graham and M. D. Rausch, *Organometallics*, 1993, **12**, 2380–2382.
20 S. Canaguier, M. Field, Y. Oudart, J. Pécaut, M. Fontecave and V. Artero, *Chem. Commun.*, 2010, **46**, 5876.
21 J. Dawson, University of Nottingham, 2010.
22 A.Perra, University of Nottingham, 2007.
23 F. H. Allen, *Acta Crystallogr. Sect. B Struct. Sci.*, 2002, **58**, 380–388.
24 J. C. Slater, *J. Chem. Phys.*, 1964, **41**, 3199.

CHAPTER FIVE

Ni^{II} and [NiFe] Complexes Incorporating a Fused Photoactive Centre for the Light-driven Production of H_2: Synthesis and Characterisation.

5.1 Introduction

A current challenge in H_2 production is to develop a clean and efficient route to produce H_2 via light-harvesting.[1] This has led to research that attempts to incorporate a photosensitiser (PS) unit and a low molecular weight catalyst for the photochemical production of H_2.[1] The absorption of light by the PS generates an excited state (PS*), which can be reduced by a suitable electron donor (ED) to form the reduced photosensitizer, PS^- (Figure 5.1). Electron transfer to the catalyst then poises the catalytic centre (Cat) in a reduced state that is required for the catalytic reduction of H^+.[2]

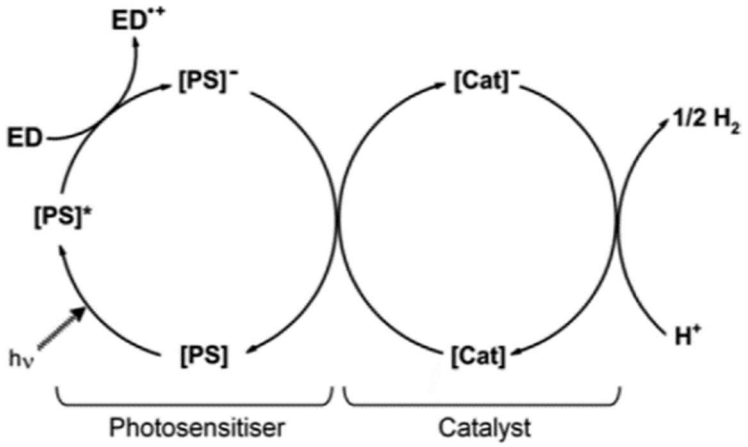


Figure 5.1: Simplified schematic of the one-electron reduction of a catalyst ([Cat]) by a photosensitiser ([PS]) proceeding via the reductive quenching of [PS]* by an electron donor (ED).

Summers *et al*. reported the synthesis of a linked dyad ([Re]-[$NiFe_2$]) containing an analogue of the active site of [NiFe] hydrogenase ([$NiFe_2$]), covalently bound to a Re-diimine photosensitiser ([Re]) (Figure 5.2).[2] This system represents the first example of a complex incorporating a PS and an analogue of the active site of the [NiFe] hydrogenase for photochemical H_2 production.[3] Picosecond- and nanosecond-TRIR spectroscopies have been used to probe the mechanisms of the decay of the excited states in [Re]-[$NiFe_2$] and in an unlinked [Re]/[$NiFe_2$] system in CH_3CN.[2] The FTIR spectrum of [Re]-[$NiFe_2$] in CH_3CN possesses six ν(CO) bands associated with the [Re] (2023, 1919, and 1901 cm^{-1}) and [$NiFe_2$] (2036, 1996, and 1957 cm^{1}) units of the molecule.[2] The evolution of these ν(CO) bands, recorded by time resolved IR spectroscopy, has allowed the photo-catalytic mechanism to be probed following irradiation of the linked dyad, to generate 10 kHz, 40−80 fs, 0.8

mJ pulses at 800 nm.[2] These measurements have provided insights into the electron transfer processes following excitation. Thus, excitation of the [Re] centre results in the population of the ^{3}MLCT excited state, [Re]*-[$NiFe_2$]. Reductive quenching of [Re]*-[$NiFe_2$] by NEt_3 forms [Re]$^-$-[$NiFe_2$] which, following electron transfer to the [$NiFe_2$] centre, forms [Re]-[$NiFe_2$]$^-$. The mechanism of this electron transfer step was probed by concentration-dependent studies which, suggest that intra- and intermolecular electron transfer processes are involved (k_{inter}= 5.9 ± 0.7×10^8 $M^{-1}s^{-1}$, k_{intra}= 1.5 ± 0.1×10^5 s^{-1}).

Analyses of the electron transfer kinetics between the PS and [$NiFe_2$] units within the covalently linked [Re]-[$NiFe_2$] dyad and within the [Re] PS/[$NiFe_2$] mixture shows that [Re]-[$NiFe_2$] possesses a slower electron transfer rate then the PS/[$NiFe_2$] mixture (k_{inter} = 3.8 ± 0.5 ×10^9 $M^{-1}s^{-1}$). [2,3] Consequently, the [Re]-[$NiFe_2$] dyad is a less efficient catalyst for H_2 production when compared to the PS/[$NiFe_2$] mixture. In addition, the [Re]-[$NiFe_2$] dyad also appears to degrade during turnover. Thus, the ester-linkage in the [Re]-[$NiFe_2$] dyad may be detrimental to electron transfer rate and the chemical stability of the system on continuous photolysis.[2] The approaches described in this chapter attempt to address some of these issues through the design and synthesis of a more robust [ReNiFe] compound.

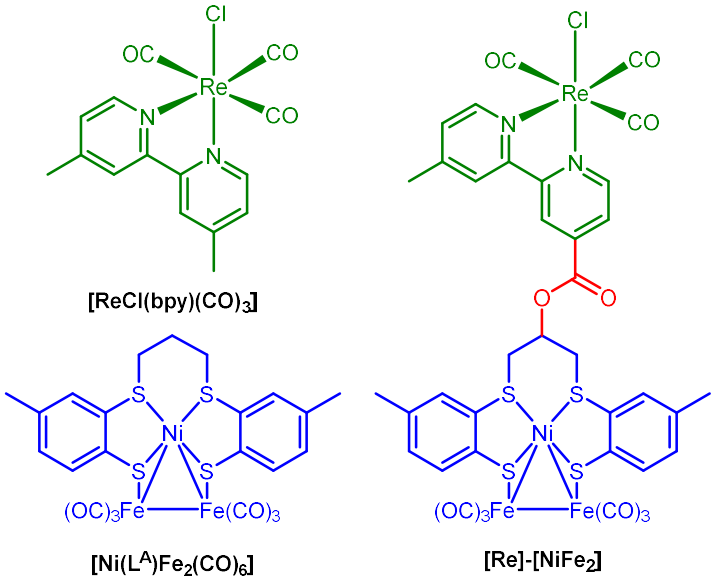


Figure 5.2: Structures of [Ni(L^A)$Fe_2(CO)_3$], [ReCl(bpy)$(CO)_3$] and [Re]-[$NiFe_2$] reported by Summers *et al.*[2]

5.2 Aims

The aims of the research described in this chapter are to synthesise a novel [NiFe] compound that incorporates a PS unit for photochemical H_2 production. The approach builds upon the work described above and seeks to directly link a [$ReCl(CO)_3$(bpy)]-type centre to a [NiFe] unit through a conjugated π-system. With the aim to provide a more efficient pathway for electron transfer between these centres compared to the [Re]-[$NiFe_2$] and [PS]/[$NiFe_2$] systems reported by Summers *et al.* (Figure 5.3).[2,3]

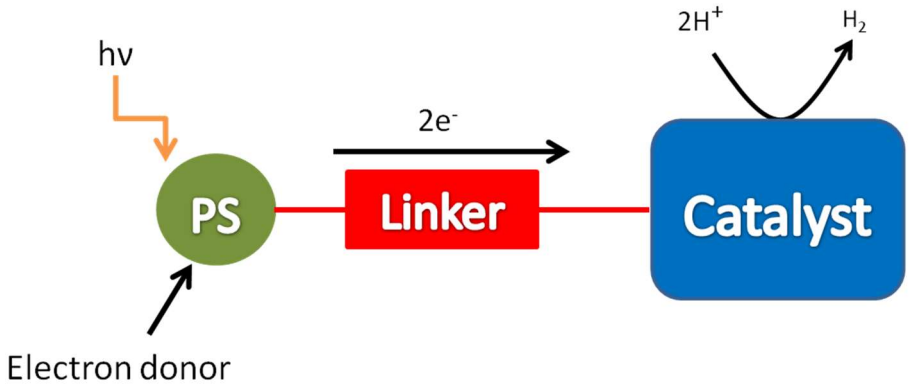


Figure 5.3: Schematic of the key components in a complex for the photocatalytic production of H_2.

We have investigated the use of a dipyridophenazine-based (dppz) linker unit that incorporates dithiolate donors to bind to a Ni^{II} centre within a [$NiFe_2$] catalytic unit and bipyridine-type N-donors to bind to a [$ReCl(CO)_3$] fragment. The carbonyl ligands at the Re centre will enable reactions and charge transfer processes to be monitored by IR spectroscopy. Dipyridophenazine (dppz) is well-studied as a ligand in complexes that support photochemistry.[4–6] Transition metal complexes containing dppz ligands have also been used widely as intercalating probes for DNA and in the study of DNA-mediated electron transfer and DNA damage.[7,8] The dppz ligand may be described as a fusion of two moieties: a phenanthroline (phen) unit and a phenazine (phz) unit that each contain π* acceptor orbitals. Charge transfer into these orbitals in a dppz-transition metal complex results in four possible low lying triplet exited states that result from MLCT or intraligand (IL) π→π* transitions localised on either of the phen or phz moieties of the ligand. (Figure 5.4).[9]

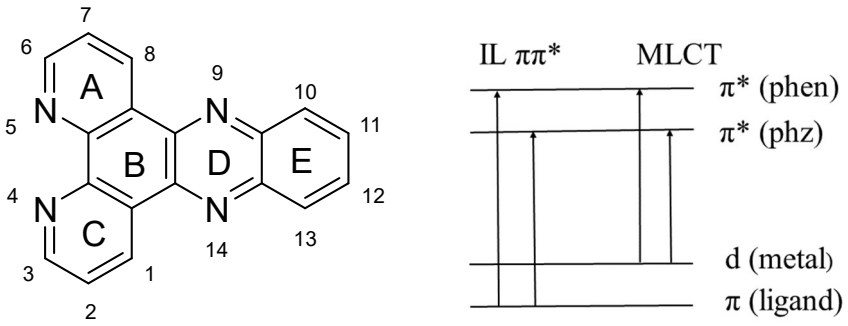


Figure 5.4: Left: The structure of the dppz ligand; A, B and C present the phen unit; B, D and E represent the phz moiety. Right: The possible excited states available in complexes containing the dppz ligand.[10]

5.3 Synthetic design

The combination of two $ReCl(CO)_3(dppz)$ units bound to a $[NiFe_2]$ unit represents the target compound, $\{Ni[(ReCl(CO)_3)_2(p\text{-}dppz(S)_2)]Fe_2(CO)_6\}$ (Figure 5.5). The target can be viewed as being composed of three key fragments: a [Re(bpy)] photosensitier unit (green) with a quinoxaline linker (red) and finally a $[NiFe_2]$ catalytic centre (blue). The incorporation of two photosensitiser units bound to the catalytic centre could each provide $1e^-$ to the $[NiFe_2]$ catalyst necessary for the $2e^-$ reduction of $2H^+$ to give H_2.

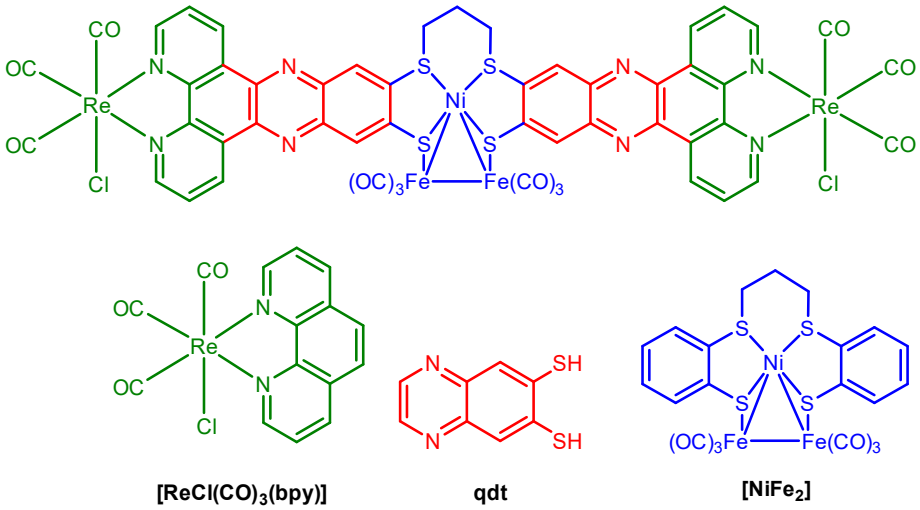
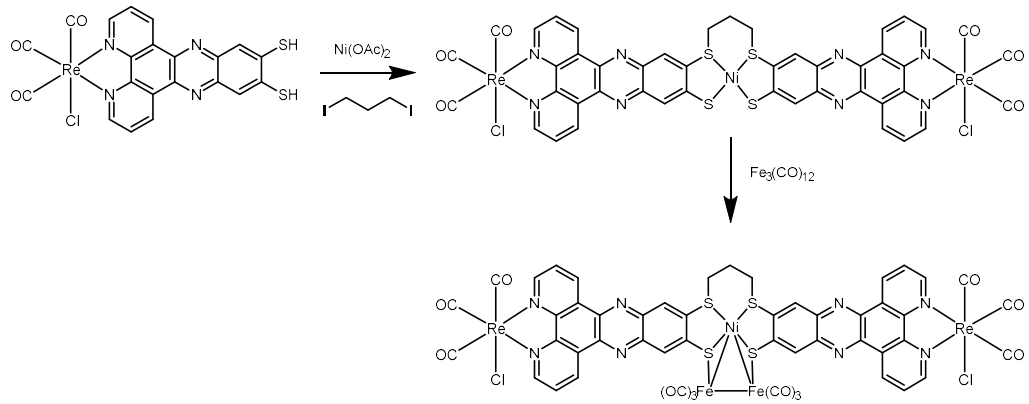


Figure 5.5: The target structure $\{Ni[(ReCl(CO)_3)_2(p\text{-}dppz(S)_2)]Fe_2(CO)_6\}$ and the three different components within the target structure, a Re(bpy) photosensitier (green) with a quinoxaline linker (red) and a $[NiFe_2]$ catalytic centre (blue).



Scheme 5.1: A proposed synthesis of $\{Ni[(ReCl(CO)_3)_2(p\text{-}dppz(S)_2)]Fe_2(CO)_6\}$.

The synthetic method employed at Nottingham for the syntheses of $[NiFe_2]$ complexes often involves the synthesis of a dithiolate ligand, which reacts with a Ni^{II} centre to give a Ni^{II}-thiolate precursor. The reaction of this precursor with a Fe-containing species generates a [NiFe] compound. For example, Wang *et al*. synthesised $[Ni(L^A)Fe_2(CO)_6]$ [$L^A = (CH_3C_6H_3S_2)_2(CH_2)_3$), Section 1.6.4, Figure 1.23] from a reaction between $[Ni(L^A)]$ and $Fe_3(CO)_{12}$.[11] The adoption of this synthetic strategy provides one route to the target $\{Ni[(ReCl(CO)_3)_2(p\text{-}dppz(S)_2)]Fe_2(CO)_6\}$ complex (Scheme 5.1). Therefore, a key target is the preparation of the novel $[ReCl(CO)_3(dppz(SH)_2)]$ complex (Figure 5.6).

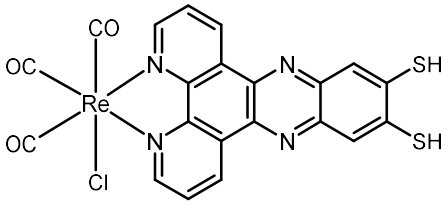
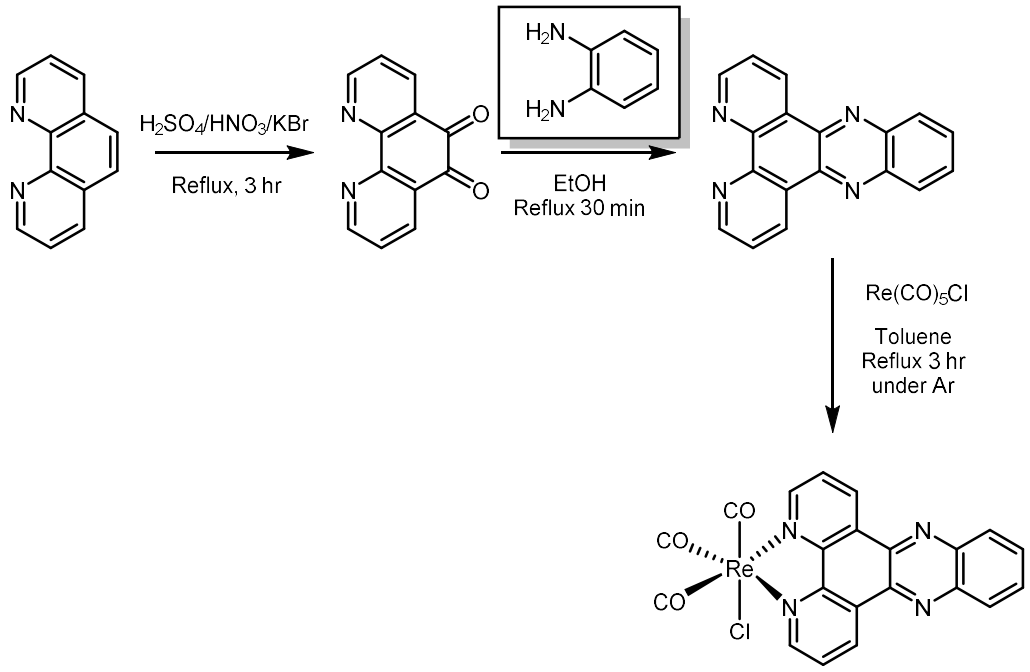


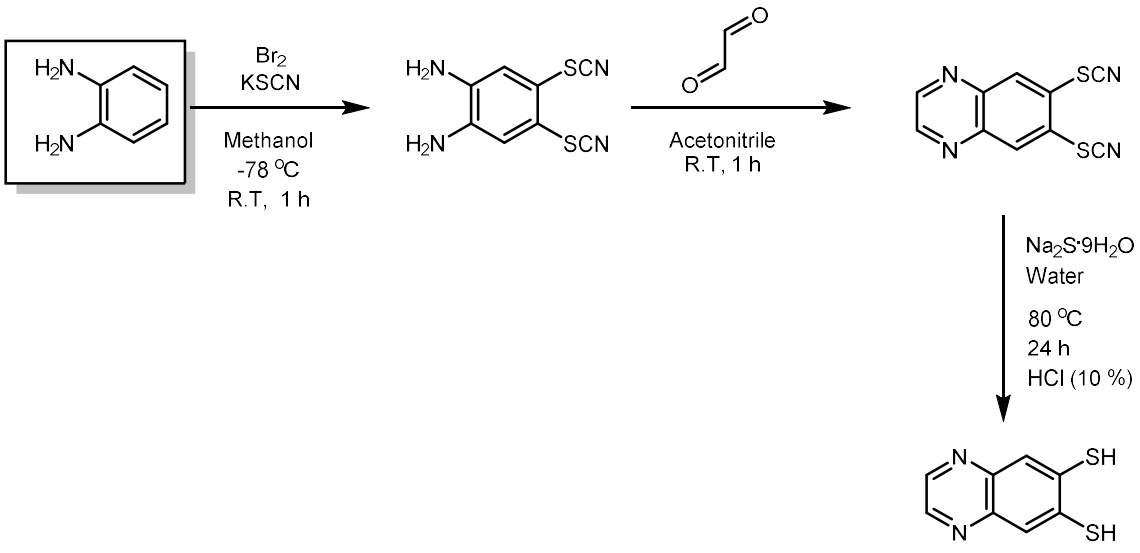
Figure 5.6: The target structure of $[ReCl(CO)_3(dppz(SH)_2)]$.

The synthetic route to $[ReCl(CO)_3(dppz)]$ is shown in Scheme 5.2 and forms the basis for a route to $[ReCl(CO)_3(dppz(SH)_2)]$.[12,13]

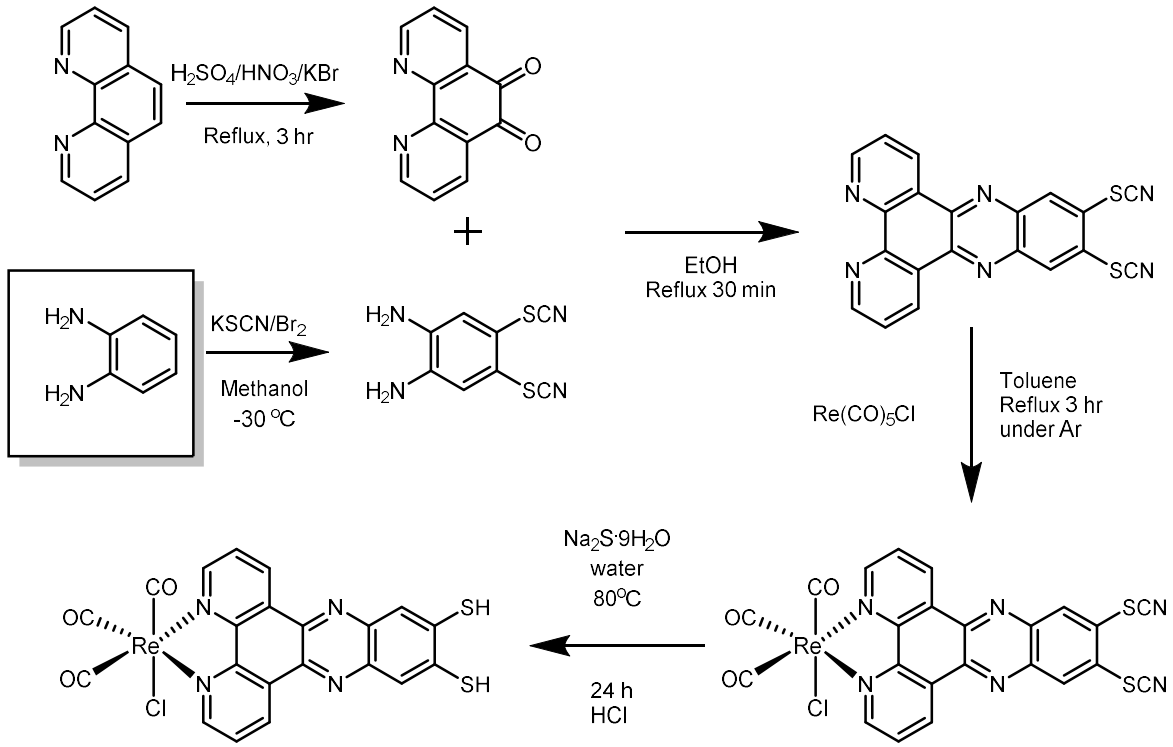


Scheme 5.2: The synthetic route of $[ReCl(CO)_3(dppz)]$.

A dppz ligand functionalised with thiocyanate substituents at the C(11) and C(12) (Figure 5.4) positions may be synthesised from a functionalized 1,2-diaminobenzene precursor through the adoption of approaches for the synthesis of 6,7-quinoxaline-dithiol ($q^{6,7}dtH_2$) (Scheme 5.3).[14–16] As the two synthetic strategies shown in Scheme 5.2 and 5.3 involved the *o*-phenylenediamine (highlighted in Scheme 5.2 and 5.3) it allows us to combine the two routes. Leading to the novel route for the synthesis of $dppz(SH)_2$ bound to a $\{ReCl(CO)_3\}$ fragment (Scheme 5.4).



Scheme 5.3: The synthetic route to quinoxaline-6,7-dithiol ($q^{6,7}dtH_2$).



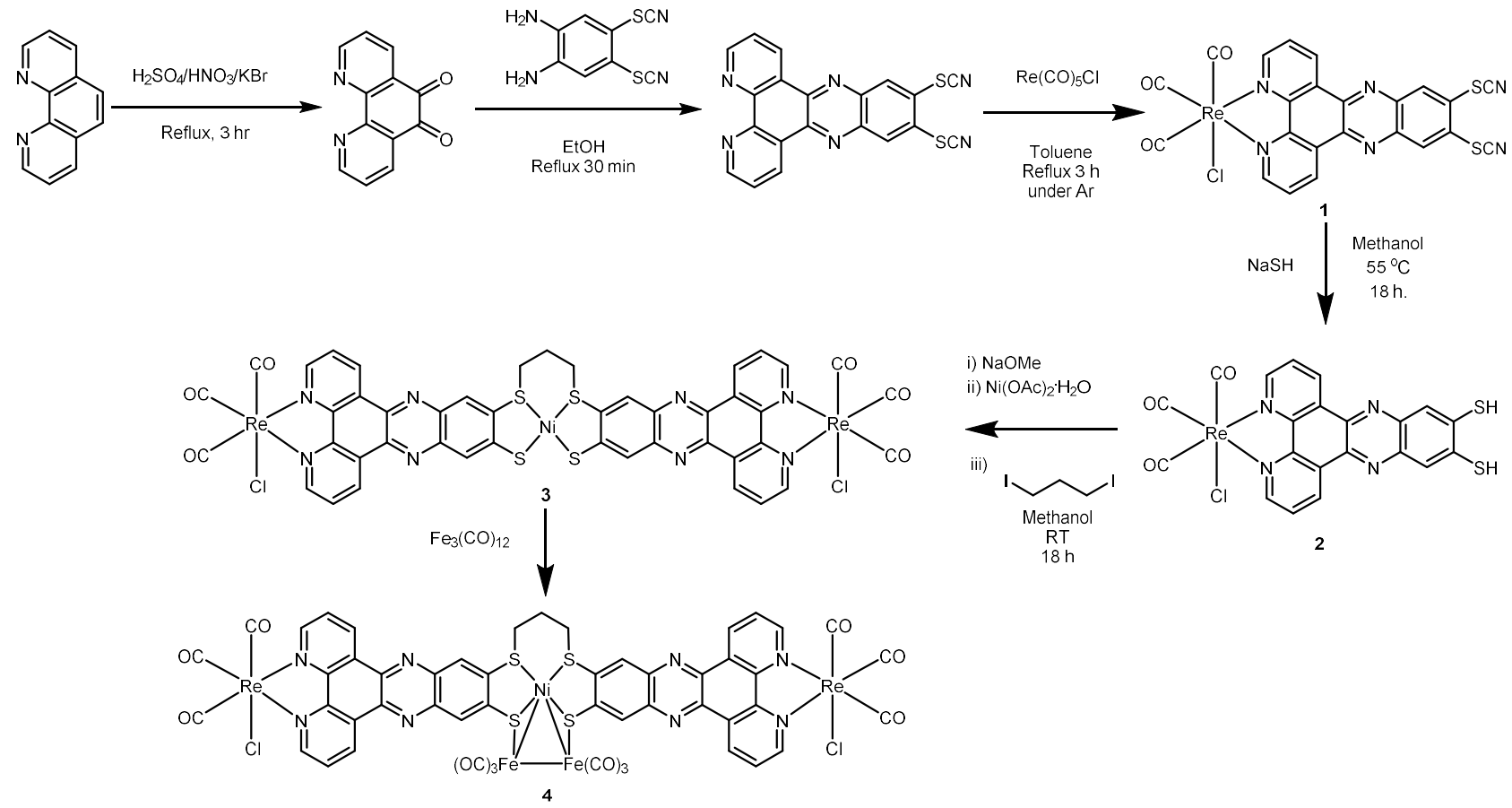
Scheme 5.4: The proposed synthetic route to $[ReCl(CO)_3(dppz(SH)_2)]$.

Our routes to $[ReCl(CO)_3(dppz(SH)_2)]$ and to $dppz(SH)_2$ evolved into two approaches for the synthesis of the target $\{Ni[(ReCl(CO)_3)_2(p\text{-}dppz(S)_2)]Fe_2(CO)_6\}$ compound:

Approach A the synthesis of $[ReCl(CO)_3(dppz(SH)_2)]$, its coordination to a Ni^{II} centre to give $\{Ni[ReCl(CO)_3(p\text{-}dppz(S)_2)]_2\}$ followed by the reaction of this unit with $Fe_3(CO)_{12}$ to give the target compound $\{Ni[(ReCl(CO)_3)_2(p\text{-}dppz(S)_2]_2Fe_2(CO)_6\}$ (Scheme 5.5).

Approach B the synthesis of $[Ni(p\text{-}dppz(S)_2)_2]$, its complexation to two $[ReCl(CO)_5]$ fragments to form $\{Ni[(ReCl(CO)_3)_2(p\text{-}dppz(S)_2)]_2\}$ followed by the reaction of this unit with $Fe_3(CO)_{12}$ to give the target compound $\{Ni[(ReCl(CO)_3)_2(p\text{-}dppz(S)_2)]Fe_2(CO)_6\}$ (Scheme 5.8).

5.4 Synthesis towards a Ni^{II} and [NiFe] compound containing a photosensitiser unit: Approach A



Scheme 5.5: A proposed synthesis for {Ni[(ReCl(CO)$_3$)$_2$(p-dppz(S)$_2$]Fe$_2$(CO)$_6$}, **4**.

The complete synthetic scheme for Approach A is shown in Scheme 5.5. This requires the synthesis of $[ReCl(CO)_3(dppz(SCN)_2)]$, **1**, which involves the assembly of a dppz ligand functionalised at the C(11) and C(12) positions by thiocyanate substituents. The coordination of the $dppz(SCN)_2$ ligand to a $[ReCl(CO)_5]$ fragment employs the methodologies of Fraser *et al.*[13] The conversion of the pendant thiocyanate groups may be accomplished by a reaction with NaSH in methanol, an adaptation of methods previously reported by Das *et al* (Scheme 5.3)[14–16] to give $[ReCl(CO)_3(dppz(SH)_2)]$, **2**. The reaction of **2** with sodium methoxide, $Ni(OAc)_2{\cdot}2H_2O$ and diiodopropane following the method of Wang *et al.*[11] gives **3** as a precursor to react with $Fe_3(CO)_{12}$ to generate the target complex, $\{Ni[ReCl(CO)_3(p\text{-}dppz(S)_2)]_2Fe_2(CO)_6\}$, **4**.

5.4.1 The synthesis of $[ReCl(CO)_3(dppz(SCN)_2)]$,1

The synthesis of $dppz(SCN)_2$ has been reported by Fraser *et al.*[13] 1,10-Phenanthroline-5,6-dione was synthesised according to the literature methodologies of Yamanda *et al.*[17] This involves the oxidation of 1,10-phenanthroline to the 5,6-dione derivative by treating 1,10-phenanthroline with a mixture of concentrated sulfuric and nitric acids, and KBr. The mixture was poured over ice and neutralised with Na_2CO_3 then extracted with CH_2Cl_2. The CH_2Cl_2 was removed under vacuum to give the desired product in a high yield, with further purification possible *via* a recrystallisation from ethanol.

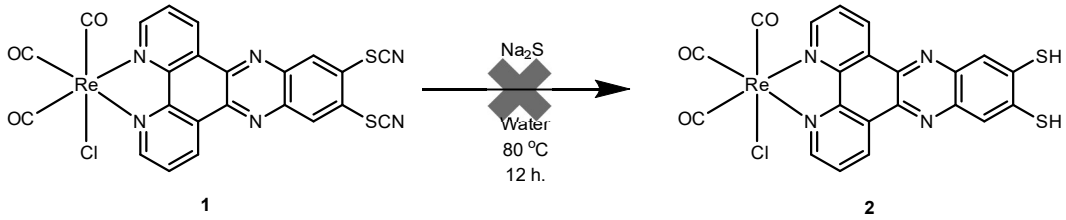
4,5-Thiocyanatobenzene-1,2-diamine was synthesised using the method reported by Brusso *et al.*[18] A mixture of *o*-phenylenediamine and KSCN was treated with bromine in methanol. The bromine solution was added dropwise at -30°C over 4 h using a syringe pump; the slow addition of the solution of bromine in methanol is crucial to improve the yield of this reaction. The mixture was warmed to room temperature and diluted with water, filtered and the filtrate was treated with ammonia solution to give a yellow precipitate which was collected *via* filtration. The crude product was dissolved in ethyl acetate and passed through a plug of silica. The isolation of 4,5-thiocyanatobenzene-1,2-diamine was confirmed by mass spectrometry and by ^1H NMR spectroscopy.

The formation of $dppz(SCN)_2$, as shown in Scheme 5.5, involves a Schiff-base condensation.[13] 1,10-Phenanthroline-5,6-dione and 4,5-thiocyanatobenzene-1,2-

diamine were heated to reflux in ethanol for 1 h to give a precipitate which was collected *via* filtration and washed with ethanol to afford the desired product. The formation of $dppz(SCN)_2$ was confirmed by mass spectrometry and by ^1H NMR spectroscopy.

$[ReCl(CO)_3(dppz(SCN)_2)]$, was prepared according to the literature methodologies of Gordon *et al*.[13] This involved the reaction of $dppz(SCN)_2$ and $ReCl(CO)_5$ at reflux in toluene for 3 h. The desired product was then collected *via* filtration and washed with diethyl ether. The formation of $[ReCl(CO)_3(dppz(SCN)_2)]$, **1**, was confirmed by mass spectrometry, and by ^1H NMR and IR spectroscopies.

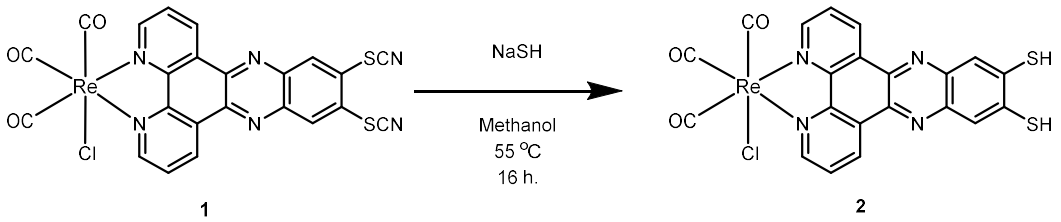
5.4.2 The synthesis of $[ReCl(CO)_3(dppz(SH)_2)]$, 2



Scheme 5.6: The attempted synthesis of $[ReCl(CO)_3(dppz(SH)_2)]$.

Our initial attempts to convert $[ReCl(CO)_3(dppz(SCN)_2)]$, **1**, into $[ReCl(CO)_3(dppz(SH)_2)]$, **2**, focussed on the adaptation of the methodologies of Das *et al.*[16] who prepared $q^{6,7}dt$ from 6,7-dithiocyanatoquinoxaline, by the treatment of 6,7-dithiocyanatoquinoxaline with $Na_2S{\cdot}xH_2O$ in water at 80 °C. We employed a variety of conditions including **1** with $Na_2S{\cdot}xH_2O$ in water at 80 °C, and **1** with $Na_2S{\cdot}xH_2O$ in a biphasic water/CH_2Cl_2 solution at a range of temperatures. However, the insoluble nature of **1** in water meant that this approach was unsuccessful.

We developed a new method that uses NaSH in methanol to achieve the desired conversion. A mixture of **1** and NaSH in methanol was stirred at 55°C for 16 h (Scheme 5.7) before the reaction mixture was cooled to room temperature. The addition of 10 % HCl solution to the reaction mixture gave a lilac precipitate which was collected by centrifugation, washed with methanol and dried under vacuum.



Scheme 5.7: The synthesis of $[ReCl(CO)_3(dppz(SH)_2)]$.

The isolation of **2** was confirmed by mass spectrometry, and by ^{1}H-NMR and IR spectroscopies. Mass spectrometry gave an isotope pattern with a parent peak at 650 m/z that matched the predicted isotope pattern for **2** (Figure 5.7). IR studies showed ν(SH) bands at 2319 cm^{-1} and three ν(CO) bands associated with the [Re] centre at 2053 cm^{-1}, 1983 cm^{-1} and 1885 cm^{-1} (Table 5.1), respectively. The three ν(CO) bands associated with **2** are shifted compared to previously reported [Re] complexes shown in Table 5.1. The shift in ν(CO) to higher wavenumber may be due to the substitution of an electron withdrawing SH group on the dppz framework. The solubility of **2** in common bench solvents is low, which limited our attempts to purify **2** by recrystallisation and/or column chromatography; elemental analysis confirmed that the product was not isolated pure.

Table 5.1: FTIR data for $[ReCl(CO)_3(dppz(SH)_2)]$ compared to previously reported [Re] centres in CH_2Cl_2.[2,13]

Complex	**ν(CO) /cm^{-1}**
$[ReCl(CO)_3(dppz)]$[13]	2025, 1923, 1900
$[ReCl(CO)_3(dppz(SCN)_2)]$[13]	2026, 1925, 1903
$[ReCl(CO)_3(dppz(SH)_2)]$	2053, 1983, 1885
[Re]-[NiFe][2]	2023, 1919, 1901

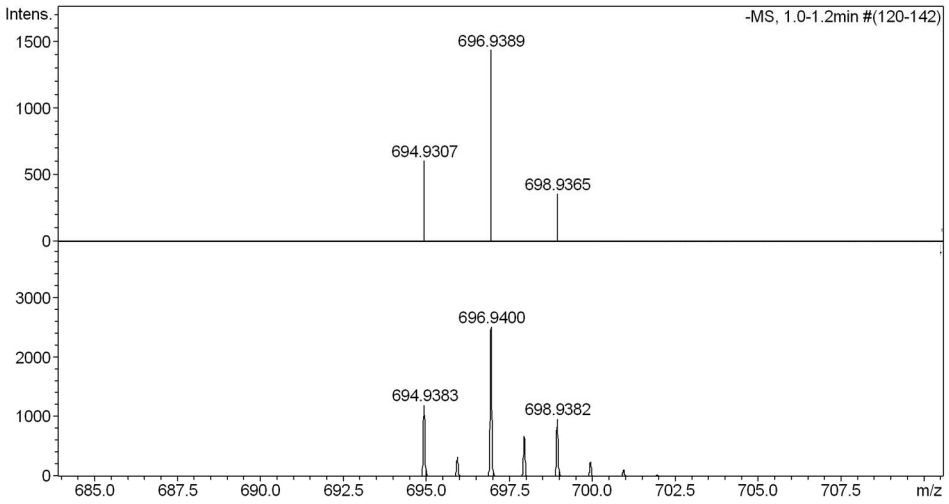


Figure 5.7: The mass spectrometry isotope pattern for [$ReCl(CO)_3$(dppz(SH)(S^-)] (Top) to predicted (Bottom).

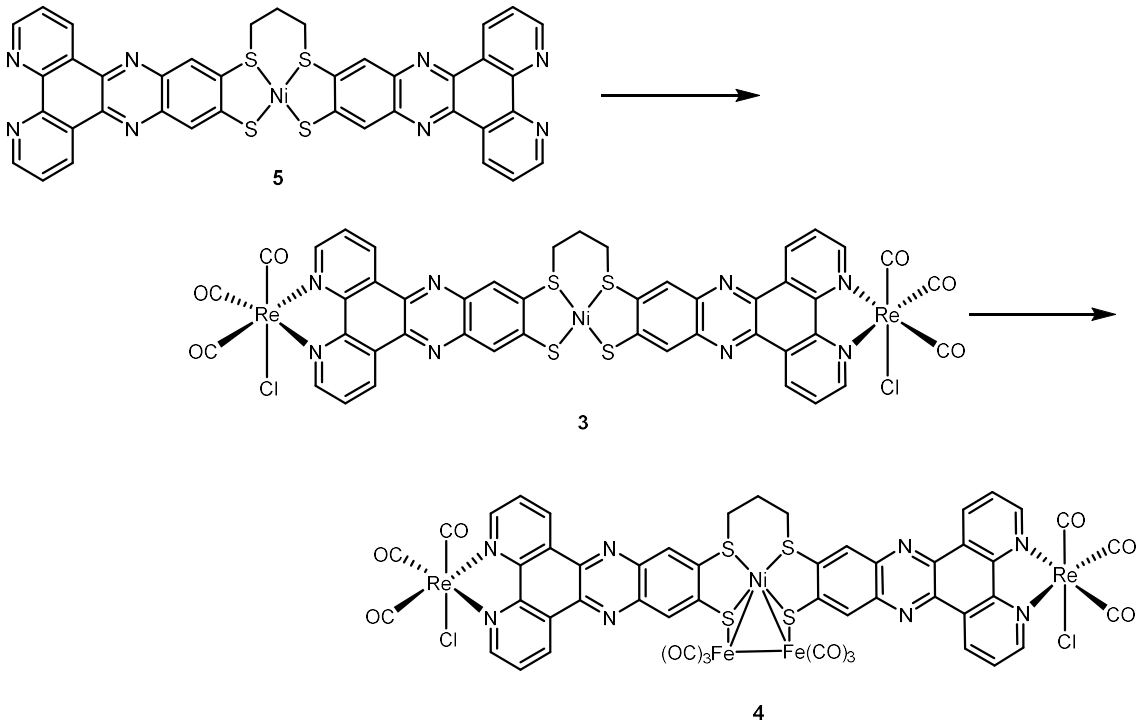
5.4.3 The Attempted Synthesis of {Ni[$ReCl(CO)_3$dppz$(S)_2]_2$}, 3

The synthesis of {Ni[($ReCl(CO)_3)_2$(p-dppz$(S)_2$)]}, **3**, was attempted from the crude **2**, following the methods of Wang *et al.*[11] (Scheme 5.5). Sodium methoxide was added to crude **2** in methanol and the mixture was stirred for 1h at room temperature. $Ni(OAc)_2{\cdot}4H_2O$ was added to the solution and the mixture stirred for a further 30 min before diiodopropane was added in the dark. This mixture was stirred for 16 h to give a dark precipitate, which was isolated by filtration. Mass spectrometry, ^{1}H-NMR and IR spectroscopic studies were undertaken in an attempt to identify the product. The solid was insoluble in most common bench solvents apart from dimethyl sulfoxide. The ^{1}H NMR spectrum of the product in dimethyl sulfoxide was broad and the product peaks could not be identified. The mass spectrum did not present isotope patterns that were consistent with a Re centre being present. Thus, the Re unit may have been displaced by Ni^{II} during the reaction and polymerisation may have occurred.

5.5 Synthesis towards a Ni^{II} and [NiFe] compound containing a photosensitiser unit: Approach B

We attempted the synthesis of the target complex {Ni[($ReCl(CO)_3)_2$(p-dppz$(S)_2$)]$Fe_2(CO)_6$}, **4** *via* an alternate route (Scheme 5.8). This approach involves the synthesis of [Ni(p-dppz$(S)_2)_2$], **5**, its complexation to two [$ReCl(CO)_5$] fragments

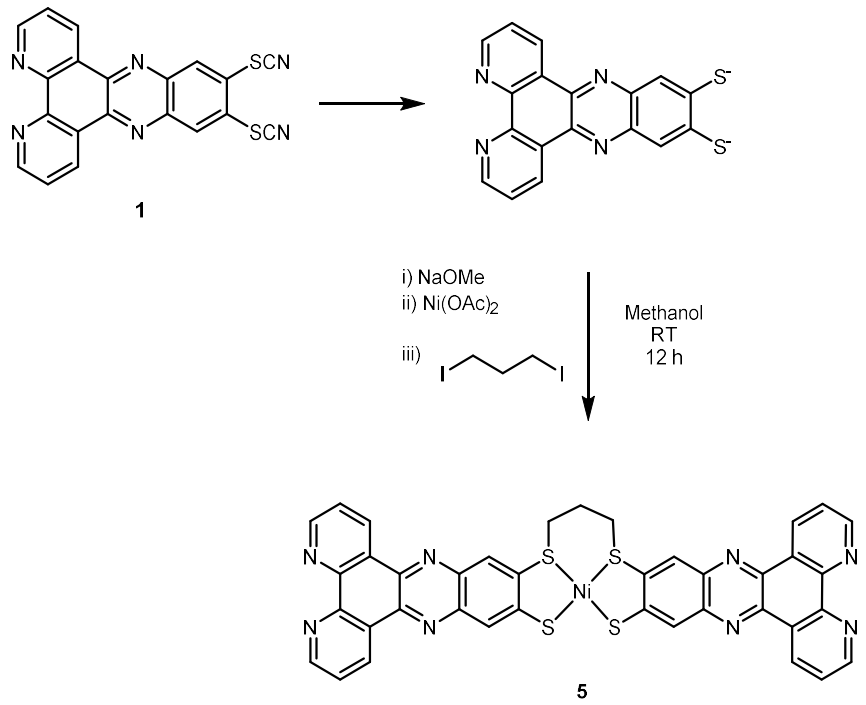
to give **3** and the reaction of **3** with $Fe_3(CO)_{12}$ to generate the target complex, {Ni[(ReCl(CO)$_3$)$_2$dppz(S)$_2$] $Fe_2(CO)_6$}, **4**.



Scheme 5.8: The alternative proposed route to {Ni[(ReCl(CO)$_3$)$_2$(p-dppz(S)$_2$)]$Fe_2(CO)_6$}.

5.5.1 The attempted synthesis of [Ni(p-dppz(S)$_2$)$_2$], 5

The preparation of [Ni(p-dppz(S)$_2$)$_2$], **5** was attempted from dppz(SCN)$_2$ in a one-pot reaction by its treatment with NaSH in methanol at 55 °C for 12 h followed by cooling to RT and a direct reaction with $Ni(OAc)_2$ in methanol (Scheme 5.11). Diiodopropane was added in the dark and the mixture was stirred for 24 h at room temperature to give a dark green solid which was collected *via* filtration and was washed with methanol and dried under vacuum.



Scheme 5.9: Proposed synthesis of [Ni(p-dppz$(S)_2)_2$], **5**.

The product of the reaction was insoluble in most common bench solvents and the product could not be identified by mass spectrometry. However, the ^{1}H NMR spectrum in dimethylsulfoxide possesses features at 9.49, 9.10, 7.70 and 7.78 ppm with a splitting pattern consistent with that of the dppz$(SCN)_2$ ligand at 9.64, 9.37, 8.88 and 7.89 ppm, and features at 3.13 ppm and 2.92 ppm that may be associated with the [Ni(p-dppz$(S)_2)_2$] product and consistent with a propane bridge being present in the product. The ^{1}H-NMR spectra reported for the [Ni(p-$q^{6,7}dt^{R1,R2}$)] (R^1 = R^2 = Me, Et, Ph; R^1 = H, R^2 = Ph) series discussed in Chapter 2, also contains doublets at *ca.* 3.1 and 2.9 ppm that have been assigned to the CH_2 groups within the propane bridge. Recrystallisations from CH_2Cl_2 with a variety of antisolvents, including methanol and pentane were attempted to purify the product and attempts were made to prepare a single crystal for X-ray diffraction studies. However, only powders could be obtained and elemental analysis confirmed these were not pure product.

5.5.2 The attempted synthesis of {Ni[ReCl$(CO)_3$(p-dppz$(S)_2$)]$_2$}, 3

The complexation of two [ReCl$(CO)_5$] fragments to **5** was attempted to prepare **3**. Crude **5** was heated to reflux in toluene with [ReCl$(CO)_5$] for 24 h and the resulting precipitate was collected *via* filtration, washed with hot toluene and recrystallised

from dichloromethane and pentane. ^{1}H-NMR and IR spectroscopic studies appear to be consistent with the formation of **3**. The ^{1}H-NMR spectrum shows features at 9.53, 9.13, 7.74, 7.81, 3.17 and 2.98 ppm that are all downshifted relative to those for the putative complex **5**. The IR spectrum (Figure 5.8) shows two carbonyl peaks at 2049 and 1954 cm^{-1} with no evidence of carbonyl bands associated with the $[Re(CO)_5Cl]$ starting material. Thus, the IR and ^{1}H NMR provided some encouragement that **3** had been formed. However, inspite of attempts to purify the product by column chromatography and recrystallisation from a variety of solvents, elemental analysis showed that the compound was not isolated pure.

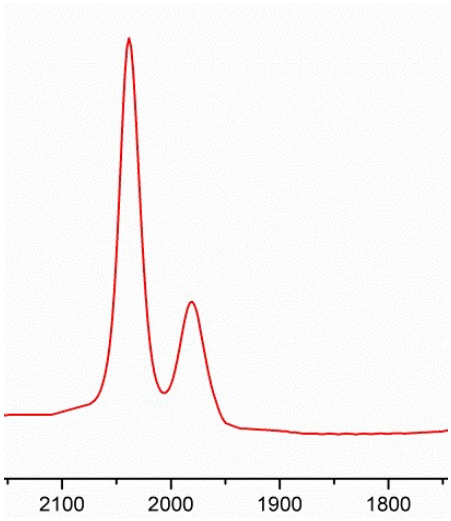


Figure 5.8: The IR spectrum of $\{Ni[(ReCl(CO)_3)_2(p\text{-}dppz(S)_2]\}$.

5.5.3 The attempted synthesis of $\{Ni[ReCl(CO)_3(p\text{-}dppz(S)_2)]_2Fe_2(CO)_6\}$, 4

The crude $\{Ni[(ReCl(CO)_3)_2(p\text{-}dppz(S)_2)]\}$ product was used in an attempt to synthesise **4**. Reactions employing a variety of conditions were attempted including stirring the reaction mixture at room temperature, heating to reflux and heating in a microwave reactor in ethanol and CH_2Cl_2 solutions; these methods have been used previously for the syntheses of [NiFe] complexes, such as $[Ni(L^A)Fe_2(CO)_6]$ (Chapter 1, Section 1.6.1).[2,11,19] We were unable to isolate the target molecule, instead the IR spectrum of the reaction mixture exhibited ν(CO) bands at 1995, 2051 and 2026 cm^{-1} associated with the formation of $Fe(CO)_5$, a $Fe_3(CO)_{12}$ decomposition product, suggesting that no reaction took place between $\{Ni[(ReCl(CO)_3)_2(p\text{-}dppz(S)_2)]\}$ and $[Fe_3(CO)_{12}]$. This may be due to the low solubility of

{Ni[(ReCl(CO)$_3$)$_2$(p-dppz(S)$_2$)]} in ethanol and CH_2Cl_2 or because {Ni[(ReCl(CO)$_3$)$_2$(p-dppz(S)$_2$)]} decomposes during the reaction.

5.6 Towards a Ni^{II} and [NiFe] compound containing a single photosensitiser unit

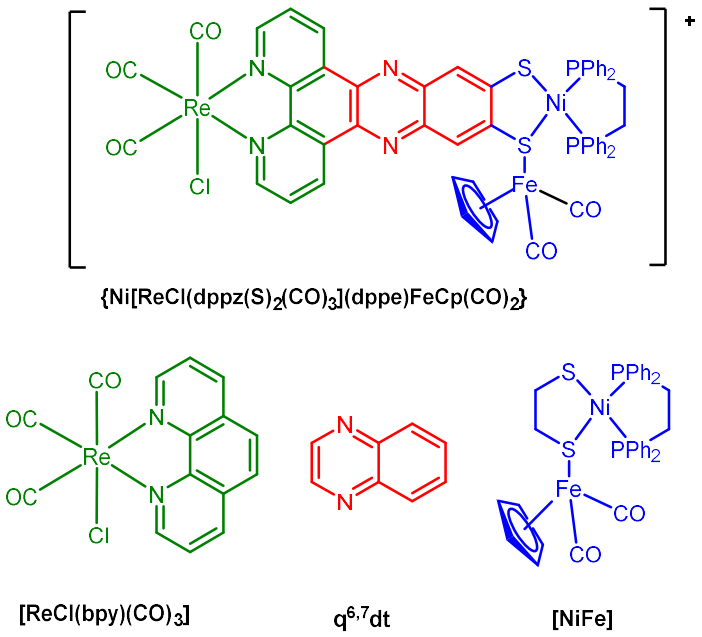
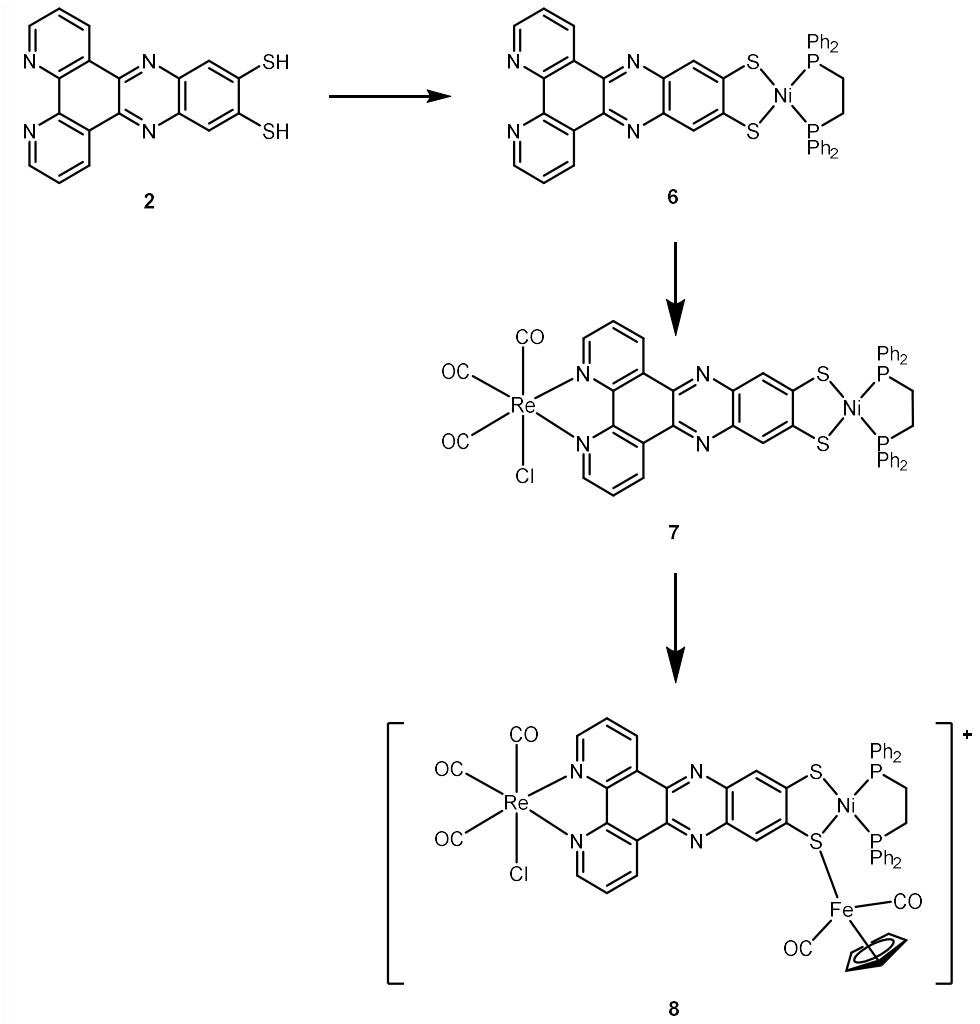


Figure 5.9: The new target structure, {Ni[ReCl(CO)$_3$(dppz(S)$_2$)](dppe)FeCp(CO)$_2$} and the three different components within the target structure, a [Re(bpy)] photosensitiser (green) with a quinoxaline linker (red) and finally a potentially catalytic [NiFe] centre (blue).

We were unable to confirm the formation {Ni[(ReCl(CO)$_3$)$_2$(p-dppz(S)$_2$)]$_2$Fe(CO)$_6$} using the approaches described in Sections 5.4 and 5.5. We therefore focussed our attention towards a [NiS_2P_2] centre incorporating a single photosensitiser unit (Figure 5.9, Scheme 5.10). This approach employs the same dithiolate-functionalised dppz ligand, synthesised in Sections 5.4 and 5.5, coordinated to a $[Ni(dppe)]^{2+}$ fragment (dppe = 1,2-bis(diphenylphosphino)ethane) to give a [NiS_2P_2] centre. This unit may be then be coordinated to a $[FeCp(CO)_2]^+$ fragment (Figure 5.9) using the same approaches developed for the syntheses of [Ni($q^{6,7}dt^{R1,R2}$)(dppe)FeCp(CO)$_2$][BF_4] ($R^1 = R^2$ = Me, Et, Ph; R^1 = H, R^2 = ^{t}Bu) as discussed in Chapter Four.

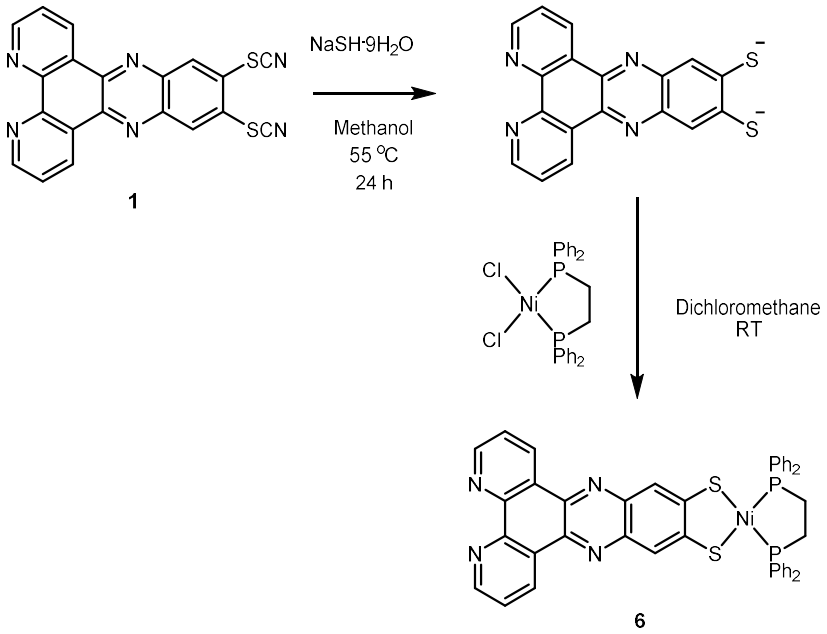


Scheme 5.10: Proposed synthetic route to a novel [NiFe] compound, **8**, containing a photosensitiser unit.

5.6.1 The synthesis of [Ni(dppz(S)$_2$)(dppe)]

The synthesis of [Ni(dppz(S)$_2$)(dppe)] was achieved by the route shown in Scheme 5.11. The dppz(SCN)$_2$ precursor (Section 5.4.1) was added to a solution of NaSH in methanol and the mixture was heated to 55 °C for 24h to give a vivid purple solution. The solution was concentrated under vacuum and a solution of [Ni(dppe)Cl_2] in CH_2Cl_2 was added dropwise at room temperature and the mixture was stirred for 18 h. Pentane was added to the resulting red solution to precipitate the crude product. The formation of [Ni(dppz(S)$_2$)dppe] was confirmed by mass spectrometry, ^{1}H-NMR, ^{13}C-NMR and ^{31}P-NMR spectroscopies. Attempts to purify the product in bulk by column chromatography using silica or alumina gel, or by recrystallisation by layering CH_2Cl_2 and pentane were unsuccessful, however, small quantities of

crystalline material suitable for X-ray crystallographic studies could be isolated by the vapour diffusion of diethyl ether into a solution of the impure product in CH_2Cl_2.



Scheme 5.11: Synthetic route to form [Ni(dppz(S)$_2$)(dppe)].

5.6.2 Single X-ray Crystallography of [Ni(dppz(S)$_2$)(dppe)]

Single crystals of [Ni(dppz(S)$_2$)(dppe)] were grown by the vapour diffusion of diethyl ether into a concentrated solution of [Ni(dppz(S)$_2$)(dppe)] in CH_2Cl_2 to give red plate crystals. The X-ray structure of [Ni(dppz(S)$_2$)(dppe)] is shown in Figure 5.10 with selected bond lengths and angles presented in Table 5.1.

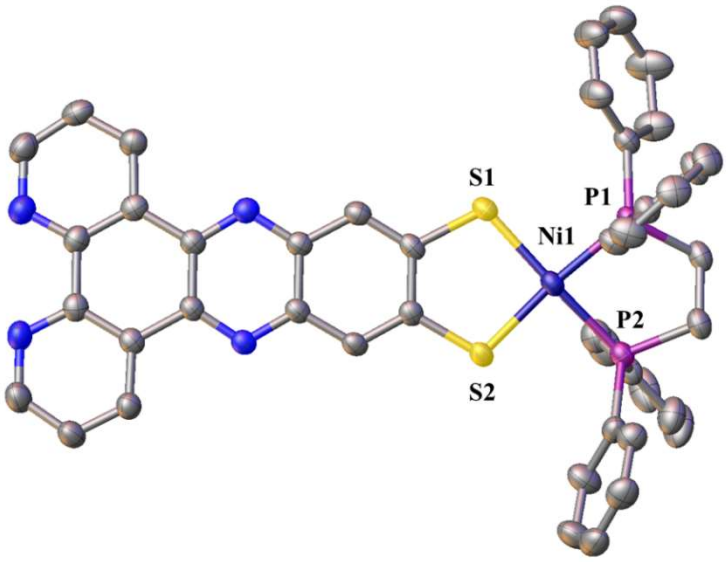


Figure 5.10: The X-ray crystal structure of [Ni(dppz(S)$_2$)(dppe)] with H atoms omitted for clarity.

Table 5.1 Selected bond distances and angles for [Ni(dppz(S)$_2$)(dppe)] and [Ni($q^{6,7}dt^{R1,R2}$)(dppe)] (R^1 = R^2 = Me, Ph; R^1 = H, R^2 = ^{t}Bu)

Bond Length/Å	**[Ni(dppz(S)$_2$)(dppe)]**	**[Ni($q^{6,7}dt^{Me,Me}$)(dppe)]**	**[Ni($q^{6,7}dt^{H,tBu}$)(dppe)]**	**[Ni($q^{6,7}dt^{Ph,Ph}$)(dppe)]**
Ni(1)-S(1)	2.1658(13)	2.1478(6)	2.1601(5)	2.1664(5)
Ni(1)-S(2)	2.1574(15)	2.1626(7)	2.1594(5)	2.1550(5)
Ni(1)-P(1)	2.1654(14)	2.1538(7)	2.1614(5)	2.1664(5)
Ni(1)-P(2)	2.1651(16)	2.1559(6)	2.1607(5)	2.1750(5)
Bond Angle/°				
S(2)-Ni(1)-S(1)	92.67(5)	93.35(2)	92.594(18)	92.275(18)
S(1)-Ni(1)-P(1)	92.33(6)	89.64(2)	90.005(18)	89.242(18)
S(2)-Ni(1)-P(2)	89.50(6)	90.89(2)	90.843(18)	90.918(18)
S(1)-Ni(1)-P(2)	170.16(6)	172.66(3)	176.54(2)	175.47(2)
S(2)-Ni(1)-P(1)	170.96(6)	169.29(3)	176.23(2)	175.44(2)
P(2)-Ni(1)-P(1)	86.84(6)	87.27(2)	86.542(19)	87.817(18)

The Ni atom in [Ni(dppz(S)$_2$)(dppe)] is bound by two phosphine donors from the dppe unit and two sulfur donors from the dppz-dithiol ligand in a distorted square planar geometry [S(1)-Ni(1)-S(2) = 92.67(5)° and P(2)-Ni(1)-P(1) = 86.84(6)°]. These angles compare well to the average S(1)-Ni(1)-S(2) and P(2)-Ni(1)-P(1) angles for the [Ni($q^{6,7}dt^{R1,R2}$)(dppe)] (R^1 = R^2 = Me, Ph; R^1 = H, R^2 = ^{t}Bu) series (92.74° and 87.2°, respectively, Table 5.1, Section 3.4.2). [Ni(dppz(S)$_2$)(dppe)] possesses average Ni-S and Ni-P distances of 2.1616(14) Å and 2.1653(15) Å, respectively, which also compare well to those of the [Ni($q^{6,7}dt^{R1,R2}$)(dppe)] (R^1 = R^2 = Me, Ph; R^1 = H, R^2 = ^{t}Bu) series (2.1585(5) and 2.1622(5) Å, respectively, Table 5.1, Section 3.4.2). Thus, taken together these data indicate that the coordination sphere about the Ni^{II} centre in [Ni(dppz(S)$_2$)(dppe)] is similar to those for [Ni($q^{6,7}dt^{R1,R2}$)(dppe)] and that the substitution of the $[q^{6,7}dt^{R1,R2}]^{2-}$ for the $[dppz(S)_2]^{2-}$ ligand has little effect on the coordination geometry.

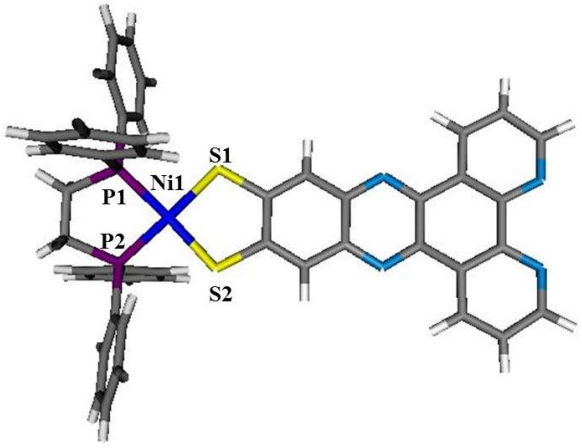


Figure 5.11: The geometry optimised structure of [Ni(dppz(S)$_2$)(dppe)] using the BP86 functional.

We undertook DFT calculations for [Ni(dppz(S)$_2$)(dppe)] to gain a qualitative description of the structure and bonding in this unit and for direct comparisons with the electronic structures of [Ni($q^{6,7}dt^{R1,R2}$)(dppe)]. A model of [Ni(dppz(S)$_2$)(dppe)] was constructed from the experimentally determined crystallographic co-ordinates for a comparison. Selected bond lengths and inter-bond angles obtained from the DFT calculations following geometry optimisation and X-ray crystallography are shown in Table 5.2. The calculated structure of [Ni(dppz(S)$_2$)(dppe)] is shown in Figure 5.11. The axis system used in the calculations places the x-axis along the bisector of the P(1)-Ni(1)-P(2) angle and the y-axis in the P(1)-Ni(1)-S(1) plane. The calculated structure broadly reproduces the experimental structure; the average Ni-S and Ni-P distances in the geometry optimised structure are within *ca.* 0.01 Å of those in the experimental structure. The calculated S(1)-Ni(1)-S(2) and P(2)-Ni(1)-P(1) angles (92.51 and 88.62°, respectively) are within *ca.* 0.2° of the angles found in the experimental structure. Thus, the similarity between the calculated and experimental geometries suggests that the DFT calculations at the BP86 level provide a reliable qualitative description of the electronic structures of [Ni(dppz(S)$_2$)dppe].

Table 5.3: Selected bond lengths (Å) and angles (°) with s.u. for the experimental and geometry optimised structures of [Ni(dppz(S)$_2$)(dppe)].

Bond Length/Å	**[Ni(dppz(S)$_2$)dppe]**	**BP86**
Ni(1)-S(1)	2.1658(13)	2.1737
Ni(1)-S(2)	2.1574(15)	2.1731
Ni(1)-P(1)	2.1654(14)	2.1707
Ni(1)-P(2)	2.1651(16)	2.1685
Bond Angle/°		
S(2)-Ni(1)-S(1)	92.67(5)	92.51
S(1)-Ni(1)-P(1)	92.33(6)	91.84
S(2)-Ni(1)-P(2)	89.50(6)	91.38
S(1)-Ni(1)-P(2)	170.16(6)	164.15
S(2)-Ni(1)-P(1)	170.96(6)	163.92
P(2)-Ni(1)-P(1)	86.84(6)	88.62

The compositions and energies of the frontier orbitals of [Ni(dppz(S)$_2$)(dppe)] and [Ni($q^{6,7}dt^{Et,Et}$)(dppe)], calculated for the gas-phase geometry optimised structures, are summarised in Table 5.3 and the frontier orbitals of [Ni(dppz(S)$_2$)(dppe)] and [Ni($q^{6,7}dt^{Et,Et}$)(dppe)] are illustrated in Figure 5.12.

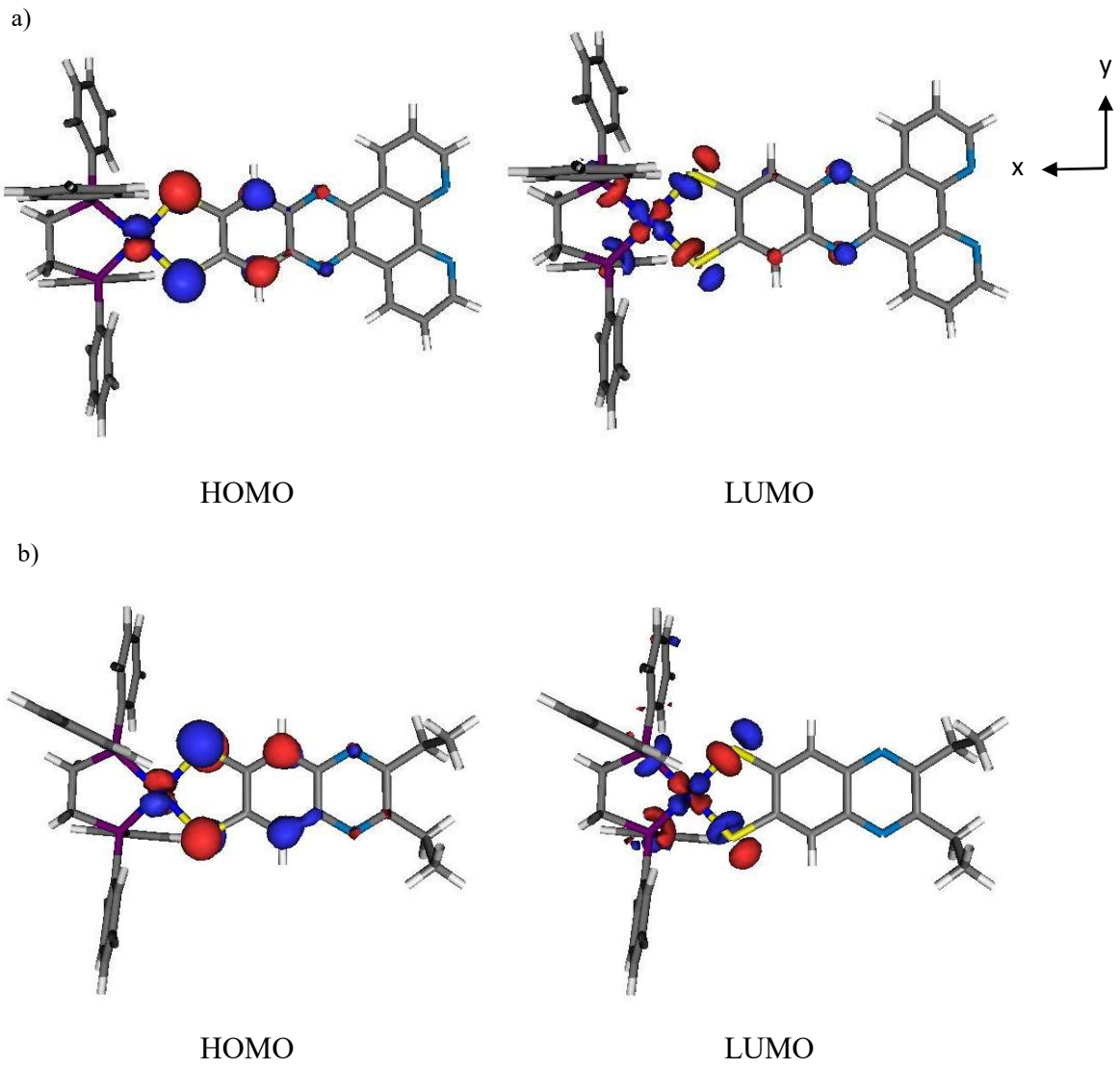


Figure 5.12: Kohn-Sham frontier orbitals for the BP86 optimised structures of a) [Ni(dppz(S)$_2$)(dppe)] and b) [Ni(q^{6,7}dt^{Et,Et})(dppe)] (Chapter Three, Section 3.7)

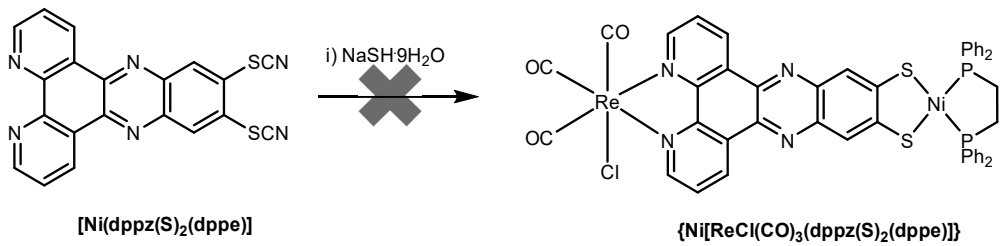
Analysis of the Kohn-Sham frontier orbitals of the optimised structure of [Ni(dppz(S)$_2$)(dppe)] shows the HOMO (Figure 5.12, a)) is delocalised across the metalladithiolate unit and involves Ni 3d_{yz}, and dithiolate-S π-combinations with Ni (20.2 %) and S (16.6%) character. The LUMO are derived from Ni 3d_{xy} and S-thiolate/thioether σ-orbital combinations. The LUMOs involve contributions from the S-donors (36.9 %) and the Ni centre (25.2 %). The natures of the frontier orbitals in [Ni(dppz(S)$_2$)(dppe)] are similar to those in [Ni(q^{6,7}dt^{Et,Et})(dppe)] (Table 5.4, Figure 5.12), however, [Ni(q^{6,7}dt^{Et,Et})(dppe)] has a higher percentage contribution from the S-dithiolate donors (25.4%) than that found for [Ni(dppz(S)$_2$)(dppe)] (16.6%). Thus, the extended aromatic ring system in the [dppz(S)$_2$]$^{2-}$ may be more

electron withdrawing than the $[q^{6,7}dt^{Et,Et}]^{2-}$ ligand with more significant delocalisation of electron density across the $[dppz(S)_2]^{2-}$ as evidenced by a N contribution to the HOMO in $[Ni(dppz(S)_2)(dppe)]$ of 4.1% (Table 5.3). We also note that the relative energies of the LUMOs in $[Ni(dppz(S)_2)(dppe)]$ and $[Ni(q^{6,7}dt^{Et,Et})(dppe)]$ (-0.1748 and -0.165 Hartrees, respectively, Table 5.3) suggest that $[Ni(dppz(S)_2)(dppe)]$ should possess a more positive redox potential for the first reduction process when compared to the reduction potential of the formal $Ni^{II/I}$ couple in $[Ni(q^{6,7}dt^{Et,Et})(dppe)]$.

Table 5.4: The nature, energy and composition of the frontier orbitals obtained from DFT calculations of $[Ni(dppz(S)_2)(dppe)]$ and $[Ni(q^{6,7}d^{Et,Et})(dppe)]$.

Compound	Designation	Orbital Nature	Energy/ Hartrees	% Contribution			
				Ni	S	N	P
$[Ni(dppz(S)_2)(dppe)]$	208a LUMO	Ni d_{xy} - S/P σ	-0.1748	25.2	36.9	9.1	0
	207a HOMO	Ni d_{yz} - S π	-0.1178	20.2	16.6	4.1	14.9
$[Ni(q^{6,7}dt^{Et})(dppe)]$	185a LUMO	Ni d_{xy} - S/P σ	-0.165	24.4	38.5	2.4	0
	184a HOMO	Ni d_{yz} - S π	-0.106	24.3	24.5	0	16.7

5.6.3 The attempted synthesis of {Ni[ReCl(CO)$_3$(dppz(S)$_2$)](dppe)}: Route A



Scheme 5.12: The attempted synthesis of {Ni[ReCl(CO)$_3$(dppz(S)$_2$](dppe)} *via* route A.

The complexation of a {ReCl(CO)$_3$} fragment to the N-donors of the dppz unit was attempted following the literature methodologies of Fraser *et al.*[13] $[Ni(dppz(S)_2)(dppe)]$ and $[ReCl(CO)_5]$ were heated to reflux in toluene for 24 h and the progress of the reaction was monitored by IR spectroscopy. The shift of the ν(CO) stretches from 2041 and 1985 cm^{-1} for the $[ReCl(CO)_5]$ starting material to 2023 and 1885 cm^{-1} for the reaction mixture suggest that the Re centre may have bound to the dppz ligand (Table 5.5, Figure 5.13). The solvent was removed under vacuum to give a red solid. The ^{1}H-NMR spectrum of this material in $(CD_3)_2SO$ exhibits features at 8.84 8.51, 7.82, 7.62-7.41 and 2.40 ppm, consistent with the

splitting pattern of a dppz unit. The ^{31}P-NMR spectrum possesses a feature at 54.7 ppm showing the peaks of the crude product have shifted relative to that for [Ni(dppz(S)$_2$)(dppe)] (59.66 ppm, Section 5.8.8). However, mass spectrometry did not appear to show evidence for the formation of the target product. The purification of {Ni[ReCl(CO)$_3$(dppz(S)$_2$)](dppe)} was attempted by recrystallisation from CH_2Cl_2 solution using pentane, hexane, methanol and diethyl ether as anti-solvents, however crystals suitable for X-ray diffraction could not be obtained and elemental analysis confirmed the product was not pure.

Table 5.4 IR ν(CO) recorded for a range of [ReCl(CO)$_3$(dppz(SCN)$_2$)], [ReCl(CO)$_3$(dppz(SH)$_2$)], {Ni[ReCl(CO)$_3$dppz(S)$_2$](dppe)} compared to [ReCl(CO)$_3$(dppz)] in CH_2Cl_2 solutions. [13]

Complex	V(CO) /cm^{-1}
[ReCl(CO)$_3$(dppz)][13]	2025, 1923, 1900
[ReCl(CO)$_3$(dppz(SCN)$_2$)]	2026, 1925, 1903
[ReCl(CO)$_3$(dppz(SH)$_2$)]	2053, 1983, 1885
[ReCl(CO)$_5$]	2041, 1985
{Ni[ReCl(CO)$_3$dppz(S)$_2$](dppe)}	2023, 1885

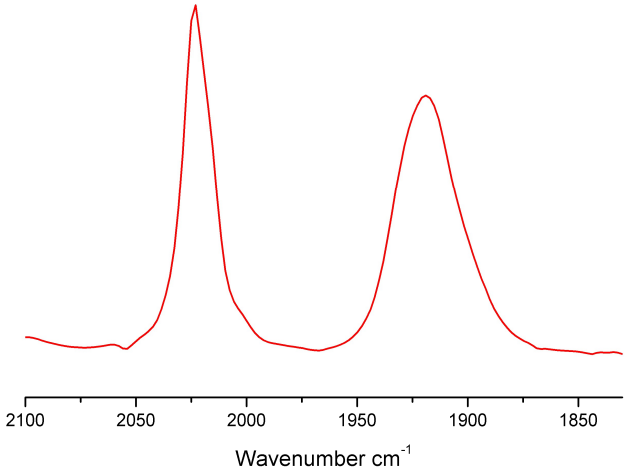
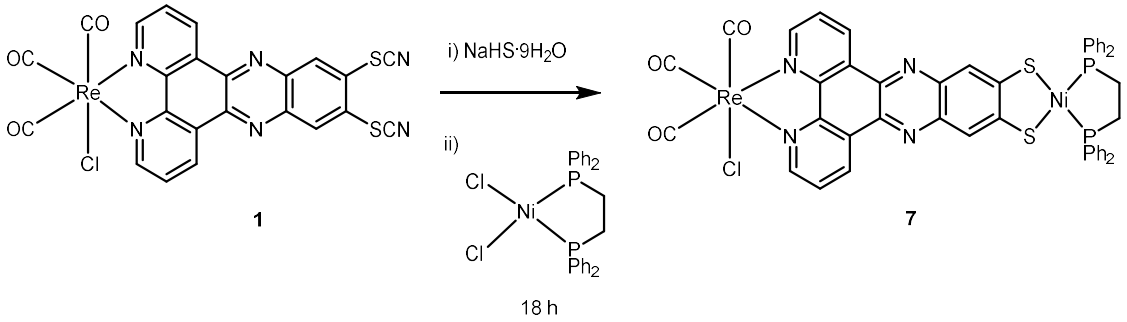


Figure 5.13: The IR spectrum of [Ni(ReCl(CO)$_3$dppz(S)$_2$)dppe].

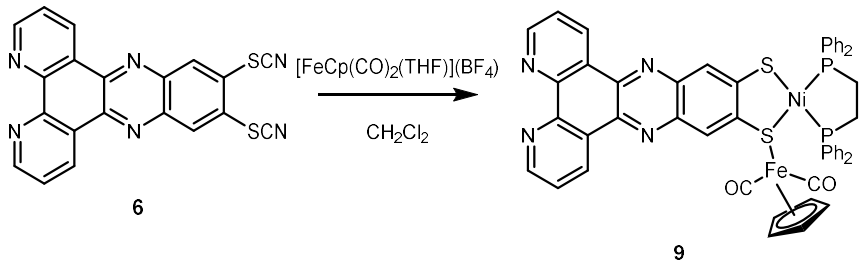
5.6.4 Attempted synthesis of [Ni(ReCl(CO)$_3$dppz(S)$_2$)dppe]: Route B



Scheme 5.13: Attempted synthesis of {Ni[ReCl(CO)$_3$dppz(S)$_2$)](dppe)} *via* route B.

Given the difficulties in isolating {Ni[ReCl(CO)$_3$(dppz(S)$_2$)](dppe)} through route A (Section 5.6.3) we investigated the coordination of a preformed [ReCl(CO)$_3$(dppz(S)$_2$)] unit to a [Ni(dppe)$_2$]$^{2+}$ fragment. [ReCl(CO)$_3$(dppz(SCN)$_2$)] was added to a solution of NaSH in methanol and heated to 55 °C for 24 h. The vivid purple solution was reduced under vacuum and a solution of [Ni(dppe)Cl$_2$] in CH_2Cl_2 was added dropwise at room temperature and the reaction mixture was stirred for 18 h. The solvent was removed under vacuum to give a red solid. Whilst the ^{1}H-NMR spectra of the crude {Ni[ReCl(CO)$_3$(dppz(S)$_2$)](dppe)} product contained peaks consistent with the data collected above for {Ni[ReCl(CO)$_3$(dppz(S)$_2$)](dppe)} *via* route A (8.84 8.51, 7.82, 7.62-7.41 and 2.40 ppm) and exhibited a feature at 54.7 ppm in the ^{31}P-NMR spectrum, the target molecule could not be identified by ES or MALDI mass spectrometry. The purification of {Ni[ReCl(CO)$_3$(dppz(S)$_2$)](dppe)} was attempted by recrystallisation from a solution of the product in CH_2Cl_2 using pentane, hexane, methanol and diethyl ether as anti-solvents. However, crystals suitable for X-ray diffraction could not be obtained and elemental analysis confirmed the product was not pure.

5.6.5 Attempted synthesis of [Ni(dppz(S)$_2$)(dppe)FeCp(CO)$_2$]



Scheme 5.14: The attempted synthesis of [Ni(dppz(S)$_2$)(dppe)FeCp(CO)$_2$].

The reaction between [Ni(dppz(S)$_2$)(dppe)] and [FeCp(CO)$_2$(THF)](BF$_4$) was carried out in an attempt to produce a [NiFe] compound containing a dppz dithiolate ligand as an analogue of the active site of [NiFe] hydrogenase. [FeCp(CO)$_2$(THF)][BF$_4$] was employed as for reactions involving [Ni(q^{6,7}dt^{Et,Et})(dppe)] and [Ni(q^{6,7}dt^{H,tBu})(dppe)](Chapter 4, Section 4.7.5) that formed [Ni(q^{6,7}dt^{Et,Et})(dppe)FeCp(CO)$_2$][BF$_4$] and [Ni(q^{6,7}dt^{H,tBu})(dppe)FeCp(CO)$_2$][BF$_4$], respectively. The reaction of [Ni(dppz(S)$_2$)(dppe)] and [FeCp(CO)$_2$(THF)][BF$_4$] (1:1) in CH_2Cl_2 at room temperature was attempted (Scheme 5.17). The reaction mixture was stirred for up

to 120 h and the progress of the reaction followed by solution IR spectroscopy. The IR spectra showed no changes in the ν(CO) stretches associated with the $[FeCp(CO)_2(THF)]^+$ unit suggesting no reaction took place.

5.7 Conclusion

This chapter describes three different approaches that have been investigated in an attempt to synthesise a novel [NiFe] catalyst incorporating one or two conjugated photosensitiser units. The first step is common to all three approaches and involves the synthesis of a novel dithiol substituted dppz ligand. This was achieved through the reduction of the known dithiocyanate substituted dppz compound with NaSH in methanol. This synthetic route was achieved through the adaptation of the known synthesis of a quinoxaline dithiolate compound (Scheme 5.2).[14,20]

The first strategy involved an adaptation of the conditions used by Wang *et al.* in their synthesis of $[Ni(L^A)Fe_2(CO)_6]$.[11] The attempted synthesis of $\{Ni[(ReCl(CO)_3)_2(dppz(S)_2)]_2Fe_2(CO)_6\}$ involved the reaction of $[ReCl(CO)_3(dppz(SH)_2)]$ with $Ni(OAc)_2$ and diiodopropane in methanol in an attempt to isolate $\{Ni[(ReCl(CO)_3)_2(p\text{-}dppz(S)_2]\}$. This reaction gave an insoluble solid with spectroscopic results suggesting that the Re centre was displaced and polymerisation had occurred.

The second strategy involved the attempted preparation of $[Ni(dppz(S)_2)]$ by the adaption of the methodologies Das *et al.*[16] and Wang *et al.*[11] used to synthesise $q^{6,7}dt^{2-}$ and $[Ni(L^A)]$, respectively. Whilst the ^{1}H-NMR spectroscopic results were encouraging, pure $[Ni(dppz(S)_2)_2]$ could not be isolated. The complexation of two $\{ReCl(CO)_3\}$ fragments was attempted and the reaction was followed by IR spectroscopy. These results and ^{1}H-NMR spectroscopic measurements provide some evidence for the formation of $\{Ni[(ReCl(CO)_3)_2(p\text{-}dppz(S)_2)]\}$ but pure compound could not be isolated.

The crude reaction mixture from the $\{Ni[(ReCl(CO)_3)_2(p\text{-}dppz(S)_2)]\}$ was used in an attempt to synthise the desired $\{Ni[(ReCl(CO)_3)_2(p\text{-}dppz(S)_2)]Fe_2(CO)_6\}$ product. A variety of conditions were explored including stirring the reaction mixture at room temperature, heating the reaction mixture at reflux and in a microwave using ethanol and CH_2Cl_2 as solvents. IR spectroscopic results suggest

that no reaction takes place and we were unable to isolate the target molecule using this synthetic method.

Throughout this work it appears that the target Ni^{II} and [NiRe] complexes may have been synthesised but their low solubility in a wide range of solvents hinders their purification, characterisation and potentially their reaction with $Fe_3(CO)_{12}$.

Given the apparent insolubilities of the compounds investigated in approaches A and B we moved attention to the synthesis of compounds containing the {Ni[ReCl(dppz(S)$_2$)(CO)$_3$](dppe)FeCp(CO)$_2$} cation (Figure 5.9). We were able to isolate and crystallographically characterise [Ni(dppz(S)$_2$)(dppe)]. The X-ray crystal structure shows coordination of the Ni^{II} centre to the dithiolate donors of the $[dppz(S)_2]^{2-}$ ligand and DFT calculations suggest that [Ni(dppz(S)$_2$)(dppe)] exhibits similar electronic structure properties to those of the of [Ni($q^{6,7}dt^{R1,R2}$)(dppe)] series of compounds (Chapter Three). Preliminary attempts to bind [Ni(dppz(S)$_2$)(dppe)] to a $[FeCp(CO)_2]^+$ fragment were unsuccessful.

5.8 Future work

Recently, it has been shown that the dinuclear Ru–M complexes, $[(bpy^{tb})_2Ru(tpphz)MCl_2]^{2+}$ (bpy^{tb} = 4,4'-di-tert-butyl-2,2'-bipyridin, tpphz = tetrapyrido[3,2-*a*:2'3'-*c*:3'',2''-*h*:2''',3'''-*j*]phenazine, M = Pd, Pt, Figure 5.14) are capable of forming H_2 under irradiation with visible light in the presence of an electron donor.[21]

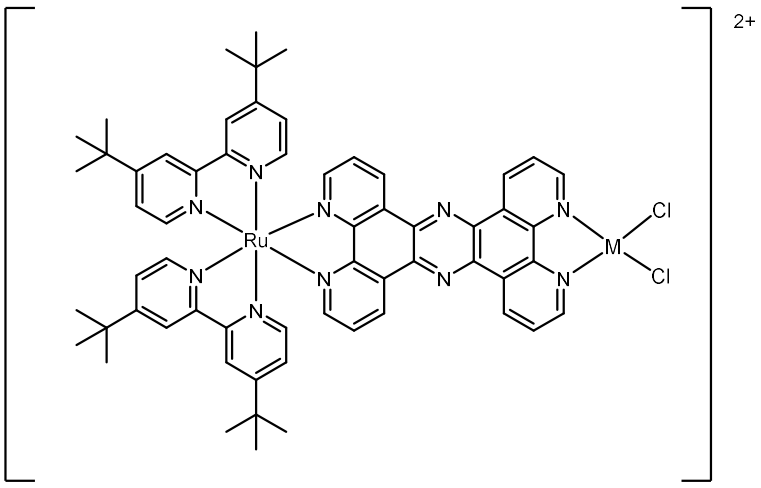


Figure 5.14: The structure of $[(bpy^{tb})_2Ru(tpphz)MCl_2]^{2+}$ (M = Pd or Pt).[21]

The incorporation of a $[(bpy^{tb})_2Ru]^{2+}$ unit as the photosensitiser provides an alternative to the $[ReCl(CO)_3]$ units used in this work. While $[(bpy^{tb})_2Ru]^{2+}$ units do not have the advantage of containing CO groups as spectroscopic probes for future time-resolved IR spectroscopic studies of the catalytic mechanism, the substitution of $\{(bpy^{tb})_2Ru\}^{2+}$ units in place of $\{ReCl(CO)_3\}$ may improve the solubility of the resulting complexes. Thus $\{Ni[(bpy^{tb})_2Ru\ dppz(S)_2]_2Fe_2(CO)_6\}^{4+}$ (Figure 5.15) could serve as a potential target in future investigations.

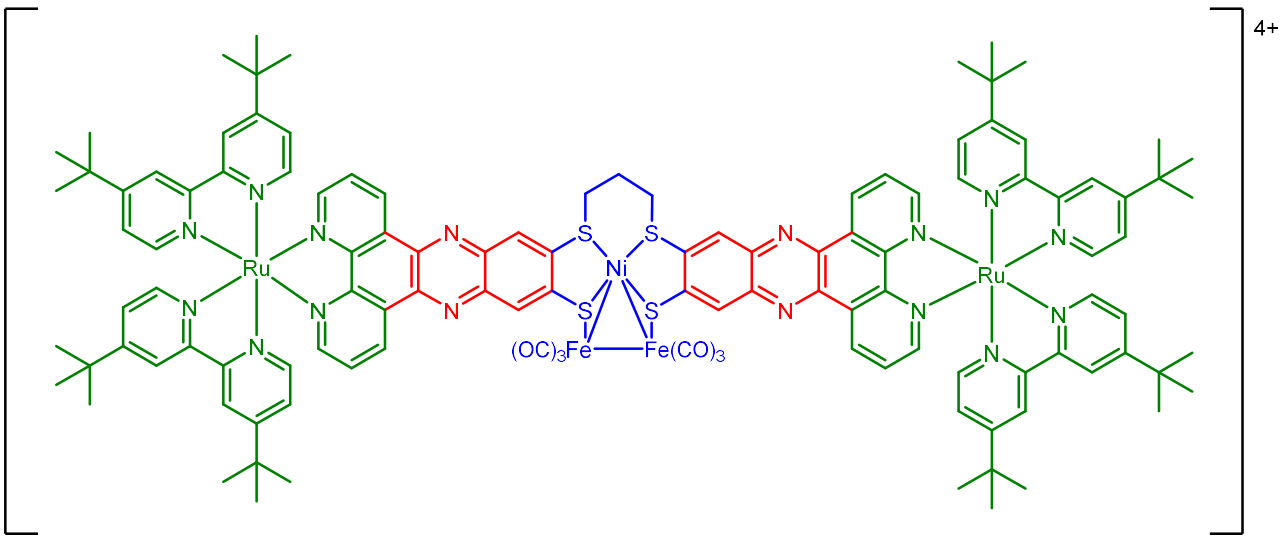


Figure 5.15: Proposed new target $\{Ni[(bpy^{tb})_2Ru\ dppz(S)_2]_2Fe_2(CO)_6\}^{4+}$.

5.9 Experimental

1,10-Phenanthroline-5,6-dione,[17] 4,5-thiocynanatobenzene-1,2-diamine,[18] dppz(SCN)$_2$[13] and [ReCl(CO)$_3$(dppz(SCN)$_2$)][13] were prepared according to literature methods.

5.9.1 The Attempted Synthesis of [ReCl(CO)$_3$(dppz(H)$_2$)] using Na$_2$S·9H$_2$O in water

Typical Procedure: A solution of [ReCl(CO)$_3$(dppz(SCN)$_2$)] (100 mg, 0.14 mmol) and Na$_2$S·9H$_2$O (154 mg, 0.64 mmol) in water (50 mL) was stirred at 70-80 °C for 2 h. Once the reaction mixture was cooled to room temperature, HCl (10 % in water, 20 mL) was added dropwise. The precipitate was collected by filtration as a brown powder. The spectroscopic data for the isolated material was inconclusive.

5.9.2 The Synthesis of Crude [ReCl(CO)$_3$(dppz(SH)$_2$)]

Typical Procedure: A solution of NaSH·9H$_2$O (83.4 mg, 0.32 mmol) in methanol (50 mL) was added to [ReCl(CO)$_5$(dppz(SCN)$_2$)] (50.0 mg, 0.07 mmol). The resulting mixture was stirred at 55 °C for 16 h. The reaction mixture was cooled to room temperature. HCl (10% in water, 20 mL) was added dropwise to give a precipitate. The precipitate was collected using a centrifuge and washed with methanol (3 x 5 mL) to give a brown powder (30.0 mg, 0.05 mmol, 66 %).

MS (ES$^-$) m/z: 650.6 [M-H]. IR (CH$_2$Cl$_2$): ν_{CO} 2519 (s), 2053 (s), 1983 (s), 1885 (s). ^{1}H NMR (400 MHz, DMSO, 298 K): δ_H 9.84 (2H, dd, J = 2 Hz, 8 Hz, ArH), 9.58 (2H, dd, J = 2 Hz, 5 Hz,ArH), 9.00 (2H, s, ArH), 8.30 (2H, dd, J = 5 Hz, 8 Hz,ArH). ^{13}C NMR δ_C (100 MHz, (CD$_3$)$_2$SO, 298 K): 153.32 (Ar-C), 149.97 (Ar-C), 139.31 (Ar-C), 137.96 (Ar-C), 134.11 (Ar-C), 132.32 (Ar-C), 130.65 (Ar-C), 129.63 (Ar-C), 121.50 (Ar-C). Elemental analysis found (calculated for C$_{21}$H$_{10}$ClN4O$_3$ReS$_2$) C 41.21 (38.68), H 2.81 (1.55), N 9.87 (8.59) %.

5.9.3 The Attempted Synthesis of {Ni[(ReCl(CO)$_3$)$_2$(p-dppz(S)$_2$)]}

Typical Procedure: A solution of NaOMe (5.51 mg, 0.10 mmol) and [ReCl(CO)$_5$(dppz(SH)$_2$)] (30 mg, 0.045 mmol) in methanol (50 mL) was stirred at room temperature for 1 h. Ni(OAc)$_2$·4H$_2$O (5.47 mg, 0.023 mmol) was added in methanol (20 mL) and the mixture was stirred for a further hour. 1,3-Diiodopropane

(0.01 mL, 0.087 mmol) in methanol (1 mL) was added dropwise and the mixture was stirred for 14 h at room temperature in the dark. The resulting precipitate was collected by filtration as a black solid (20.0 mg, 0.01 mmol, 60.8 %).

Elemental analysis, found (calculated for $C_{46}H_{26}Cl_2N_8NiO_6Re_2S_4$) C 45.11 (38.99), H 2.65 (1.85), N 6.46 (7.91) %.

5.9.4 The Attempted Synthesis of [Ni(p-dppz(S)$_2$)]

Typical Procedure: A solution of $NaSH{\cdot}9H_2O$ (626 mg, 2.50 mmol) in methanol (50 mL) was added to dppz(SCN)$_2$ (500 mg, 1.26 mmol). The resulting mixture was stirred at 55 °C for 16 h. Once the reaction mixture had cooled to room temperature the mixture was filtered. $Ni(OAc)_2{\cdot}4H_2O$ (150 mg, 0.63 mmol) in methanol (100 mL) was added dropwise and the solution was stirred for 30 mins. 1,3-Diiodopropane (0.07 mL, 0.63 mmol) in methanol (1 mL) was added dropwise and the mixture was stirred for 14 h at room temperature in the dark. The resulting mixture was reduced under vacuum and washed with pentane (3 x 20 mL) to give a dark green solid (1.30 g, 0.92 mmol, 73 %).

^{1}H NMR (400 MHz, $(CD_3)_2SO$, 298 K): δH 9.49 (4H, dd, *J* = 2 Hz, 8 Hz, ArH), 9.10 (4H, dd, *J* = 2 Hz, 3 Hz, ArH), 7.78 (4H, s, ArH), 7.70 (4H, dd, *J* = 3 Hz, 8 Hz, ArH). 3.13 (2H, t, *J* = 8 Hz CH_2), 2.92 (2H, q, *J* = 8 Hz CH_2). Elemental analysis found (calculated for $C_{39}H_{22}N_8NiS_4$) C 56.71 (59.33), H 1.73 (2.81), N 11.76 (14.19) %.

5.9.5 The Synthesis of Crude {Ni[(ReCl(CO)$_3$)$_2$(p-dppz(S)$_2$)]}

Typical Procedure: A mixture of [Ni(dppz(S)$_2$)$_2$] (100.0 mg, 0.12 mmol) and $ReCl(CO)_5$ (86 mg, 0.24 mmol) in toluene (20 mL) was heated to reflux for 24 h. The reaction mixture was cooled to room temperature and the precipitate was collected by filtration and washed with toluene (2 x 10 mL) to give a fine black powder.

IR (CH_2Cl_2): ν_{CO} 2049 (s), 1954 (s). ^{1}H NMR (400 MHz, DMSO, 298 K): δH 9.53 (4H, t, ArH), 9.13 (4H, d, ArH), 7.74 (4H, m, ArH), 7.81 (4H, s, ArH), 3.17 (4H, t, CH_2), 2.98 (4H, q, CH_2). Elemental analysis, found (calculated for $C_{46}H_{26}Cl_2N_8NiO_6Re_2S_4$) C 41.07 (38.99), H 2.49 (1.85), N 9.25 (7.91) %.

5.9.6 The Attempted Synthesis of $[Ni(dppz(S)_2)_2Fe_2(CO)_6]$

Method One

In a typical procedure, $[Ni(dppz(S)_2)_2]$ (50.0 mg, 0.06 mmol) and $Fe_3(CO)_{12}$ (30.0 mg, 0.06 mmol) were stirred in ethanol or CH_2Cl_2 (10 mL) at room temperature or under reflux for up to 24 h. The reactions were monitored using *ex situ* infrared spectroscopy and by mass spectrometry. No consistent spectroscopic data could be obtained for a [NiFe]-containing compound.

Method Two

Typical Procedure: A mixture of $[Ni(dppz(S)_2)_2]$ (50.0 mg, 0.06 mmol) and $Fe_3(CO)_{12}$ (30.0 mg, 0.06 mmol) in CH_2Cl_2 (3 mL) were stirred in a 10 mL microwave reactor vessel. In the microwave reactor, the reaction mixture was heated at 95 °C (100 W, maximum 95 psi) for up to 60 mins. The reactions were monitored using *ex-situ* infrared spectroscopy and mass spectrometry. No consistent spectroscopic data could be obtained for [NiFe]-containing compound.

5.9.7 The Synthesis of Crude $[Ni(dppz(S)_2)(dppe)]$

A solution of $NaSH{\cdot}9H_2O$ (83.4 mg, 0.32 mmol) in methanol (50 mL) was added to $[Re(CO)_5(dppz(SCN)_2)]$ (50.0 mg, 0.07 mmol). The resulting mixture was stirred at 55 ^{0}C for 16 h. Once the reaction mixture was cooled to room temperature a solution of $[Ni(dppe)Cl_2]$ (169 mg, 0.32 mmol) in CH_2Cl_2 (20 mL) was added to the reaction mixture drop wise. The reaction was stirred for 3 h at room temperature. The solvent was removed under reduced pressure to give a red solid. $[Ni(dppz(S)_2)(dppe)]$ was recrystallisation from layering dichloromethane/pentane.

MS (ESI^+) m/z: 802.09 $[M+H]^+$. ^{1}H NMR (400 MHz, $(CD_3)_2SO$, 298 K): δ_H 9.47 (2H, dd, J = 2 Hz, 8 Hz, ArH), 9.12 (2H, dd, J = 2 Hz, 5 Hz,ArH), 8.09 (2H, s, ArH), 8.30 (2H, dd, J = 5 Hz, 8 Hz,ArH). 7.90-781 (10H, m, ArH), 7.64 -7.51 (10H, m, ArH) 2.90 (4H, d, J = 5 Hz CH_2). ^{13}C NMR (400 MHz, $(CD_3)_2SO$, 298 K): δ_C 152.8 (Ar-C), 149.2 (Ar-C), 137.7 (Ar-C), 133.5 (Ar-C), 132.1 (Ar-C), 131.6 (Ar-C), 129.8 (Ar-C), 127.3 (Ar-C), 126.8 (Ar-C), 123.8 (Ar-C), 121.3 (Ar-C), 20.2 (CH_2). ^{31}P NMR (400 MHz, $(CD_3)_2SO$, 298 K): δ_P 59.66 (s). Elemental analysis found (calculated for $C_{44}H_{32}N_4NiP_2S_2$): C 63.91 (65.93), H 4.68 (4.02), N 6.03 (6.99) %.

5.9.8 The attempted synthesis of {Ni[ReCl(CO)$_3$(dppz(S)$_2$)](dppe)}: Method 1

Typical Procedure: A mixture of [Ni(dppz(S)$_2$)(dppe)] (100 mg, 0.12 mmol) and ReCl(CO)$_5$ (86.0 mg, 0.24 mmol) in toluene (20 mL) was heated to reflux for 24 h. The reaction mixture was cooled to room temperature and the precipitate was collected by filtration to give a fine black powder.

IR (CH_2Cl_2): ν_{CO} 2023 (s), 1917 (s), ^{1}H NMR (400 MHz, $(CD_3)_2SO$, 298 K): δ_H 9.62 (2H, dd, ArH), 9.38 (2H, dd, ArH), 8.12 (2H, s, ArH), 7.95 (2H, dd, ArH). 7.88-7.79 (10H, m, ArH), 7.54 -7.43 (10H, m, ArH) 2.90 (4H, d, CH_2). ^{31}P NMR (400 MHz, $(CD_3)_2SO$, 298 K): δ_P 54.7 (s). Elemental analysis calculated for $C_{44}H_{32}N_4NiP_2S_2$: C 61.35(65.93), H 3.17 (4.02), N 5.82 (6.99) %.

5.9.9 The attempted synthesis of {Ni[ReCl(CO)$_3$(dppz(S)$_2$)](dppe)}: Method 2

Typical Procedure: A solution of $NaSH{\cdot}9H_2O$ (83.4 mg, 0.32 mmol) in methanol (50 mL) was added to [ReCl(CO)$_3$(dppz(SCN)$_2$)] (50.0 mg, 0.07 mmol). The resulting mixture was stirred at 55 °C for 16 h. Once the reaction mixture was cooled to room temperature a solution of [Ni(dppe)Cl_2] (168 mg, 0.32 mmol) in CH_2Cl_2 (20 mL) was added to the reaction mixture drop wise. The reaction was stirred for 18 h at room temperature. The solution was removed in *vacuo* to give a red solid. The product was recrystallised from a solution of CH_2Cl_2 by layering with pentane.

IR (CH_2Cl_2): ν_{CO} 2023 (s), 1917 (s), ^{1}H NMR (400 MHz, $(CD_3)_2SO$, 298 K): δ_H 9.62 (2H, dd, ArH), 9.38 (2H, dd, ArH), 8.12 (2H, s, ArH), 7.95 (2H, dd, ArH). 7.88-7.79 (10H, m, ArH), 7.54 -7.43 (10H, m, ArH) 2.90 (4H, d, CH_2). ^{31}P NMR (400 MHz, $(CD_3)_2SO$, 298 K): δ_P 59.1 (s). Elemental analysis calculated for $C_{47}H_{32}ClN_4NiO_3P_2ReS$: C 61.84 (50.99), H 3.81 (2.91), N 5.90 (5.06) %.

5.10 References

1 L. Sun, B. Akermark and S. Ott, *Coord. Chem. Rev.*, 2005, **249**, 1653–1663.

2 P. A. Summers, J. A. Calladine, F. Ghiotto, J. Dawson, X.-Z. Sun, M. L. Hamilton, M. Towrie, E. S. Davies, J. McMaster, M. W. George and M. Schröder, *Inorg. Chem.*, 2016, **55**, 527–536.

3 P. A. Summers, J. Dawson, F. Ghiotto, M. W. D. Hanson-Heine, K. Q. Vuong, E. S. Davies, X.-Z. Sun, N. A. Besley, J. McMaster, M. W. George and M. Schröder, *Inorg. Chem.*, 2014, **53**, 4430–4439.

4 H. D. Stoeffler, N. B. Thornton, S. L. Temkin and K. S. Schanze, *J. Am. Chem. Soc.*, 1995,

117, 7119–7128.

5 M. R. Waterland, K. C. Gordon, J. J. McGarvey and P. M. Jayaweera, *Dalt. Trans.*, 1998, 609–616.

6 B. Schäfer, H. Görls, M. Presselt, M. Schmitt, J. Popp, W. Henry, J. G. Vos and S. Rau, *Dalton Trans.*, 2006, 2225–31.

7 A. Friedman, C. . Kumar, N. . Turro and J. . Barton, *Nucleic Acids Res.*, 1991, **19**, 2595–2602.

8 K. E. Erkkila, D. T. Odom and J. K. Barton, *Chem. Rev.*, 1999, **99**, 2777–2796.

9 J. Fees, W. Kaim, M. Moscherosch, W. Matheis, J. Klima, M. Krejcik and S. Zalis, *Inorg. Chem.*, 1993, **32**, 166–174.

10 P. Summers, The University of Nottingham, 2013.

11 Q. Wang, J. E. Barclay, A. J. Blake, E. S. Davies, D. J. Evans, A. C. Marr, E. J. L. McInnes, J. McMaster, C. Wilson and M. Schröder, *Chem. Eur. J.*, 2004, **10**, 3384–3396.

12 C. M. Dupureur and J. K. Barton, *Inorg. Chem.*, 1997, **36**, 33–43.

13 M. G. Fraser, A. G. Blackman, G. I. S. Irwin, C. P. Easton and K. C. Gordon, *Inorg. Chem.*, 2010, **49**, 5180–5189.

14 G. Durgaprasad, R. Bolligarla and S. K. Das, *J. Organomet. Chem.*, 2012, **706**–**707**, 37–45.

15 R. Bolligarla, S. N. Reddy, G. Durgaprasad, V. Sreenivasulu and S. K. Das, *Inorg. Chem.*, 2013, **52**, 66–76.

16 R. Bolligarla, G. Durgaprasad and S. K. Das, *Inorg. Chem. Commun.*, 2011, **14**, 809–813.

17 M. Yamada, Y. Tanaka, Y. Yoshimoto, S. Kuroda and I. Shimao, *Bull. Chem. Soc. Jpn.*, 1992, **65**, 1006–1011.

18 J. L. Brusso, O. P. Clements, R. C. Haddon, M. E. Itkis, A. A. Leitch, R. T. Oakley, R. W. Reed and J. F. Richardson, *J. Am. Chem. Soc.*, 2004, **126**, 8256–8265.

19 A. Perra, Q. Wang, A. J. Blake, E. S. Davies, J. McMaster, C. Wilson and M. Schröder, *Dalton Trans.*, 2009, **373**, 925–931.

20 G. Durgaprasad, R. Bolligarla and S. K. Das, *J. Organomet. Chem.*, 2011, **696**, 3097–3105.

21 M. G. Pfeffer, B. Schäfer, G. Smolentsev, J. Uhlig, E. Nazarenko, J. Guthmuller, C. Kuhnt, M. Wächtler, B. Dietzek, V. Sundström and S. Rau, *Angew. Chem. Int. Ed. Engl.*, 2015, **54**, 5044–8.

Conclusions

In this thesis the design, synthesis and characterisation of novel Ni^{II} and [NiFe] complexes that have potential as functional analogues of the active site of the [NiFe] hydrogenase has been described. [NiFe] and Ni^{II} complexes can exhibit reduction processes that are located principally at the metal centres[1–5] and for these systems, the removal of electron density from metal centres can shift the potential of a formal Ni^{II}/Ni^{I} process to more positive potentials and reducing the overpotential required for the catalytic reduction of H^+. Our strategy has been to incorporate electron withdrawing quinoxaline rings into the ligand framework and which may also provide protonation and/or proton relay sites close to the Ni^{II} core and raise the potential of the formal Ni^{II}/Ni^{I} couple. We incorporated quinoxaline rings into complexes possessing NiS_4 (Chapter 2) and NiS_2P_2 (Chapter 3) cores.

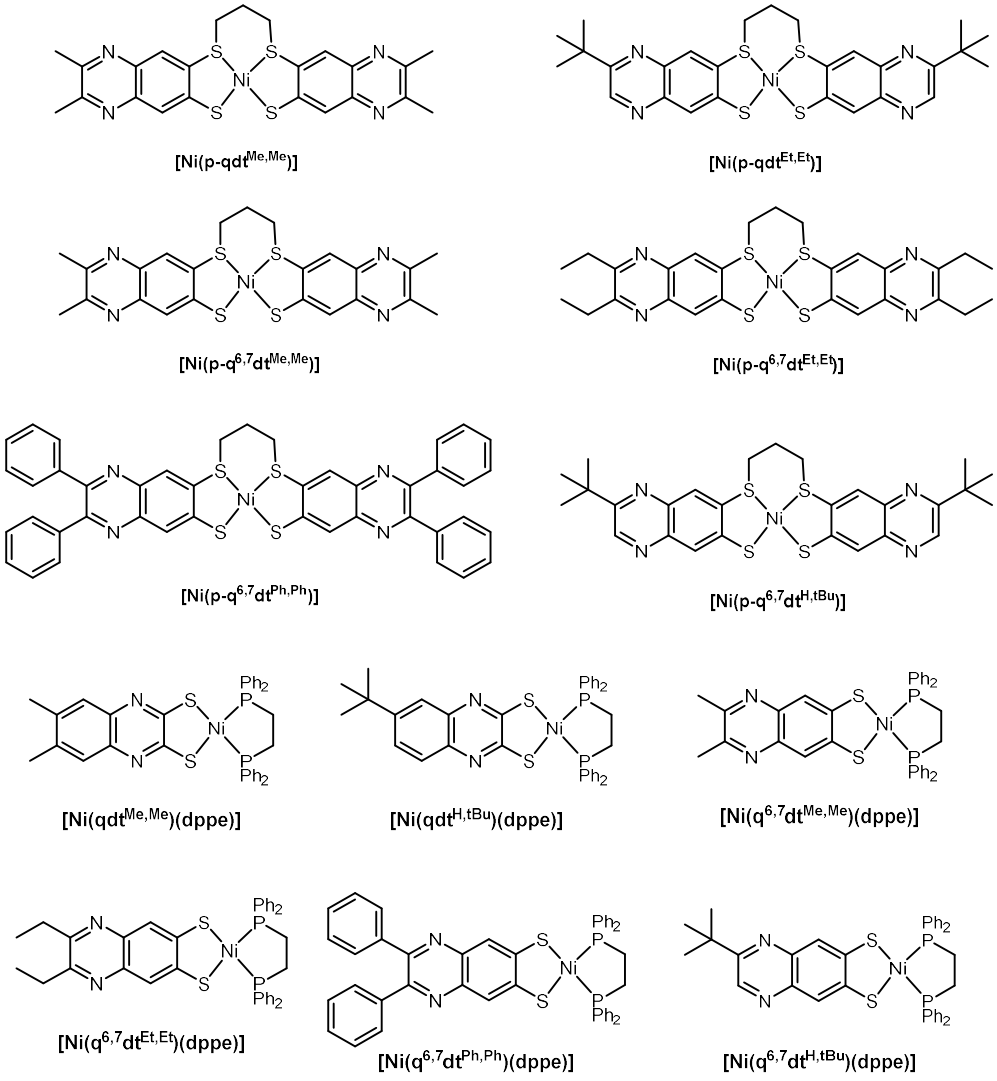


Figure 1: The Ni^{II} quinoxaline-based complexes synthesised in Chapters Two and Three.

Attempts to isolate [Ni(p-qdt^{R1,R2})] (R^1 = R^2 = Me; R^1 = H, R^2 = ^{t}Bu) proved challenging and was hindered by low yielding reactions and difficulties in purifying products. In contrast our approach of developing synthetic routes to Ni^{II} complexes *via* quinoxaline-6,7-dithiol precursors, in which the quinoxaline N atoms are further removed from the metal centre, allowed access to a range of [Ni(p-q^{6,7}dt^{R1,R2})] (R^1 = R^2 = Me, Et, Ph; R^1 = H, R^2 = ^{t}Bu) complexes. The complexes were characterised by X-ray crystallography, electrochemistry, spectroelectrochemistry and the reduction products characterised by EPR spectroscopy, where appropriate. These measurements, supported by the results from DFT calculations suggest that these complexes support a formal $Ni^{II/I}$ reduction process that is localised at the NiS_4 unit. Electrocatalytic studies show that [Ni(p-q^{6,7}dt^{Et,Et})], [Ni(q^{6,7}dt^{H,tBu})] and [NiL^A] are potential electrocatalysts for H^+ reduction that takes place at catalytic potentials at *ca.* -1.7 V *vs* Fc^+/Fc. Each complex appears to be relatively robust being stable in acid for up to 24 h. Preliminary screening of [Ni(p-q^{6,7}dt^{Et,Et})], [Ni(p-q^{6,7}dt^{H,tBu})] and [NiL^A] to [Ni(L^A)$Fe_2(CO)_6$], suggest that [Ni(p-q^{6,7}dt^{Et,Et})], [Ni(p-q^{6,7}dt^{H,tBu})] and [NiL^A] demonstrate higher catalytic activities (-2.15, -1.80 and – 2.15 A x 10^{-4}, respectively) than [Ni(L^A)$Fe_2(CO)_6$] (-0.73 A x 10^{-4}). Previous research has focussed on multinuclear [NiFe]-containing clusters *e.g.* [Ni(L^A)$Fe_2(CO)_6$], inspired by the active site of the [NiFe] hydrogenases. The results presented in this thesis demonstrate that mononuclear NiS_4 complexes should not be discounted as catalysts for the production of H_2 and that the incorporation of quinoxaline rings within the ligand framework may also provide a route to increase the potential of the $Ni^{II/I}$ redox couple by *ca.* 0.2 V.

Given that the monomeric NiS_4 complexes described in Chapter 2 appear to support the catalytic production of H_2, the syntheses and characterisations of Ni^{II} complexes containing 1,2-bis(diphenylphosphino)ethane (dppe) and one quinoxaline-dithiolate ligand were investigated. We found that the syntheses and purifications of these NiS_2P_2 complexes was relatively facile when compared to the syntheses of the NiS_4 complexes. [Ni(qdt^{R1,R2})(dppe)]$^{0/-}$ (R^1 = R^2 = Me; R^1 = H, R^2 = ^{t}Bu) and [Ni(q^{6,7}dt^{R1,R2})(dppe)]$^{0/-}$ (R^1 = R^2 = Me, Et, Ph; R^1 = H, R^2 = ^{t}Bu) were characterised by X-ray diffraction, electrochemistry, UV/vis spectroelectrochemistry and EPR spectroscopy as appropriate. This combination of techniques, together with DFT

calculations enabled the unambiguous assignment of the first reduction process to a formal $Ni^{II/I}$ couple. Catalytic studies showed that [Ni($qdt^{R1,R2}$)(dppe)] (R^1 = R^2 = Me; R^1 = H, R^2 = ^{t}Bu) and [Ni($q^{6,7}dt^{R1,R2}$)(dppe)] (R^1 = R^2 = Me, Et, Ph; R^1 = H, R^2 = ^{t}Bu) are potential electrocatalysts for H_2 production. Whilst screening of the catalytic activity of [Ni($q^{6,7}dt^{Me,Me}$)(dppe)] to [Ni(L^A)$Fe_2(CO)_6$] suggest that the catalytic activity of [Ni($q^{6,7}dt^{Me,Me}$)(dppe)] (-1.91 A x 10^{-4}) is comparable to the catalytic activity of [Ni(L^A)$Fe_2(CO)_6$] (-1.43 A x 10^{-4}), the catalytic process occurs at more negative potentials. Nevertheless the long term stabilities of [Ni($qdt^{R1,R2}$)(dppe)] and [Ni($q^{6,7}dt^{R1,R2}$)(dppe)], together with their ease of synthesis, when compared to [Ni(L^A)$Fe_2(CO)_6$], makes them excellent candidates for future investigations and developments as catalysts for the production of H_2.

In Chapter 4 the monomeric $Ni^{II}S_4$ and $Ni^{II}S_2P_2$ complexes synthesised in Chapters 2 and 3, respectively, were used as precursors to heteronuclear [NiFe]-containing complexes. Previous research at Nottingham has demonstrated that the coordination of a [Fe] fragment to a Ni^{II} centre can make the potential of the formal $Ni^{II/I}$ couple more positive by *ca.* 0.3 V. The syntheses of [Ni(p-$q^{6,7}dt^{R1,R2}$)$Fe_2(CO)_6$] and [Ni(p-$q^{6,7}dt^{R1,R2}$)FeCp$(CO)_2$](BF_4) (R^1 = R^2 = Me, Et, Ph; R^1 = H, R^2 = ^{t}Bu) were confirmed by FTIR spectroscopies and [Ni(p-$q^{6,7}dt^{Me,Me}$)$Fe_2(CO)_6$] was characterised by X-ray crystallography; [Ni(p-$q^{6,7}dt^{Me,Me}$)$Fe_2(CO)_6$] possesses a similar $NiFe_2$ structure as for [Ni(L^A)$Fe_2(CO)_6$].[6] Cyclic voltammetric studies of [Ni(p-$q^{6,7}dt^{Et,Et}$)$Fe_2(CO)_6$] and [Ni(p-$q^{6,7}dt^{H,tBu}$)$Fe_2(CO)_6$] undergo reduction processes that are *ca.* 0.25 V more positive than their respective Ni^{II} precursors and which are *ca.* 0.1 V more positive than that of [Ni(L^A)$Fe_2(CO)_6$]. However, the purification of [Ni(p-$q^{6,7}dt^{R1,R1}$)$Fe_2(CO)_6$] and [Ni(p-$q^{6,7}dt^{R1,R2}$)FeCp$(CO)_2$](BF_4) proved difficult and once isolated the complexes appeared to readily decompose in solution. Consequently we were unable to assess the catalytic activity of [Ni(p-$q^{6,7}dt^{R1,R2}$)$Fe_2(CO)_6$] and [Ni(p-$q^{6,7}dt^{R1,R2}$)FeCp$(CO)_2$](BF_4) towards the production of H_2.

Chapter Five describes attempts to synthesise Ni^{II} and [NiFe] complexes incorporating a photosensitiser unit, based on a dithiolate-substituted dipyridophenazine dppz (dppz$(S)_2$) ligand. We were able to prepare and structurally characterise [Ni(dppz$(S)_2$)(dppe)] that possesses a pendant bipydridyl unit within the

ligand framework for coordination to $[ReCl(CO)_3]$ or $[Ru(bipy)_2]^{2+}$-based fragments. IR and mass spectrometric evidence for the synthesis of $[ReCl(CO)_3(dppz(SH)_2)]$ provides encouragement that $[Ni(dppz(S)_2)(dppe)]$ may be coordinated to a photosensitizer, however a complete synthesis of $\{Ni[ReCl(CO)_3dppz(S)_2]_2Fe_2(CO)_6\}$ was unsuccessful.

The research accomplished in this thesis demonstrates that monomeric Ni^{II} complexes in S-rich coordination environments and that contain ligands that incorporate quinoxaline rings can catalyse the production of H_2. These monomeric NiS_4 and NiS_2P_2 complexes are excellent candidates for further study, notably in assessments of turnover number and quantifications of the H_2 produced as measured by gas chromatography.[7] The results described in this thesis also raise the question about the nature of the active sites of the [NiFe] hydrogenases and why Nature employs a bimetallic centre when it appears that a monomeric Ni^{II} centre in a S-rich coordination sphere is capable of supporting the catalytic production of H_2. Given that it appears that Fe-centre in the [NiFe] hydrogenases remain in a formal low-spin Fe^{II} state; the role of the Fe-centre may be to modulate the redox potential of the [NiFe] centre to ensure that catalysis occurs within the biological potential window.

Conclusion References

1 C. Tard and C. J. Pickett, *Chem. Rev.*, 2009, **109**, 2245–74.

2 B. E. Barton, C. M. Whaley, T. B. Rauchfuss and D. L. Gray, *J. Am. Chem. Soc.*, 2009, **131**, 6942–3.

3 B. E. Barton and T. B. Rauchfuss, *J. Am. Chem. Soc.*, 2010, **132**, 14877–14885.

4 S. Canaguier, M. Field, Y. Oudart, J. Pécaut, M. Fontecave and V. Artero, *Chem. Commun.*, 2010, **46**, 5876.

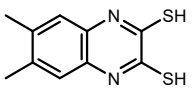
5 M. Rakowski DuBois and D. L. DuBois, *Chem. Soc. Rev.*, 2009, **38**, 62–72.

6 Q. Wang, J. E. Barclay, A. J. Blake, E. S. Davies, D. J. Evans, A. C. Marr, E. J. L. McInnes, J. McMaster, C. Wilson and M. Schröder, *Chem. Eur. J.*, 2004, **10**, 3384–96.

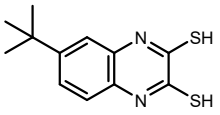
7 A. Perra, E. S. Davies, J. R. Hyde, Q. Wang, J. McMaster and M. Schröder, *Chem. Commun.*, 2006, **10**, 1103–5.

Appendix

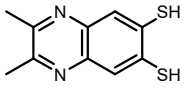
A.1 Ligands and complexes



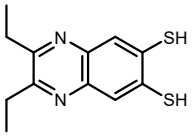
qdt^{Me,Me}H$_2$



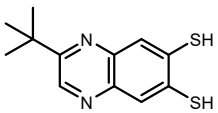
qdt^{H,tBu}H$_2$



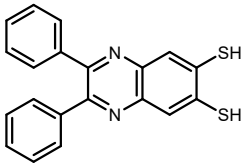
q^{6,7}dt^{Me,Me}H$_2$



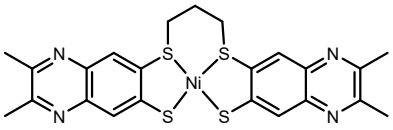
q^{6,7}dt^{Et,Et}H$_2$



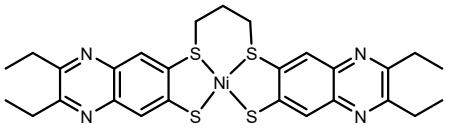
q^{6,7}dt^{H,tBu}H$_2$



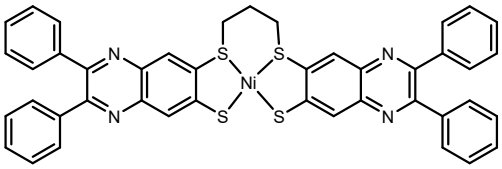
q^{6,7}dt^{Ph,Ph}H$_2$



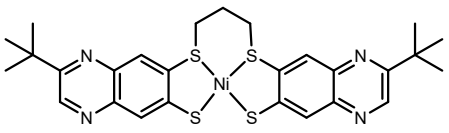
[Ni(p-q^{6,7}dt^{Me,Me})]



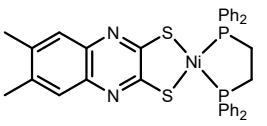
[Ni(p-q^{6,7}dt^{Et,Et})]



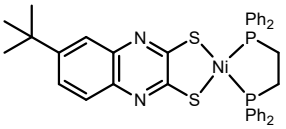
[Ni(p-q^{6,7}dt^{Ph,Ph})]



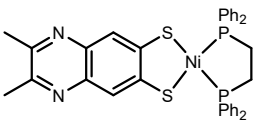
[Ni(p-q^{6,7}dt^{H,tBu})]



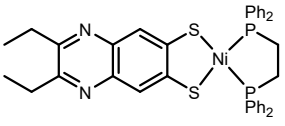
[Ni(qdt^{Me,Me})(dppe)]



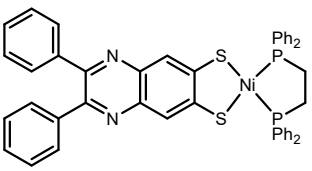
[Ni(qdt^{H,tBu})(dppe)]



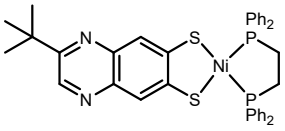
[Ni(q^{6,7}dt^{Me,Me})(dppe)]



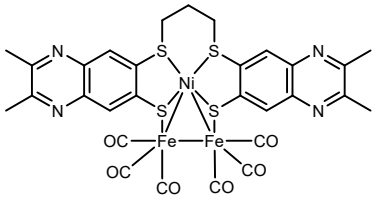
[Ni(q^{6,7}dt^{Et,Et})(dppe)]



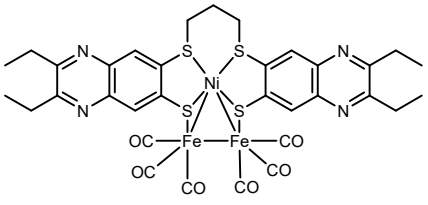
[Ni(q^{6,7}dt^{Ph,Ph})(dppe)]



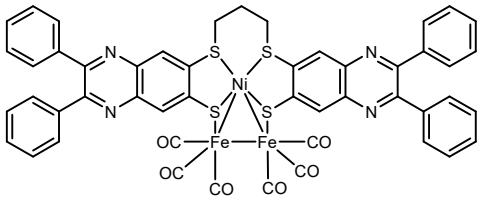
[Ni(q^{6,7}dt^{H,tBu})(dppe)]



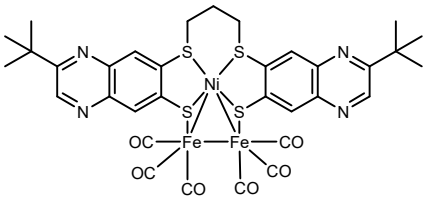
[Ni(p-q^{6,7}dt^{Me,Me})$_2$Fe$_2$(CO)$_6$]



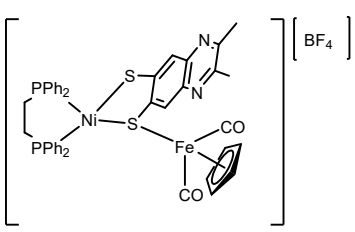
[Ni(p-q^{6,7}dt^{Et,Et})$_2$Fe$_2$(CO)$_6$]



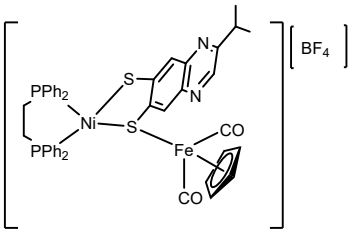
[Ni(p-q^{6,7}dt^{Ph,Ph})$_2$Fe$_2$(CO)$_6$]



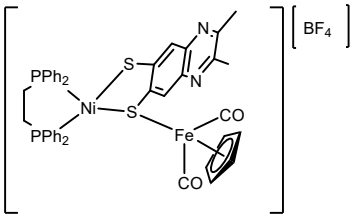
[Ni(p-q^{6,7}dt^{tBu,H})$_2$Fe$_2$(CO)$_6$]



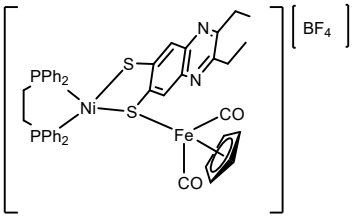
[Ni(qdt^{Me,Me})(dppe)FeCp(CO)][BF$_4$]



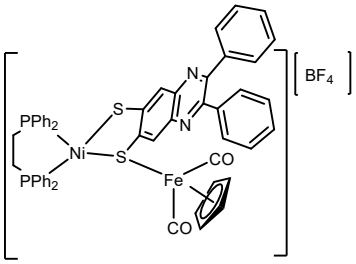
[Ni(qdt^{tBu,H})(dppe)FeCp(CO)][BF$_4$]



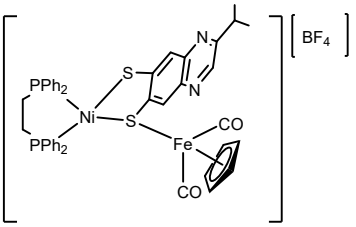
[Ni(q^{6,7}dt^{Me,Me})(dppe)FeCp(CO)][BF$_4$]



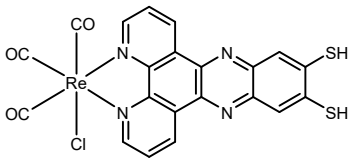
[Ni(q^{6,7}dt^{Et,Et})(dppe)FeCp(CO)][BF$_4$]



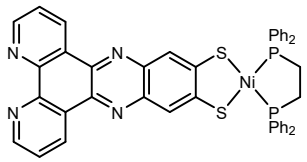
[Ni(q^{6,7}dt^{Ph,Ph})(dppe)FeCp(CO)][BF$_4$]



[Ni(q^{6,7}dt^{tBu,H})(dppe)FeCp(CO)][BF$_4$]



[Re(Cl(CO)$_3$dppz(SH$_2$)$_2$]



[Ni(dppz(S)$_2$(dppe)]

A.2 Experimental and technique details

Unless otherwise stated, the reagents were used as received from the suppliers (Sigma-Aldrich, Acros Organic and Fluka) and all the reactions, manipulations and transfers were performed under an inert atmosphere of pure argon using standard Schlenk techniques. Solvents were dried and degassed following standard procedures and stored under Ar in Young's ampoules over molecular sieves (pore

size 4 Å). Trifluoroacetic acid (TFA), $CDCl_3$, $(CD_3)_2SO$ and CD_2Cl_2 were obtained from SigmaAldrich, degassed with Ar, used without any further purification and the deuterated solvent was stored over molecular sieves (pore size 4 Å). The high-purity gas Ar was obtained from BOC gases and used without any further purification.

The ^{1}H and ^{13}C NMR spectra were recorded variously on a Bruker AV(III)400, Bruker AV400, Bruker DPX400 or Bruker AV(III)400 HD spectrometers all operating at 400.2 and 100.6 MHz, respectively, or a JEOL EX270 spectrometer operating at 270 and 68 MHz respectively; chemical shifts are quoted in parts per million and are relative to tetramethylsilane.

Infrared spectra were recorded on a Nicolet Avatar 360 FTIR spectrometer and solution infrared spectra were recorded using sealed solution cells with either CaF_2 or KBr windows. NMR spectra were recorded either on Bruker DPX300, DPX400 or AV400 spectrometers. ^{1}H decoupled ^{31}P-NMR spectra were referenced to 85% H_3PO_4. Mass spectra (ESI) were recorded by the Mass Spectrometry Service at the University of Nottingham.

ICP-OES data were recorded on a Perkin Elmer Optima 2000 Optical Emission Spectrometer. Elemental microanalyses were carried out variously using an Exeter Analytica CE-440 Elemental Analyzer by Tong Liu at The University of Nottingham and a Carlo Erba CE1108 Elemental Analyzer by Stephen Boyer at the Microanalysis Service, London Metropolitan University, U.K.

Electrochemical measurements were made using an Autolab PGSTAT302N potentiostat. All solutions were purged with a stream of Ar prior to use. Cyclic voltammograms were performed using a three-electrode system, with a glassy carbon working electrode (6.7 mm diameter), a Pt wire secondary electrode and a saturated Ag/AgCl reference electrode. Before each measurement, the glassy carbon working electrode was cleaned *via* a polishing pad. All potentials are referenced to the Fc^+/Fc couple that was used as an internal standard. Cyclic voltammograms were recorded for solutions of compound (*ca*. 1 mM) with $[N^nBu]_4[BF_4]$ (0.4 M) as supporting electrolyte. Assessments of electrochemical reversibility were made based on comparison of the magnitude of ΔE_p to that of the internal standard (Fc^+/Fc or $FeCp^*_2{}^+/FeCp^*_2$), the independence of E_p^a and E_p^c to scan rate, the ratio of i_p^a to

i_p^c and the proportionality of i_p^a and i_p^c to scan rate. Where appropriate the Nicholson equation (**1**) was employed to account for the sloping baseline of the voltammogram.

$$\frac{ipc}{ipa} = \frac{(ipc)0}{ipa} + \frac{(i\lambda)0 \times 0.485}{ipa} + 0.086$$

Equation 1*:* Nicholson Equation.[1]

Coulometric measurements were performed with an H-cell at 273 K in CH_2Cl_2 containing $[N^nBu_4][BF_4]$ (0.4 M); the cell consisted of a Pt/Rh gauze basket working electrode separated by a glass frit from a Pt/Rh gauze secondary electrode. The saturated Ag/AgCl reference electrode was placed at the centre of the working electrode and the solution was stirred rapidly during electrolysis using a magnetic stirring bar.

Cyclic voltammetry experiments for the screening of catalytic activity were conducted using a sealed single compartment electrochemical cell purged with Ar. Five additions of 0.1 mL of a 0.5 M CH_2Cl_2 solution of TFA were added *via* gastight syringes (Hamilton TLL, Series 1700, Model 1702 and 1705) to a 5 mL CH_2Cl_2 solution of the catalyst (1 mM) with 0.4 M $[N^nBu_4][BF_4]$.

The UV/vis spectroelectrochemical experiments were carried out at 273 K or 243 K with an optically transparent electrode mounted in a modified quartz cuvette with an optical pathlength of 0.5 mm. A three-electrode configuration consisting a Pt/Rh gauze working electrode, a Pt wire secondary electrode (in a fritted PTFE sleeve) and a saturated Ag/AgCl electrode, chemically isolated from the test solution via a bridge tube containing electrolyte solution and terminated in a porous frit, was used in the cell. The potential at the working electrode was controlled by a Sycopel Scientific Ltd. DD10M potentiostat. The UV-visible spectra were recorded on a Perkin Elmer Lambda 16 spectrophotometer. The spectrometer cavity was purged with N_2 and temperature control at the sample was achieved by flowing cooled N_2 across the surface of the cell.

X-band EPR spectra were recorded on a Bruker EMX spectrometer at the University of Nottingham. Frozen solution spectra were collected using a Wilmad quartz EPR Dewar with liquid N_2. The simulations of the EPR spectra were performed using the Bruker WINEPR SimFonia package.

A.2 Computational details

DFT calculations were performed using the Amsterdam Density Functional (ADF) suite of programs, version 2014.01.[2] Models derived from crystallographically obtained structures were used for geometry optimisations and no constraints were placed on these optimisations.

Slater type orbitals triple plus polarisation basis sets using the ZORA/TZP database of the ADF suite were employed, with scalar relativistic approaches used within the ZORA Hamiltonian for the inclusion of relativistic effects. The functionals of Becke[3] and Perdew[4] were used. COSMO[5] solvation functions were employed.

Molecular models were manipulated using the program ArgusLab, optimised structures were visualised using Mercury[6] and plots of calculated electronic structures were produced using Molekel[7] and ADF.[2]

A.3 Crystallographic data

Crystallographic measurements were made by the Crystal Structure Service at the University of Nottingham using one of the following instruments: Agilent GV 1000 Atlas or SuperNova diffractometer with CCD area detector and CuKα (λ 1.5418 Å) microfocus X-ray source and ω scans. Temperatures were regulated with an Oxford Cryosystems openflow cryostat.[8] Empirical absorptions were applied using SADABS.[9] Structures were solved either by direct methods or charge flipping methods using the program OLEX2.[10] When necessary crystallographic data were treated using the PLATON program SQUEEZE routine.[11] Crystal structure diagrams were produced with the ORTEP-3 software version 2.02.[12] H-atoms were constrained to the parent site. The absorption correction was done using the multi-scan method (based on symmetry-related measurements). Computer Programs used: CrysAlisPro (Agilent 2012).

The identification codes for the structures are as follow:

Compound	Identifier
$q^{6,7}dt^{Me,Me}(SCN)_2$	OGLSLA
$q^{6,7}dt^{Et,Et}(SCN)_2$	CGSALB

$q^{6,7}dt^{H,tBu}(SCN)_2$	OGLSLC
$q^{6,7}dt^{Ph,Ph}(SCN)_2$	CGSALA
[Ni(p-$q^{6,7}dt^{Et,Et}$)]	GDJMLB
[Ni(p-$q^{6,7}dt^{H,tBu}$)]	NIGLSR
[Ni($qdt^{Me,Me}$)(dppe)]	MPJMLD
[Ni($qdt^{H,tBu}$)(dppe)]	DMJMAA
[Ni($q^{6,7}dt^{Me,Me}$)(dppe)]	NIGLST
[Ni($q^{6,7}dt^{Et,Et}$)(dppe)]	NIGLSL
[Ni($q^{6,7}dt^{H,tBu}$)(dppe)]	NIGLSH
[Ni($q^{6,7}dt^{Ph,Ph}$)(dppe)]	NIGLSN
[Ni(p-$q^{6,7}dt^{Me,Me}$)$Fe_2(CO)_6$]	NIGLSF
[Ni($q^{6,7}dt^{Et,Et}$)dppeFeCp$(CO)_2$]	NIGLSQ
[Ni($q^{6,7}dt^{H,tBu}$)dppeFeCp$(CO)_2$]	NIGLSO
[Ni(dppz$(S)_2$)(dppe)]	NIGLSJ

	OGLSLA	**CGSALB**	**OGLSLC**
Crystal data			
Chemical formula	$C_{12}H_8N_4S_2$	$C1_4H_{12}N_4S_2$	$C1_4H_{12}N_4S_2$
M_r	290.07	300.40	300.40
Crystal system, space group	Triclinic, *P*1	Monoclinic, $P2_1/n$	Monoclinic, $P2_1/c$
Temperature (K)	120(2)	120(2)	120(2)
a, b, c (Å)	4.5878(4), 10.6381(8), 13.4671(12)	7.9006(5), 18.7061(13), 9.4329(7)	11.4580(4), 19.3075(6), 6.6941(3)
α, β, γ (°)	108.048 (7), 98.444 (7), 91.387 (6)	90, 90.658(6), 90	90, 104.832(4), 90
V (Å^3)	616.45 (9)	1394.00(17)	1431.56(9)
Z	2	4	4
Radiation type	CuKα	CuKα	CuKα
μ (mm^{-1})	4.81	3.41	3.33
Crystal size (mm)	0.18 × 0.08 × 0.01	0.12 × 0.07 × 0.02	0.20 × 0.10 × 0.03
Data Collection			
Diffractometer	SuperNova, Dual, Cu at zero, Atlas	SuperNova, Dual, Cu at zero, Atlas	SuperNova, Dual, Cu at zero, Atlas
Absorption correction	Gaussian *CrysAlis PRO*	Gaussian *CrysAlis PRO*	Gaussian *CrysAlis PRO*
T_{min}, T_{max}		0.934, 0.984	0.681, 0.912
No. of measured, independent and observed [I > 2s(I)] reflections	5317, 2418, 2173	5584, 2761, 2436	19147, 2875, 2675
R_{int}	0.030	0.0406	0.036
$(\sin\theta/\lambda)_{max}$ (Å^{-1})	0.624	0.625	0.625
Refinement			
R[F^2 > 2σ(F^2)], *w*R(F^2), *S*	0.079, 0.235, 1.10	0.0616, 0.1717, 1.186	0.033, 0.092, 1.07
No. of reflections	2418	2761	2875
No. of parameters	165	183	184
No. of restraints	0	0	0
$\Delta\rho_{max}$, $\Delta\rho_{min}$ (e Å^{-3})	1.84, −0.35	0.52, -0.47	0.34/-0.32

	CGSALA	**GDJMLB**	**NIGLSR**
Crystal data			
Chemical formula	$C_{22}H_{12}N_4S_2$	$C_{27}H_{30}N_4NiS_4 \cdot CH_4O$	$C_{27}H_{30}N_4NiS_4$
M_r	396.48	629.54	682.42
Crystal system, space group	Monoclinic, *Pn*	Orthorhombic, *Pbca*	Monoclinic, $P2_1/c$
Temperature (K)	120(0)	120(0)	120(0)
a, b, c (Å)	5.9778 (3), 16.2054 (8), 9.7734 (5)	16.5849 (9), 8.2917 (5), 40.760 (3)	12.1704 (5), 7.3069 (4), 33.3778 (11)
α, β, γ (°)	91.224 (5), 90, 90	93.847 (4), 90, 90	93.847 (4), 90, 90
V (Å^3)	946.56 (8)	5605.1 (6)	2961.5 (2)
Z	2	8	4
Radiation type	Cu *K*α	Cu *K*α	Cu *K*α
m (mm^{-1})	2.67	4.02	5.45
Crystal size (mm)	0.21 × 0.02 × 0.01	0.62 × 0.09 × 0.02	0.09 × 0.04 × 0.03
Data Collection			
Diffractometer	GV1000, Atlas	GV1000, Atlas	XtalLAB PRO *MM007*, PILATUS3 R 200K
Absorption correction	Gaussian *CrysAlis PRO*	Gaussian *CrysAlis PRO*	Gaussian *CrysAlis PRO*
T_{min}, T_{max}	0.873, 0.984	0.688, 0.969	0.987, 0.996
No. of measured, independent and observed [I > 2s(I)] reflections	6409, 2740, 2529	15009, 5548, 4572	31554, 5217, 4473
R_{int}	0.052	0.076	0.081
$(\sin\theta/\lambda)_{max}$ (Å^{-1})	0.624	0.624	0.595
Refinement			
R[F2 > 2s(F2)], wR(F2), S	0.038, 0.088, 1.03	0.084, 0.226, 1.08	0.186, 0.457, 1.13
No. of reflections	2740	5548	5217
No. of parameters	253	349	331
No. of restraints	2	0	0
$\Delta\rho_{max}$, $\Delta\rho_{min}$ (e Å^{-3})	0.22, −0.25	0.94, −0.98	2.28, −1.95

	MPJMLD	**DMJMAA**	**NIGLST**
Crystal data			
Chemical formula	$C_{39}H_{36}Cl_2N_2NiP_2S_2 \cdot CCl_3$	$C_{36}H_{32}N_2NiP_2S_2 \cdot 0.5(CH_2Cl_2)$	$C_{36}H_{32}N_2NiP_2S_2$
M_r	823.82	719.87	677.40
Crystal system, space group	Monoclinic, $P2_1/c$	Monoclinic, $P2_1/n$	Monoclinic, $P2_1/n$
Temperature (K)	120(0)	120(0)	120(0)
a, b, c (Å)	14.6642(8), 20.2343(7), 14.2375(8)	45.188 (8), 9.6289 (3), 25.363 (4)	9.5961(3), 18.6190 (6), 17.5717 (5)
α, β, γ (°)	90, 114.669(7), 90	143.22 (4), 90, 90	90.757 (3), 90, 90
V (Å^3)	3839.0(4)	6608 (4)	3139.27 (16)
Z	4	8	4
Radiation type	CuKα	CuKα	CuKα
m (mm^{-1})	4.70	3.92	3.32
Crystal size (mm)	0.34 × 0.07 × 0.04	0.77 × 0.14 × 0.06	0.21 × 0.13 × 0.09
Data Collection			
Diffractometer	GV1000, Atlas	GV1000, TitanS2	GV1000, TitanS2
Absorption correction	Gaussian *CrysAlis PRO*	Gaussian *CrysAlis PRO*	Gaussian *CrysAlis PRO*
T_{min}, T_{max}	0.539,0.870	0.315, 0.862	0.679, 0.811
No. of measured, independent and observed [I > 2s(I)] reflections	20393, 7565, 6067	28375, 13019, 11140	8772, 5258, 4599
R_{int}	0.041	0.044	0.028
$(\sin\theta/\lambda)_{max}$ (Å^{-1})	0.622	0.625	0.625
Refinement			
R[F2 > 2s(F2)], wR(F2), S	0.049, 0.127, 1.02	0.046, 0.123, 1.02	0.035, 0.094, 1.02
No. of reflections	7565	13019	5258
No. of parameters	448	806	390
No. of restraints	36	0	0
$\Delta\rho_{max}$, $\Delta\rho_{min}$ (e Å^{-3})	1.00, −0.64	1.26, −0.57	0.48, −0.26

	NIGLSL	**NIGLSH**	**NIGLSN**
Crystal data			
Chemical formula	$C_{38}H_{36}N_2NiP_2S_2$	$C_{38}H_{36}N_2NiP_2S_2 \cdot 2(CH_2Cl_2)$	$C_{46}H_{36}N_2NiP_2S_2 \cdot CH_2Cl_2$
M_r	707.47	875.31	886.46
Crystal system, space group	Tetragonal, $P4_32_12$	Monoclinic, $P2_1/n$	Monoclinic, $P2_1/n$
Temperature (K)	120(0)	120(0)	120(0)
a, b, c (Å)	15.94185 (15), 13.3836 (2)	13.1652 (2), 12.9763 (3), 23.7478 (5)	9.3864 (2), 18.6460 (4), 23.2848 (5)
α, β, γ (°)	90, 90, 90	95.8021 (17), 90, 90	90.956 (2), 90, 90
V (Å^3)	3401.35 (9)	4036.16 (13)	4074.68 (16)
Z	4	4	4
Radiation type	Cu *K*α	Cu *K*α	Cu *K*α
m (mm^{-1})	3.09	5.09	3.88
Crystal size (mm)	0.26 × 0.21 × 0.10	0.38 × 0.24 × 0.17	0.08 × 0.06 × 0.05
Data Collection			
Diffractometer	GV1000, TitanS2	SuperNova, Dual	SuperNova, Dual
Absorption correction	Gaussian *CrysAlis PRO*	Gaussian *CrysAlis PRO*	Gaussian *CrysAlis PRO*
T_{min}, T_{max}	0.542, 0.762	0.443, 0.701	0.942, 0.962
No. of measured, independent and observed [I > 2s(I)] reflections	7602, 3273, 3143	17509, 8028, 7377	36473, 8203, 7419
R_{int}	0.041	0.025	0.028
$(\sin\theta/\lambda)_{max}$ (Å^{-1})	0.622	0.624	0.625
Refinement			
R[F2 > 2s(F2)], wR(F2), S	0.041, 0.109, 1.03	0.033, 0.085, 1.04	0.032, 0.083, 1.03
No. of reflections	3273	8028	8203
No. of parameters	205	463	505
No. of restraints	0	0	0
$\Delta\rho_{max}$, $\Delta\rho_{min}$ (e Å^{-3})	0.36, −0.31	0.55, −0.54	1.25, −0.79

	NIGLSF	**NIGLSQ**	**NIGLSO**
Crystal data			
Chemical formula	$C_{29}Fe_2N_4NiO_6S_4$ ·2(CCl)	$C_{45}H_{42}FeN_2NiO_2P_2S_2$ ·2(CH_2Cl_2)·BF_4	$C_{45}H_{41}FeN_2NiO_2P_2S_2$ ·2(CH_2Cl_2)·BF_4
M_r	893.92	1140.09	1139.08
Crystal system, space group	Triclinic, *P*1	Monoclinic, $P2_1/n$	Triclinic, *P*1
Temperature (K)	120(0)	120(0)	120(0)
a, b, c (Å)	10.6433(11), 12.0963(9, 15.3020(13)	15.9175(6), 19.3666(7), 18.2322(7)	10.8877(4), 13.9106(5), 16.2917(6)
α, β, γ (°)	68.431(7), 71.790(9), 8.299(7)	111.183 (4), 90, 90	89.734(3), 87.807(3), 84.784(3)
V (Å^3)	1732.2 (3)	5240.6 (4)	2455.44 (17)
Z	2	4	2
Radiation type	Cu *K*α	Cu *K*α	Cu *K*α
m (mm^{-1})	11.36	6.31	6.73
Crystal size (mm)	0.14 × 0.10 × 0.02	0.20 × 0.11 × 0.08	0.16 × 0.10 × 0.08
Data Collection			
Diffractometer	SuperNova, Dual	GV1000, AtlasS2	GV1000, TitanS2
Absorption correction	Gaussian *CrysAlis PRO*	Gaussian *CrysAlis PRO*	Gaussian *CrysAlis PRO*
T_{min}, T_{max}	0.302, 0.815	0.544, 0.760	0.596, 0.761
No. of measured, independent and observed [I > 2s(I)] reflections	8262, 5444, 4387	42515, 10408, 7355	30914, 9699, 8078
R_{int}	0.068	0.072	0.065
$(\sin\theta/\lambda)_{max}$ (Å^{-1})	0.626	0.622	0.624
Refinement			
R[F2 > 2s(F2)], wR(F2), S	0.137, 0.372, 2.24	0.104, 0.331, 1.22	0.054, 0.149, 1.04
No. of reflections	5444	10408	9699
No. of parameters	450	688	616
No. of restraints	2	208	11
$\Delta\rho_{max}$, $\Delta\rho_{min}$ (e Å^{-3})	3.63, −2.06	1.91, −1.15	1.29, −1.00

	NIGLSJ		
Crystal data			
Chemical formula	$C_{44}H_{32}N_4NiP_2S_2$		
M_r	802.01		
Crystal system, space group	Triclinic, *P*1		
Temperature (K)	120(0)		
a, b, c (Å)	15.0806(8), 15.9987(7), 19.8239(5)		
α, β, γ (°)	82.030 (3), 79.891 (3), 76.748 (4)		
V (Å^3)	4559.0 (4)		
Z	4		
Radiation type	Cu *K*α		
m (mm^{-1})	2.38		
Crystal size (mm)	0.35 × 0.15 × 0.03		
Data Collection			
Diffractometer	SuperNova, Dual		
Absorption correction	Gaussian *CrysAlis PRO*		
T_{min}, T_{max}	0.909, 0.985		
No. of measured, independent and observed [I > 2s(I)] reflections	35372, 18151, 14312		
R_{int}	0.050		
$(\sin\theta/\lambda)_{max}$ (Å^{-1})	0.628		
Refinement			
R[F2 > 2s(F2)], wR(F2), S	0.097, 0.316, 1.24		
No. of reflections	18151		
No. of parameters	955		
No. of restraints	0		
$\Delta\rho_{max}$, $\Delta\rho_{min}$ (e Å^{-3})	3.31, −0.86		

A.4 References

1 R. S. Nicholson and I. Shain, *Anal. Chem.*, 1964, **36**, 706–723.

2 G. te Velde, F. M. Bickelhaupt, E. J. Baerends, C. Fonseca Guerra, S. J. A. van Gisbergen,

J. G. Snijders and T. Ziegler, *J. Comput. Chem.*, 2001, **22**, 931–967.

3 A. D. Becke, *Phys. Rev. A*, 1988, **38**, 3098–3100.

4 J. P. Perdew, *Phys. Rev. B*, 1986, **33**, 8822–8824.

5 A. Klamt and G. Schüürmann, *J. Chem. Soc., Perkin Trans. 2*, 1993, 799–805.

6 C. F. Macrae, P. R. Edgington, P. McCabe, E. Pidcock, G. P. Shields, R. Taylor, M. Towler and J. van de Streek, *J. Appl. Crystallogr.*, 2006, **39**, 453–457.

7 H. Portmann, S; Luthi, *Chimia (Aarau).*, 2000, **54**, 766–770.

8 J. Cosier and A. M. Glazer, *J. Appl. Crystallogr.*, 1986, **19**, 105–107.

9 G. M. Sheldrick, *Acta Crystallogr. Sect. A Found. Crystallogr.*, 1990, **46**, 467–473.

10 O. V. Dolomanov, L. J. Bourhis, R. J. Gildea, J. A. K. Howard and H. Puschmann, *J. Appl. Crystallogr.*, 2009, **42**, 339–341.

11 A. L. Spek, *Acta Crystallogr. Sect. D Biol. Crystallogr.*, 2009, **65**, 148–155.

12 L. J. Farrugia, *J. Appl. Crystallogr.*, 2012, **45**, 849–854.